UNIVERSITY OF CALIFORNIA,
IRVINE

An Investigation of Anodic Aluminum Oxide for Electronic and MEMS Applications

DISSERTATION

submitted in partial satisfaction of the requirements
for the degree of

DOCTOR OF PHILOSOPHY

in Electrical and Computer Engineering

by

Dogukan Yildirim

Dissertation Committee:
Professor Guann-Pyng Li, Chair
Professor Ozdal Boyraz
Professor Michael Green

2016

DEDICATION

To

my parents and sister

TABLE OF CONTENTS

LIST OF FIGURES

Page

LIST OF TABLES

Page

ACKNOWLEDGMENTS

I would like to express my deepest appreciation to my committee chair, Professor Guann-Pyng Li, for his valuable advice, suggestions, guidance, and support throughout my thesis. I would also like to thank to my committee members Professor Ozdal Boyraz and Professor Michael Green for their time and reviews. I would also like to thank Dr. Mark Bachman for his recommendations, contributions, and help. I am also thankful to the Republic of Turkey Ministry of National Education for doctoral scholarship and to the Broadcom foundation for doctoral fellowship.

CURRICULUM VITAE

Dogukan Yildirim

EDUCATION

Doctor of Philosophy in Electrical and Computer Engineering — **September 2016**
University of California, Irvine — Irvine, California

Master of Science in Electrical and Computer Engineering — **September 2011**
University of California, Irvine — Irvine, California

Bachelor of Science in Electrical and Electronics Engineering — **June 2007**
Sakarya University — Adapazarı, Sakarya

RESEARCH EXPERIENCE

Graduate Researcher — **September 2011-July 2016**
University of California, Irvine — Irvine, California

TEACHING EXPERIENCE

Teaching Assistant — **Spring Quarter, 2015**
University of California, Irvine — Irvine, California

Teaching Assistant — **Winter Quarter, 2015**
University of California, Irvine — Irvine, California

PUBLICATIONS

"Deep, High Aspect Ratio Etches in Alumina Films for MEMS and Advanced Packages" — **May-June 2016**
Electronic Components and Technology Conference

"On the Design of High Performance Spiral Inductors for Communication System in a Package (CSIP)" — **May-June 2015**
Electronic Components and Technology Conference

ABSTRACT OF THE DISSERTATION

An Investigation of Anodic Aluminum Oxide for Electronic and MEMS Applications

By

Dogukan Yildirim

Doctor of Philosophy in Electrical and Computer Engineering

University of California, Irvine, 2016

Professor Guann-Pyng Li, Chair

In this dissertation, we have explored the use of a highly anisotropic film, porous anodic aluminum oxide (AAO) for electronic and MEMS applications. In the first part, AAO templates integrated with ferromagnetic material were studied for spiral inductors as a magnetic core. In the second part, the applications of AAO as a structure material, a mold for electroforming, and a sacrificial layer for MEMS applications were demonstrated.

There is a strong demand for high performance and quality spiral inductors for radio frequency integrated circuits (RFIC). For this purpose, ferromagnetic materials are integrated into the spiral inductors to improve their performance and miniaturize their size. However, spiral inductors with ferromagnetic cores suffer from poor performance at high frequencies due to ferromagnetic resonance effect and eddy current loss occurrence in the layer of ferromagnetic materials. Since AAO templates are self-laminated and patterned, these drawbacks are solved by integration of ferromagnetic materials into the nanopores of AAO templates. By using nickel electroplated AAO templates as a magnetic core, we presented 21% enhancement of inductance value at 5 GHz with a quality factor of 14.48.

High precision, high aspect ratio structures are needed for a variety of microelectromechanical systems (MEMS) applications. The most common technology for producing high aspect ratio structures for MEMS is deep reactive ion etching (DRIE). Despite the successes of the DRIE process for MEMS applications, it has several significant shortcomings which limit its adoption for many microstructure applications. The DRIE process is expensive, time consuming, requiring expensive dedicated etching equipment, and primarily useful for etching structures in silicon, making it unlikely to be used for non-silicon applications. Other technologies, such as LIGA and SU-8 are highly specialized, and while they can be used for making simple structures, they are generally not useful for producing MEMS-like structures. Since AAO templates are highly anisotropic and can be prepared at various thicknesses, deep vertical structures with high aspect ratios can be formed by a simple low cost wet etching process. Various types of MEMS structures were fabricated by using this technique.

INTRODUCTION

Porous anodic aluminum oxide (AAO) templates have attracted much research interest in recent years due to their potential applications in electronics, magnetics, photonics, electrochemistry, and nanotechnology. AAO is a self-ordered nanoporous template that consists of a hexagonal array of cells with uniform and parallel straight cylindrical nanopores perpendicular to the template surface. AAO templates can be obtained by a two-step anodization process of aluminum in some electrolytes. Anodization of aluminum is a low cost process for the fabrication of large arrays of nanostructures with a very large aspect ratios (pore depth divided by pore diameter), which is not possible with standard lithographic techniques. AAO provides desirable features such as uniform pore sizes (5 to 400 nm), high pore densities (10^8-10^{11} /cm^2), and high aspect ratios. These features of AAO templates can be controlled by optimizing anodization conditions such as electrolyte, voltage, temperature, and time.

In this dissertation, highly anisotropic nature of AAO templates has been explored for electronic and MEMS applications. In the first part, AAO templates integrated with ferromagnetic material were studied for spiral inductors as a magnetic core. In the second part, the applications of AAO templates as a structure material, a mold for electroforming, and a sacrificial layer for MEMS applications were demonstrated.

There is a strong demand for high quality and performance integrated RF components such as, transformers, filters, oscillators, regulators, and matching networks for radio frequency integrated circuits (RFIC). One of the fundamental passive elements for implementation of those components into RFIC is inductors. However, inductance and quality factor of the spiral inductors do not scale efficiently with the number of turns, leading to excessive area

consumption and limited operating frequency. Thus, it is essential to increase inductance and quality factor of spiral inductors at high operating frequency and to miniaturize their size for realization of RFIC.

To further miniaturize the size, lower the cost, improve the performance, and increase the operating frequency of spiral inductors, integration of ferromagnetic materials into an air core inductor has attracted much research interest. Ferromagnetic materials act as the flux-amplifying components in spiral inductors and correspondingly, inductance and quality factor enhancement and area occupation reduction can be achieved in these inductors. However, spiral inductors with ferromagnetic cores suffer from poor performance at high frequencies due to ferromagnetic resonance (FMR) effect and eddy current loss occurrence in the layer of ferromagnetic materials. These two shortcomings of ferromagnetic materials need to be addressed properly in order to use them in spiral inductors.

The first drawback of the magnetic materials (FMR frequency) can be solved by patterning the magnetic film into small segments since pattering the magnetic film increases FMR frequency by increasing the anisotropy field. The second drawback of the magnetic materials (eddy current loss) can be solved by laminating the magnetic film into multiple layers with dielectric interlayer since laminating the magnetic film suppresses the eddy current loss. Considering that the most efficient way of concentrating magnetic flux in spiral inductors is to have magnetic materials fully surround the spiral inductors, the use of patterning and laminating film for fabricating the inductor is a very complex and challenging process.

The electroplating of a ferromagnetic material into AAO template is known to be the most simple and cost effective method to enhance the FMR frequency and suppress the eddy current loss. Ferromagnetic nanowires have high saturation magnetization, high effective

anisotropy field, high permeability, high FMR frequency and low eddy current loss due to the high aspect ratio of nanowires. Moreover, the magnetic properties of ferromagnetic nanowires can be tuned by applying an external DC magnetic field. Since AAO templates are self-laminated and patterned, they can be easily integrated with a spiral inductor without adding the complexities of fabrication process.

High precision, high aspect ratio structures are needed for a variety of microelectromechanical systems (MEMS) applications. For most MEMS applications, such structures are typically 50 microns to several hundred microns tall, and have pattern resolutions of a few microns. These can be used to form structural or electromechanical components for microsystems. Currently, there are only a few processes available to the MEMS designer for producing deep etches. These include LIGA, photostructurable glass such as Fotorun, photostructurable polymers such as SU-8 and PSR. The most common technology for producing high aspect ratio structures for MEMS is deep reactive ion etching (DRIE), sometimes referred to as the "Bosch" process, which uses a high energy plasma process to perform deep vertical etches in silicon.

Despite the successes of the DRIE process for MEMS applications, it has several significant shortcomings which limit its adoption for many microstructure applications. Although efforts have been made to use DRIE for etching glass and sapphire structures, DRIE is primarily useful for etching structures in silicon, making it unlikely to be used for non-silicon applications or for applications requiring low cost materials. The DRIE process is expensive and time consuming, requiring expensive dedicated etching equipment, use of corrosive gasses, including SF_6 and C_4F_6, produces non-uniform etches across a wafer, and requires many minutes, sometimes even hours, of etch time on the tool.

Other technologies, such as LIGA and SU-8 are highly specialized, and while they can be used for making simple structures, they are generally not useful for producing MEMS-like structures, which require additional materials, and sacrificial etches or undercut etches. Both produce only extruded structures (2.5D) of a single material. LIGA is specialized for producing simple mold inserts for precision injection molding, while SU-8 is useful primarily for making simple plastic structures.

Since AAO templates are highly anisotropic and can be prepared at various thicknesses, they can be used in producing high aspect ratio structures for MEMS applications. When AAO templates are etched in a simple wet etchant, they result in deep etch structures that have very high aspect ratios. The relatively low cost for the material, combined with low cost of etchant and ease of processing, make this an attractive alternative to expensive, complex processes such as DRIE. AAO can be processed to include other films, such as metals, to produce complex structures. In addition to use the AAO templates as a sacrificial layer, they can be used as a structure material and a mold for electroforming. Indeed, aluminum oxide is a mechanically strong material and has excellent dielectric properties, making this a compelling alternative to silicon for producing MEMS structures.

This dissertation is organized into five chapters. Chapter 1 gives an overview of porous anodic aluminum oxide templates, discusses anodization process and mechanism and stages of pore formation, and demonstrates the fabrication of highly-ordered open-through porous AAO templates. Chapter 2 gives an overview of electrodeposition methods, magnetism and magnetic material classifications, magnetic anisotropy, and discusses the magnetic properties of nickel nanowire arrays electrodeposited in AAO templates. Chapter 3 gives an overview of spiral inductors and TRL calibration, and discusses the spiral inductor fabrication with nickel

electroplated AAO templates as a magnetic core. Chapter 4 focuses on the applications of AAO templates as a structure material, a mold for electroforming, and a sacrificial layer for MEMS applications. Finally, Chapter 5 concludes this dissertation with a summary of the work done and suggests future works.

CHAPTER 1

POROUS ANODIC ALUMINUM OXIDE (AAO)

Porous anodic aluminum oxide (AAO) templates have attracted much research interest in recent years due to their potential applications in electronics, magnetics, photonics, electrochemistry, and nanotechnology **[1-10]**. AAO is a self-ordered nanoporous template that consists of a hexagonal array of cells with uniform and parallel straight cylindrical nanopores perpendicular to the template surface **[11-16]**. AAO templates can be obtained by a two-step anodization process of aluminum in some electrolytes **[17]**. After the first anodization, AAO template is removed and hexagonal texture is obtained on aluminum substrate to serve as a self-assembled mask for the second anodization. The anodization time of the first step has a considerable effect on the ordering of nanopores. As the anodization time of the first step increases, cells of the nanopores are rearranged and defect-free regions are obtained in large domains **[2]**. Therefore, after the long period of first anodization step, the second anodization step is sufficient to obtain highly ordered AAO templates. Anodization of aluminum is a low cost process for the fabrication of large arrays of nanostructures with a very large aspect ratio (pore depth divided by pore diameter), which is not possible with standard lithographic techniques **[18]**. AAO provides desirable features such as uniform pore sizes (5 to 400 nm), high pore densities (10^8-10^{11} /cm^2), and high aspect ratios **[19-20]**. These features of AAO templates can be controlled by optimizing anodization conditions such as electrolyte, voltage, temperature, and time.

1.1. Anodization of Aluminum

Anodization process is an electrochemical oxidation of aluminum foil at constant dc voltages in weak acidic electrolytes. Anodization of aluminum forms porous anodic aluminum oxide layer that consists of a hexagonal array of cells with uniform and cylindrical nanopores. During this process, a hemispherical continuous and insulating alumina layer is also formed between the bottom of the pore and the aluminum substrate; and is called barrier layer **[20, 21]**. Schematic diagram of a porous anodic alumina (AAO) template is shown in Figure 1.1.

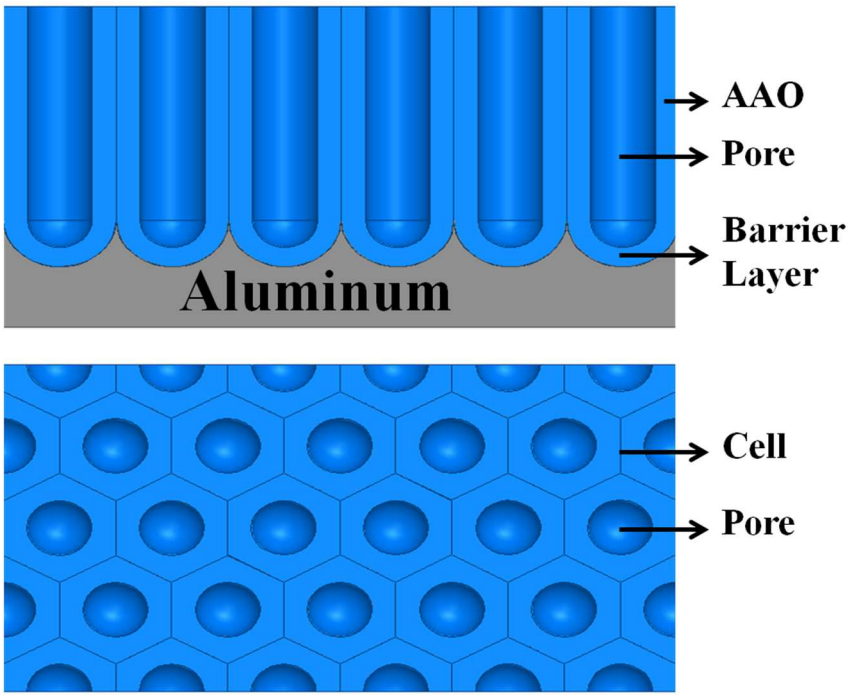

Figure 1.1. Schematic diagram of a porous AAO template.

The structural features of AAO templates, including pore diameter, cell size, barrier layer thickness, and AAO thickness can be controlled by adjusting anodization conditions such as type and concentration of electrolyte, applied voltage, temperature, and anodization time. The major acid electrolytes used in anodization process are sulfuric acid (H_2SO_4) **[15, 23, 24]**, oxalic acid ($H_2C_2O_4$) **[12, 19-22]**, and phosphoric acid (H_3PO_4) **[25-27]** solutions. In order to obtain uniform

and cylindrical pore distribution, type and concentration of electrolyte needs to be determined properly for a given anodization voltage. The specific anodization voltage for self-ordering of nanopores is 25V for sulfuric acid, 40V for oxalic acid, and 195V for phosphoric acid **[28]**. The type and concentration of electrolyte has an effect on pore diameter. Small, medium, and large pore diameters are formed by using sulfuric, oxalic, and phosphoric acid solutions, respectively. Applied voltage is one of the most important anodization conditions and has significant effect on cell size, pore diameter, barrier layer thickness, and oxide growth rate. The interpore distance (center to center distance between neighboring pores) is equal to the hexagonal cell size and it is proportional to the applied voltage (2.5 nm/V) **[13, 28, 29]**. The pore diameter is also proportional to the applied voltage (0.9 nm/V) under mild anodization conditions **[28]**. The thickness of the barrier layer is also proportional to the anodization voltage (1.3 nm/V) as well as interpore distance and pore diameter **[28]**. Higher applied voltages accelerate the anodization process and therefore oxide growth rate increases. Temperature has also considerable effect on pore formation. In general, temperature of the electrolyte is kept as low as $0^{o}C \sim 2^{o}C$ to prevent dissolution of formed oxide layer in acidic electrolyte and to avoid a local heating at pore bottoms. The local heat causes inhomogeneous electric field distribution at pore bottoms and leads breakdown of the oxide layer. In order to prevent effect of the heat, electrolytes are also stirred vigorously. Agitation is also an important treatment to maintain the stable growth of oxide layer **[25]**. Moreover, oxide growth rate is affected by the temperature. Lower temperatures decelerates the oxide growth rate, however, provides uniform pore formation. The thickness of the oxide layer has a linear relationship with anodization time. Thicker AAO templates can be obtained by long period of anodization. Major acidic electrolytes and optimum anodization conditions for self-ordered AAA templates are shown in Table 1.1.

Table 1.1. Major acidic electrolytes and optimum anodization conditions

Electrolyte	Concentration (M)	Voltage (V)	Cell Size (nm)	Temperature (^oC)	Pore Density (pores/cm^2)
Sulfuric acid	0.3	25	63	0 ± 2	~10^{11}
Oxalic acid	0.3	40	100	0 ± 2	~10^{10}
Phosphoric acid	0.3	195	500	0 ± 2	~10^9

The degree of hexagonal ordering decreases when the anodization process is performed outside the self-ordering regimes **[28, 30]**. In a given electrolyte, applied voltages higher than the optimum value results in 'breakdown' or 'burning' of the formed oxide layer caused by catastrophic flow of electric current on the aluminum substrate **[31]**.

1.2. Mechanisms of Pore Formation

One of the proposed and most commonly accepted mechanisms for pore formation is the mechanical stress model **[14]**. Based on this model, the mechanical stress coming from volume expansion of aluminum during oxide formation at the oxide/metal interface is proposed to cause repulsive forces between neighboring pores. These repulsive forces lead the formation of self-ordered pores in anodization process. The volume expansion of aluminum depends on applied voltage. Moderate anodization voltages result in moderate volume expansion, therefore, are most suitable to obtain self-ordered pore arrays. In case of high anodization voltages, no repulsive forces are expected between neighboring pores, therefore, large volume expansion takes place and results irregular pore formation.

The self-ordered pore arrays in anodic aluminum oxide forms from electric field assisted oxide dissolution at the electrolyte/oxide interface and oxide growth at the oxide/metal interface

[14]. When external voltage is applied, aluminum dissolves into Al^{3+} cations at anode and hydrogen ions are reduced to produce hydrogen gas at cathode.

$$Al(s) \rightarrow Al^{3+}(aq) + 3e^{-} \quad (1)$$

$$6H^{+}(aq) + 6e^{-} \rightarrow 3H_2(g) \quad (2)$$

Some of aluminum cations migrate through the barrier oxide layer and are ejected into the electrolyte at the electrolyte/oxide interface. Some of them react with oxygen containing ions (O^{2-} or OH^{-}) within the barrier layer and forms aluminum oxide. The dissolution of some aluminum cations leads porous oxide growth. In addition, the hydration reaction of the oxide layer takes place at electrolyte/oxide interface leading to dissolution and thinning of aluminum oxide **[15]**. Dissolution reaction of aluminum oxide can be written as

$$Al_2O_3(s) + 6H^{+}(aq) \rightarrow 2Al^{3+}(aq) + 3H_2O(l) \quad (3)$$

Oxygen anions react with aluminum at oxide/metal interface and forms aluminum oxide.

$$2Al(s) + 3O^{2-}(aq) \rightarrow Al_2O_3(s) + 6e^{-} \quad (4)$$

The overall chemical reaction for aluminum oxidation can be written as

$$2Al(s) + 3H_2O(l) \rightarrow Al_2O_3(s) + 6H^{+}(aq) + 6e^{-} \quad (5)$$

Since oxidation of aluminum takes place at the entire pore bottom simultaneously, the oxide layer can only expand in the vertical direction. Under steady state regime, field-enhanced oxide dissolution and oxide growth rates are in equilibrium; therefore, each pore grows perpendicular

to the aluminum surface with a constant thickness of barrier layer. Schematic diagram of pore formation in an acidic electrolyte is shown in Figure 1.2.

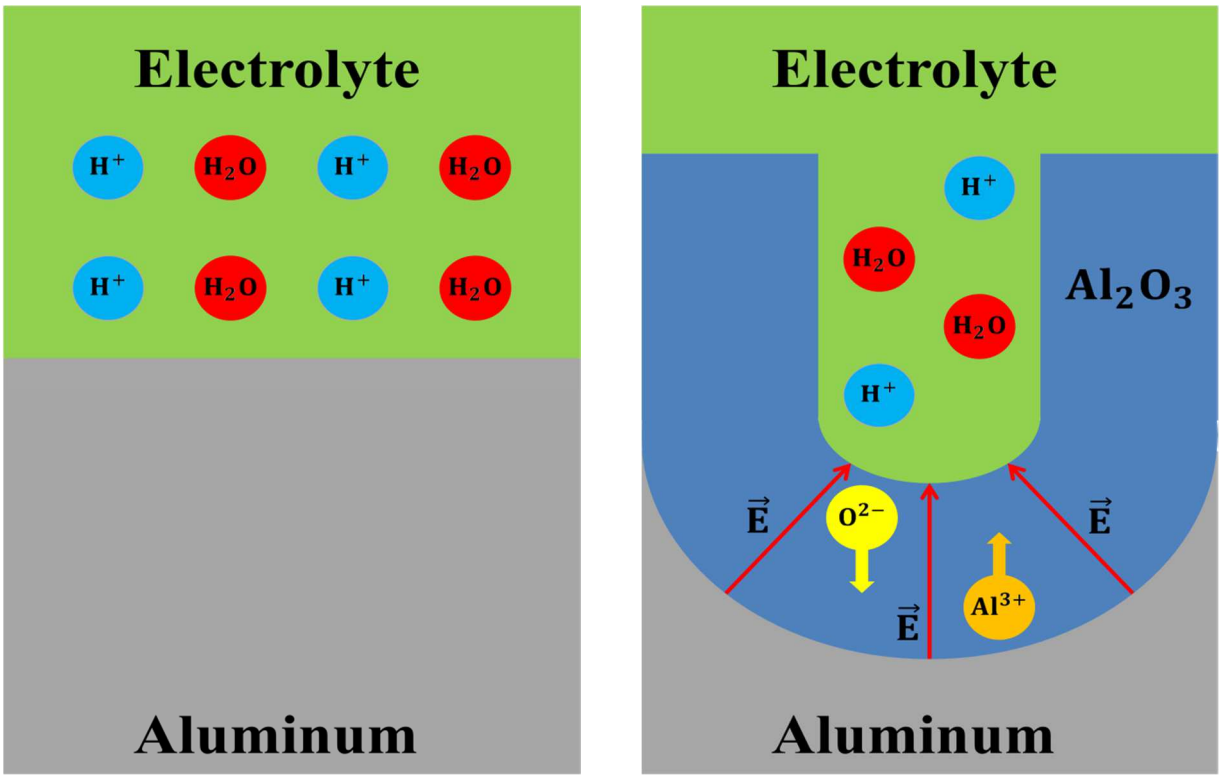

Figure 1.2. Schematic diagram of pore formation based on mechanical strength model.

The atomic density of aluminum in aluminum oxide is by a factor of two lower than in metallic aluminum **[14, 15]**. This volumetric expansion factor arises from the difference in the density of aluminum in aluminum oxide (3.2 g/cm^3) and that of metallic aluminum (2.7 g/cm^3). Based on this, two times of volume expansion of aluminum oxide is expected according to the original volume of aluminum. However, the volumetric expansion factor is less than two under normal experimental conditions **[15]**. This is due to the ejection of some of the Al^{3+} cations into the electrolyte and dissolution of aluminum oxide at electrolyte/oxide interface. The volume

expansion of aluminum oxide is strongly depends on anodization conditions such as applied voltage, electrolyte concentration, and electric field created by applied voltage. Therefore, the experimental volume expansion factor can range from 0.8 to 1.6 **[14]** which can be determined by the Pilling-Bedworth ratio (R_{PB}) **[32, 33]**. Pilling-Bedworth ratio is defined as the ratio of the molecular volume of oxide to the molecular volume of metal where the oxide is created; and is expressed as

$$R_{PB} = \frac{\text{Molecular volume of oxide}}{\text{Molecular volume of metal}} = \frac{M_{oxide}/\rho_{oxide}}{n\ M_{metal}/\rho_{metal}} \tag{6}$$

where M_{oxide} and M_{metal} refer to the molecular weights of oxide and metal, and ρ_{oxide} and ρ_{metal} refer to the densities of oxide and metal, and n is the number of metal atoms per one oxide molecule. The Pilling-Bedworth ratio can be written for aluminum and aluminum oxide as

$$R_{PB} = \frac{M_{Al_2O_3}/\rho_{Al_2O_3}}{n\ M_{Al}/\rho_{Al}} \tag{7}$$

In general, if the R_{PB} is less than 1, tensile stress arises in the oxide, oxide film is too thin and provides no protective effect. If the R_{PB} is greater than 2, large compressive stress arises, oxide film chips off and provides no protective effect. If the R_{PB} is greater than 1 but less than 2, moderate compressive stress arises, oxide film is passivating and provides a protective effect against further surface oxidation. The reported R_{PB} values such as 1.23 **[26]** and 1.4 **[15]** under optimal anodization conditions indicate the moderate mechanical stress in the oxide layer which leads ordered pore growth.

Another proposed mechanism to explain the generation and self-ordering of the pores and the formation of the hemispherical pore bottom is equifield strength model **[34, 35]**. Based on

this model, there is equilibrium between dissolution of oxide at electrolyte/oxide interface and oxidation of aluminum at oxide/metal interface. The dissolution reaction of oxide is expressed as

$$Al_2O_3 + nH_2O \rightarrow 2Al^{3+} + (3 + n - x)O^{2-} + xOH^- + (2n - x)H^+ \quad (8)$$

where n is the ratio of the dissociation rate of water to the dissolution rate of oxide, and x indicates the ratio of O^{2-} and OH^- anions. The oxidation reactions of aluminum by oxygen containing anions (O^{2-} and OH^-) which are produced from dissociation of water are expressed as

$$2Al + 3O^{2-} \rightarrow Al_2O_3 + 6e^- \quad (9)$$

$$2Al + 3OH^- \rightarrow Al_2O_3 + 3H^+ + 6e^- \quad (10)$$

The thickness of the barrier oxide layer (d_B), dissolution rate, oxidation rate, and electric filed strength (E_B) across the barrier oxide layer are all constant at a steady state under certain anodization conditions. Pore initiation and pore growth mechanism based on equifield strength model is shown in Figure 1.3. The electrolyte/oxide interface is represented by ABC and oxide/metal interface is represented by A'B'C'. A thin layer of barrier oxide is formed immediately when anodization voltage is applied. At the early stage of anodization, dissolution of oxide layer leads to pit growth due to the point defects in the oxide film. The thickness of oxide layer at BB' is smaller than at AA' and CC' after pit formation and causes relatively higher oxidation rate at B'. As a result of high electric strength at BB', the shape of the ABC surface is replicated at the oxide/metal interface. As anodization continues, a single pore moves down and penetrates the aluminum by leading a hemispherical pore bottom. At steady state

regime, uniform field strength is achieved at the whole electrolyte/oxide interface (DABCE) and oxide/metal interface (D'A'B'C'E'). Therefore, pore growth continues with a constant barrier oxide layer thickness of d_B.

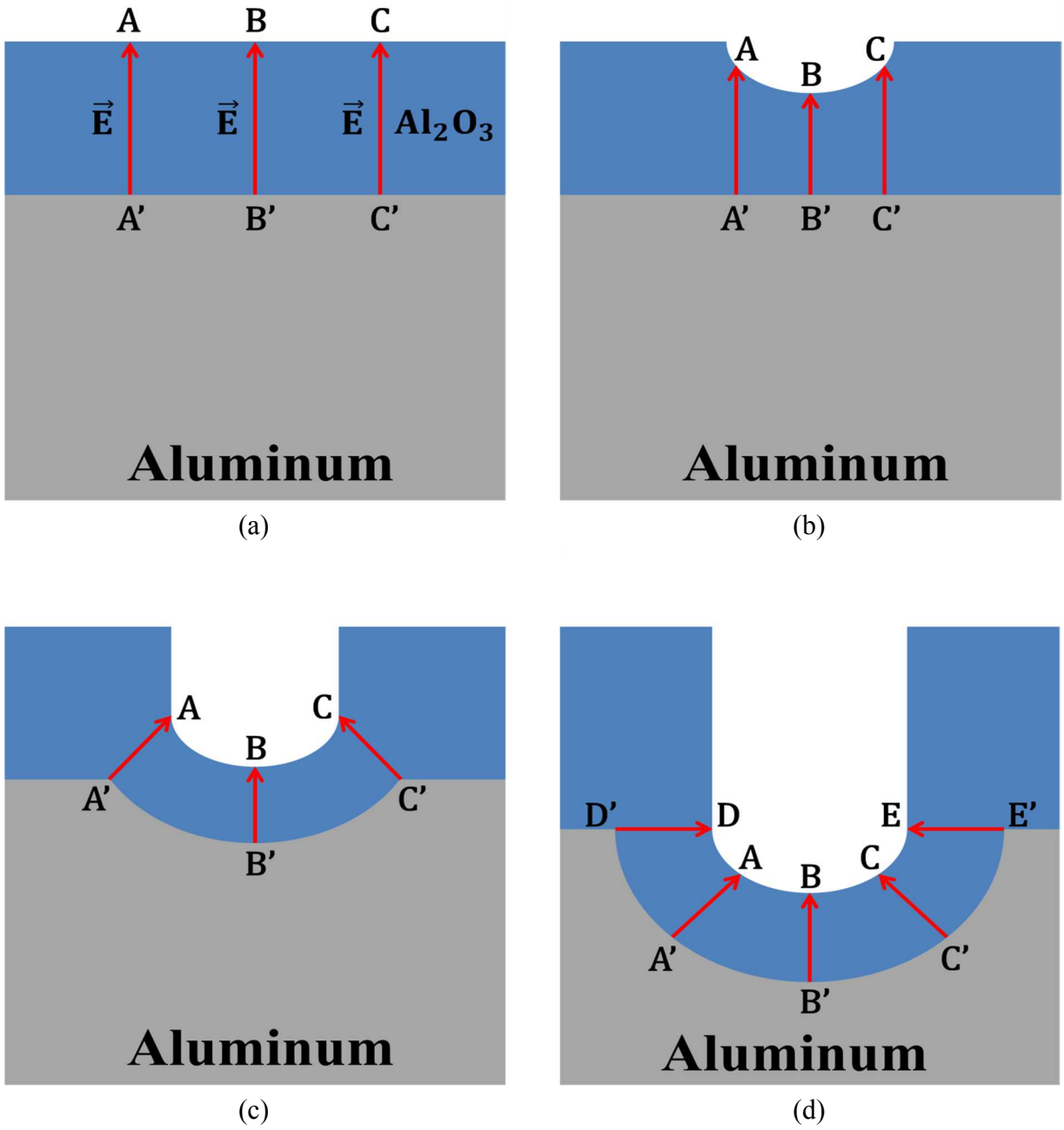

Figure 1.3. Schematic diagram of pore formation based on equifield strength model.

According to the equifield strength model, the oxide layer can move not only downwards but also sideways since electric field strength along DD' and EE' in the pore wall is the same as that at the pore bottom **[34]**. The self-adjustment of pores during anodization is depicted in Figure 1.4 by using a two-pore model. When two pores are separated as shown in Figure 1.4(a), they will expand and the neighboring walls of these two pores will move towards each other until two walls merge with a thickness of $2d_B$ (Figure 1.4(b)). Both pore bottoms are still hemispherical at this stage. The oxidation rate at joined position (B) is much higher than at any other position due to the migration of oxygen anions from both sides. Therefore, the joined position (B) will move down to a lower position (D) as shown in Figure 1.4(c). The dissolution rate of oxide at positions A and C will be faster than the oxidation rate at position D. As a result, oxide layer thickness will decrease and the wall thickness between pores become $2d_W$ which is smaller than $2d_B$. Therefore, pore bottoms are not perfectly hemispherical at this final stage.

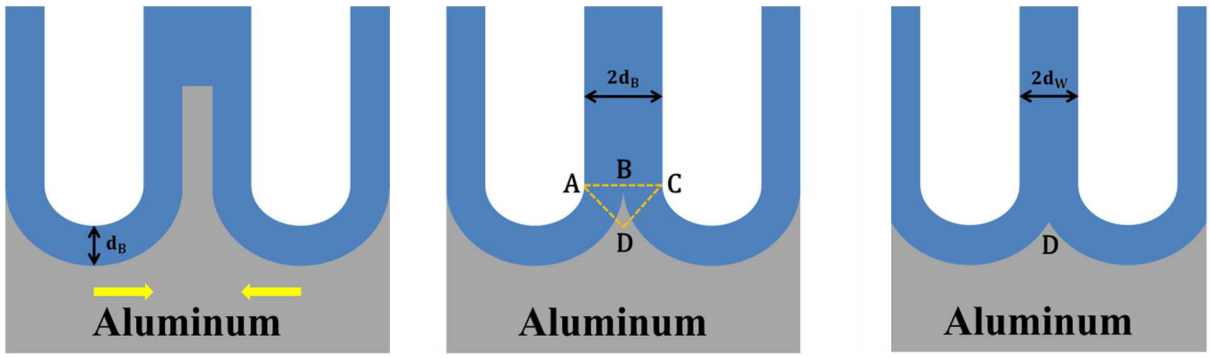

(a) (b) (c)

Figure 1.4. Schematic diagram of self-adjustment of pores.

1.3. Current Transient and Stages of Pore Formation in Anodization Process

Pore formation in anodic aluminum oxide consists of four stages that are detectable by monitoring the current transient **[36, 37]**. The current density curve as a function of time during anodization process is shown in Figure 1.5. In the first stage, a barrier oxide layer starts to form as the anodization potential is applied to the aluminum substrate. During the growth of the barrier layer, resistance of the substrate increases considerably and current density decreases sharply. In the second stage, the barrier oxide layer reaches a certain thickness when the current density curve shows a minimum value. In the third stage, pore nuclei formation and pore growth take place by local dissolution of the barrier layer due to the applied electric field. During the dissolution of the barrier layer, surface area increases and resistance of the substrate decreases, therefore, current density curve starts to increase. In the fourth stage, surface area reaches a constant value resulting in a stable current density curve. At this final stage, pores grow continuously with a constant thickness of barrier layer since oxide dissolution and formation rates are in equilibrium.

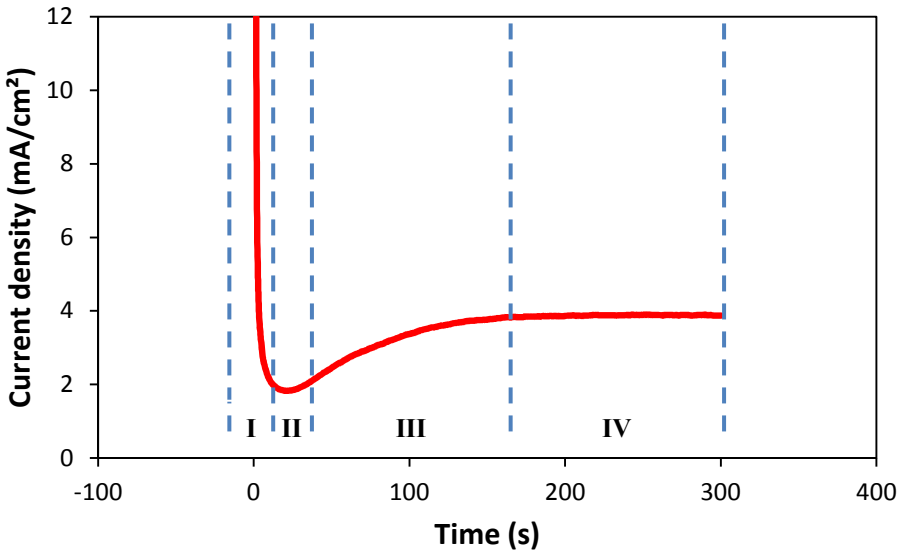

Figure 1.5. Current density curve as a function of time.

1.4. Two-step Anodization Process

Pore formation in anodic aluminum oxide templates initiates randomly on aluminum substrate and the degree of pore ordering is very low in the initial stage of anodization process. As anodization progress under appropriate conditions, self-organization process takes place and highly-ordered pore arrangement is obtained. The pore arrangement at oxide/metal interface is ordered and the pore arrangement at electrolyte/oxide interface is not ordered and reflects the initial pore nucleation sites that were produced at the early stages of anodization process **[15]**. In order to obtain highly-ordered pore arrangement at electrolyte/oxide interface, a special technique called two-step anodization is applied **[12, 38]**. In the first step, a long period of anodization is performed to form highly-ordered pore arrangement at oxide/metal interface. As the duration of the first step increases, domains in the bottom of porous oxide layer form on larger areas and more uniform pore distribution is obtained. After the first step, anodic aluminum oxide layer is selectively removed by wet chemical etching. After AAO removal, the surface of the aluminum substrate keeps the hexagonal texture of the pore tips which serves as a self-assembled mask for the second anodization step. Then, the second step is performed under same anodization conditions. Since highly-ordered concave pattern on aluminum substrate acts as initiation sites for pore formation in the second step, densely packed, uniform, straight, and parallel pore channels are obtained throughout the entire AAO layer **[39]**. Schematic diagram of two-step anodization process is shown in Figure 1.6.

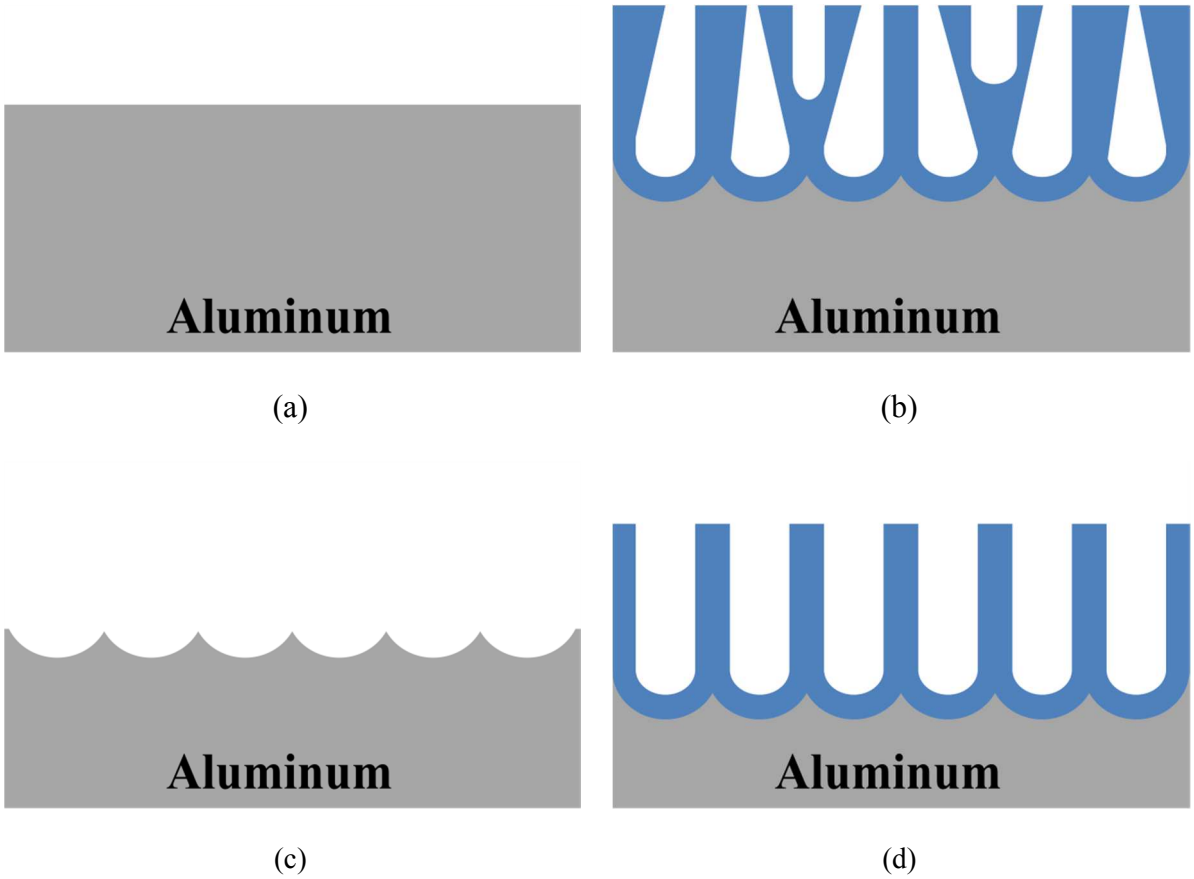

Figure 1.6. Schematic diagram of two-step anodization process.

1.5. Pore Density and Porosity in Anodic Aluminum Oxides

The pore density is defined as number of pores per unit area of AAO templates and expressed as **[28, 40]**

$$\rho = \frac{2}{\sqrt{3}D_{int}^2} \text{ x } 10^{14} \quad \text{pores/cm}^2 \tag{11}$$

where D_{int} is the interpore distance. According to the equation above, the pore density is inversely proportional to the square of the interpore distance. As mentioned earlier, the interpore distance is proportional to the applied voltage. Under optimum anodization conditions,

approximate pore densities of 10^{11}, 10^{10}, and 10^{9} are obtained in sulfuric, oxalic, and phosphoric acid electrolytes respectively.

The porosity is defined as the ratio of the volume of the pores (voids) to the total volume of the mass and expressed as a percentage **[26, 28, 40]**.

$$P(\%) = \frac{\pi}{2\sqrt{3}}\left(\frac{D_p}{D_{int}}\right)^2 x\ 100 \tag{12}$$

where D_p is the pore diameter. According to the expression, the porosity is mainly determined by the ratio of the pore diameter to the interpore distance. This ratio (D_p/D_{int}) is controlled by the electric field strength ($\vec{E}$) at the barrier oxide layer and decreases with increasing $\vec{E}$ during anodization **[31]**. In addition to the effect of $\vec{E}$ on porosity, the porosity of AAO templates is directly governed by the relative dissociation rate of water at the electrolyte/oxide interface **[34, 35]**, and can be obtained as

$$P = \frac{3}{n+3} \tag{13}$$

where n is the ratio of the dissociation rate of water to the dissolution rate of aluminum oxide. The n value is dependent on the electric field strength. In a steady state regime, the electric field strength is constant according to the proposed equifield strength model, and the n value and, therefore, the porosity are constant. However, under a stronger electric field, the dissociation rate of water will increase which results an increase of the n value, therefore, the porosity will decrease. The variation of the porosity of AAO as a function of n is shown in Figure 1.7 **[34, 35]**. As reported in **[31]**, the porosity decreased with increasing anodization voltage from ~35% at 5V to ~10% at 40V when aluminum was anodized in 0.3M oxalic acid electrolyte. According to the

Figure 1.7, this decrease of porosity can be explained with an increase of the n value from 5.6 to 27.

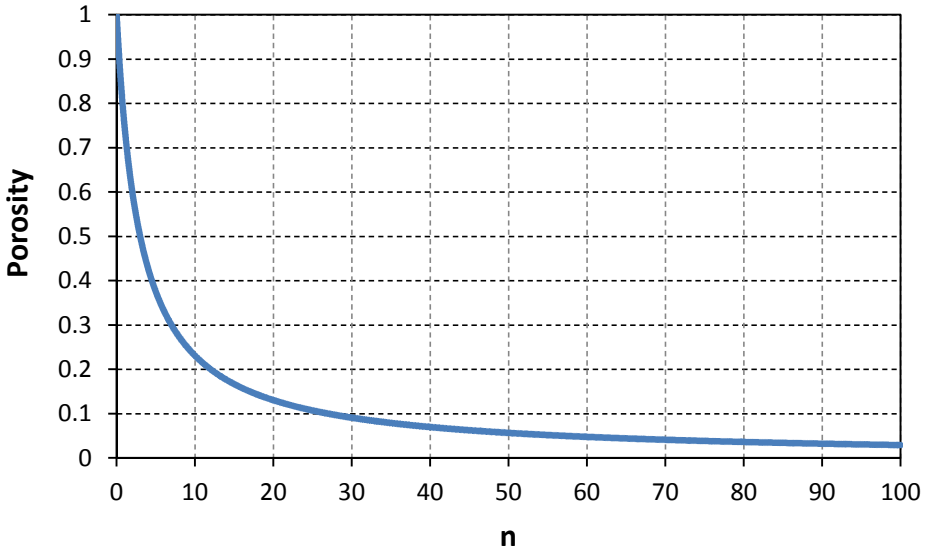

Figure 1.7. Porosity of AAO as a function of n.

The porosity of AAO templates is also determined by pore-filling method **[41, 42]**. In this method, aluminum is first anodized in an acid electrolyte to form porous-type anodic oxide layer and subsequently re-anodized in a neutral electrolyte to form barrier-type oxide layer under a constant current condition. New oxide layer gradually forms simultaneously within the pores and underneath the barrier layer of the pre-formed porous AAO since both O^{2-} anions and Al^{3+} cations contribute to the oxide formation at the oxide/metal interface and electrolyte/oxide interface, respectively. Voltage-time transient is monitored during re-anodization process. The movement of O^{2-} and Al^{3+} ions and voltage-time transient during re-anodization process is shown in Figure 1.8 **[41, 42]**. The non-zero value of voltage at t = 0 is due to the original barrier layer of pre-formed porous AAO.

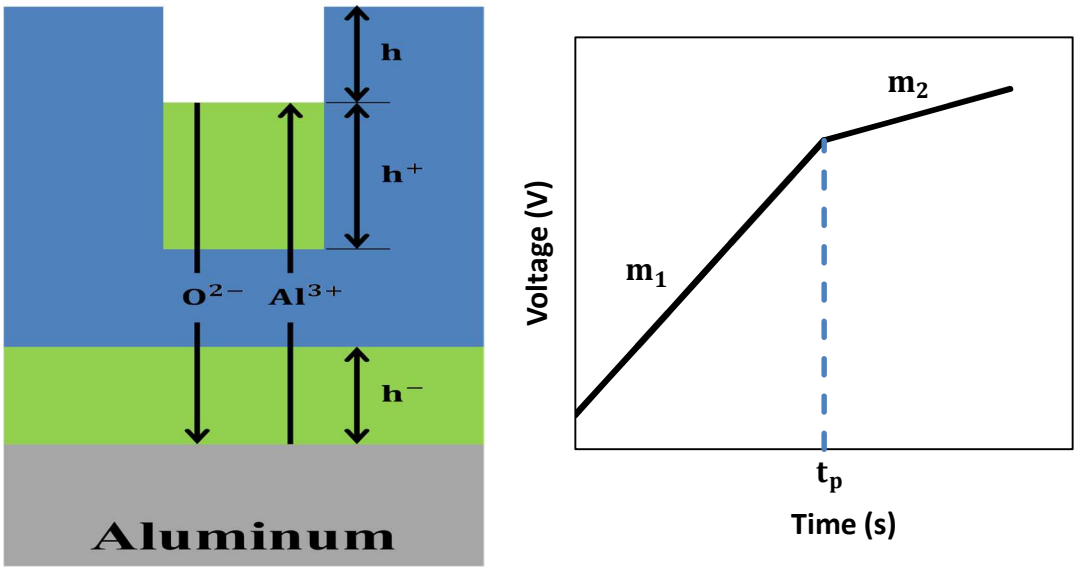

(a) (b)

Figure 1.8. Schematic diagrams of (a) ion movement and (b) voltage-time transient during re-anodization process.

The complete pore-filling is accompanied by the change of the slope at the time t_p due to the sudden increase of the electrolyte/oxide interfacial area. For the time $t < t_p$,

$$\rho\left[P\frac{dh^+}{dt}+\frac{dh^-}{dt}\right]=\frac{jM}{nFk} \tag{14}$$

where $\rho(=2.95\ g/cm^3)$ is the density of oxide, P is the porosity of porous AAO, dh^+/dt and dh^-/dt are the rates of the increase of the barrier oxide thickness at the electrolyte/oxide and oxide/electrolyte interfaces, respectively, j is the current density, M is the atomic weight of aluminum, n(=3) is the number of electrons associated with the oxide formation, F is the Faraday's constant, and k(=0.505) is the weight fraction of aluminum in the oxide. The transport number of Al^{3+} cations is defined by the ratio of the weight of new oxide formed in the pore per unit time to the total weight of new oxide formed per unit time and expressed as

$$T_{Al^{3+}} = \left(P\frac{dh^+}{dt}\right)\Big/\left(P\frac{dh^+}{dt} + \frac{dh^-}{dt}\right) \quad (15)$$

Similarly, the transport number of O^{2-} anions is expressed as expressed as

$$T_{O^{2-}} = \left(\frac{dh^-}{dt}\right)\Big/\left(P\frac{dh^+}{dt} + \frac{dh^-}{dt}\right) \quad (16)$$

The slopes m_1 and m_2 of the voltage-time transient are given by

$$m_1 = \frac{1}{K}\left(\frac{dh^+}{dt} + \frac{dh^-}{dt}\right) \quad (17)$$

and

$$m_2 = \frac{1}{K}\left(P\frac{dh^+}{dt} + \frac{dh^-}{dt}\right) \quad (18)$$

where K(nm/V) is the ratio of the barrier layer thickness to the voltage, and considered to be a constant. From equations 14-18, the porosity of porous AAO is given by

$$P = \frac{T_{Al^{3+}}(m_2/m_1)}{1-(1-T_{Al^{3+}})(m_2/m_1)} \quad (19)$$

As a result, the porosity of porous AAO can be determined by measuring m_1 and m_2 with known transport number of Al^{3+} cations.

1.6. Fabrication of Highly-Ordered Open-Through Porous Anodic Aluminum Oxide Templates

In order to fabricate nanostructures into the pores of AAO templates, demanding removal of the hemispherical barrier layer between pore bottom and aluminum substrate is needed. Different methods have been developed to remove the barrier layer completely.

In the first method, the barrier layer is removed by cathodic polarization process in a neutral potassium chloride (KCl) solution **[19, 20]**. During this process, the barrier layer is dissolved by OH^- ions generated at the pore bottom. However, this method has led to pore walls being dissolved as well as the barrier layer by these ions so that an increase in the pore diameter is typically observed. Cathodic polarization time to dissolve the barrier layer is dependent on the AAO template thickness, thus limiting the removal of the barrier layer in AAO templates thicker than 20 μm. Since dissolution of the barrier layer and the pore wall occurs simultaneously, a longer cathodic polarization time damages the AAO template. To alleviate this time sensitive process, additional process control in reducing anodization voltage is required to thin the barrier layer at the end of the anodization before performing cathodic polarization process.

In the second method, the barrier layer is removed by electrochemical voltage pulse detachment process **[37, 43-46]**. During this process, a short voltage pulse of 5-10V higher than the anodization voltage is applied in perchloric acid ($HClO_4$) containing solution to detach the AAO template from the aluminum substrate and freestanding AAO template is obtained. However AAO templates formed with high anodization voltage have relatively thick barrier layer and thus several times of voltage pulse is required for detachment of AAO template. It has been reported that the uniformity of the detached side of AAO template is quite low compared to the top surface, in challenging a reproducible process for uniform and open-through

AAO template **[44]**. In addition, perchloric acid may form explosive mixtures with organic compounds, implying a not very robust process **[44]**.

In the third method, the barrier layer is removed by wet chemical etching solution such as phosphoric acid (H_3PO_4) or electrochemical etching solution such as KCl without the need to remove the AAO template from the substrate. During this process, a thin layer in the range of 0.4-2 um of aluminum is evaporated on single layer or multilayer substrates such as Si **[29]**, Si/Pt/Ti **[47]**, Si/Au **[48, 49]**, Si/SiO_2/Ti/Pt, Si/Ti **[50, 51]**, Glass/SiO_2/ITO **[52]**, Glass/ITO/Ti **[53]**, Si/Ta **[54]**, Glass/ITO **[55]**, and Si/Ti/Au **[56]**. The barrier layer between the AAO template and these substrates has an inverted morphology with voids and is different from that of alumina templates grown on aluminum substrates.

In the fourth method, the barrier layer is removed by the wet chemical etching of free standing AAO template in a phosphoric acid solution. During this process, aluminum substrate is removed in saturated solutions such as mercury(II) chloride ($HgCl_2$) **[12-15, 57, 58]**, iodine-methanol **[59]**, stannic chloride ($SnCl_4$) **[60]**, or cupric chloride and hydrochloric acid ($CuCl_2 \cdot HCl$) **[61, 62]**. Subsequently, the barrier layer is removed and pores are widened by wet chemical etching in a phosphoric acid solution.

In this work, we investigated the wet chemical etching removal process of the barrier layer in highly-ordered porous AAO templates fabricated by two anodization solutions of aluminum; one by oxalic acid and the other sulfuric acid electrolytes. The morphology of these templates were characterized and compared by scanning electron microscopy (SEM). The applicability of this method for two types of anodized templates was systematically studied and free-standing open-through AAO templates were obtained.

1.6.1. Experimental

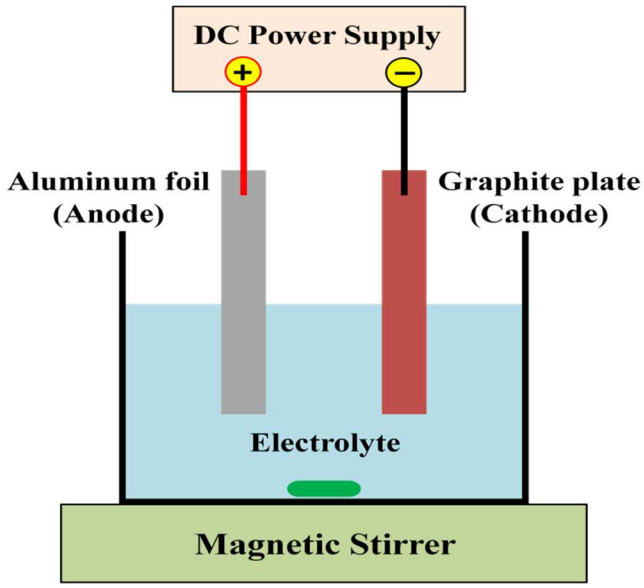

Figure 1.9. Schematic diagram of anodization setup

High purity (99.99%) aluminum foils of 0.25 mm thickness were used for anodization process. These aluminum foils were ultrasonically degreased in acetone and isopropyl alcohol, and then rinsed in deionized water. Prior to anodization, native oxide layer on aluminum foils were removed in a mixture solution of H_3PO_4 (6 wt %) and CrO_3 (2 wt %) at 65℃ for 10 min. The aluminum foil was used as the anode and a graphite plate was used as the cathode in anodization process. Schematic diagram of anodization setup is shown in Figure 1.9. The AAO templates were prepared by using a two-step anodization process in either oxalic or sulfuric acid solutions for different pore sizes. The solutions were stirred vigorously using a magnetic stirrer in order to accelerate the diffusion of the heat that evolved from samples. In the first anodization step, the aluminum foils were anodized either in a 0.3M oxalic acid ($C_2H_2O_4$) solution at 60V and at 1℃ for 2 h, or in a 0.3M sulfuric acid (H_2SO_4) solution at 25V and 1°C for 2 h. After the first anodization, the alumina template was removed in a mixture solution of H_3PO_4 (6 wt %)

and CrO_3 (2 wt %) at 65℃ for 40 min. After AAO removal, the surface of the aluminum substrate kept the hexagonal texture of the pore tips which served as a self-assembled mask for the second anodization process. The second anodization step was performed for 3 h for oxalic acid anodized samples and for 6 h for sulfuric acid anodized samples under the same process conditions as the first anodization step. At the end of second anodization, highly-ordered porous anodic aluminum oxide templates were obtained with pore size of 55 nm and 20 nm for oxalic acid and sulfuric acid solutions, respectively.

After two-step anodization process, a 0.5 cm^2 area was opened on the backside of the template by etching the aluminum substrate in an aqueous solution of $CuCl_2 \cdot HCl$ at room temperature, and the surrounding aluminum was retained as a support. Then, the remaining alumina barrier layer at the bottom of the pores was removed in a 10 wt% phosphoric acid (H_3PO_4) solution at 30℃ for 36 min and 14 min for oxalic and sulfuric acid anodized templates, respectively. Photoresist was used to protect the top surface of the template from etching solutions. During this process, pore diameters increased slightly and open-through AAO templates were obtained. Figure 1.10 shows the schematic diagram of barrier layer removal process to obtain open-through porous AAO templates. The process steps are (a) fabrication of AAO template, (b) photoresist coating on top surface, (c) removal of aluminum foil, (d) removal of barrier layer and pore widening, and (e) removal of photoresist and obtaining open-through AAO template, respectively. The morphologies and pore structures of porous AAO templates anodized in oxalic and sulfuric acid solutions were characterized by scanning electron microscope.

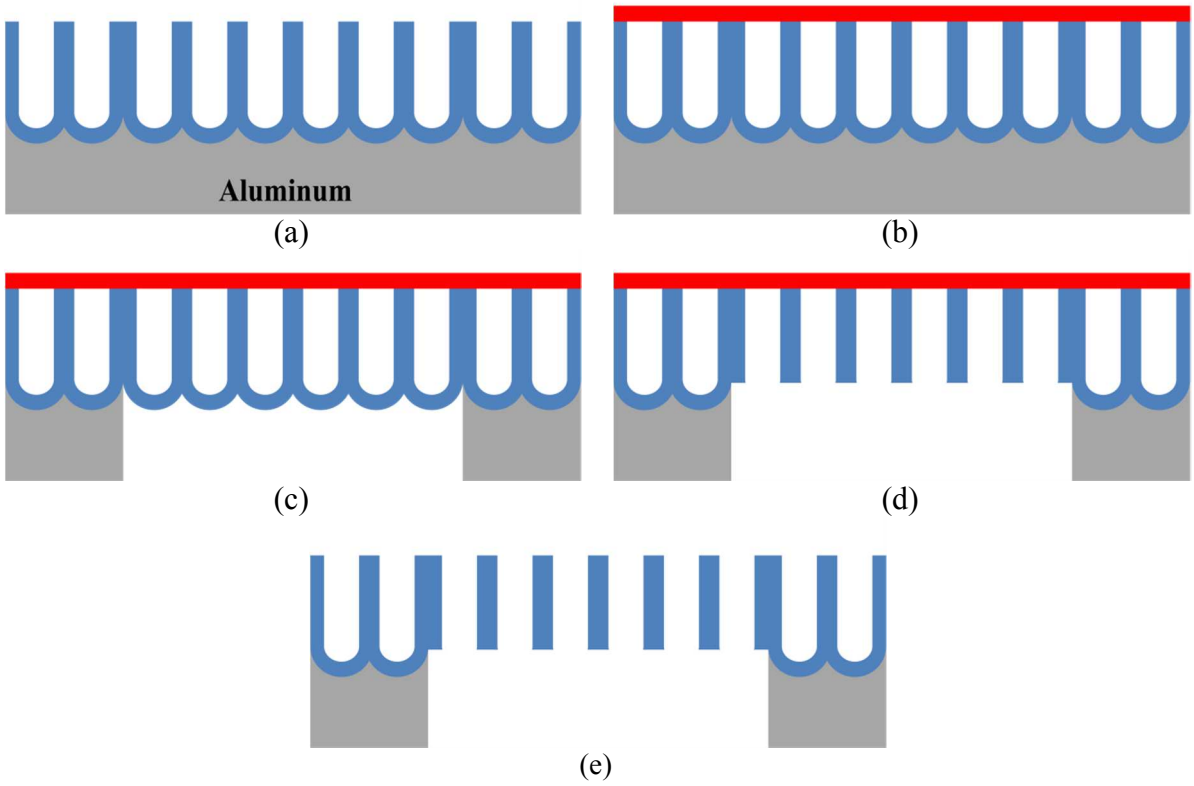

Figure 1.10. Schematic diagram of barrier layer removal process.

1.6.2. Results and Discussion

The current density curves as a function of time for anodization processes in oxalic and sulfuric acid solutions are shown in Figure 1.11. According to the current density curves for both oxalic and sulfuric acid anodized samples, there are some important differences between first and second anodization processes. The time for reaching the lowest and constant current density for the second anodization process is shorter than this for the first anodization process. The reason is that porous structure is not yet formed at the beginning of the first anodization and therefore pore nucleation, pore growth, and reaching the steady-state regime takes longer time. However, it takes shorter time in the second anodization process due to the formation of pore patterning on aluminum substrate after the first anodization process. The observed value of the lowest and

constant current density is also higher in the second anodization process due to the large surface area on patterned aluminum substrate.

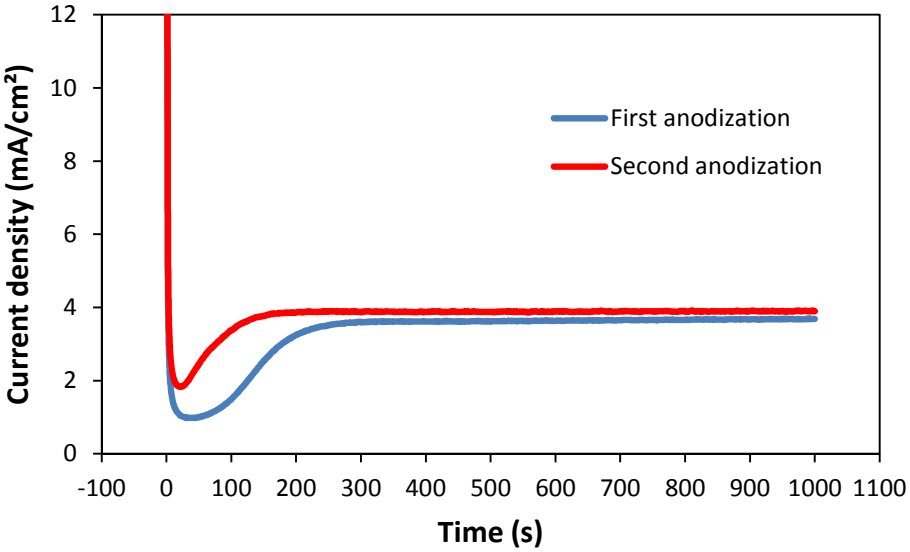

(a) Oxalic acid anodized sample

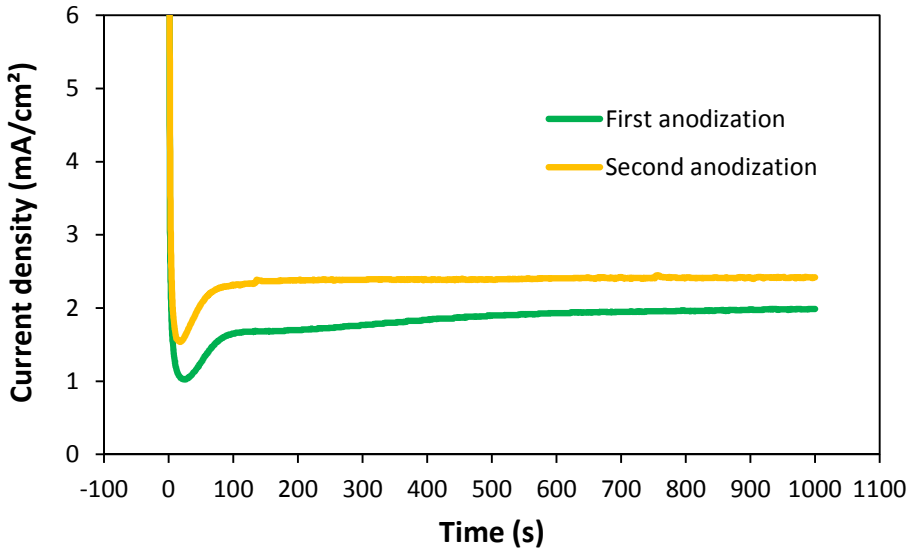

(b) Sulfuric acid anodized sample

Figure 1.11. Current density curves as a function of time for anodization processes.

According to the current density curves, it takes approximately 3.2 min to reach the maximum current density of 3.86 mA/cm^2 in the second anodization process in oxalic acid solution.

It takes approximately 1.5 min to reach the maximum current density of 2.3 mA/cm^2 in the second anodization process in sulfuric acid solution. The measured current density is approximately proportional to the anodization voltage under equilibrium conditions. As a result, current density is higher in oxalic acid anodized sample (60V anodization voltage) than sulfuric acid anodized sample (25V anodization voltage). Since large pore structures are formed in oxalic acid compared to sulfuric acid, longer times are required to reach the steady-state region in anodization process.

The SEM images of the AAO templates anodized in oxalic and sulfuric acid solutions are shown in Fig. 1.12 (a)-(c) and (d)-(f), respectively. According to the Fig. 1.12 (a) and (c), the average pore diameter and interpore distance were measured to be 55 nm and 150 nm, respectively for oxalic and were measured to be 20 nm and 63 nm, respectively for sulfuric acid anodized templates. Both measured values were very well correlated with the applied anodization potential as mentioned earlier. The approximate thickness of the AAO templates in both electrolytes was measured to be 18 μm. The calculated pore densities were $5.13x10^9\ pores/cm^2$ and $2.91x10^{10}\ pores/cm^2$ for oxalic and sulfuric acid anodized templates, respectively. Fig. 1.12 (b) and (e) show the bottom side of the templates after aluminum removal process for oxalic and sulfuric acid anodized templates, respectively. In both cases, hexagonally ordered barrier layers were observed at the bottom of the pores. Finally, the bottom side of the templates after barrier layer removal and pore widening processes are shown in Fig. 1.12 (c) and (f) in oxalic and sulfuric acid solutions. According to the SEM images, the average pore diameter increased to 70 nm in oxalic acid and 30 nm in sulfuric acid anodized samples due to the pore widening process. The calculated porosities after second anodization and pore widening processes were 12.19% and 19.75% for oxalic acid and 9.14% and 20.56% for

sulfuric acid anodized templates, respectively. The aspect ratios were calculated to be 257 and 600 for oxalic and sulfuric acid anodized samples, respectively.

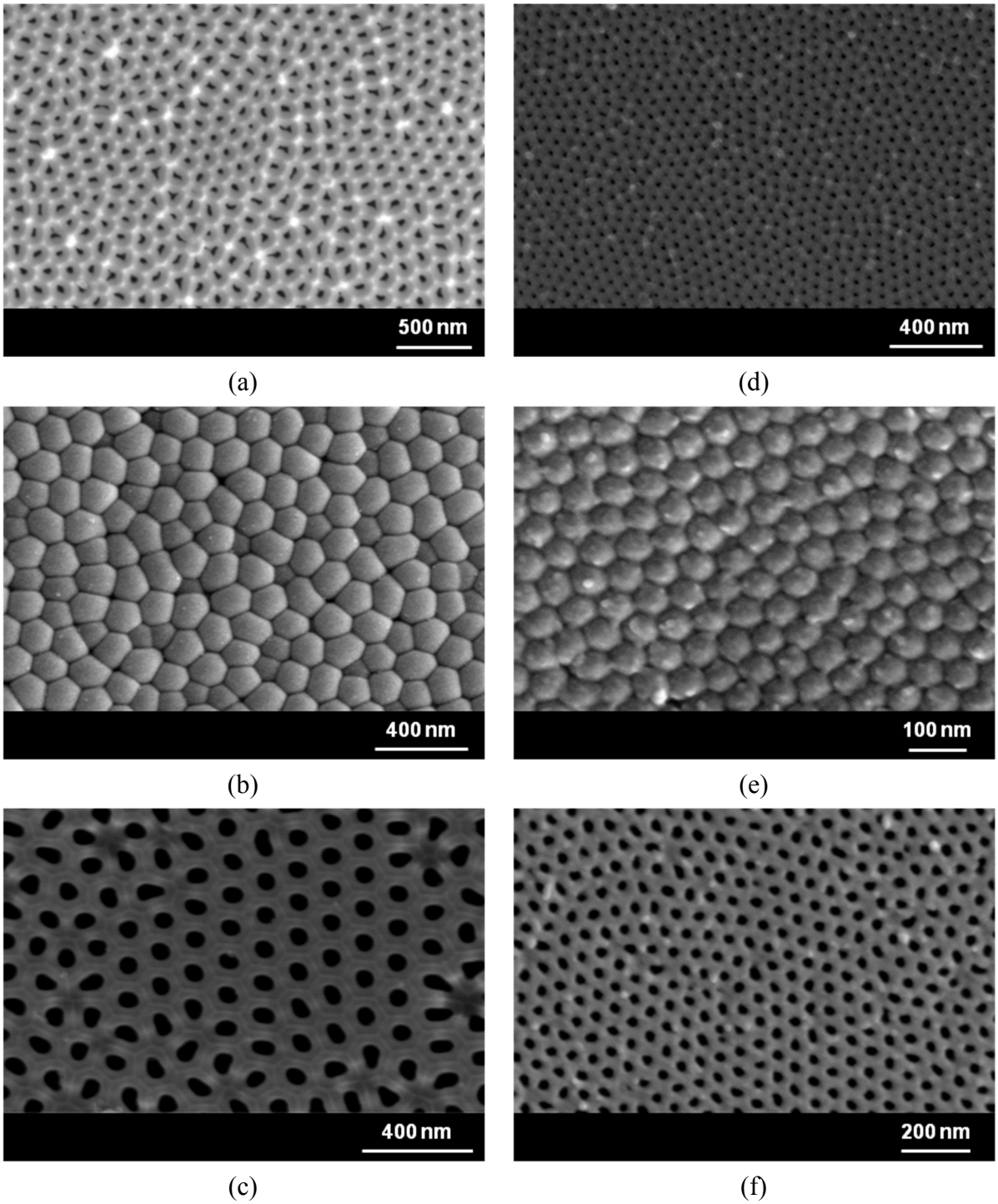

Figure 1.12. SEM images of the AAO templates anodized in oxalic (a-c) and sulfuric (d-f) acid solutions.

The anodization conditions and morphological characteristics of AAO templates are shown in Table 1.2; where C is the concentration of the electrolytes, V is the applied voltage, T is the temperature, D_{int} is the interpore distance, D_{p1} is the pore diameter after second anodization step, D_{p2} is the pore diameter after pore widening process, t_1 is the first anodization time, t_2 is the second anodization time, ρ is the pore density, P_1 is the porosity after second anodization step, and P_2 is the porosity after pore widening process.

Table 1.2. Anodization conditions and morphological characteristics of AAO templates

Electrolyte	**C (M)**	**V (V)**	**T (°C)**	**D_{int} (nm)**	**D_{p1} (nm)**	**D_{p2} (nm)**	**t_1 (h)**	**t_2 (h)**	**ρ pores/cm^2**	**P_1 (%)**	**P_2 (%)**
Oxalic acid	0.3	60	0 ± 2	150	55	70	2	3	$5.13x10^9$	12.19	19.75
Sulfuric acid	0.3	25	0 ± 2	63	20	30	2	6	$2.91x10^{10}$	9.14	20.56

The pore diameter distributions of oxalic and sulfuric acid anodized templates were analyzed with ImageJ program. Figure 1.13 (a) shows the pore diameter distributions of top side of oxalic acid anodized template. The pore diameter distributions of bottom side (after barrier layer removal and pore widening processes) of oxalic acid anodized template are shown in Figure 1.13 (b). The average pore diameter of the top side is found to be 55 nm and bottom side is found to be 70 nm which confirms the measurement results from SEM images. The pore diameter distributions of top and bottom sides of sulfuric acid anodized template are shown in Figure 1.13 (c) and (d), respectively. The average pore diameter of the top side is found to be 20 nm and bottom side is found to be 30 nm which is very well correlated with the measurement results from SEM images.

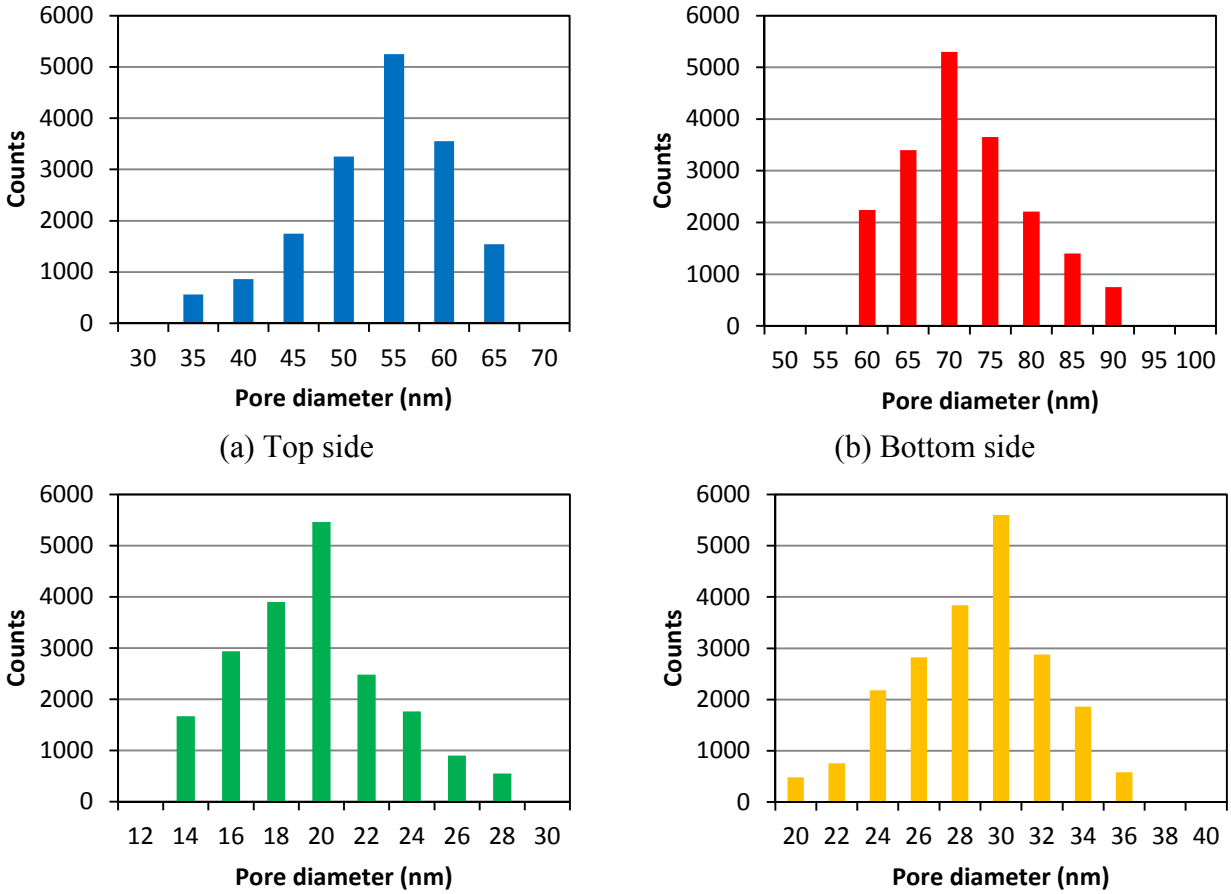

Figure 1.13. Pore diameter distributions of oxalic acid (a-b) and sulfuric acid (c-d) anodized templates.

The cross-sectional SEM images of the AAO templates anodized in oxalic and sulfuric acid solutions are shown in Figure 1.14 (a)-(c) and (d)-(f), respectively. Figure 1.14 (a) and (d) show the cross-section of the AAO templates before the removal of aluminum substrate. Figure 1.14 (b) and (e) show the cross-section of the AAO templates after the removal of the aluminum substrate. Since aluminum etching solution does not attack the AAO template, the barrier layer thickness remained unchanged. The measured barrier layer thicknesses were 78 nm in oxalic and 33 nm in sulfuric acid anodized samples which are correlated with anodization voltage **[28]**. Finally, Figure 1.14 (c) and (f) depict open-through AAO templates after complete removal of

the barrier layer. The increase of the pore diameter due to the thinning of the pore cell wall was also observed from the cross-sectional SEM images.

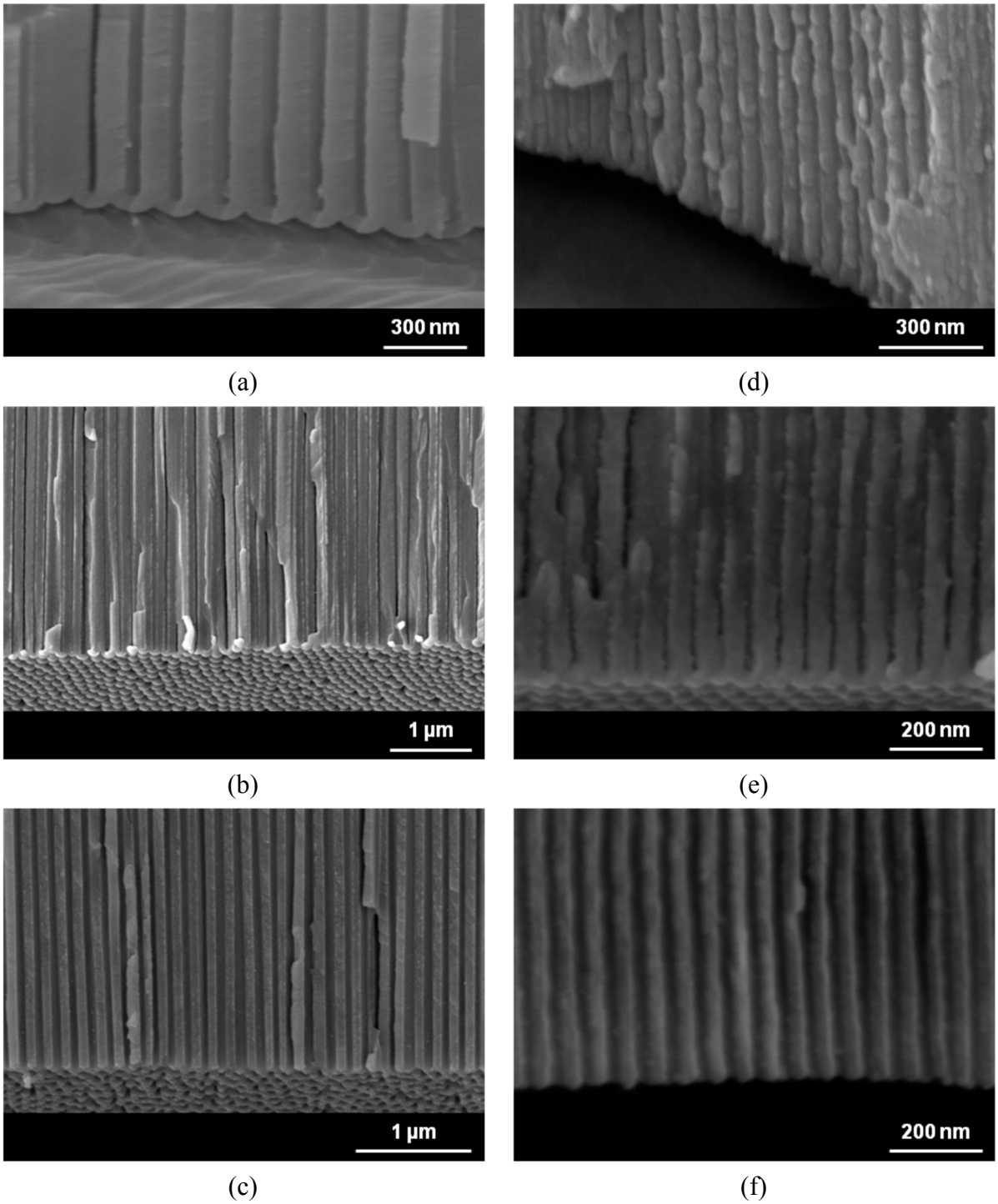

Figure 1.14. Cross-sectional SEM images of the AAO templates anodized in oxalic (a-c) and sulfuric (d-f) acid solutions.

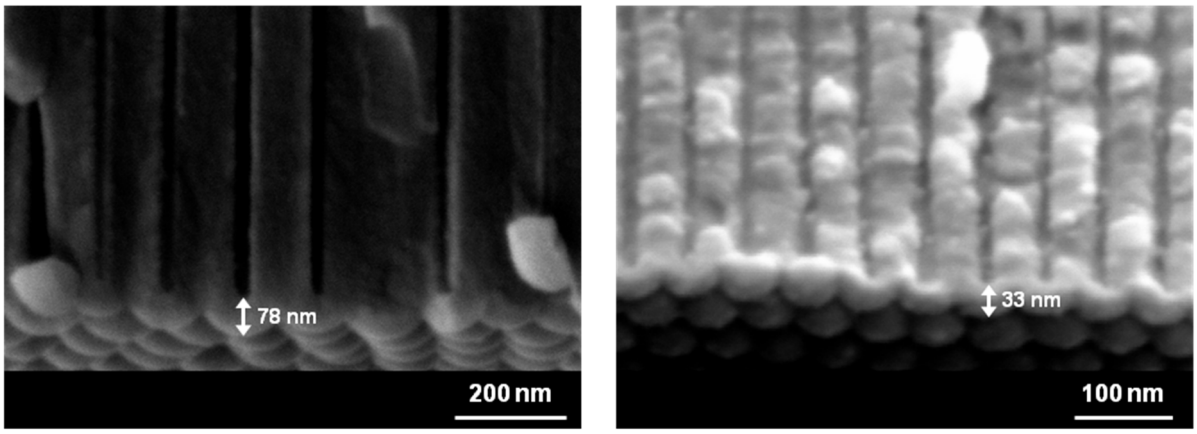

(a) (b)

Figure 1.15. SEM images of the barrier layer grown in oxalic (a) and sulfuric (b) acid solutions.

As seen from the SEM images in Figure 1.12 and Figure 1.14, the barrier layer of the AAO templates were removed successfully by wet chemical etching in phosphoric acid after aluminum substrate removal. Even though the barrier layers differ in thickness (Figure 1.15), barrier layer removal process was accomplished by adjusting the etching time. No damage occurred in the AAO templates by using this controllable method and hexagonal pore patterns of the AAO templates were preserved.

1.6.3. Conclusions

Highly ordered porous AAO templates were fabricated by two-step anodization process in oxalic and sulfuric acid electrolytes. The average pore diameter and interpore distance were measured to be 70 nm and 150 nm, respectively for oxalic acid and were measured to be 30 nm and 63 nm, respectively for sulfuric acid anodized templates. Pore diameter distributions were analyzed with ImageJ program and average pore diameters of oxalic and sulfuric acid anodized templates were confirmed. The approximate thickness of the AAO templates in both electrolytes was measured to be 18 μm. The calculated porosities after second anodization and pore widening

processes were 12.19% and 19.75% for oxalic acid and 9.14% and 20.56% for sulfuric acid anodized templates, respectively. The calculated aspect ratios were 257 and 600 and the measured barrier layer thicknesses were 78 nm and 33 nm in oxalic and sulfuric acid anodized samples. The proportionality of the interpore distance, pore diameter, and barrier layer thickness to the anodization voltage was observed. The calculated pore densities were $5.13x10^{9}$ pores/ cm^{2} and $2.91x10^{10}$ pores/cm^{2} for oxalic and sulfuric acid anodized templates, respectively. The pore arrangements showed polycrystalline structures. Open-through porous AAO templates were obtained after complete removal of the aluminum substrate and the barrier layer by wet chemical etching processes. As a result, the fabricated highly ordered open-through AAO templates can be used as a building block for growth of nanowires, nanorods, and nanotubes with unique electrical, magnetic, optical, and chemical properties.

CHAPTER 2

FABRICATION OF NANOWIRE ARRAYS IN POROUS ANODIC ALUMINUM OXIDE TEMPLATES BY ELECTRODEPOSITION

Fabrication of nanowire arrays has attracted great interest among researchers due to their promising applications in a large variety of fields such as high-density perpendicular magnetic memories **[63-65]**, giant magnetoresistance (GMR) sensors **[66, 67]**, surface-enhanced Raman scattering **[68-72]**, negative index metamaterials **[73-75]**, nano-optics and molecular electronics **[76, 77]**, biological labeling **[78, 79]**, field-emission electron emitters **[80-83]**, and gas sensors **[84-87]**. Template-assisted fabrication of nanowire arrays by using porous anodic aluminum oxide is simple and cost-effective method and does not utilize time-consuming, expensive, and sophisticated processes as in electron beam lithography **[58, 88, 89]**. Porous AAO is an ideal template to synthesis of nanowire arrays due to its high pore density, high aspect ratio, controllable pore diameter and length, large surface area, good mechanical strength, and thermal stability **[7, 58]**. Nanowire arrays can be fabricated by filling the desirable materials into the nanopores of AAO template. The most straightforward and versatile method for fabrication of nanowire arrays into the AAO template is electrochemical deposition from an electrolyte **[22, 88]**. During electrochemical deposition, the growth of nanowire arrays starts at the pore bottom and continues to the pore opening. As a result, uniform, straight, parallel, and high aspect ratio nanowire arrays are obtained by this fast and well-controlled electrochemical deposition method for their promising applications.

2.1. Electrodeposition

Electrodeposition is a process to reduce metal cations of a desired material from an electrolyte for producing a dense, uniform, and adherent metal coating on an electrode by using electrical current. The electrolytic cell is the main part of the electrodeposition process. An electrical current is passed through a cell containing electrolyte, the anode, and the cathode. Figure 2.1 shows a schematic diagram of electrolytic cell for copper electrodeposition from copper sulfate solution.

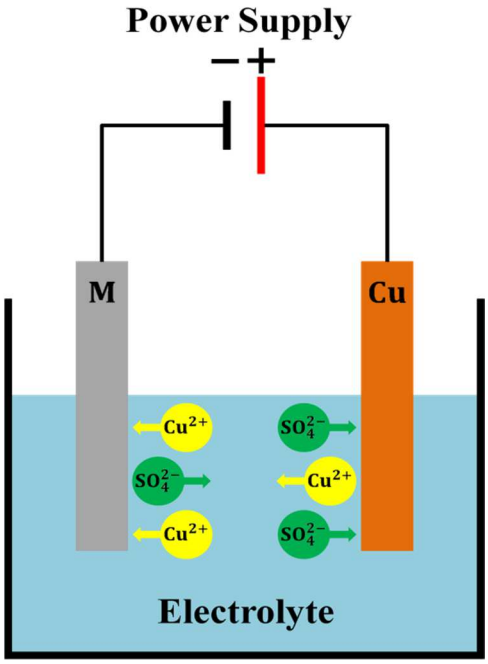

Figure 2.1. Schematic diagram of electrolytic cell for copper electrodeposition.

In an electrolytic cell, the anode is the electrode made of the metal to be deposited and the cathode is the electrode on which the electrodeposition is to be done. Electrodeposition solution called electrolyte contains ions of the metal to be deposited as well as other ions for electrical conductivity and completes an electrical circuit between two electrodes. Under application of electric current by power supply, positively charged copper ions in the electrolyte

move toward the cathode and negatively charged sulfate ions move toward the anode. This migration of ions constitutes the electric current in electrolyte. The migration of electrons between electrodes through power supply constitutes the electric current in the external circuit. When copper ions reach the cathode, they are reduced to metallic form and metal atoms are deposited onto the surface of cathode. At the same time, copper anode is oxidized and metal atoms are dissolved into the electrolyte. The rate of dissolution of anode is equal to the rate of deposition of cathode during electrodeposition process. Therefore, the ions in the electrolyte are continuously replenished by the anode. The chemical reaction at anode is called oxidation and given by

$$\mathrm{Cu} \rightarrow \mathrm{Cu}^{2+} + 2\mathrm{e}^{-} \tag{20}$$

where copper is oxidized to Cu^{2+} cations by losing two electrons. The Cu^{2+} cations associate with the SO_4^{2-} anions to form copper sulfate (CuSO_4) in the electrolyte. If a noble metals such as platinum is used as the anode, the overall chemical reaction at the anode is the oxidation of water and is given by

$$2\mathrm{H}_2\mathrm{O} \rightarrow 4\mathrm{H}^{+} + \mathrm{O}_2 + 4\mathrm{e}^{-} \tag{21}$$

The chemical reaction at the cathode is called reduction and given by

$$\mathrm{Cu}^{2+} + 2\mathrm{e}^{-} \rightarrow \mathrm{Cu} \tag{22}$$

where Cu^{2+} cations are reduced to metallic copper by gaining two electrons.

2.2. Electrodeposition Methods

Three different electrodeposition methods can be used for fabrication of nanowire arrays in porous anodic aluminum oxide templates. These methods are shown in Figure 2.2.

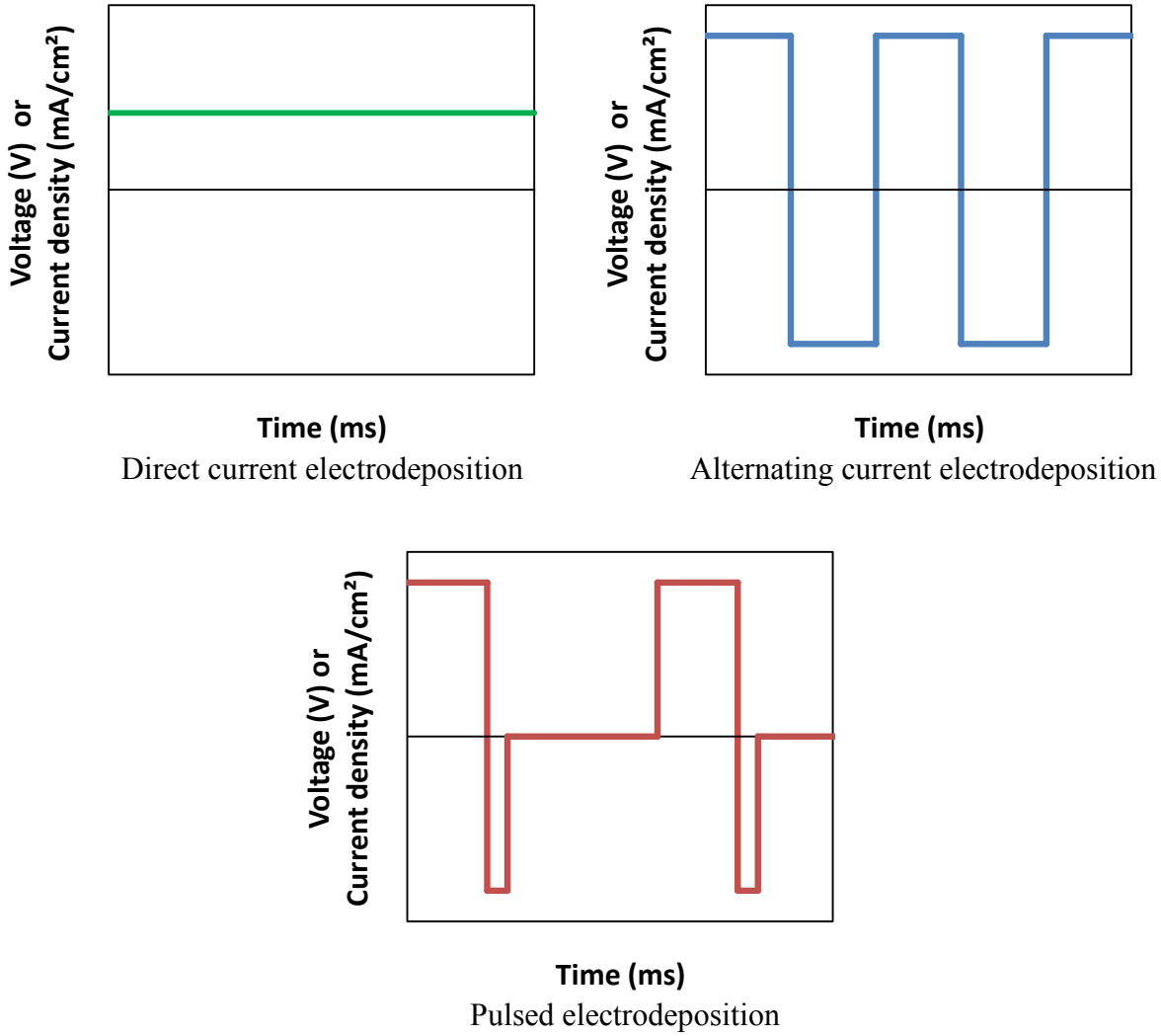

Figure 2.2. Schematic diagram of electrodeposition methods.

2.2.1. Direct Current Electrodeposition (DC)

In order to fabricate nanowire arrays by using DC electrodeposition, free-standing open-thorough AAO templates need to be obtained. First, a sufficiently thick AAO is formed on the aluminum substrate. Second, the aluminum substrate and barrier layer are removed by wet

chemical etching process and free-standing open-through AAO template is obtained. After that, a thin metal film is deposited either by evaporation or sputtering techniques on one side of the AAO template surface to serve as a conductive layer for electrodeposition process. DC electrodeposition can then be performed using either two- or three-electrodes to fabricate nanowire arrays by applying constant voltage or current. Nanowires grow from bottom to top of the pores. Therefore, the length of nanowires can be controlled by deposition time and current density. The electrodeposition process is governed by the Faraday's laws which take into account the AAO template parameters such as pore diameter, pore density, and porosity as well as filling efficiency **[90]**. It is possible to widen the pore diameter of AAO template by wet chemical etching in order to obtain different sizes of nanowires' diameter. Several materials such as silver **[91]**, palladium **[58]**, nickel **[48, 60, 61, 92, 93, 97]**, iron **[93, 99]**, cobalt **[93, 100]**, nickel-iron **[94, 95, 96]**, and cobalt-copper **[98]** have been deposited in free-standing open-through porous AAO templates by DC electrodeposition. However, DC electrodeposition is very unstable and uniform filling of the pores cannot be achieved **[88]**. This is due to increment of pH at cathodic side which leads to partial removal of the barrier layer, hole formation in the barrier layer, and local deposition in this pore **[88, 110]**. In addition, preparation of AAO templates for DC electrodeposition is demanding and free-standing AAO templates need to be thick (>20 μm) and stable enough to be handled **[88, 95]**.

2.2.2. Alternating Current Electrodeposition (AC)

In the case of AC electrodeposition, porous AAO template is kept on the aluminum substrate and barrier layer is thinned homogeneously by voltage reduction process. In order to thin barrier layer, applied voltage is reduced stepwise at the end of second anodization step

[88, 91]. In each voltage reduction step, barrier layer is thinned and dendrite pore formation occurs at the barrier layer. The thinning process leads to a considerable decrease in barrier layer thickness for the electrons to tunnel through the barrier layer during AC electrodeposition **[88]**. The rectifying property of barrier layer allows the pores to be filled with desired material uniformly by AC electrodeposition. Under alternating voltage or current, barrier layer conducts preferentially and allows the reduction of ions in the pores during the cathodic half cycles without allowing reoxidation during the anodic half cycles **[7]**. Several materials such as copper **[7, 101]**, cobalt **[102, 107]**, iron **[63, 103, 104, 105]**, gold **[106]**, nickel **[108]**, and bismuth **[108]** have been deposited in porous AAO templates by AC electrodeposition. Both thin and thick porous AAO templates can be used for AC electrodeposition and the process is relatively simpler compared to DC electrodeposition. However, a time consuming and sensitive barrier layer thinning process is required in AC electrodeposition. Due to the existence of the thin barrier layer at the pore bottom, a high deposition voltage (~10-25V) and a high frequency (several hundred Hz) are used during AC electrodeposition which cause hydrogen evolution and therefore may inhibit the deposition **[88, 108, 109]**. Since material is deposited on barrier layer, it is not possible to obtain self-standing nanowire arrays on the aluminum substrate after the removal of AAO template. Another disadvantage of this method is that the pores cannot be widened to larger diameters since delimitation of the AAO template from the aluminum substrate takes place. Moreover, multilayer nanowires cannot be fabricated by AC electrodeposition method since it does not provide alternating deposition voltage or current pulses. As a result, AC electrodeposition method through the barrier layer is a complicated process since pore-filling efficiency (percentage of filled pores) is largely dependent on deposition conditions such as

deposition voltage, frequency, waveform (sine, square, and triangle), pulse polarity, and sequence **[7]**.

2.2.3. Pulsed Electrodeposition (PED)

Pulsed electrodeposition method was adopted in order to overcome the limitations of DC and AC electrodeposition **[88]**. This method can be applied to both free-standing open-through AAO templates and AAO templates that are formed on the aluminum or different kind of substrates. In contrast to alternating voltage pulses, current pulses are applied in PED which allow better control over the deposition parameters such as deposition rate and ion concentration at the deposition interface **[88]**. During electrodeposition, ion concentration decreases at the pore bottom which leads hydrogen evolution in the pores and inhibits the deposition. For this reason, in PED, a relatively long delay time (t_{off}) is introduced between two successive deposition pulses in order to replenish the ion concentration at the pore bottom. Since deposition interfaces are supplied sufficiently with ions by introducing a delay time, hydrogen evolution is prevented; uniform and homogenous pore-filling is obtained during PED. Pulsed electrodeposition also eliminates the template damage which was observed in continuous deposition **[7, 107]**. In addition, PED conditions are not affected by the depth of the pores; therefore, it can be applied to high aspect ratio AAO templates. In pulsed electrodeposition, the cathodic (deposition) pulse is followed by the anodic pulse **[8, 88, 111]**. The benefit of a short pulse of positive polarization after the deposition pulse is to discharge the capacitance of the barrier layer, to interrupt the electric field at the deposition interface immediately, and to deplete the impurities. The positive pulse also repairs discontinuities in the barrier layer. Several materials

such as silver **[8]**, copper **[7]**, nickel **[10, 88, 113]**, iron **[112]**, cobalt **[111]**, and nickel-iron **[113]** have been deposited in porous AAO templates by pulsed electrodeposition.

2.3. Magnetism

2.3.1. The Origin of Magnetism

In magnetic materials, a magnetic field is produced due to the movement of electrons within the material **[114]**. There are two kinds of electron movement such as orbital and spin, and each has a magnetic moment associated with it. The types of electron movement are shown in Figure 2.3.

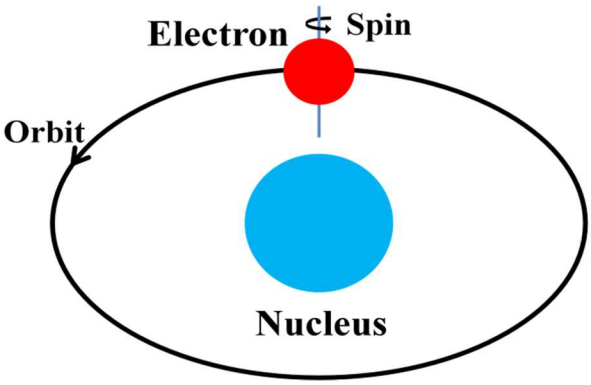

Figure 2.3. The movement of an electron around the nucleus in an orbit.

The magnetic moment of an electron due to the orbital motion is given by

$$\mu_{orbital} = (\text{area of loop})(\text{current}) \tag{23}$$

therefore, $\mu_{orbital}$ in CGS unit system,

$$\mu_{orbital} = -(\pi r^2)\left(\frac{ev}{2\pi rc}\right) = -\frac{evr}{2c} \tag{24}$$

where e is the charge of the electron, v is the velocity of the electron, r is the radius of the orbit, and c is the velocity of light. The negative sign indicates that the electrons are negatively charged particles. It is useful to express the magnetic moment of the electron in terms of its angular momentum. The angular momentum of an electron is given by

$$\mathrm{N} = \mathrm{mrv} \tag{25}$$

where m is the mass of the electron. Therefore, the magnetic moment of the electron in terms of its angular momentum is given by

$$\mu_{\mathrm{orbital}} = -\left(\frac{\mathrm{e}}{2\mathrm{mc}}\right)\mathrm{N} \tag{26}$$

The constant of $(\mathrm{e}/2\mathrm{mc})$ is known as gyromagnetic ratio and is given by

$$\gamma = \frac{\mathrm{e}}{2\mathrm{mc}} = \frac{\mu}{\mathrm{N}} \tag{27}$$

Therefore, gyromagnetic ratio is defined as the ratio of the magnitude of the magnetic moment to the magnitude of the angular momentum of any particle or system. Based on Bohr's theory of the atom, the angular momentum of the electron is determined by the orbital quantum number l ,

$$\ell = 0, 1, 2, \ldots, (\mathrm{n} - 1) \tag{28}$$

where n is the principal quantum number of the electron. Therefore, the angular momentum of the electron associated with a particular value of ℓ is given by

$$\mathrm{N} = \ell \mathrm{h}/2\pi \tag{29}$$

where h is the Planck's constant. By using Equation (29) in (26), magnetic moment of the electron can be obtained as

$$\mu_{\text{orbital}} = -\left(\frac{e}{2mc}\right)(\ell h/2\pi) = -\frac{eh\ell}{4\pi mc} \tag{30}$$

As a result, electrons in an atom can only take certain specified values of magnetic moment depending on orbital quantum number ℓ.

The magnetic moment of an electron due to the spin motion is given by

$$\mu_{\text{spin}} = -2\left(\frac{e}{2mc}\right)N_{\text{spin}} \tag{31}$$

where N_{spin} is the intrinsic angular momentum due to the spin of the electron and is defined by

$$N_{\text{spin}} = sh/2\pi \tag{32}$$

where s is the spin quantum number and its value is either +1/2 or -1/2. According to the Equation (31), a factor of 2 is introduced in the case of spin motion of the electron in comparison to a factor of 1 in the case of orbital motion of the electron in Equation (26). Therefore, this factor can be replaced by a symbol of g and magnetic moment can be written as

$$\mu_{\text{spin}} = -g\left(\frac{e}{2mc}\right)\left(\frac{sh}{2\pi}\right) \tag{33}$$

where g is the Landé's splitting factor or spectroscopic splitting factor and is given by

$$g = 1 + \frac{J(J+1) + S(S+1) - L(L+1)}{2J(J+1)} \tag{34}$$

where J is the total angular momentum quantum number, S is the spin quantum number, and L is the orbital quantum number. For $s = |1/2|$ the magnetic moment of the electron due to the spin motion is obtained as

$$\mu_{spin} = -\frac{eh}{4\pi mc} \tag{35}$$

The magnetic moment due to spin motion and that due to orbital motion in the first orbit are equal. This amount of magnetic moment is called Bohr magneton and is given by

$$\text{Bohr magneton} = \mu_B = eh/4\pi mc = 0.927 \text{ x } 10^{-20} \text{ erg/Oe (CGS)} \tag{36}$$

$$\mu_B = eh/4\pi m = 9.27 \text{ x } 10^{-24} \text{ A/m}^2 \text{ (SI)} \tag{37}$$

$$\mu_B = \mu_0 \, eh/4\pi m = 1.17 \text{ x } 10^{-29} \text{ Wb} \cdot \text{m (SI)} \tag{38}$$

The nucleus also has a small magnetic moment due to its intrinsic spin of protons. Since the nucleus has no orbital motion, it does not have orbital magnetic moment. The magnetic moment of nucleus is given by

$$\mu_{nucleus} = \frac{eh}{4\pi m_p c} \tag{39}$$

where m_p is the mass of proton. The unit of the magnetic moment of the proton is known as nuclear magneton. As the mass of proton is greater than that of electron, the magnetic moment of the nucleus is smaller by a factor of 1000. Since the magnetic moment of the nucleus is very small compared to that of the electrons, its influence on magnetic properties of materials can be neglected.

2.3.2. Classification of Magnetic Materials

The magnetic materials are classified in terms of their magnetic behavior as diamagnetic, paramagnetic, ferromagnetic, antiferromagnetic, and ferrimagnetic. Different magnetic materials have different magnetic properties due to the interaction between the neighboring atomic magnetic dipole moments which may be zero, small, or large. In paramagnetic materials, permanent magnetic dipoles do not interact with each other and are randomly distributed in the absence of the magnetic field. In ferromagnetic materials, permanent magnetic dipoles interact with each other so heavily that they align in parallel. These materials have very large magnetization under applied magnetic field. In antiferromagnetic materials, the interactions between magnetic dipoles are such that they align antiparallel to each other. Magnetization of these materials is zero since the magnitudes of the magnetic dipole moments are equal. In ferrimagnetic materials, the permanent magnetic dipoles interact with each other to align themselves antiparallel; however, the magnitudes of the magnetic dipole moments are not equal. Therefore, there is a large magnetization in these materials which is less than that of ferromagnetic materials. Diamagnetic materials have no permanent magnetic dipoles. Magnetic dipole orientations are shown in Figure 2.4.

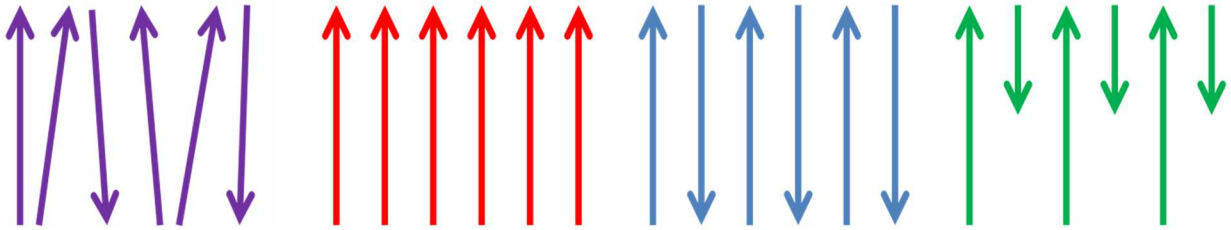

Figure 2.4. Magnetic dipole orientations of magnetic materials.

2.3.2.1. Diamagnetism

In diamagnetic materials, the atoms have no permanent magnetic moments when there is no external magnetic field. This is due to the fact that the vector sum of magnetic moments of electrons is zero. When an external magnetic field is applied, electrons move in the orbit around the nucleus, and therefore, a current is induced within the atom by Lenz's law of electromagnetic induction. This induced current gives a magnetic moment to an atom in the opposite direction to that of the applied filed. As a result, the magnetic flux density B decreases and becomes less than the applied magnetic field H. The susceptibility of diamagnetic materials is small and negative, typically in the order of -10^{-6}, and therefore, the relative permeability is slightly less than 1. Since the susceptibility of diamagnetic materials is determined by the electron structure, it does not depend on temperature and intensity of an external magnetic field. Consequently, materials having zero initial magnetic moment such as copper, gold, silver, silicon, bismuth, diamond, graphite, germanium are diamagnetic.

2.3.2.2. Paramagnetism

In paramagnetic materials, the atoms have permanent magnetic moments due to the unpaired electron spins when there is no external magnetic field. These magnetic moments are randomly distributed and do not interact with each other in the absence of external magnetic field. When an external magnetic field is applied, these magnetic moments have a tendency to align themselves in the same direction as the applied field. As a result, magnetic flux density becomes more than the applied field and the relative permeability is slightly greater than the unity. However, as the temperature increases, thermal agitation of the atoms opposes this tendency and tends to randomize the atomic magnetic moments. Hence paramagnetic materials

exhibit weak inherent magnetization and their susceptibility is small, positive and inversely proportional to the temperature. With increase in temperature, the susceptibility decreases and becomes negative at elevated temperatures. This behavior can be explained by Curie law and is expressed as

$$\chi = C/T \tag{40}$$

where C is the Curie constant and T is the temperature in Kelvin. The magnetic moments of materials that obey this law are localized at the atomic or ionic sites and there is no interaction between neighboring magnetic moments. The more general expression for susceptibility of paramagnetic materials based on temperature is given by Curie-Weiss law as

$$\chi = C/(T - \theta) \tag{41}$$

where θ is the temperature constant which can either be positive, negative, or zero. When θ is nonzero, there is an interaction between neighboring magnetic moments, and the material is only paramagnetic above a certain transition temperature. If θ is positive, then the material is ferromagnetic below the transition temperature which corresponds to the Curie temperature. If θ is negative, then the material is antiferromagnetic below the transition temperature which corresponds to the Néel temperature. This equation is only valid when the material is in paramagnetic state. Platinum, aluminum, tin, manganese, titanium, and iridium are some of the paramagnetic elements.

2.3.2.3. Ferromagnetism

In ferromagnetic materials, the atoms have permanent magnetic moments due to the unpaired electron spins as in paramagnetic materials. When an external magnetic field is applied, the magnetic moments line up in the same direction as that of the applied field. Ferromagnetic materials have very large relative permeability and their susceptibility is also very large and positive. Under applied field, a small change in the dimensions of ferromagnetic materials occurs which is known as magnetostriction. This effect is given by the magnetostriction coefficient which is the ratio of the change in dimension ($\Delta\ell$) to the original dimension(ℓ), and expressed as

$$\lambda = \Delta\ell/\ell \tag{42}$$

The most common ferromagnetic materials are iron, cobalt, and nickel. The susceptibility of ferromagnetic materials is sensitive to the temperature. The degree of alignment of the magnetic moments, and therefore, the value of susceptibility decreases as the temperature increases. Above a certain temperature, ferromagnetic materials become paramagnetic. This transition temperature is called the Curie temperature (T_C). The Curie temperatures of iron, cobalt, and nickel are 1043°K, 1400°K, and 627°K, respectively. Ferromagnetic materials consist of a large number of small regions called magnetic domains. A magnetic domain is a region within a ferromagnetic material where the atomic magnetic moments are parallel and aligned with a particular direction. The domains are separated by domain walls. The magnetization within each magnetic domain points in a uniform direction; however, the magnetization of different magnetic domains may point in different directions. As a result, the resultant magnetization may be zero or very small. Figure 2.5 shows the schematic of a material divided into four magnetic domains

with the magnetization in different directions. According to the magnetic domain configuration in Figure 2.5, the net magnetization is zero since magnetization in each domain is same and opposite.

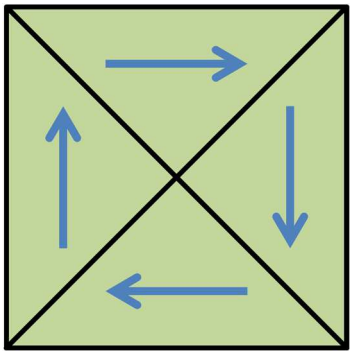

Figure 2.5. Magnetic domain configuration in ferromagnetic materials.

When an external magnetic field is applied in a particular direction, magnetic domains having magnetization in the same direction grow in size by the rotation of magnetization direction and the movement of the domain walls. As the external magnetic field increases, whole material becomes a single domain and saturation of the magnetization occurs. Domain wall motion and magnetization under applied external magnetic field is shown in Figure 2.6.

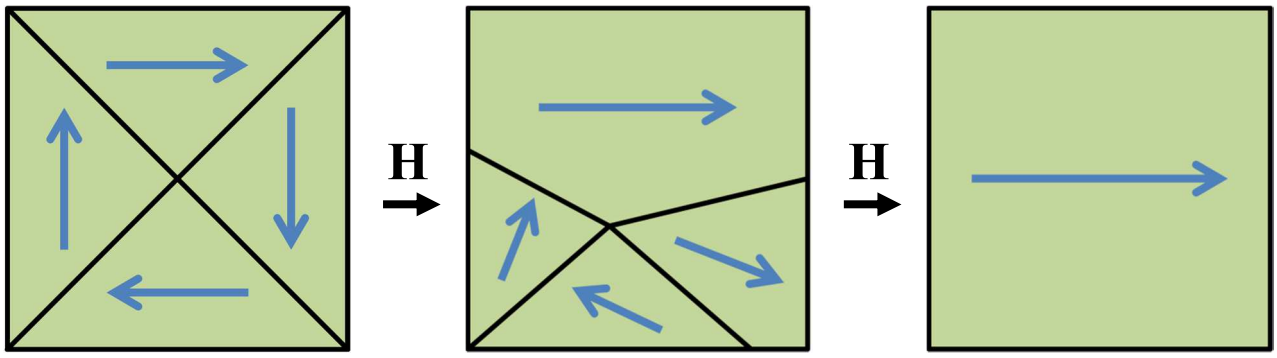

Figure 2.6. Domain wall motion and magnetization under applied external magnetic field.

Ferromagnetic materials exhibit the phenomenon of magnetic hysteresis. The relationship between magnetic flux density (B) and applied magnetic field (H) depends on previous magnetization of a ferromagnetic material. A typical B-H curve of a ferromagnetic material is shown in Figure 2.7. We need to note that there is a nonlinear relationship between B and H. In addition, permeability (μ) is given by the ration B/H at any point on the curve. If we assume that the ferromagnetic material is initially unmagnetized, as H is increased, curve a-b is produced. This curve is referred to as the initial magnetization curve. At point b, all magnetic dipoles are aligned within the ferromagnetic material, and therefore, magnetization (M) saturates. After reaching saturation, H is decreased from its value at point b back to zero and curve b-c is produced. According to the figure, when H is reduced to zero, B does not follow the initial curve due to the irreversibility of the domain wall displacements and it lags behind H. This phenomenon of B lagging behind H is called magnetic hysteresis. At point c, magnetic field is zero but magnetic flux density is not zero and has a value due to the existence of magnetic domains still aligned in the original direction of the applied magnetic field. The value of B at point c is called residual or remanent flux density (B_r). The ferromagnetic material is now magnetized and can serve as a permanent magnet owing to the fact that a large fraction of its magnetic domains have remained aligned. Reversing the direction of magnetic field and increasing its intensity causes magnetic flux density to decrease from B_r at point c to zero at point d. The reverse magnetic field required to reduce the magnetic flux density from B_r to zero is called coercive field (H_c). If the intensity of magnetic field is increased further in negative direction, curve d-e is produced and magnetization saturates at point e. Finally, magnetic field is reduced to zero and is then increased again in the positive direction, and curve e-b is produced. As a result, a closed loop of B-H curve which is also called hysteresis loop is obtained. The

hysteresis loop shows that the magnetization process in ferromagnetic materials depends not only on the external magnetic field H, but also on the magnetic history of the ferromagnetic material. The specific shape and extent of the hysteresis loop varies from one material to another. Materials characterized by narrow hysteresis loops are called soft ferromagnetic materials. These materials can be easily magnetized and demagnetized. Materials characterized by wide hysteresis loops are called hard ferromagnetic materials. These materials cannot be easily demagnetized by an external magnetic field since they have a large remanent magnetization. Therefore, hard ferromagnetic materials are used in the fabrication of permanent magnets.

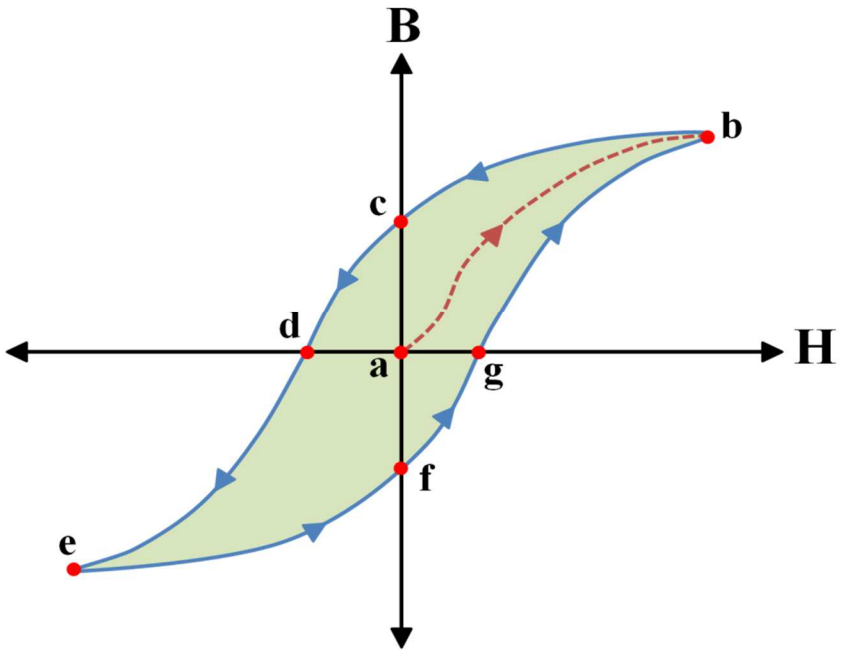

Figure 2.7. Hysteresis curve of a ferromagnetic material.

The relationship between magnetic flux density, applied magnetic field, and magnetization is given by

$$B = \mu_o(H + M) \tag{43}$$

where μ_o is the permeability of free space ($4\pi \times 10^{-7}$ H/m) and magnetization M is defined by the magnetic dipole moment per unit volume and is expressed as

$$M = \lim_{\Delta v \to 0} \left(\sum_{k=1}^{N} m_k \Big/ \Delta v \right) \tag{44}$$

where N is the number of atoms, Δv is the given volume, and m_k is the magnetic moment of kth atom. The relationship in Equation (43) holds for all materials whether they are linear or not. For linear materials, magnetization is directly proportional to the applied magnetic field as

$$M = \chi_m H \tag{45}$$

where χ_m is the magnetic susceptibility of the material and is a measure of how susceptible the material is to becoming magnetized. Substituting Equation (45) into Equation (43) yields

$$B = \mu_o(H + \chi_m H) = \mu_o(1 + \chi_m)H = \mu_o \mu_r H = \mu H \tag{46}$$

where μ is the permeability of the material and μ_r is the relative permeability of the material and is given by

$$\mu_r = 1 + \chi_m = \mu/\mu_o \tag{47}$$

When a ferromagnetic material is subjected to repeating cycles of magnetization, it results in hysteresis loss which is a power loss and appears in the form of heat. Hysteresis loss is equal to the energy consumed in magnetizing and demagnetizing a ferromagnetic material and is proportional to the area enclosed in the hysteresis loop, the frequency of the alternating current, and the volume of the material. Therefore, magnetic cores used in alternating magnetic fields

such as transformers are made from materials whose hysteresis loops are narrow in order to keep the hysteresis loss low. Hysteresis loss per unit volume is given by

$$\text{Hysteresis loss } (\text{cm}^{-3}) = \frac{\text{BHAf}}{4\pi} \text{ ergs/second} \tag{47}$$

$$\text{Hysteresis loss } (\text{cm}^{-3}) = \frac{\text{BHAf x } 10^{-7}}{4\pi} \text{ Watts} \tag{48}$$

where A is the area of the hysteresis loop, and f is the frequency of the alternating current. Hysteresis loss can also be expressed by using the Steinmetz formula as

$$\text{Hysteresis loss } (\text{cm}^{-3}) = \eta B_{\text{max}}^{1.6} \text{f x } 10^{-7} \text{ Watss} \tag{49}$$

where η is the hysteresis coefficient for the ferromagnetic material and B_{max} is the maximum flux density.

2.3.2.4. Antiferromagnetism

In antiferromagnetic materials, magnetic moments of electrons are equal and oriented in opposite directions due to the exchange interaction between neighboring atoms. Therefore, the net magnetization of these materials is zero and they behave in the same way as paramagnetic materials. Similar to ferromagnetic materials, these materials become paramagnetic above a transition temperature which is known as the Néel temperature. Chromium is the only element in the periodic table that exhibits antiferromagnetism at room temperature and its Néel temperature is 310°K. Another example to antiferromagnetic materials is manganese oxide (MnO) in which Mn^{+} ion has a magnetic moment. Unlike the susceptibility of ferromagnetic materials,

the susceptibility of antiferromagnetic materials increases as the temperature is increased. Antiferromagnetic materials are less common compared to the other materials and are mostly observed at low temperatures.

2.3.2.5. Ferrimagnetism

In ferrimagnetic materials, magnetic moments of electrons are aligned antiparallel and are not equal in magnitude. The exchange interaction between neighboring atoms leads to parallel alignment in some of the crystal sites and antiparallel alignment of others. Therefore, these materials have a large magnetization which is less than that of ferromagnetic materials. Ferrimagnetic materials have magnetic domains and similar magnetic behavior as in ferromagnetic materials; however, they have lower saturation magnetization. Most ferrites such as barium ferrite ($BaO \cdot 6Fe_2O_3$), strontium ferrite ($SrO \cdot 6Fe_2O_3$), manganese ferrite ($MnO \cdot 6Fe_2O_3$), and cobalt ferrite ($CoO \cdot 6Fe_2O_3$) which are the complex oxide compounds of various metals and oxygen are ferrimagnetic.

2.4. Magnetic Anisotropy

The dependence of magnetic properties of materials on a preferred direction is called magnetic anisotropy. In other words, the magnetic properties depend on the direction in which they are measured. Magnetic anisotropy strongly affects the shape of the hysteresis loops and controls the coercivity and remanence. Magnetically isotropic materials have no preferential direction for their magnetic moments in the absence of an external applied magnetic field. However, magnetically anisotropic materials align their magnetic moments in certain directions

without external magnetic field. There are several sources of magnetic anisotropy such as magnetocrystaline anisotropy, shape anisotropy, stress anisotropy, and exchange anisotropy.

2.4.1. Magnetocrystalline Anisotropy

Magnetocrystalline anisotropy depends on the crystallographic directions of the material. The direction of easy magnetization of a crystal is the direction of spontaneous magnetization of magnetic domains in the demagnetized state. Nickel has a face-centered cubic crystal structure and it is shown in Figure 2.8 (a). The easy and hard magnetization directions of nickel are [111] and [100], respectively. Iron has a body-centered cubic crystal structure and it is shown in Figure 2.8 (b). The easy and hard magnetization directions of iron are [100] and [111], respectively. The difference between the easy and hard magnetization directions is that in order to produce the same saturation magnetization, stronger magnetic field is required in the hard magnetization direction than that in the easy magnetization direction.

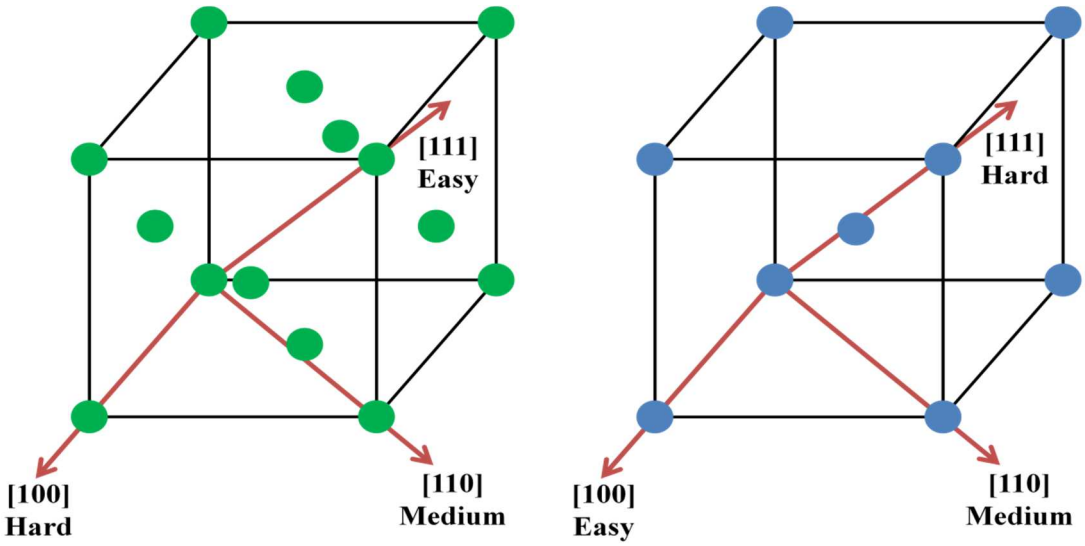

(a) Nickel (b) Iron

Figure 2.8. Crystal structures of nickel and iron.

Magnetocrystalline anisotropy may also be regarded as a force which tends to hold the magnetization in certain crystallographic directions in a crystal. When an external magnetic field is applied to the material which is against the easy magnetization direction, energy is stored in the crystal. This energy is called magnetocrystalline anisotropy energy E. This energy can be expressed in terms of a series expansion of the direction cosines of saturation magnetization (M_s) relative to the crystal axes. In a cubic crystal, assuming a, b, and c are the angles between saturation magnetization and the crystal axes, and α_1, α_2, and α_3 are the cosines of these angles which are called direction cosines, then magnetocrystalline anisotropy energy can be expressed as

$$E = K_0 + K_1(\alpha_1^2\alpha_2^2 + \alpha_2^2\alpha_3^2 + \alpha_3^2\alpha_1^2) + K_2(\alpha_1^2\alpha_2^2\alpha_3^2) + \cdots \quad (50)$$

where K_0, K_1, K_2, … are magnetocrystalline anisotropy constants for a particular material at a particular temperature and expressed in erg/cm^3 (CGS) or J/m^3 (SI). K_0 is independent of angle and usually ignored. Higher powers are not needed and sometimes K_2 is so small that it can be neglected. Therefore, K_1 is the dominant constant that determines the change in the energy when the saturation magnetization vector rotates one direction to another. The value of E based on the particular direction of M_s is given in Table 2.1.

Table 2.1. Magnetocrystalline anisotropy energies for particular directions in a cubic crystal

Direction	**a**	**b**	**c**	$\boldsymbol{\alpha_1}$	$\boldsymbol{\alpha_2}$	$\boldsymbol{\alpha_3}$	**E**
[100]	0°	90°	90°	1	0	0	K_0
[110]	45°	45°	90°	$1/\sqrt{2}$	$1/\sqrt{2}$	0	$K_0 + K_1/4$
[111]	54.7°	54.7°	54.7°	$1/\sqrt{3}$	$1/\sqrt{3}$	$1/\sqrt{3}$	$K_0 + K_1/3 + K_2/27$

The sign of K_1 determines the direction of easy magnetization when K_2 is zero. If K_1 is positive, then $E_{100} < E_{110} < E_{111}$, and $< 100 >$ is the easy magnetization direction since E is the minimum when saturation magnetization is in that direction. Therefore, iron and the cubic ferrites containing cobalt have positive values of K_1. If K_1 is negative, then $E_{111} < E_{110} < E_{100}$, and $< 111 >$ is the easy magnetization direction. Therefore, nickel and all cubic ferrites that contain little or no cobalt have negative values of K_1. The easy magnetization direction depends on both K_1 and K_2 when K_2 is not zero. The magnetization directions in a cubic crystal based on K_1 and K_2 are given in Table 2.2.

Table 2.2. Magnetization directions in a cubic crystal

$\mathbf{K_1}$	positive	positive	positive	negative	negative	negative
$\mathbf{K_2}$	$+\infty$ to $\frac{-9K_1}{4}$	$\frac{-9K_1}{4}$ to $-9K_1$	$-9K_1$ to $-\infty$	$-\infty$ to $\frac{9\lvert K_1\rvert}{4}$	$\frac{9\lvert K_1\rvert}{4}$ to $9\lvert K_1\rvert$	$9\lvert K_1\rvert$ to $+\infty$
Easy	[100]	[100]	[111]	[111]	[110]	[110]
Medium	[110]	[111]	[100]	[110]	[111]	[100]
Hard	[111]	[110]	[110]	[100]	[100]	[111]

In addition to nickel and iron, the other most common ferromagnetic material is cobalt. Cobalt has a hexagonal close-packed crystal structure and it is shown in Figure 2.9. The easy magnetization direction is the hexagonal c axis [0001] and all directions in the basal plane (the plane perpendicular to the c axis) are hard magnetization direction. Therefore, the magnetocrystalline anisotropy energy depends on the angle (θ) between the saturation magnetization and the c axis and expressed as

$$E = K_0' + K_1'\cos^2\theta + K_2'\cos^4\theta + \cdots \quad (51)$$

The energy equation can be rewritten by putting $\cos^2\theta = 1 - \sin^2\theta$ as below

$$E = K_0 + K_1\sin^2\theta + K_2\sin^4\theta + \cdots \quad (52)$$

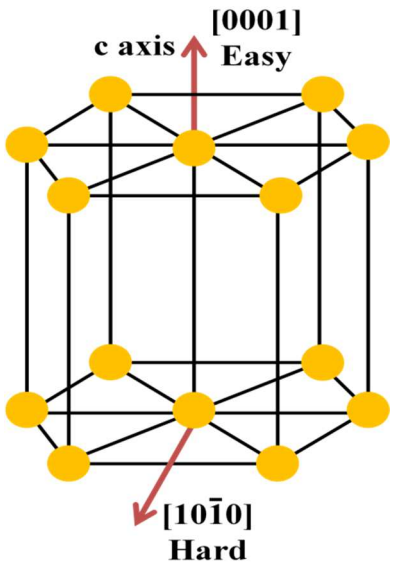

Figure 2.9. Crystal structure of cobalt.

When K_1 and K_2 are both positive, energy is minimum for $\theta = 0°$ and the c axis is the easy magnetization axis. A crystal with a single easy magnetization axis is called uniaxial crystal. When K_1 and K_2 are both negative, energy is minimum for $\theta = 90°$ and easy magnetization axis is perpendicular to the c axis. When K_1 and K_2 have opposite signs, the situation is more complicated. When $K_1 > 0$ and $K_2 > -K_1$, the c axis is an easy axis. When $K_1 > 0$ and $K_2 < -K_1$, the basal plane is an easy plane. When $K_1 < 0$ and $K_2 < -K_1/2$, the basal plane is an easy plane. When $-2K_2 < K_1 < 0$, there is an easy cone of magnetization. The magnetocrystalline anisotropy constants of several magnetic materials at room temperature are shown in Table 2.3.

Table 2.3. Magnetocrystalline anisotropy constants

Material	Crystal Structure	$K_1(10^5\ erg/cm^3)$	$K_2(10^5\ erg/cm^3)$
Ni	Cubic	-0.5	-0.2
Fe	Cubic	4.8	±0.5
$NiO \cdot Fe_2O_3$	Cubic	-0.62	---
$FeO \cdot Fe_2O_3$	Cubic	-1.1	---
$CoO \cdot Fe_2O_3$	Cubic	20	---
$MnO \cdot Fe_2O_3$	Cubic	-0.3	---
$MgO \cdot Fe_2O_3$	Cubic	-0.25	---
Co	Hexagonal	45	15
$BaO \cdot 6Fe_2O_3$	Hexagonal	33	---
$SrO \cdot 6Fe_2O_3$	Hexagonal	35	14
MnBi	Hexagonal	89	27
YCo_5	Hexagonal	550	---

2.4.2. Shape Anisotropy

If a particle is perfectly spherical in shape, the external applied magnetic field will magnetize it to the same extent in any direction. If a particle is not perfectly spherical, then magnetization of the particle along the long axis will be easier than along the short axis; since the demagnetizing field will not be equal for all directions. The magnetic field within a magnetic material produced by the magnetic moments of the magnetic material is called demagnetizing field. The demagnetizing field along a short axis is stronger than along a long axis; therefore, shape of a magnetic particle is another source of magnetic anisotropy. Shape anisotropy is associated with the magnetostatic energy which originates from the interactions among magnetic dipoles. The magnetostatic energy is also called the demagnetizing energy of the particle and is expressed as

$$E_{ms} = \frac{1}{2} H_d M \tag{53}$$

where H_d is the demagnetizing field and M is the magnetization. The demagnetizing field is expressed as

$$H_d = N_d M \tag{54}$$

where N_d is the demagnetizing factor. Therefore, magnetostatic energy equation can be written in terms of N_d as

$$E_{ms} = \frac{1}{2} N_d M^2 \quad \text{erg/cm}^3 \quad \text{(CGS)} \tag{55}$$

$$E_{ms} = \frac{1}{2} \mu_0 N_d M^2 \quad \text{J/m}^3 \quad \text{(SI)} \tag{56}$$

In rod-like specimens, the demagnetizing energy is much less along the long axis than along the short axis due to the demagnetizing field strength along these axes. Figure 2.10 shows a prolate spheroid as an example of rod-like specimen. According to the figure, the short axis is defined as 'a' $(a = b)$, the long axis is defined as 'c', and the angle between magnetization and long axis is defined as'θ'. The magnetostatic energy for a prolate ellipsoid is given as

$$E_{ms} = \frac{1}{2} [(M\cos\theta)^2 N_c + (M\sin\theta)^2 N_a] \tag{57}$$

where N_c and N_a are demagnetizing factors along c and a, respectively. The energy equation can be rewritten by putting $\cos^2\theta = 1 - \sin^2\theta$ as below

$$E_{ms} = \frac{1}{2} M^2 N_c + \frac{1}{2} (N_a - N_c) M^2 \sin^2\theta \tag{58}$$

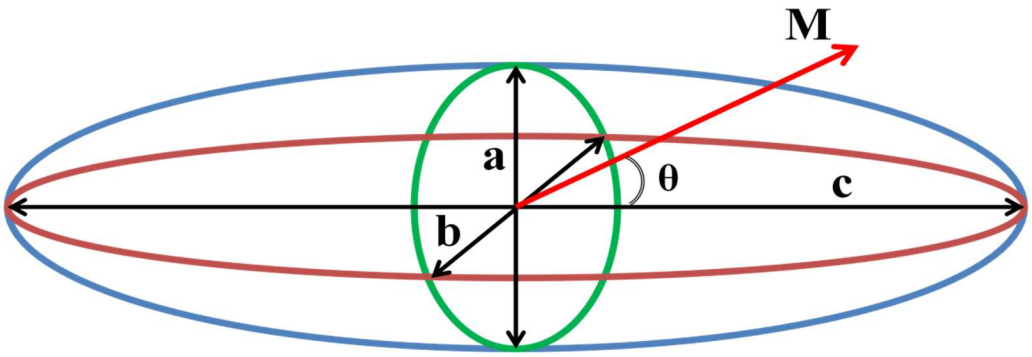

Figure 2.10. Prolate spheroid.

The long axis of the specimen behaves as same as the easy axis of the crystal and the shape anisotropy constant (K_s) is given by

$$K_s = \frac{1}{2}(N_a - N_c)M^2 \quad \text{erg/cm}^3 \quad \text{(CGS)} \tag{59}$$

$$K_s = \frac{1}{2}\mu_0(N_a - N_c)M^2 \quad \text{J/m}^3 \quad \text{(SI)} \tag{60}$$

As a result, magnetization in prolate spheroid ($a = b$ and $c > a$) is easy along the c axis and hard along any axis normal to c. In oblate spheroid (disk), $a < b$ and $b = c$; therefore, magnetization is hard along the shot axis a and is easy along the long axis c. In spherical specimens, $a = b = c$, $N_a = N_c$, and $K_s = 0$; therefore, shape anisotropy disappears. According to the Equation (59), the strength of the shape anisotropy depends both on the axial ratio (c/a) of the specimen which determines ($N_a - N_c$) and the value of the magnetization. Figure 2.11 shows the value of the shape anisotropy constant K_s as a function of the axial ratio for a prolate spheroid of polycrystalline cobalt which has saturation magnetization (M_s) of $1422\ \text{emu/cm}^3$ **[115]**.

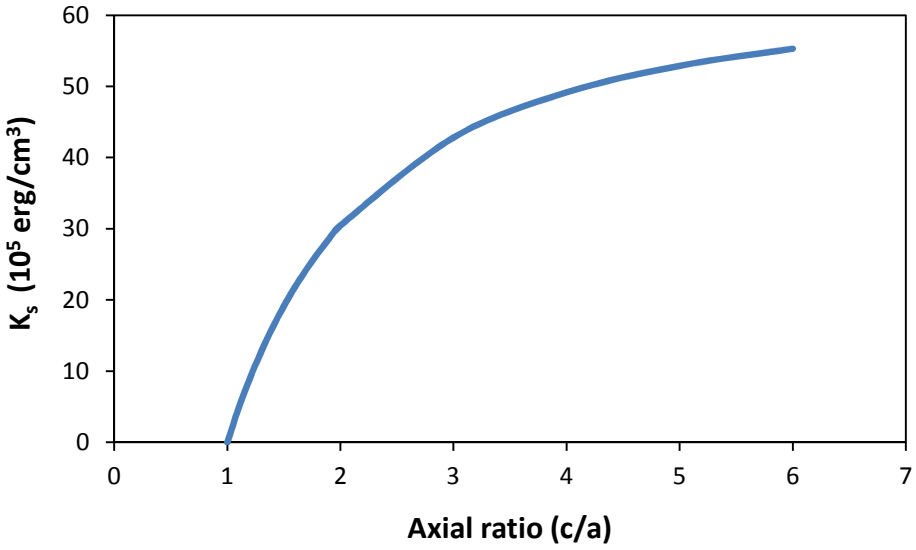

Figure 2.11. Shape anisotropy constant as a function of axial ratio of a prolate spheroid.

Shape anisotropy constant is about $45x10^5$ erg/cm^3 for the axial ratio of 3.5; which is equal to the value of the first magnetocrystalline anisotropy constant (K_1) of cobalt. Therefore, we can conclude that a prolate spheroid of saturated cobalt with axial ratio of 3.5 and without any crystal anisotropy has the same uniaxial anisotropy as a spherical cobalt crystal.

2.4.3. Stress Anisotropy

Mechanical stress which is another source of magnetic anisotropy can change the domain structure, therefore, magnetic properties of magnetic materials. Two types of mechanical stresses such as compressive and tensile stress can be applied to the material. These stresses can increase or decrease the low-field magnetic properties such as permeability and remanence. For example, the magnetostriction of nickel is negative; therefore, a compressive stress increases the permeability and a tensile stress decreases the permeability. The magnetostriction of iron is

positive at low magnetic fields, then zero, and then negative at high magnetic fields. As a result, its magnetic behavior varies under stress **[116]**. There is a relation between the magnetostriction (λ) of a magnetic material and its magnetic behavior under stress. The effect of stress on magnetization is called the magnetomechanical effect. For instance, if a material has positive magnetostriction, applied tensile stress which tends to elongate the materials will increase the magnetization and applied compressive stress will decrease the magnetization. Figure 2.12 shows the effect of mechanical stress on magnetization curve of a material with positive magnetostriction. Material has a magnetization of 'a' at H_{app} under zero stress. When a stress (+σ) is applied, magnetization raises to 'b' at constant magnetic field, and the remanent magnetization which is 'c' under zero stress increases to 'd'. However, no magnetization is produced when a stress is applied to a demagnetized specimen. Magnetization curves starts at origin with or without the application of stress in demagnetized state of the material.

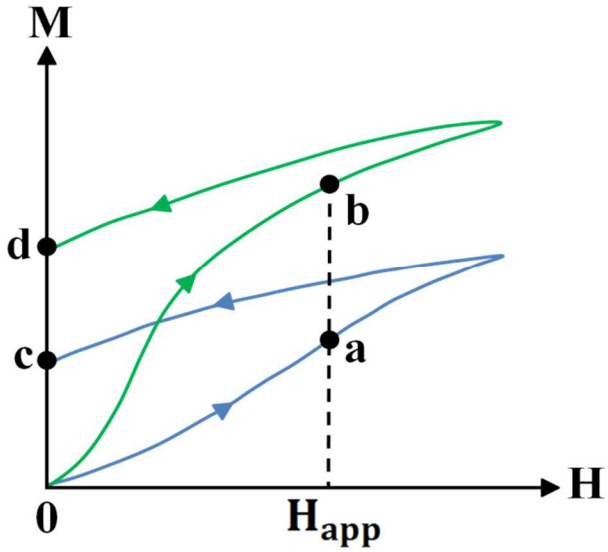

Figure 2.12. Effect of mechanical stress on magnetization curve of a material with positive magnetostriction (blue line: zero stress, green line: under stress).

The direction of saturation magnetization (M_s) within a magnetic domain is controlled by magnetocrystalline anisotropy which is characterized by the first anisotropy constant (K_1) in the absence of stress. When a stress is applied to the material, the direction of M_s is controlled by both K_1 and σ. Therefore, the energy equation for cubic crystals can be expressed as

$$E_{ms} = K_1(\alpha_1^2\alpha_2^2 + \alpha_2^2\alpha_3^2 + \alpha_3^2\alpha_1^2) - \frac{3}{2}\lambda_{100}\sigma\left(\alpha_1^2\gamma_1^2 + \alpha_2^2\gamma_2^2 + \alpha_3^2\gamma_3^2\right) \\ -3\lambda_{111}\sigma(\alpha_1\alpha_2\gamma_1\gamma_2 + \alpha_2\alpha_3\gamma_2\gamma_3 + \alpha_3\alpha_1\gamma_3\gamma_1) \quad (61)$$

where α_1, α_2, α_3 are the direction cosines of saturation magnetization, γ_1, γ_2, γ_3 are the direction cosines of stress, and λ_{100}, λ_{111} are the saturation magnetostrictions in the directions of [100] and [111], respectively when the crystal is magnetized. The fist term of Equation (61) is the magnetocrystalline anisotropy energy. The next two terms which combine magnetostriction and stress form the magnetoelastic energy (E_{me}). Based on the equation, the direction of M_s is controlled by magnetocrystalline anisotropy when K_1 is much larger than $\lambda_{100}\sigma$ and $\lambda_{111}\sigma$. In the case of opposite situation, the direction of M_s is controlled by the stress. If the magnetostriction is isotropic, $\lambda_{100} = \lambda_{111} = \lambda_s$ and the magnetoelastic energy is simplified as

$$E_{me} = -\frac{3}{2}\lambda_s\sigma\cos^2\theta \quad (62)$$

where θ is the angle between M_s and σ. The magnetoelastic energy equation can be rewritten by putting $\cos^2\theta = 1 - \sin^2\theta$ as below

$$E_{me} = \frac{3}{2}\lambda_s\sigma\sin^2\theta \quad (63)$$

The effect of stress on magnetic behavior of a material can be determined by these equations. In addition, the response of a material to the stress depends on the sign of the product of magnetostriction and stress. For instance, a material with positive magnetostriction under tensile stress behaves like one with negative magnetostriction under compressive stress. According to the Equation (63), the magnetoelastic energy is zero when M_s and σ are parallel since $\theta = 0°$ and it has a maximum value of $3/2\,\lambda_s\sigma$ when they are right angles and $\lambda_s\sigma$ is positive. It has a minimum value when they are right angles and $\lambda_s\sigma$ is negative.

In summary, stress by itself can cause domain wall motion under a zero external magnetic field. Furthermore, it can create an easy axis of magnetization. Therefore, when stress exists, stress anisotropy should be considered along with other anisotropies such as magnetocrystalline and shape. All of these three anisotropies are in the same form of $E = K_u \sin^2\theta$. The magnetoelastic energy equation can be rewritten as

$$E_{me} = K_\sigma \sin^2\theta \tag{64}$$

where K_σ is the stress anisotropy constant which is given by $3/2\,\lambda_s\sigma$. If the product of $\lambda_s\sigma$ is positive, the axis of stress is an easy axis. If this product is negative, the axis of the stress is a hard axis. All three anisotropies are summarized in Table 2.4 in terms of uniaxial anisotropy constants (K_u).

Table 2.4. Comparison of uniaxial anisotropy constants

Source of Anisotropy	Anisotropy Constant
Magnetocrystalline	$K_u = K_1$
Shape	$K_u = K_s = 1/2\,(N_a - N_c)M^2$
Stress	$K_u = K_\sigma = 3/2\,\lambda_s\sigma$

2.4.4. Exchange Anisotropy

Exchange anisotropy occurs in multilayers of ferromagnetic and antiferromagnetic materials. Due to the exchange coupling between those materials, the magnetization curve of ferromagnetic material shifts. Exchange anisotropy was discovered in 1956 **[117]**. Single-domain particles of cobalt were taken and partially oxidized to form cobalt oxide layer. The combination of Co and CoO particles were then cooled down to 77°K under strong external magnetic field of 10 kOe, and its magnetization curve was measured at that temperature. As a result, magnetization curve of oxide-coated cobalt particles was shifted to the left under applied magnetic field. If no magnetic field is applied during cooling, magnetization curve is symmetrical and normal. Another example of exchange anisotropy is the disordered nickel-manganese (Ni_3Mn) alloy **[118]**. When the composition of Ni_3Mn was cooled from 300°K to 4.2°K in 5 kOe applied external magnetic field, the magnetization curve was shifted to the left with positive remanence. Since both Co-CoO particles and Ni_3Mn alloy show unidirectional anisotropy rather than uniaxial anisotropy, the anisotropy energy is proportional to the firs power of the cosine and expressed as

$$E = -K\cos\theta \tag{65}$$

where K is the anisotropy constant and θ is the angle between M_s and applied magnetic field.

The unusual shifted magnetization curve of Co-CoO particles is due to the exchange coupling between the spins of ferromagnetic Co and antiferromagnetic CoO at the interface between them. When a strong magnetic field is applied, the cobalt is magnetically saturated but the cobalt oxide is weakly influenced. However, the spins of the first layer of cobalt in the oxide are aligned parallel to the spins in the metal due to the exchange force between the spins of

adjacent cobalt atoms. When the particles are cooled in external magnetic field, the direction of the spins changes, the symmetry breaks, and domains form in the oxide. If a strong magnetic field is applied in negative direction, the direction of spins in the cobalt reverses, and the exchange coupling at the interface forces to reverse the direction of spin in the oxide. Due to the strong magnetocrystalline anisotropy of the antiferromagnet, partial rotation of a few spins occurs at the interface. When the applied magnetic field is removed, the up spins in the oxide at the interface force the spins in the metal to rotate up and therefore the initial state is restored with a positive remanence. This behavior is shown in Figure 2.13.

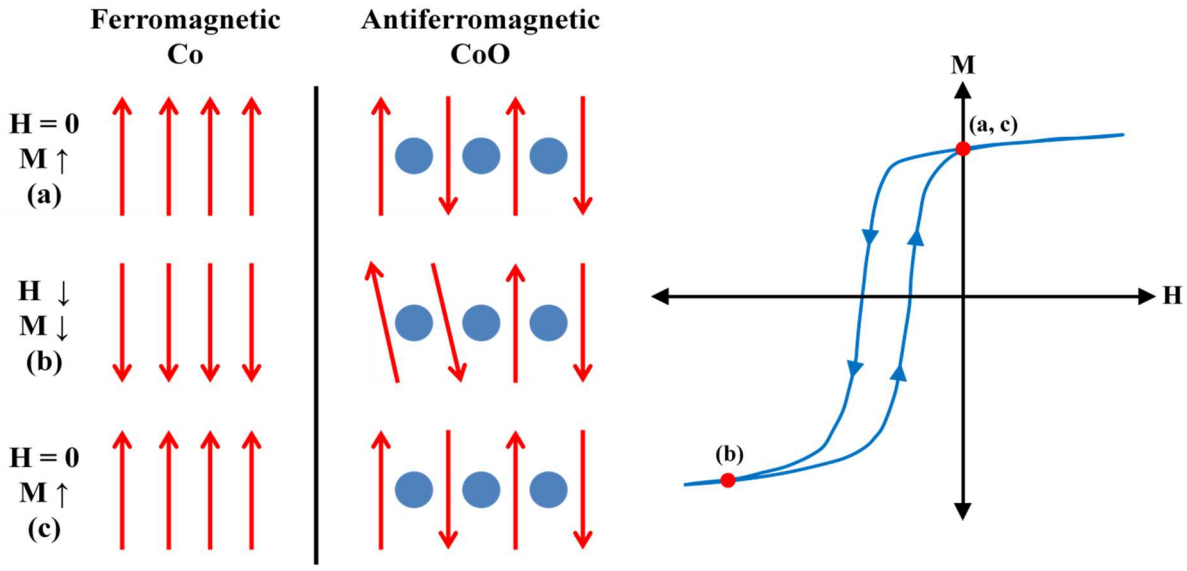

Figure 2.13. Mechanisms of the shifted magnetization curve in Co-CoO particles. Red arrows represent spins on cobalt atoms and blue circles represent oxygen atoms.

In summary, three conditions should be satisfied for exchange anisotropy. The first one is the cooling through Néel temperature in the presence of an applied magnetic field. The second one is the intimate contact between ferromagnet and antiferromagnet for exchange coupling at the interface. The third one is the strong magnetocrystalline anisotropy in antiferromagnet.

The importance of magnetic field assisted cooling is to provide a single easy magnetization direction to the particles. If the particles are cooled in the absence of magnetic field, the exchange coupling occurs at all interfaces which leads normal magnetization curve with zero remanence. In addition, exchange anisotropy can be seen not only in a two-phase system such as Co-CoO but also it can be seen in a single-phase system such as Ni_3Mn due to the inhomogeneity of the composition.

2.5. Magnetic Properties of Nickel Nanowire Arrays Electrodeposited in Anodic Aluminum Oxide Templates

Highly-ordered porous anodic aluminum oxide templates are suitable and inexpensive for large scale fabrication of magnetic nanowire arrays with desired magnetic properties by electrodeposition. Since porous AAO templates provide high pore density, high aspect ratio, and controllable pore diameter and length, magnetic properties of nanowire arrays can be enhanced and differ significantly from their bulk counterparts. Magnetic nanowires such as nickel **[93, 97, 119, 120]**, iron **[93, 99, 103, 104]**, and cobalt **[93, 121, 122]** were electrodeposited in AAO templates and their static and dynamic magnetic properties were studied. Magnetic nanowire arrays have high saturation magnetization, high effective anisotropy field, high permeability, high ferromagnetic resonance frequency and low eddy current loss due to the high aspect ratio of nanowires **[123, 124, 125]**. Moreover, the magnetic properties of magnetic nanowires can be tuned by applying an external DC magnetic field. As a result, electrochemical synthesis of magnetic nanowires in AAO templates is very interesting and promising for potential technological applications.

In this work, nickel nanowire arrays were fabricated in two types of AAO templates with different pore diameters and the effect of pore diameter on magnetic properties of nanowire arrays was studied.

2.5.1. Experimental

Two types of highly-ordered AAO templates were prepared by using a two-step anodization process in either oxalic or sulfuric acid solutions for different pore diameters. After two-step anodization process, a 2 cm^2 area was opened on the back side of the template by etching the aluminum substrate in an aqueous solution of $CuCl_2 \cdot HCl$ at room temperature, and the surrounding aluminum was retained as a support. Then, the remaining alumina barrier layer at the bottom of the pores was removed in a 10 wt% phosphoric acid solution at 30℃ for 36 min and 14 min for oxalic and sulfuric acid anodized templates, respectively. Photoresist was used to protect the top surface of the template from etching solutions. During this process, pore diameters increased slightly due to the pore widening and open-through AAO templates were obtained. Finally, a 200 nm Au layer was coated onto one side of the template by electron-beam evaporation to serve as the working electrode in a two-electrode cell. A nickel anode was used as the counter electrode.

The electrodeposition process was carried out in a commercial Ni bath (Techni Nickel HT-2, Technic Inc.) by pulsed electrodeposition method. Nickel was electrodeposited by applying constant current pulses of 8 mA/cm^2 for 200 ms. Consequently, a delay time of 600 ms was inserted between two successive deposition pulses to recover the concentration of metal ions at the deposition interface. This delay time is very important to improve the homogeneity of the electrodeposition and to limit the hydrogen evolution **[88]**. During the electrodeposition process,

the Ni solution was magnetically stirred at 400 rpm and kept at a constant temperature of 45ºC. The pH of the solution was maintained at 4.0. Figure 2.14 shows the schematic diagram of electrodeposition process.

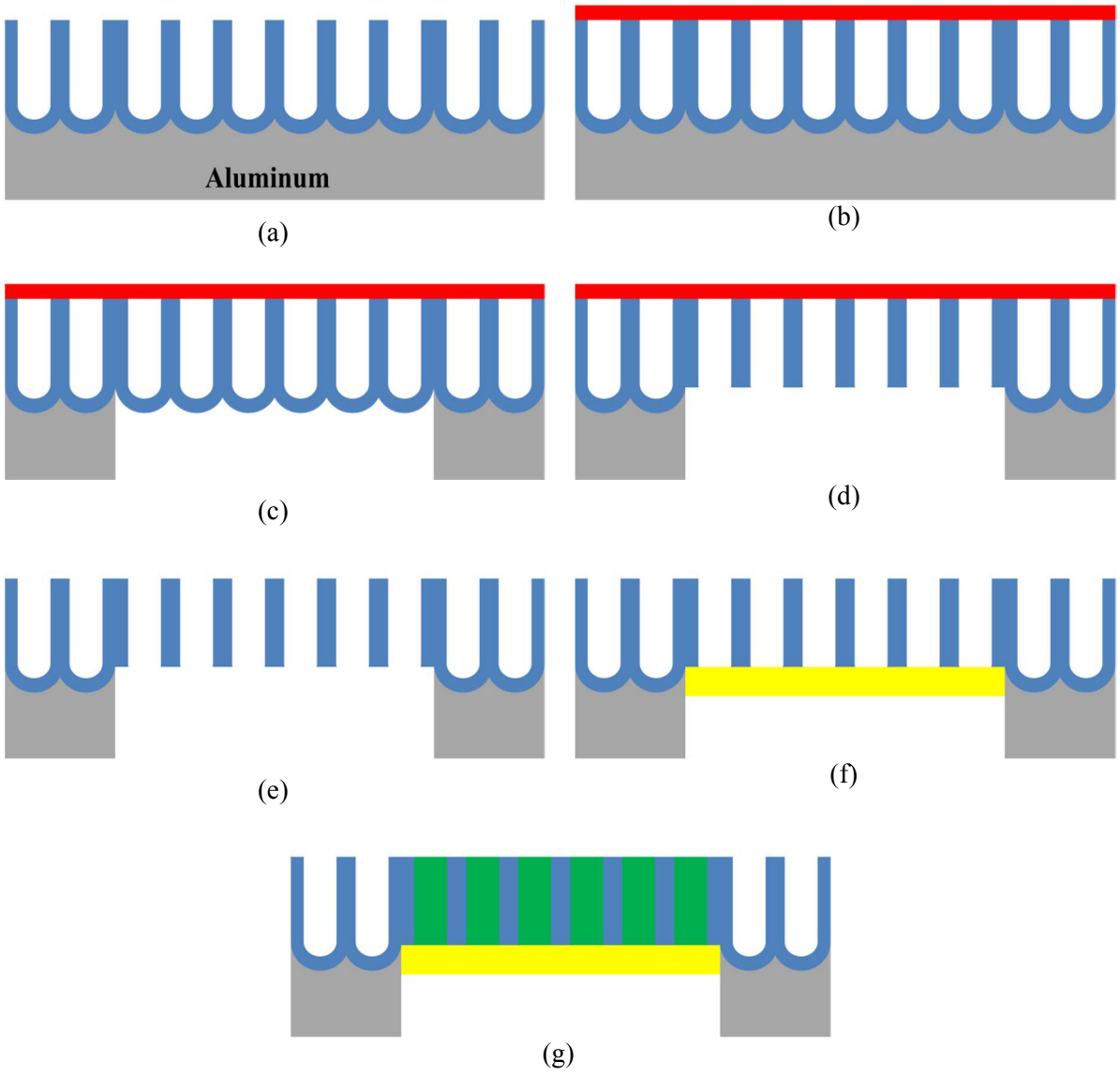

Figure 2.14. Schematic diagram of electrodeposition process.

The process steps are (a) fabrication of AAO template, (b) photoresist coating on top surface, (c) removal of aluminum foil, (d) removal of barrier layer and pore widening,

(e) removal of photoresist and obtaining open-through AAO template, (f) Au evaporation on one side of the AAO template, and (g) Ni electrodeposition into nanopores, respectively.

The morphology of Ni nanowire arrays was investigated by scanning electron microscopy (FEI Magellan 400 XHR SEM) and focused ion beam milling (FEI Quanta 3D FEG FIB). The elemental analysis of the Ni nanowires was examined by energy dispersive X-ray spectroscopy (EDS, Oxford Instruments) attached to SEM. The structural characterization of the Ni nanowires was performed by X-ray diffraction (Rigaku Smartlab XRD) with Cu Kα radiation in the range of $40° \leq 2\theta \leq 100°$. The magnetic measurements of Ni nanowire arrays were carried out at room temperature using a superconducting quantum interference device vibrating sample magnetometer (Quantum Design SQUID VSM) with the magnetic field applied parallel and perpendicular to the nanowires. The angle-dependent ferromagnetic resonance (FMR) measurements were performed in a resonant cavity at a constant frequency of 9.7 GHz (X band) using a spectrometer (Bruker EMX Spectrometer).

2.5.2. Results and Discussion

The SEM images of Ni electrodeposited AAO templates anodized in oxalic acid solution is shown in Figure 2.15. Almost 100% of nanopores of AAO template were filled with nickel. Figure 2.15 (a) shows the top side of the AAO template after focus ion-milling by about 2 μm. The average nanowire diameter was measured to be 70 nm which was very well correlated with initial average pore diameter. Figure 2.15 (b) shows the cross-sectional SEM image of nanowire arrays. Figure 2.15 (c) and (d) show the Ni nanowires after dissolving the AAO template in 0.5M sodium hydroxide (NaOH) solution at room temperature. The average nanowire length was measured to be 15 μm.

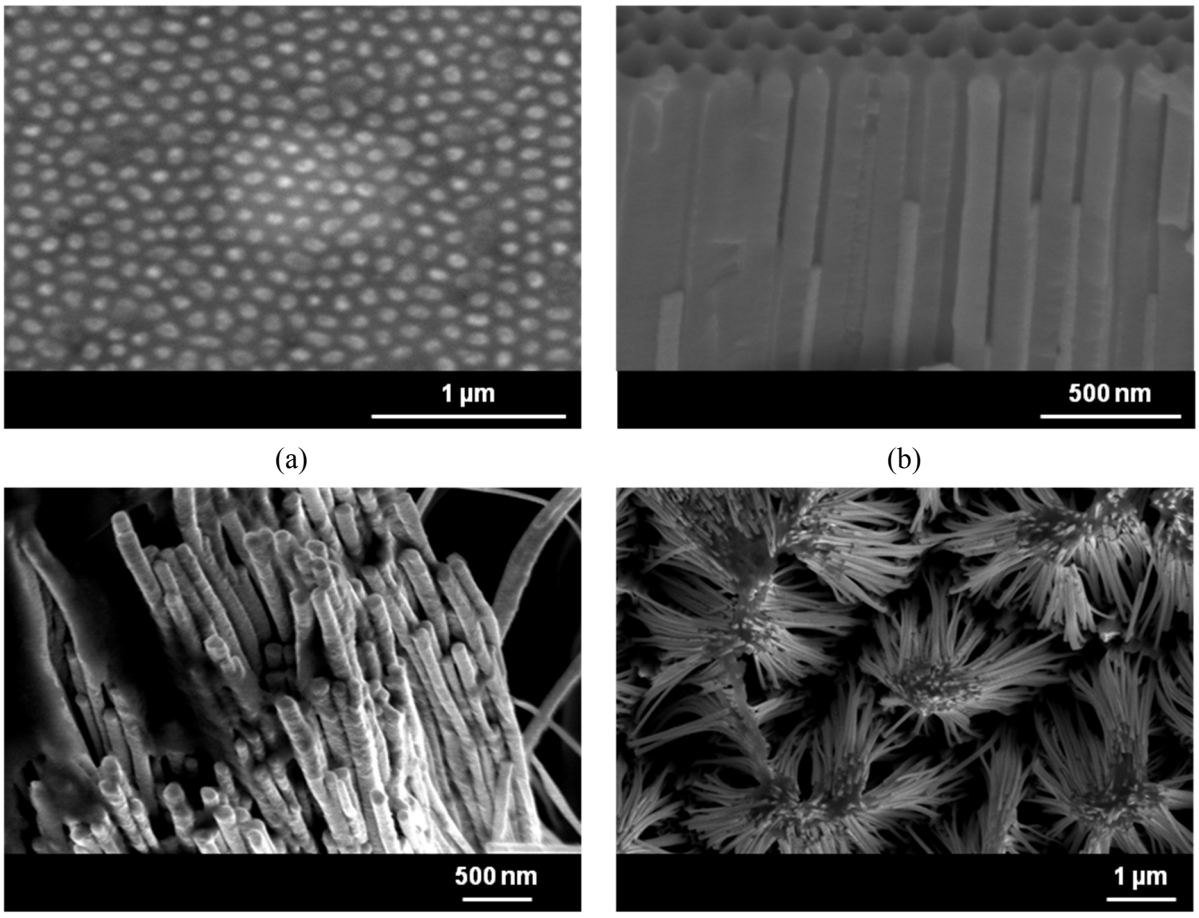

Figure 2.15. SEM images of Ni electrodeposited AAO templates anodized in oxalic acid solution.

The SEM images of Ni electrodeposited AAO templates anodized in sulfuric acid solution is shown in Figure 2.16. Most of the nanopores of the AAO template were successfully electrodeposited with Ni. Figure 2.16 (a) shows the top side of the AAO template after focus ion-milling by about 2 µm. The average Ni nanowire diameter was measured to be 30 nm. Figure 2.16 (b) shows the Ni nanowires after dissolving the AAO template in 0.5M NaOH solution at room temperature. The average nanowire length was measured to be 15 µm.

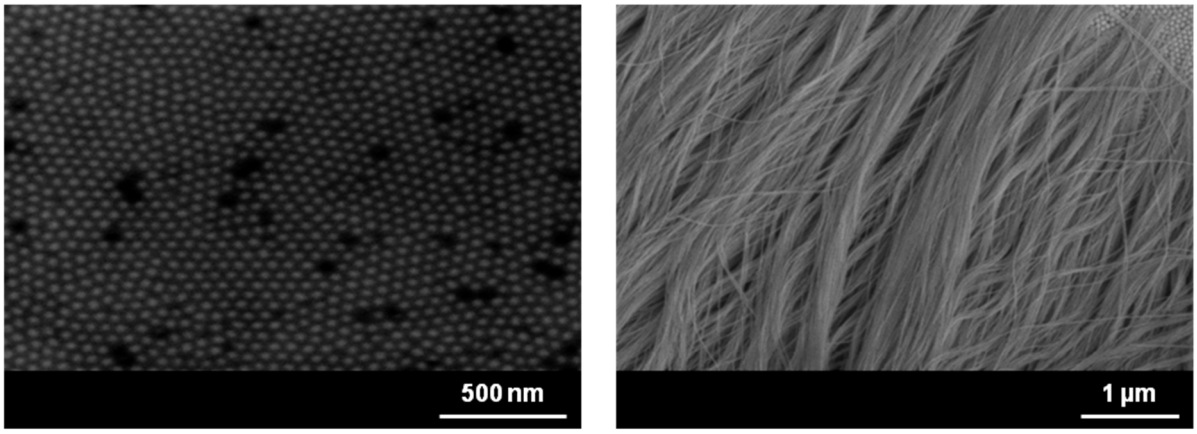

(a) (b)

Figure 2.16. SEM images of Ni electrodeposited AAO templates anodized in sulfuric acid solution.

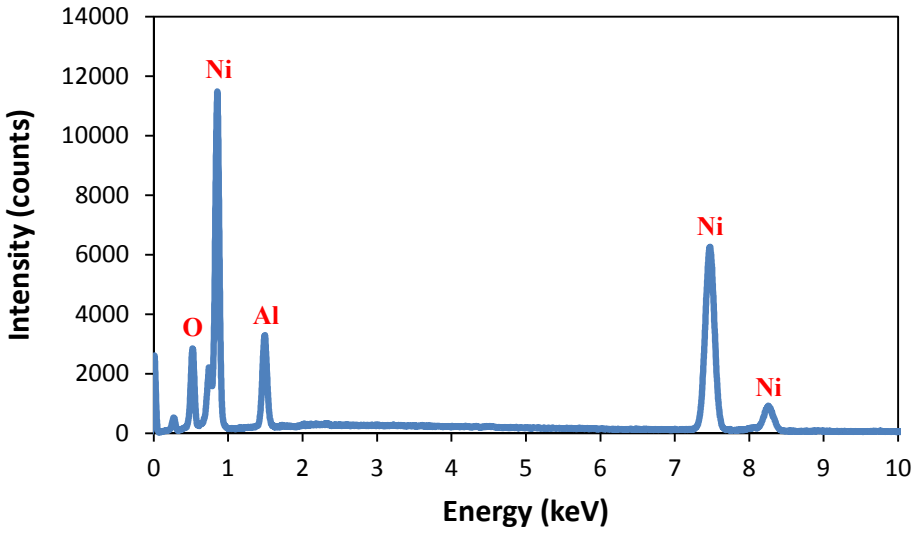

Figure 2.17. EDX spectra of Ni nanowires.

Figure 2.17 shows the EDX spectra of Ni nanowires after dissolving the AAO template partially. The EDX spectra clearly show the presence of Ni along with Al and O and confirm the electrodeposition of pure (100 wt%) Ni nanowires. Al and O have come from the AAO template.

From the EDX spectra, X-ray emission lines of Ni are Lα, Kα, and Kβ which have peaks at 0.851, 7.478, and 8.265 keV, respectively. Al has a Kα peak at 1.487 keV and O has a Kα peak at 0.525 keV.

Figure 2.18 shows the XRD pattern of Ni nanowires electrodeposited in AAO template. The diffraction peaks of Ni at the angles of $2\theta = 44.487°, 51.844°, 76.350°, 92.904°$, and $98.431°$ corresponds to (111), (200), (220), (311), and (222) reflection planes of the face centered cubic (fcc) Ni crystal structure, respectively. The peak corresponds to (111) plane with high intensity shows the preferential growth plane of Ni. The different peaks observed from the XRD pattern inferred that Ni nanowires are not single crystals but consist of polycrystalline fcc arrangement. Furthermore, additional Au and Al_2O_3 peaks were observed. The Au peaks arise from the consucting layer deposited on one side of the AAO template for electrodeposition.

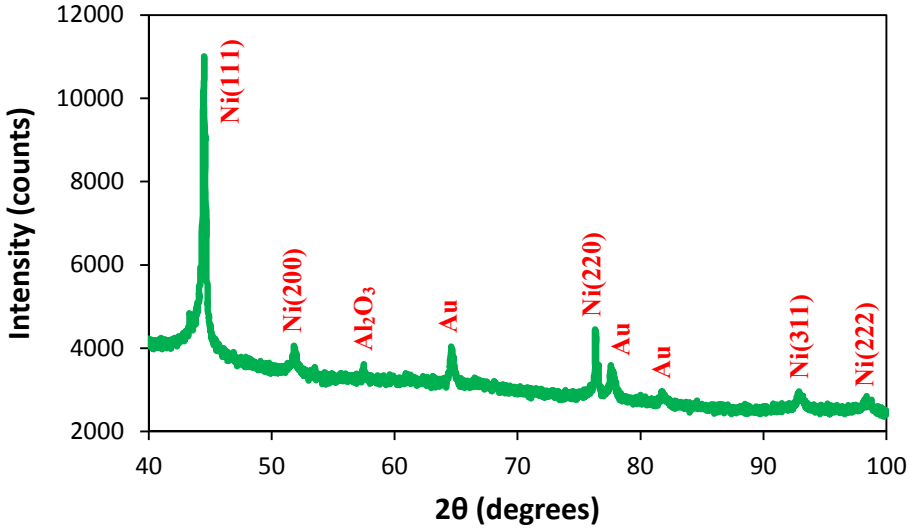

Figure 2.18. XRD pattern of Ni nanowires.

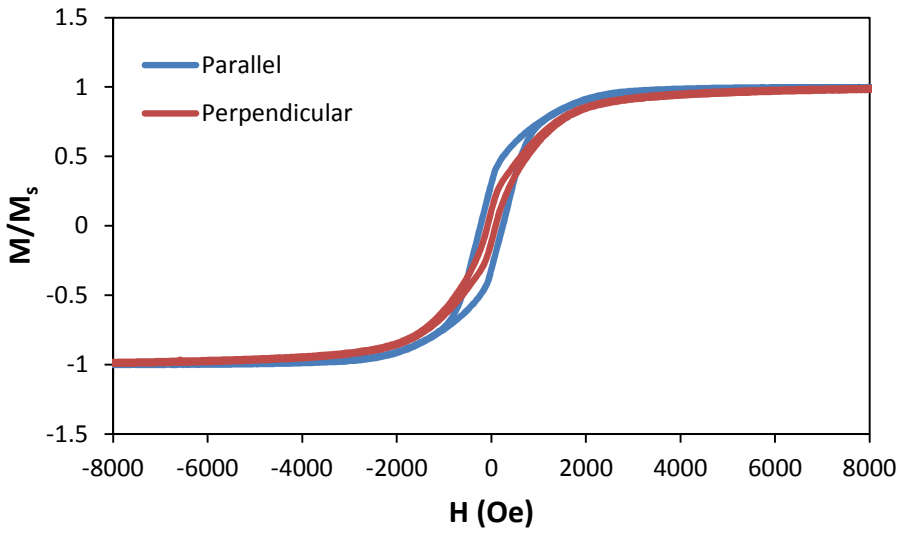

Figure 2.19. Hysteresis curves of Ni nanowire arrays of oxalic acid anodized sample with the applied field parallel (blue line) and perpendicular (red line) to the nanowires.

Figure 2.19 shows the hysteresis curves of Ni nanowire arrays of oxalic acid anodized sample with the magnetic field applied parallel ($\theta = 0°$, θ being the angle between the applied magnetic field and nanowire axis) and perpendicular ($\theta = 90°$) to the nanowires. Measurements were performed at room temperature. The normalized hysteresis curves were obtained by dividing the measured magnetic moments by the high field magnetic moment. From the hysteresis curves, when the field was applied parallel to the nanowires, hysteresis curve exhibited a large coercivity (H_c), a large remanent magnetization (M_r), large squareness (s), and and a small saturation field (i.e., the field necessary to reach the saturation magnetization, M_s). In contrast, when the field was applied perpendicular to the nanowires, hysteresis curve exhibited a small coercivity, remanent magnetization and squareness, and large saturation field. Therefore, this indicates that the easy axis of the sample is parallel to the nanowires and the hard axis of the sample is perpendicular to the nanowires. The coercivity of nanowire arrays were measured to be 240 and 90 Oe for applied magnetic field parallel and perpendicular to the nanowire arrays,

respectively. The squareness (M_r/M_s) values were measured to be 0.3 and 0.1 for easy and hard axis, respectively.

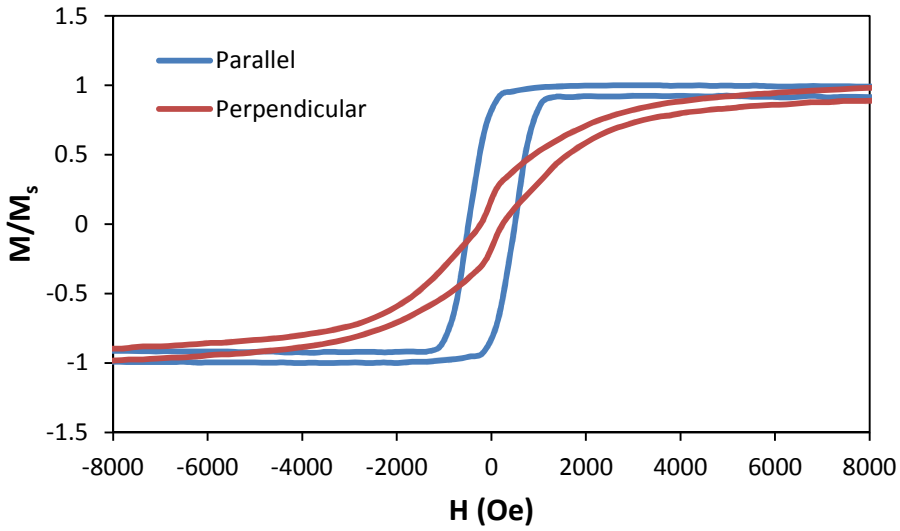

Figure 2.20. Hysteresis curves of Ni nanowire arrays of sulfuric acid anodized sample with the applied field parallel (blue line) and perpendicular (red line) to the nanowires.

Figure 2.20 shows the hysteresis curves of Ni nanowire arrays of sulfuric acid anodized sample with the magnetic field applied parallel and perpendicular to the nanowires. Based on the hysteresis curves, the easy axis of the sample is parallel to the nanowires and the hard axis of the sample is perpendicular to the nanowires. The coercivity of nanowire arrays were measured to be 499 and 252 Oe for applied magnetic field parallel and perpendicular to the nanowire arrays, respectively. The squareness values were measured to be 0.8 and 0.17 for easy and hard axis, respectively. As a comparison, sulfuric acid anodized sample has enhanced coercivity and squareness for both easy and hard axes than the oxalic acid anodized sample due to the high aspect ratio. Therefore, it is important to note that coercivity and squareness depend on the aspect ratio of the Ni nanowires.

Conventional ferromagnetic resonance (FMR) technique was used to study the dynamic behavior of the Ni nanowire arrays. In the room temperature FMR measurements, the microwave pumping field (h_{rf}) had a frequency of 9.7 GHz (X band) and was always oriented perpendicular to the applied magnetic field (H_o) and to the nanowire axis. The FMR derivative spectra of each sample were measured for varying angles of applied magnetic field from 0° to 180° in steps of 30°. Figure 2.21 shows the schematic representation of FMR measurements.

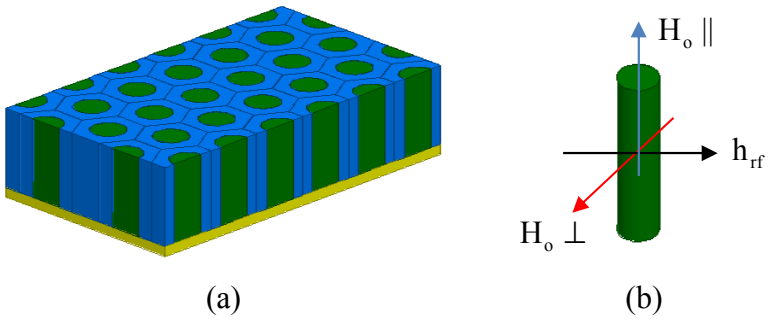

Figure 2.21. Schematic representation of FMR measurements. (a) Ni nanowires electrodeposited in AAO template. (b) Orientation of applied magnetic field and microwave pumping field.

A theoretical model has been used to explain the angular dependence of resonance field. The nanowires are considered to be close to an infinite cylinder due to their high aspect ratio. The FMR condition of nanowire arrays can be obtained from the total free energy density of an infinite cylinder **[125]**,

$$E = K_{eff}\sin^2\theta - M_s H_o[\sin\theta\sin\theta_H\cos(\phi - \phi_H) + \cos\theta\cos\theta_H] \quad (66)$$

where the first term represents effective anisotropy energy and the second term represents the Zeeman energy of the nanowire array. (θ, ϕ) and (θ_H, ϕ_H) are the polar and azimuthal angles of

the magnetization (M) and the applied magnetic field (H_o), respectively. The coordinate system used for the theoretical model is shown in Figure 2.22.

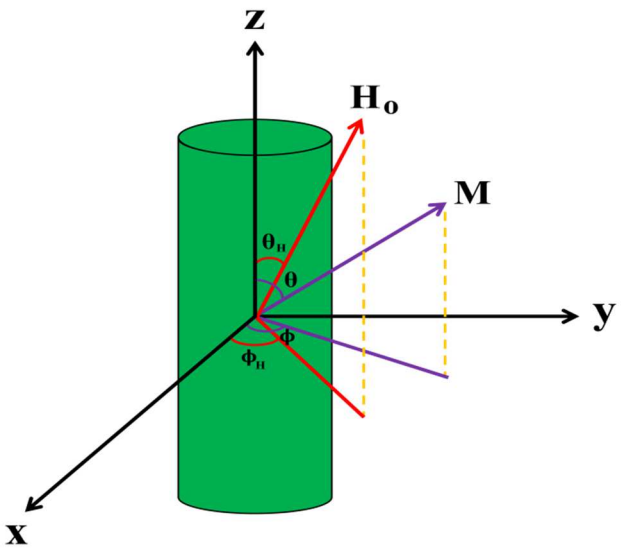

Figure 2.22. The coordinate system for the theoretical model.

The effective uniaxial anisotropy parameter is,

$$K_{eff} = \pi M_s^2 (1 - 3P) + K_u \tag{67}$$

where the first term represents the shape demagnetization energy of the nanowire array and the second term represents the additional second-order uniaxial anisotropy with the symmetry axis along the nanowire direction **[123, 125, 126]**. P is the porosity (packing density) of the nanowires and is defined in Equation (12) as $P = (\pi/2\sqrt{3})(D_p/D_{int})^2$.

The ferromagnetic resonance condition is obtained from the second derivatives of the total free energy density by the formalism of Smith and Beljers **[127]** as

$$\left(\frac{\omega}{\gamma}\right)^2 = \frac{(E_{\theta\theta}E_{\phi\phi} - E_{\theta\phi}^2}{(M_s \sin\theta)^2}\Big|_{\theta=\theta_o,\phi=\phi_o} \tag{68}$$

Therefore, the FMR dispersion relation is obtained as **[119, 121, 125]**

$$\left(\frac{\omega}{\gamma}\right)^2 = [H_{eff}\cos 2\theta_0 + H_0\cos(\theta_0 - \theta_H)][H_{eff}\cos^2\theta_0 + H_0\cos(\theta_0 - \theta_H)] \tag{69}$$

where $\omega = 2\pi f$, f is the microwave frequency, $\gamma = g\mu_B/\hbar$ is the gyromagnetic ratio, g is the Landé factor, μ_B is the Bohr magneton, and $\hbar$ is the reduced Planck constant. The angle θ_0 corresponds to the equilibrium angle of the magnetization and is determined from the minimization of the total free energy density with respect to θ for each H_0 and θ_H. Energy minimization is defined as **[120]**

$$E_\theta = \frac{dE}{d\theta}\Big|_{\theta=\theta_0} = 0 \tag{70}$$

$$dE/d\theta = M_s H_{eff}\sin\theta_0\cos\theta_0 + M_s H_0 \sin(\theta_0 - \theta_H) = 0 \tag{71}$$

$$H_{eff}\sin\theta_0\cos\theta_0 + H_0 \sin(\theta_0 - \theta_H) = 0 \tag{72}$$

Equations (69) and (72) are solved iteratively to obtain effective anisotropy field (H_{eff}) and g. At $\theta_H = 0^o$ (parallel) or $\theta_H = 90^o$ (perpendicular), the equality $\theta_H = \theta_0$ in Equation (69) leads to two relatively simple ferromagnetic resonance conditions, which may be used to evaluate the H_{eff} and g. H_{eff}^2 can be neglected in Equation (69) at resonance at high frequencies since $H_{eff}^2 \ll H_0^2$ and $\theta_H \cong \theta_0$. By using the trigonometric identity of $\cos 2\theta_H + \cos^2\theta_H = 3\cos^2\theta_H - 1$, Equation (69) is simplified to **[120]**

$$H_0 \cong \frac{\omega}{\gamma} + \frac{H_{eff}(1 - 3\cos^2\theta_H)}{2} \tag{73}$$

In Equation (73), when $\cos^2\theta_H = 1/3$ ($\theta_H \cong 55^o$), the second term vanishes so that the resonance field (H_0) is independent of the effective anisotropy field. Therefore, gyromagnetic ratio (γ) can be obtained. The effective anisotropy field (H_{eff}) in Equation (69) is mainly determined by following three contributions: the shape anisotropy field H_{shape} (which can develop magnetization easy axis parallel to the nanowire axis), the dipolar interaction field $H_{dipolar}$ (which can develop magnetization easy axis perpendicular to the nanowire axis), and an additional second order uniaxial anisotropy field H_u. The shape anisotropy field is defined as $H_{shape} = 2\pi M_s$ (where M_s is the saturation magnetization). The dipolar interaction field is defined as $H_{dipolar} = 6\pi M_s P$. The dipolar interaction field has two components: $2\pi M_s P$ (due to the charges on the lateral surface) and $4\pi M_s P$ (due to the charges on the top and the bottom surfaces). The second order uniaxial anisotropy field is defined as $H_u = 2K_u/M_s$ (where K_u is the second order uniaxial anisotropy constant) and it might be positive or negative depending on the orientation of the anisotropy field towards the nanowire axis **[128]**. It is positive for parallel orientation and negative for perpendicular orientation. Therefore, the effective anisotropy field is defined as **[128, 129]**

$$H_{eff} = H_{shape} - H_{dipolar} \pm H_u \tag{74}$$

$$H_{eff} = 2\pi M_s - 6\pi M_s P \pm (2K_u/M_s) \tag{75}$$

$$H_{eff} = 2\pi M_s(1 - 3P) \pm (2K_u/M_s) \tag{76}$$

In addition, $P = 0$ for an isolated nanowire and $P = 1$ for a continuous film.

A typical sequence of FMR derivative spectra measured at 9.7 GHz as a function of θ_H is shown in Figure 2.23 for Ni nanowire arrays with a diameter of 70 nm and a length of 15 μm. In all cases, the resonance field (H_0) of the absorption peak increases by changing the angle from parallel (0^o) to perpendicular (90^0) to the nanowire axis that is in accordance with the nanowire axis being the easy axis.

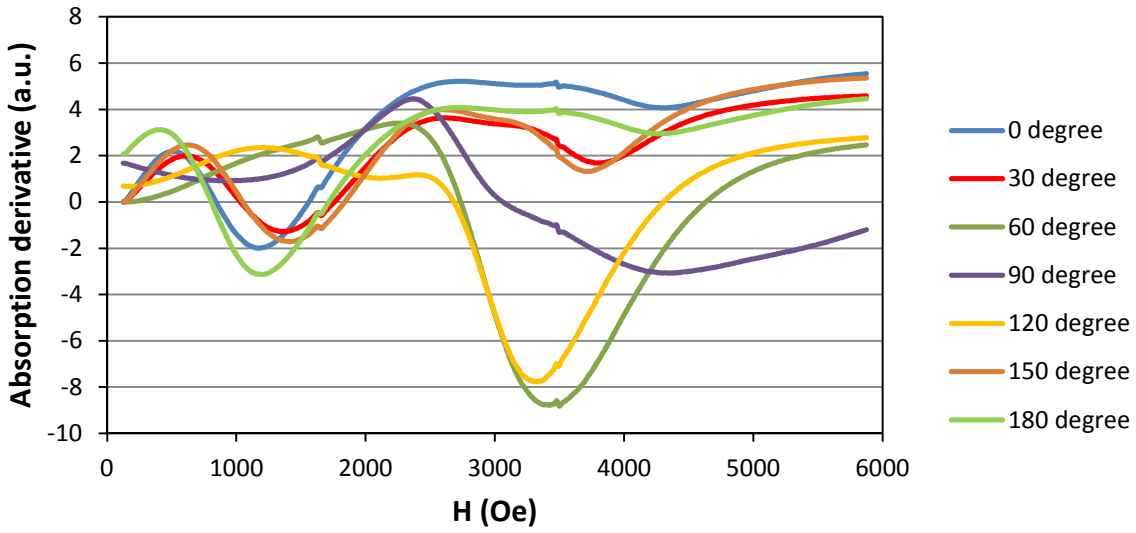

Figure 2.23. FMR derivative spectra of Ni nanowire arrays with a diameter of 70 nm.

The angular dependence of the resonance field is shown in Figure 2.24. According to the Equation (73), the calculated H_{eff} and g values were 1.48 kOe and 2.98, respectively. The amplitude ($H_{0,max} - H_{0,min}$) and the plot shape of the H_0 versus θ_H are directly related to the amplitude and sign of the effective anisotropy field. The bell shape of the angular dependence of the resonance field curve indicates a positive effective anisotropy field.

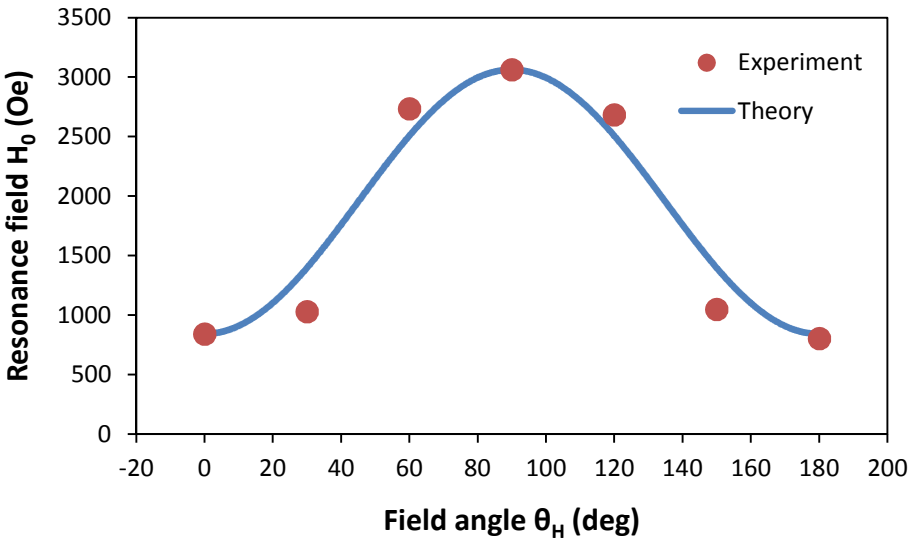

Figure 2.24. Angular dependence of resonance field for Ni nanowires with a diameter of 70 nm.

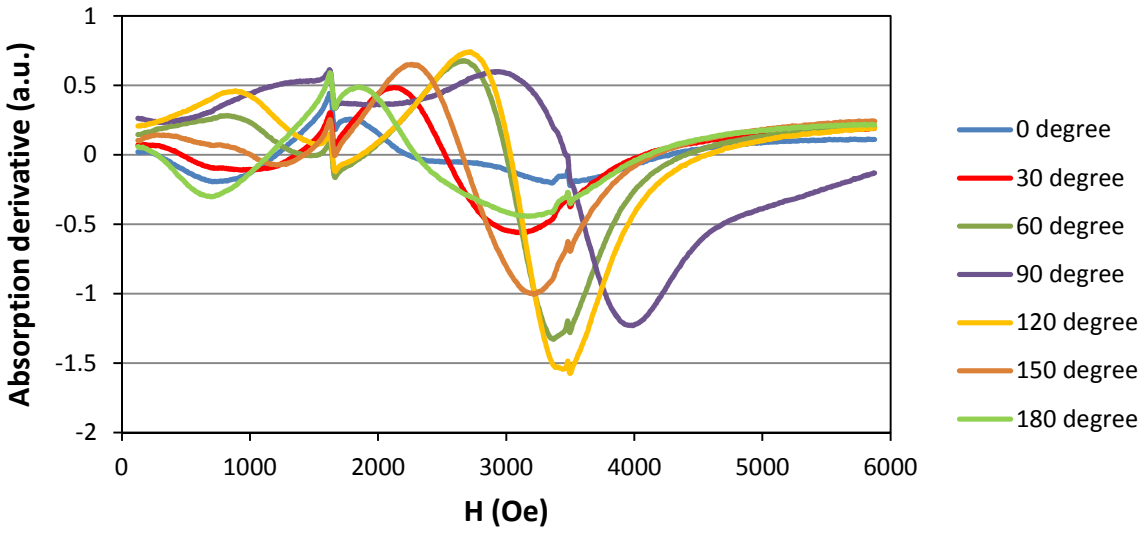

Figure 2.25. FMR derivative spectra of Ni nanowire arrays with a diameter of 30 nm.

Figure 2.25 shows the FMR derivative spectra measured at 9.7 GHz as a function of θ_H for Ni nanowire arrays with a diameter of 30 nm and a length of 15 μm. In this sample, the general bell shape of the angular dependence of the resonance field is a signature of a positive effective anisotropy field, that is, an easy axis parallel to the nanowires. The angular dependence

of the resonance field is shown in Figure 2.26. According to the Equation (73), the calculated H_{eff} and g values were 0.819 kOe and 2.27, respectively. The variation of resonance field for both samples was usually observed and reported for Ni nanowire arrays **[92, 120, 124, 125, 130]**.

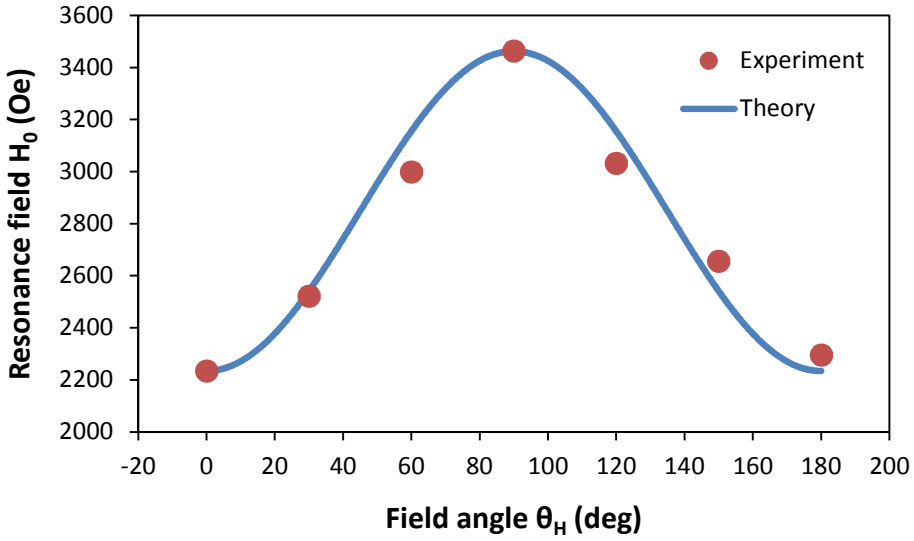

Figure 2.26. Angular dependence of resonance field for Ni nanowires with a diameter of 30 nm.

In addition to conventional FMR, vector network analyzer (VNA) FMR is used to study the dynamic behavior of nanowire arrays and extract the H_{eff} and g factor. In VNA FMR, frequency is swept at constant applied magnetic field and resonance frequency as a function of applied magnetic field is obtained. The FMR dispersion relation defined in Equation (69) can be reduced for the particular cases for the magnetic field applied parallel and perpendicular to the nanowire axis **[123]**.

For $H_{eff} > 0$ and H_0 is parallel to the nanowire axis,

$$\left(\frac{\omega}{\gamma}\right)_{\parallel} = (H_{eff} + H_0) \tag{77}$$

For $H_0 < H_{eff}$ and H_0 is perpendicular to the nanowire axis,

$$\left(\frac{\omega}{\gamma}\right)_{\perp}^{2} = (H_{eff}^2 - H_0^2) \tag{78}$$

For $H_0 > H_{eff}$ and H_0 is perpendicular to the nanowire axis,

$$\left(\frac{\omega}{\gamma}\right)_{\perp}^{2} = (H_0 - H_{eff})H_0 \tag{79}$$

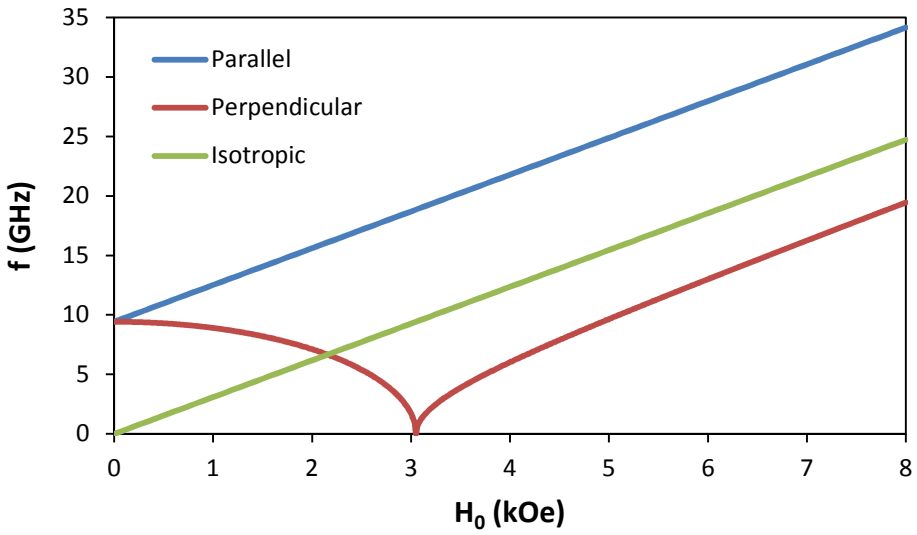

Figure 2.27. Resonance frequencies as a function of applied magnetic field for an isolated Ni nanowire.

As shown in Figure 2.27, when the magnetic field is applied parallel to the nanowire axis (easy axis), the resonance frequency varies linearly with the magnetic field intensity. The slope is given by γ and the zero field frequency is given by γH_{eff}. In contrast, when the magnetic field is applied perpendicular to the nanowire axis (hard axis), the resonance frequency goes off ($\omega = 0$) corresponds to the effective anisotropy field. Finally, the dashed line Figure 2.27 corresponds to an isotropic medium.

2.5.3. Conclusions

Two types of highly-ordered AAO templates were fabricated by using a two-step anodization process in either oxalic or sulfuric acid solutions for different pore diameters. Ni nanowires were deposited into the nanopores of AAO templates by pulsed electrodeposition. Most of the nanopores of the AAO templates were filled with nickel. In oxalic acid anodized AAO templates, the average nanowire diameter and length were measured to be 70 nm and 15 μm, respectively. In sulfuric acid anodized AAO templates, the average nanowire diameter and length were measured to be 30 nm and 15 μm, respectively. The presence and purity (100 wt %) of deposited Ni nanowires were examined and confirmed by EDX spectra. The XRD pattern showed that Ni nanowires are not single crystals but consist of polycrystalline fcc arrangement. The preferential growth plane of Ni nanowires was (111) due to the high intensity in XRD pattern. Based on the hysteresis curves of Ni nanowire arrays (70 nm and 30 nm in diameter), the easy axis of magnetization was parallel to the nanowires and the hard axis of magnetization was perpendicular to the nanowires. The coercivity and squareness of nanowire arrays with 70 nm diameter were measured to be 240 and 90 Oe, 0.3 and 0.1 for easy and hard axis, respectively. The coercivity and squareness of nanowire arrays with 30 nm diameter were measured to be 499 and 252 Oe, 0.8 and 0.17 for easy and hard axis, respectively. The nanowire arrays with 30 nm diameter have enhanced coercivity and squareness for both easy and hard axes than the nanowire arrays with 70 nm diameter due to the high aspect ratio. Therefore, we can conclude that coercivity and squareness depend on the aspect ratio of the nanowires. The FMR derivate spectra of both nanowire arrays showed similar dynamic behavior which confirms that easy magnetization axis is along the nanowire axis. Both Ni nanowire arrays have positive effective anisotropy filed due to the bell shape of the angular dependence of the resonance field.

The calculated effective anisotropy field and g value were 1.48 kOe and 2.98 for Ni nanowires with 70 nm diameter. The calculated effective anisotropy field and g value were 0.819 kOe and 2.27 for Ni nanowires with 30 nm diameter. Consequently, nanowires fabricated by the integration of magnetic materials into the AAO templates with different pore diameters are very useful to tune the magnetic properties of the magnetic materials and are strong candidates for advanced data storage and microwave applications.

CHAPTER 3

FABRICATION OF SPIRAL INDUCTORS WITH MAGNETIC CORES

There is a strong demand for high quality and performance integrated RF components such as, transformers, filters, oscillators, regulators, and matching networks for radio frequency integrated circuits (RFIC). One of the fundamental passive elements for implementation of those components into RFIC is inductors. Among various means in integrating inductors into RFIC, spiral inductors have attracted most attention owing to its compact design and small form factor. However, inductance and quality factor of the spiral inductors do not scale efficiently with the number of turns, leading to excessive area consumption and limited operating frequency **[131].** Thus, it is essential to increase inductance and quality factor at high operating frequency and compact size of spiral inductors for realization of RFIC.

To further miniaturize the size, lower the cost, improve the performance, and increase the operating frequency of spiral inductors for RFIC, integration of ferromagnetic materials into an air core inductor has attracted much research interest. Ferromagnetic materials act as the flux-amplifying components in spiral inductors and correspondingly, inductance (L) and quality factor (Q) enhancement and area occupation reduction can be achieved in these inductors **[132]**. Different combinations of ferrites and soft magnetic metal-alloy films have been reported for integration into spiral inductors attributed to their magnetic and electrical properties such as high saturation magnetization, controllable anisotropy, single domain state, and high resistivity **[131, 133-138]**. However, spiral inductors with ferromagnetic cores suffer from poor performance at high frequencies due to ferromagnetic resonance (FMR) effect and Eddy current

loss occurrence in the layer of ferromagnetic materials **[139]**. These two shortcomings of ferromagnetic materials need to be addressed properly in order to use them in spiral inductors.

The first drawback of the magnetic materials (ferromagnetic resonance frequency) can be solved by patterning the magnetic film into small segments since pattering the magnetic film increases FMR frequency by increasing the anisotropy field **[134, 135, 137, 138]**. The second drawback of the magnetic materials (Eddy current loss) can be solved by laminating the magnetic film into multiple layers with dielectric interlayer since laminating the magnetic film suppresses the Eddy current loss **[134, 135, 138, 140]**. Considering that the most efficient way of concentrating magnetic flux in spiral inductors is to have magnetic materials fully surround the spiral inductors, the use of patterning and laminating film for fabricating the inductor is a very complex and challenging process.

The electroplating of a ferromagnetic material into AAO template is known to be the most simple and cost effective method to enhance the FMR frequency and suppress the Eddy current loss. Ferromagnetic nanowires have high saturation magnetization, high effective anisotropy field, high permeability, high FMR frequency and low Eddy current loss due to the high aspect ratio of nanowires **[123-125]**. Moreover, the magnetic properties of ferromagnetic nanowires can be tuned by applying an external DC magnetic field. Since AAO templates are self-laminated and patterned, they can be easily integrated with a spiral inductor without adding the complexities of fabrication process.

3.1. Design Parameters for Planar Spiral Inductors

Figure 3.1 shows the layouts of planar spiral inductors. The layout design parameters that characterize the spiral inductor geometry are the inner diameter (D_{in}), the outer diameter (D_{out}), the width of the conductor (w), the spacing between adjacent conductors (s), the number of turns (n), the average diameter (D_{avg}), the inductor length (l), and the inductor area (A).

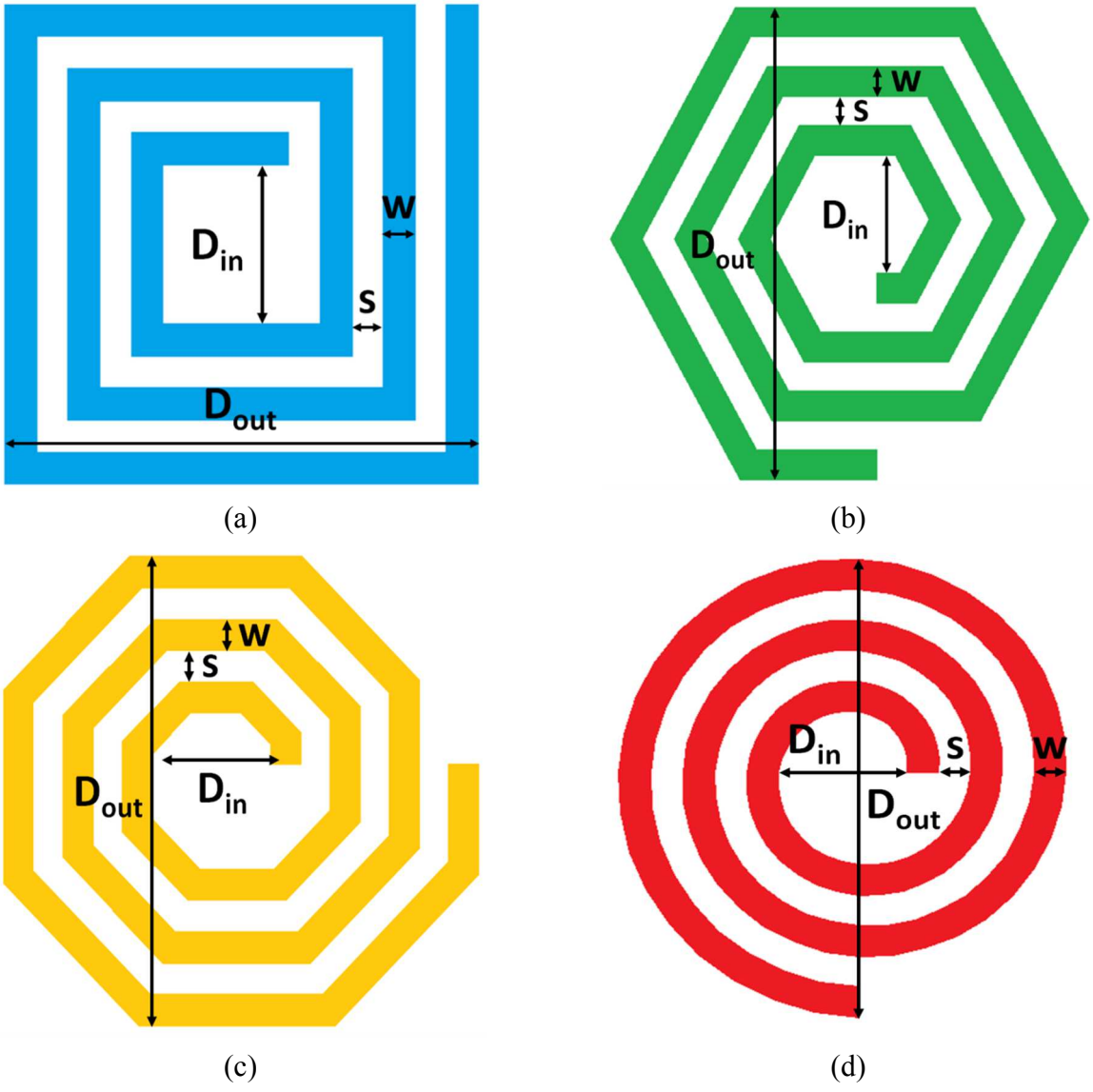

Figure 3.1. Planar spiral inductor layouts. (a) square, (b) hexagonal, (c) octagonal, and (d) circular.

The outer diameter, the average diameter, and the fill ratio of the spiral inductor are defined as **[141]**,

$$D_{out} = D_{in} + 2nw + 2(n-1)s \tag{80}$$

$$D_{avg} = (D_{out} + D_{in})/2 \tag{81}$$

$$\rho = (D_{out} - D_{in})/(D_{out} + D_{in}) \tag{82}$$

The length **[141]** and the area **[142, 143]** of the spiral inductor are defined as,

$$l = N_{side}\, D_{avg}\, n \tan(\pi/N_{side}) \tag{83}$$

$$A = (D_{out})^2 \tag{84}$$

where N_{side} is the number of sides of the spiral inductor polygonal shape.

3.2. DC Inductance Expressions for Planar Spiral Inductors

Figure 3.2 shows the equivalent circuit model of the spiral inductor. In this model, L is the series inductance, R is the series resistance, and C is the series capacitance of the spiral inductor.

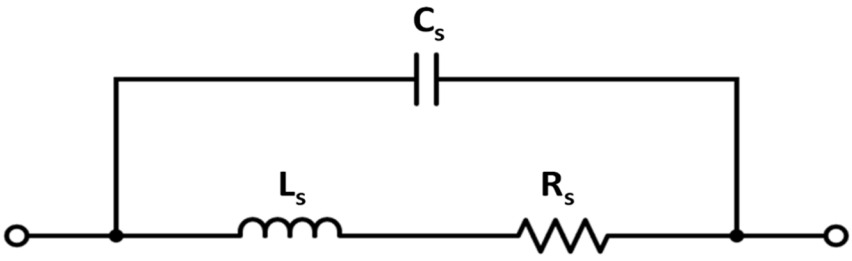

Figure 3.2. Equivalent circuit model of the spiral inductor.

The series resistance of the spiral inductor is expressed as **[141, 143, 144]**,

$$R_s = \frac{\rho\, l}{w\, \delta\, (1 - e^{-t/\delta})} = \frac{l}{\sigma\, w\, \delta\, (1 - e^{-t/\delta})} \tag{85}$$

Where ρ is the resistivity of the conductor, l is the total length of the conductor, w is the width of the conductor, δ is the conductor skin depth, σ is the conductivity of the conductor, and t is the thickness of the conductor. The skin depth is a measure of how closely electric current flows into the surface of a conductor and is a function of frequency. The skin depth is defined as **[144]**,

$$\delta = \sqrt{\frac{2\,\rho}{\omega\,\mu}} = \sqrt{\frac{\rho}{\pi\,\mu\,f}} \tag{86}$$

where $\mu = \mu_o \mu_r$ is the permeability ($\mu_o = 4\pi 10^{-7}$ H/m, permeability of free space; μ_r: relative permeability of a material), and f is the frequency.

The series capacitance of the spiral inductor is mainly due to the overlap capacitances between the spiral conductors and the under-pass conductor which connects the input port to the output port. The series capacitance is expressed as **[141, 143, 144]**,

$$C_s = n_c\, w^2\, \frac{\varepsilon_{ox}}{t_{ox,M1-M2}} \tag{87}$$

where n_c is the number of overlaps, $\varepsilon_{ox} = \varepsilon_o \varepsilon_r$ is the permittivity of the oxide ($\varepsilon_o = 8.854\text{x}10^{-12}$ F/m, permittivity of free space; ε_r: relative permittivity of a material) and $t_{ox,M1-M2}$ is the thickness of oxide between spiral and the under-pass.

Several accurate expressions for series inductance of spiral inductors have been developed. These expressions were summarized below.

3.2.1. Modified Wheeler Expression

Modified Wheeler formula was developed with a simple modification of the original Wheeler formula and is expressed as **[145]**,

$$L_{mw} = K_1 \mu \frac{n^2 D_{avg}}{1 + K_2 \rho} \tag{88}$$

where ρ is the fill ratio, D_{avg} is the average diameter, and are defined previously. The coefficients of K_1 and K_2 are layout dependent and are shown in Table 3.1 for different spiral inductor layouts. The fill ratio represents how hollow the spiral inductor is. If the fill ratio is small, the spiral inductor is hollow ($D_{out} \approx D_{in}$). If the fill ratio is large, the spiral inductor is full ($D_{out} \gg D_{in}$). Two inductors with the same average diameter but different fill ratios have different inductor values. The full inductor has a smaller inductance value since its inner turns are closer to the center of the spiral and therefore contribute less positive mutual inductance and more negative mutual inductance **[145]**.

Table 3.1. Coefficients for modified Wheeler formula

Layout	$\mathbf{K_1}$	$\mathbf{K_2}$
Square	2.34	2.75
Hexagonal	2.33	3.82
Octagonal	2.25	3.55

3.2.2. Current Sheet Expression

Current sheet expression was obtained by approximating the sides of the spirals by symmetrical current sheets of equivalent current densities **[145]**. For instance, four identical

current sheets are obtained in the case of square spiral inductors. The current sheets on opposite sides are parallel to each other; however the current sheets on the same sides are orthogonal. The sheets with orthogonal current sheets have zero mutual inductance; therefore the total inductance is obtained by evaluating the self inductance of one sheet and the mutual inductance between opposite current sheets. The self and mutual inductances are evaluated by using the concepts of geometric mean distance (GMD), arithmetic mean distance (AMD), and arithmetic mean square distance (AMSD). The current sheet expression is defined as **[145]**,

$$L_{gmd} = \frac{\mu\, n^2\, D_{avg}\, c_1}{2}\left(\ln\frac{c_2}{\rho} + c_3\,\rho + c_4\,\rho^2\right) \tag{89}$$

where the coefficients of c_i are layout dependent and are shown in Table 3.2.

Table 3.2. Coefficients for current sheet expression

Layout	$\mathbf{c_1}$	$\mathbf{c_2}$	$\mathbf{c_3}$	$\mathbf{c_4}$
Square	1.27	2.07	0.18	0.13
Hexagonal	1.09	2.23	0.00	0.17
Octagonal	1.07	2.29	0.00	0.19
Circle	1.00	2.46	0.00	0.20

3.2.3. Data Fitted Monomial Expression

Date fitted monomial expression is expressed as **[145]**,

$$L_{mon} = \beta\, D_{out}^{\alpha_1}\, w^{\alpha_2}\, D_{avg}^{\alpha_3}\, n^{\alpha_4}\, s^{\alpha_5} \tag{90}$$

where the coefficients β and α_i are layout dependent and are shown in Table 3.3. The coefficients in the monomial expression were obtained by various regression and data-fitting techniques. The monomial expression is useful like the other expressions since it is simple, accurate, and can be used for optimal design of planar spiral inductors with geometric programming which uses monomial models **[143]**.

Table 3.3. Coefficients for data fitted monomial expression

Layout	**β**	$\boldsymbol{\alpha_1}$	$\boldsymbol{\alpha_2}$	$\boldsymbol{\alpha_3}$	$\boldsymbol{\alpha_4}$	$\boldsymbol{\alpha_5}$
Square	$1.62x10^{-3}$	-1.21	-0.147	2.40	1.78	-0.03
Hexagonal	$1.28x10^{-3}$	-1.24	-0.174	2.47	1.77	-0.049
Octagonal	$1.33x10^{-3}$	-1.21	-0.163	2.43	1.75	-0.049

3.2.4. Jenei's Expression

Jenei *et al.* **[146]** have developed an accurate physics-based closed-form expression for the inductance as a function of geometrical parameters. Since this expression is physics-based, it is scalable. Based on this expression, spiral inductor is divided into segments and the total length of the spiral inductor is expressed as,

$$l_{\text{total}} = (4\text{n} + 1)\text{D}_{\text{in}} + (4\text{N}_\text{i} + 1)\text{N}_\text{i}(\text{w} + \text{s}) \tag{91}$$

where n is the number of turns, N_i is the integer part of n, w is the metal width, and s is the spacing between segments. Therefore, the lateral structure of a spiral inductor is determined by n, w, s, and D_{in} or l_{total}. The total inductance of a spiral inductor consists of the inductor self-inductance (L_{self}), total negative mutual inductance (M^-), and total positive mutual

inductance (M^+). The self-inductance of a straight segment ($L_{self,seg}$) with a length of l_{seg} is defined as,

$$L_{self,seg} = \frac{\mu_o}{2\pi} l_{seg} \left(\ln \frac{2l_{seg}}{w+t} + 0.5 \right) \tag{92}$$

The self-inductance of a square spiral inductor is expressed as the sum of 4n self-inductance of segments with the average length of $l_{AV,seg,square} = l/4n$,

$$L_{self} = \frac{\mu_o}{2\pi} l \left(\ln \frac{l}{n(w+t)} - 0.2 \right) \tag{93}$$

Anti-parallel segments of a square inductor contribute to the negative mutual inductance. The sum of all interactions between segments can be approximated by an equivalent of $2n^2$. Since the average distance between segments on the opposite sides of a square spiral inductor is equal to the average segment length, the total negative mutual inductance is expressed as a very simple function of the total length (l) and number of turns (n) as,

$$M^- = 2 \cdot 2 \cdot n^2 \left(\frac{\mu_o}{2\pi} \frac{l}{4n} 0.47 \right) = 0.47 \frac{\mu_o}{2\pi} l\, n \tag{94}$$

The last constitutive factor of the total inductance is the total positive mutual inductance which contributes interactions between parallel segments on the same side of a square inductor. The average distance (d^+) for the constituting factor of positive mutual inductance can be calculated by closed formula as

$$d^+ = (w+s) \frac{(3n - 2N_i - 1)(N_i + 1)}{3(2n - N_i - 1)} \tag{95}$$

The total positive mutual inductance is

$$M^{+} = \frac{\mu_o}{2\pi} l(n-1)\left[\ln\left(\sqrt{1+\left(\frac{l}{4nd^{+}}\right)^2}+\frac{l}{4nd^{+}}\right)-\sqrt{1+\left(\frac{4nd^{+}}{l}\right)^2}+\frac{4nd^{+}}{l}\right] \quad (96)$$

Therefore, the total inductance of a square spiral inductor (L_{square}) is expressed as,

$$L_{square} = L_{self} - M^{-} + M^{+} \quad (97)$$

$$L_{square} = \frac{\mu_o}{2\pi} l\left(\ln\frac{l}{n(w+t)} - 0.2\right) - 0.47\ \frac{\mu_o}{2\pi}\ l\ n + \frac{\mu_o}{2\pi} l(n-1)\left[\ln\left(\sqrt{1+\left(\frac{l}{4nd^{+}}\right)^2}+\frac{l}{4nd^{+}}\right)-\sqrt{1+\left(\frac{4nd^{+}}{l}\right)^2}+\frac{4nd^{+}}{l}\right] \quad (98)$$

In this expression, there are no unphysical fitting factors and all of the parameters are only geometry parameters of the spiral inductor as mentioned earlier. Therefore, this expression is a closed-form equation for the total inductance.

3.2.5. Greenhouse's Expression

Greenhouse **[147]** has derived an inductance expression for thin-film planar inductors with rectangular cross-sections based on the inductance calculations of Grover **[148]**. The self –inductance of a straight conductor with a rectangular cross-section is expressed as,

$$L_{self,conductor} = 2l\left(\ln\frac{2l}{w+t} + 0.50049 + \frac{w+t}{3l}\right) \quad (99)$$

where l is the wire length in cm, w is the conductor width in cm, t is the conductor thickness in cm, and L_{self} is the inductance in nH. In the case of rectangular planar inductors, the mutual inductances between parallel conductor segments contribute to the total inductance of the inductor. Parallel conductor segments in which current flow is in the same direction have positive mutual inductance. On the other hand, parallel conductor segments in which current flow is opposite in direction have negative mutual inductance. Therefore, the general inductance expression for a rectangular inductor is given as,

$$L_T = L_0 + M^+ - M^- \tag{100}$$

where L_T is the total inductance, L_0 is the sum of the self-inductances of all the straight segments, M^+ is the sum of the positive mutual inductances, and M^- is the sum of the negative mutual inductances. The mutual inductance between two parallel conductors is a function of the length and of the geometric mean distance (GMD) between them. The mutual inductance is defined as,

$$M = 2lQ \tag{101}$$

where l is the length in cm and Q is the mutual inductance parameter which can be computed as,

$$Q = \ln\left[\frac{l}{GMD} + \sqrt{1 + \left(\frac{l}{GMD}\right)^2}\right] - \sqrt{1 + \left(\frac{GMD}{l}\right)^2} + \frac{GMD}{l} \tag{102}$$

Geometric mean distance between the two conductors which is approximately equal to the pitch of the conductors is given as,

$$\ln \mathrm{GMD} = \ln \mathrm{d} - \left[\frac{1}{12(\mathrm{d/w})^2} + \frac{1}{60(\mathrm{d/w})^4} + \frac{1}{168(\mathrm{d/w})^6} + \frac{1}{360(\mathrm{d/w})^8} + \frac{1}{660(\mathrm{d/w})^{10}} + \cdots\right] \tag{103}$$

where w is the width of the conductor and d is the pitch of the conductors.

3.2.6. Bryan's Expression

Bryan's expression for the inductance of a planar square coil is given as **[149]**,

$$\mathrm{L_{square}} = 0.141\ \mathrm{a\ n^{5/3}} \log\ [8(\mathrm{a/c})] \tag{104}$$

where the inductance is in μH and dimensions are in inches. In terms of dimensions in cm and natural logarithms, the expression is defined as,

$$\mathrm{L_{square}} = 0.0241\ \mathrm{a\ n^{5/3}} \ln\ [8(\mathrm{a/c})] \tag{105}$$

where $\mathrm{a} = (\mathrm{D_{out}} + \mathrm{D_{in}})/4$, $\mathrm{c} = (\mathrm{D_{out}} - \mathrm{D_{in}})/2$, and n is the number of turns.

3.2.7. Asgaran's Expression

Similar to Jenei **[146]**, Asgaran **[150]**, has developed a new accurate physics-based closed-form expression for the inductance of square and polygonal spiral inductors. As in Greenhouse's expression **[147]**, the total self inductance, positive mutual inductance, and negative mutual inductance values are calculated to obtain total inductance as below,

$$\mathrm{L_{tot}} = \mathrm{L_{s,tot}} + \mathrm{M_{tot}^{+}} - \mathrm{M_{tot}^{-}} \tag{106}$$

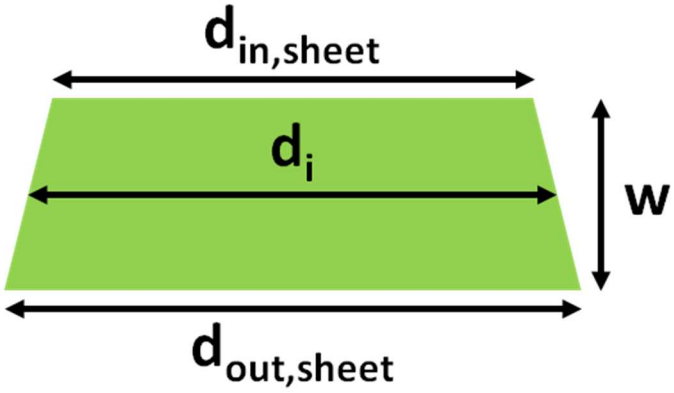

Figure 3.3. Trapezoidal current sheet.

In this expression, the thickness of the conductor is neglected and conductor is approximated as a current-carrying sheet since the thickness of the conductor is usually much smaller than its width. The self-inductance of a trapezoidal current sheet which is shown in Figure 3.3 is expressed as **[151]**,

$$L_{s,i} = \frac{\mu_0 d_i}{2\pi}\left[\ln\left(\frac{2d_i}{w}\right) + 0.5 + \frac{w}{3d_i}\left(\sqrt{2} - \ln\left(1+\sqrt{2}\right)\right)\right] \tag{107}$$

where $d_i = \left(d_{out,sheet} + d_{in.sheet}\right)/2$ is the average length and w is the width of the sheet. For a square spiral inductor with n turns, there are 4n trapezoidal current carrying sheets with average lengths varying from d_1 to d_n, where $d_i = d_1 + 2(i-1)(w+s)$ and $d_1 = d_{in} + w$. The total self-inductance is the sum of self-inductances of 4n current sheets each and is expressed as,

$$L_{s,tot} = 4\sum_{i=1}^{n} L_{s,i} = \frac{2\mu_0 n}{\pi}\left[d_{avg}\left(0.5 + \ln\left(\frac{2d_{avg}}{w}\right)\right) + 0.178\, w\right] \tag{108}$$

where $d_{avg} = (d_1 + d_n)/2 = (d_{in} + d_{out})/2$.

The negative mutual inductance is the sum of mutual inductances between parallel conductors on the opposite sides since the direction of current flow is opposite. The total negative mutual inductance is defined as,

$$M_{tot}^{-} = \frac{2\mu_0}{\pi}\left(\ln\left(1+\sqrt{2}\right)+1-\sqrt{2}\right)n^2 d_{avg} = \frac{2\mu_0}{\pi}\,(0.47)n^2 d_{avg} \tag{109}$$

The positive mutual inductance is the sum of mutual inductances between parallel conductors of on the same sides since the direction of current flow is the same. The total positive mutual inductance is defined as,

$$\begin{aligned} M_{tot}^{+} = \frac{2\mu_0}{\pi}\Bigg[& N(2n-N-1)d_s\left(\ln\left(\frac{2d_s}{w+s}\right)-1\right) \\ & -2d_s(\ln(P)+(n-N)\ln(N!)) \\ & +\frac{\sqrt{2}-\ln\left(1+\sqrt{2}\right)}{3}N(N+1)(3n-2N-1)(w+s)\Bigg] \end{aligned} \tag{110}$$

where N is the integer part of n, $d_s = d_{avg} + (w/2)$, and $P = 1!\,2!\,\ldots(N-1)!$ The expressions for the total self-inductance, negative mutual inductance, and positive mutual inductance have derived for square inductors and can be applied to polygonal inductors such as octagonal **[150]**. The total inductance is then calculated by inserting all inductance values into Equation (106).

3.3. TRL Calibration

Vector network analyzer (VNA) is used to determine the scattering parameters of microwave devices in desired frequency band. A VNA measures both the magnitude and phase information of the scattering parameters (S-parameters). Microwave devices without coaxial

connectors cannot be connected directly to the coaxial ports of the VNA. Therefore, the device under test (DUT) can be characterized by using some test fixtures for in-fixture measurements or high frequency probes for on-wafer measurements. However, every measurement system exist some imperfections that cause measurement errors.

Typical VNA measurement errors can be analyzed in three categories such as systematic, random, and drift errors. Systematic errors are the most significant source of measurement uncertainty and are caused by imperfections in the test equipment (VNA) and test setup components such as cables, probes, and fixtures. These systematic errors can be characterized through calibration and removed during measurement process. There are six types of systematic errors: directivity and crosstalk errors relating to signal leakage, source and load impedance mismatches relating to reflections, frequency response errors caused by reflection, and transmission tracking within the test receivers. Random errors vary as a function of time and are not predictable; therefore, they cannot be removed through calibration. Random errors are caused by instrument noise, switch repeatability, and connector repeatability. However, these errors can be reduced by increasing the source power, narrowing the intermediate (IF) bandwidth, and using the trace averaging. Drift errors occur when the measurement system's performance changes after a calibration. These errors are caused by temperature variation and can be removed by additional calibration. Drift errors can be minimized by constructing a measurement environment with stable ambient temperature.

In order to obtain accurate S-parameter measurements, all of the systematic errors due to the imperfections such as internal VNA, cable, and probe errors up to the DUT have to be removed. Figure 3.4 shows the reference planes for on-wafer measurements.

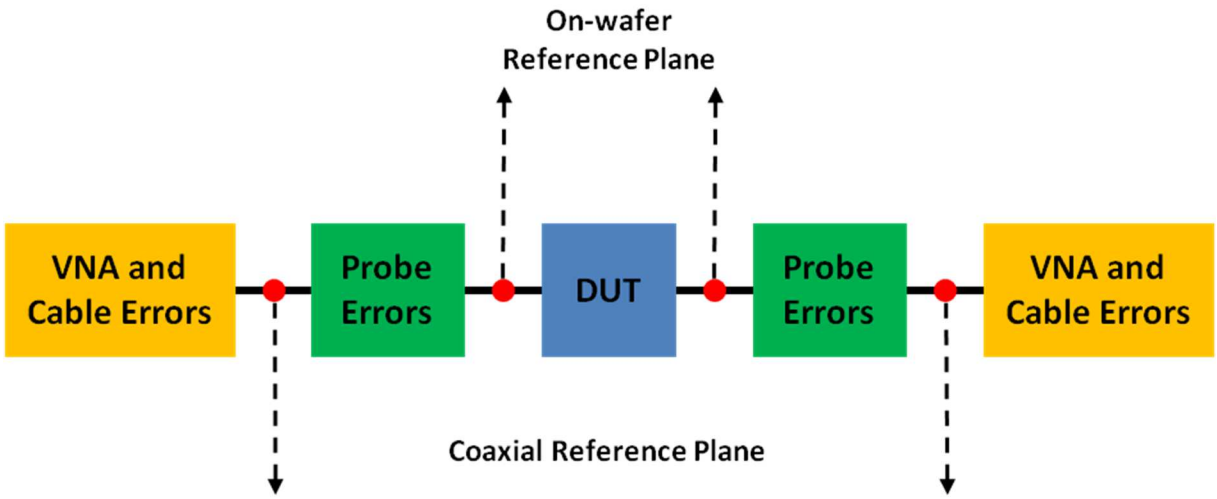

Figure 3.4. Reference planes for on-wafer measurements.

The effects of systematic errors on DUT are repeatable and can be measured by VNA in a stable measurement environment. The process of determining these errors and removing them is called measurement calibration. During measurement calibration, different known devices (calibration standards) are used. The number and type of the calibration standards depend on the calibration technique and the systematic errors are determined based on the difference between known and measured responses of the calibration standards. Once the systematic errors are determined, these errors are mathematically removed that is called error-correction. As mentioned earlier, there are six measurement errors in forward and reverse directions, yielding a total of 12 errors for two-port measurements. The 12-term error model is one of the fundamental error models for VNAs and is shown if Figure 3.5 for two-port measurements. The error terms in the model are E_{DF} (forward directivity), E_{SF} (forward source match), E_{RF} (forward reflection tracking), E_{LF} (forward load match), E_{TF} (forward transmission tracking), E_{XF} (forward isolation), E_{DR} (reverse directivity), E_{SR} (reverse source match), E_{RR} (reverse reflection tracking), E_{LR} (reverse load match), E_{TR} (reverse transmission tracking), E_{XR} (reverse isolation).

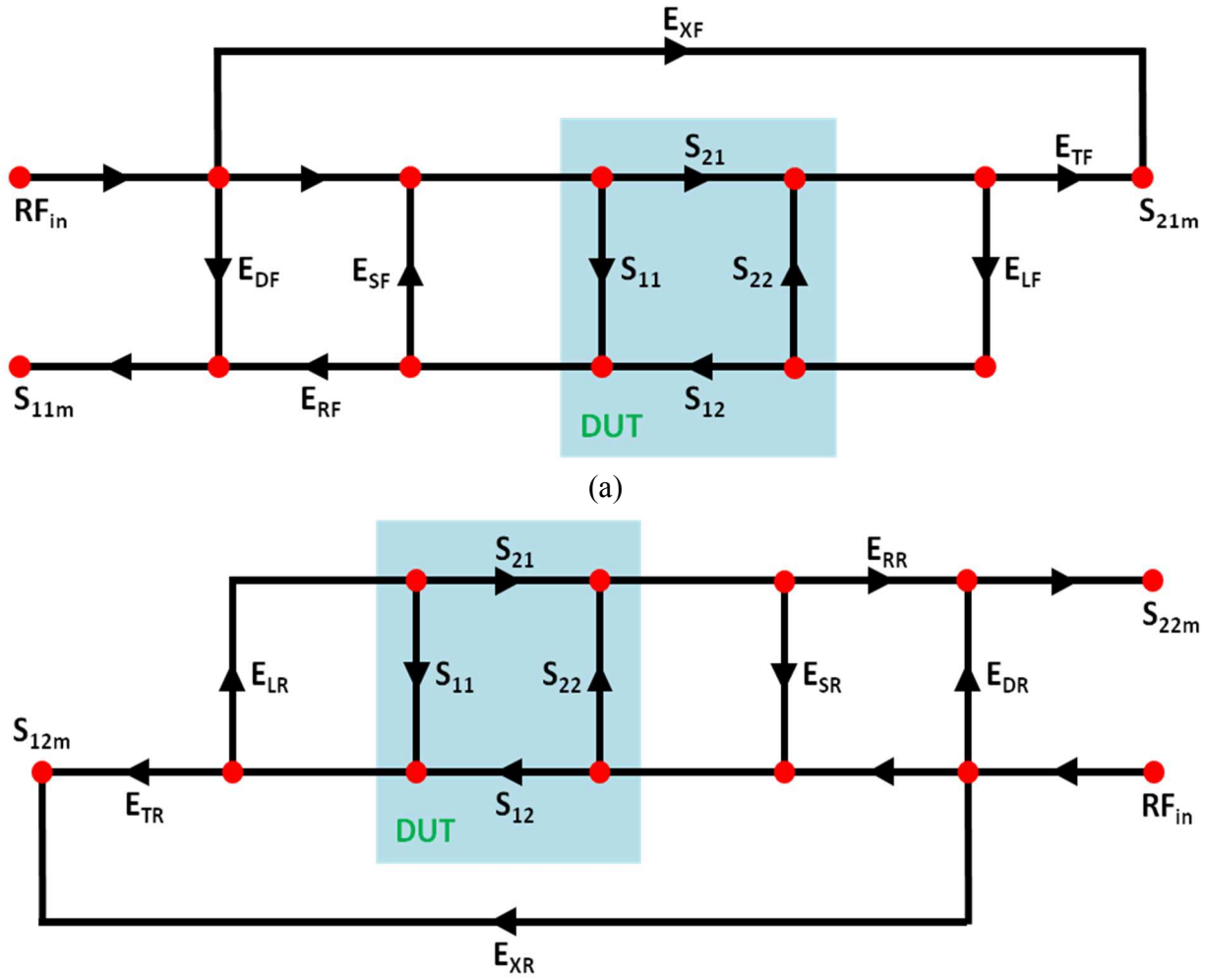

Figure 3.5. 12-term error model for two-port measurements. (a) Forward direction. (b) Reverse direction.

These twelve error terms are determined by the calibration algorithms. The most frequently used calibration techniques are SOLT (short-open-load-thru) and TRL (thru-reflect-line). Generally SOLT calibration is used for coaxial measurements and is performed by measuring four different standards. In SOLT calibration, each standard has to be precisely known. Any imperfections in calibration standards affect the measurements. Therefore this

calibration technique is usually limited to lower frequencies (less than 10 GHz). In SOLT calibration, the twelve error terms of the model are determined independently for each port. Six unknowns in the forward direction are determined by measuring the short, open, and load on the first port and a thru between the first and second ports. Six unknowns in the reverse direction are determined by the same process for the second port. However, it is more difficult to implement SOLT calibration for non-coaxial measurements. Therefore, TRL calibration **[152]** is used instead of SOLT calibration. TRL calibration technique relies on transmission lines rather than precisely known standards as in SOLT. Since TRL calibration is based on transmission lines, it has some advantages over SOLT. Transmission lines have been used and are understood very well. In addition, transmission lines are the simplest elements to analyze in non-coaxial measurements. Moreover, their impedance can be determined accurately from physical dimensions and material properties. TRL calibration uses only three standards to completely determine the error model. Thru is a connection of port 1 and port 2 directly or with a short length of transmission line. Reflect is a connection of identical one-port high reflection coefficient devices (open or short) to each port. Line is a connection of port 1 and port 2 with a transmission line which is quarter wavelength longer than the thru at the center frequency. In TRL calibration, the reflection coefficient of the reflect standard and the propagation constant of the line are not need to be known exactly. These parameters can be obtained through the calibration process. Therefore TRL calibration offers better accuracy than SOLT calibration even at high frequencies. TRL calibration is basically an error box removal process and its error model is fixed. The 8-term error model of TRL calibration is shown in Figure 3.6.

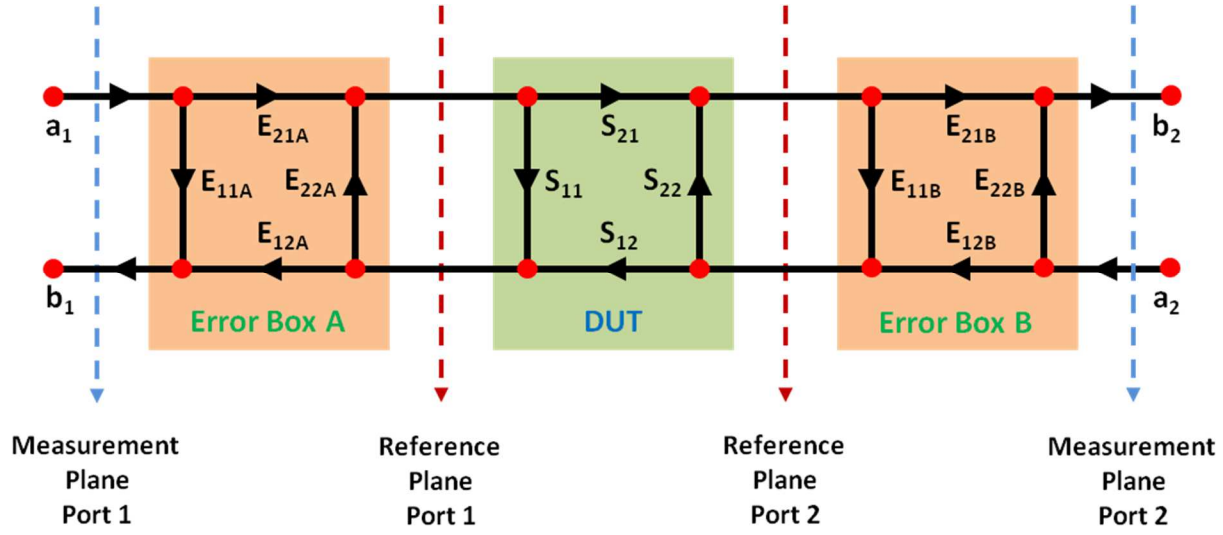

Figure 3.6. 8-term error model of TRL calibration.

Although TRL error model is slightly different than 12-term error model, the traditional error terms can be derived as follows:

$$\begin{aligned} E_{21A} \cdot E_{12A} &= E_{RF} & \qquad E_{21B} \cdot E_{12B} &= E_{RF} \\ E_{11A} &= E_{DF} & \qquad E_{11B} &= E_{DR} \\ E_{22A} &= E_{SF}\,, E_{LR} & \qquad E_{22B} &= E_{SR}\,, E_{LF} \\ E_{21A} \cdot E_{21B} &= E_{TF} & \qquad E_{12A} \cdot E_{12B} &= E_{TR} \end{aligned} \tag{111}$$

In order to derive TRL calibration and de-embed the DUT, error boxes will be represented by their transfer parameters. Figure 3.7 shows the simplified error model of TRL calibration. The transfer matrixes of the error boxes are defined as,

$$\begin{bmatrix} b_1 \\ a_1 \end{bmatrix} = \frac{1}{E_{21}} \begin{bmatrix} E_{12}E_{21} - E_{11}E_{22} & E_{11} \\ -E_{22} & 1 \end{bmatrix} \begin{bmatrix} a_2 \\ b_2 \end{bmatrix} = T_{A,B} \begin{bmatrix} a_2 \\ b_2 \end{bmatrix} \tag{112}$$

where a and b represent the incident and reflected waves, respectively. Error terms are determined by obtaining the transfer matrices of the error boxes.

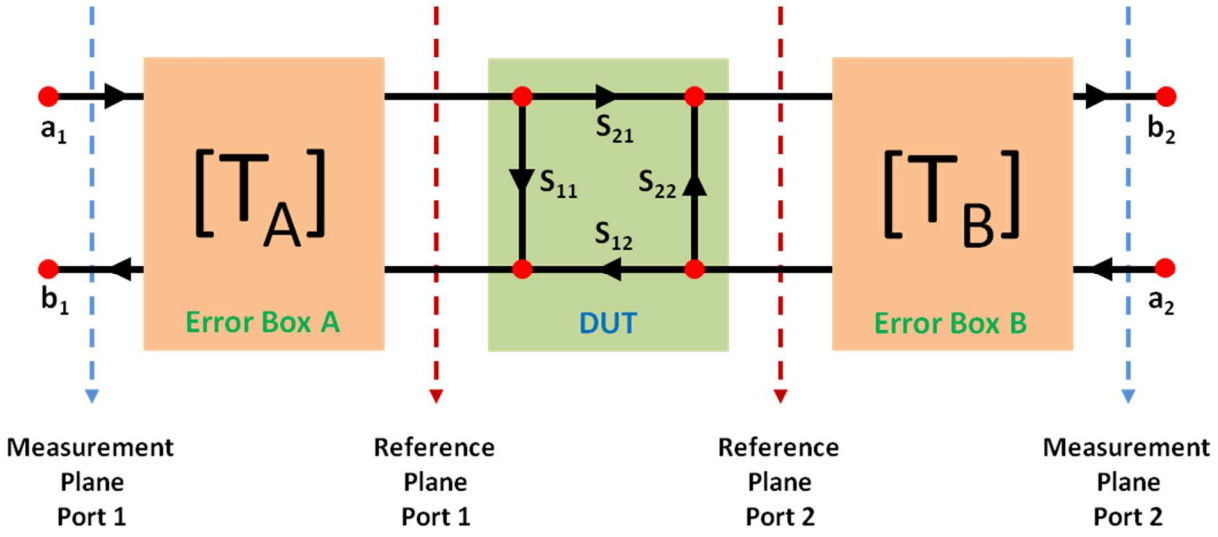

Figure 3.7. Simplified 8-term error model of TRL calibration.

The basic TRL calibration process is shown in Figure 3.8. Before we derive the TRL calibration, calibration steps can be explained briefly. For the thru calibration step, reference planes of port 1 and port 2 are connected and transmission frequency response and port match are measured in both directions. Four measurements are obtained in this step. For the reflect calibration step, the same reflective standard (short or open) is connected to each test port and its reflection coefficient is measured. Two measurements are obtained in this step. For the line calibration step, a transmission line is inserted between two ports and frequency response and port match are measured in each direction. Four measurements are obtained in this step. Ten measurements are obtained in total, resulting ten equations.

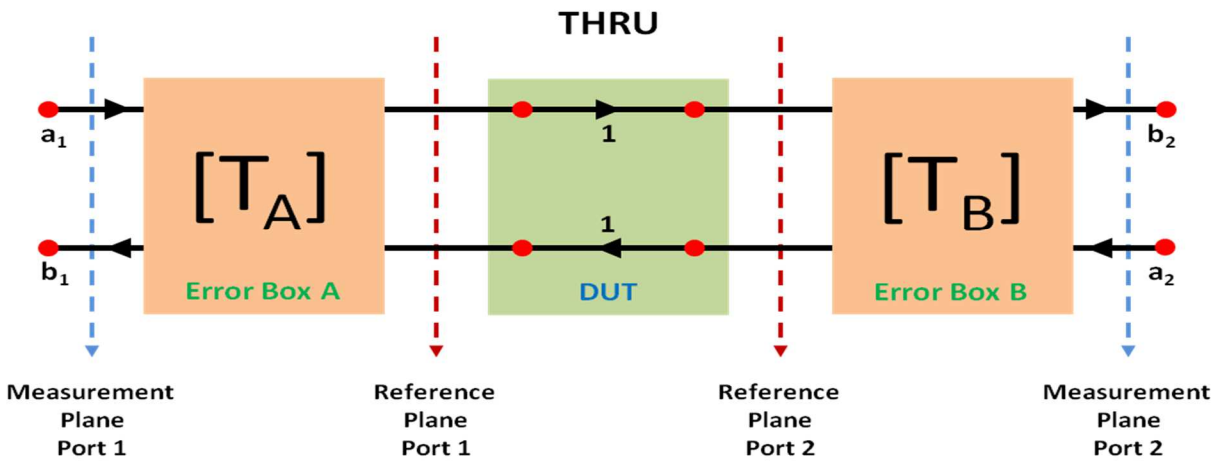

(a)

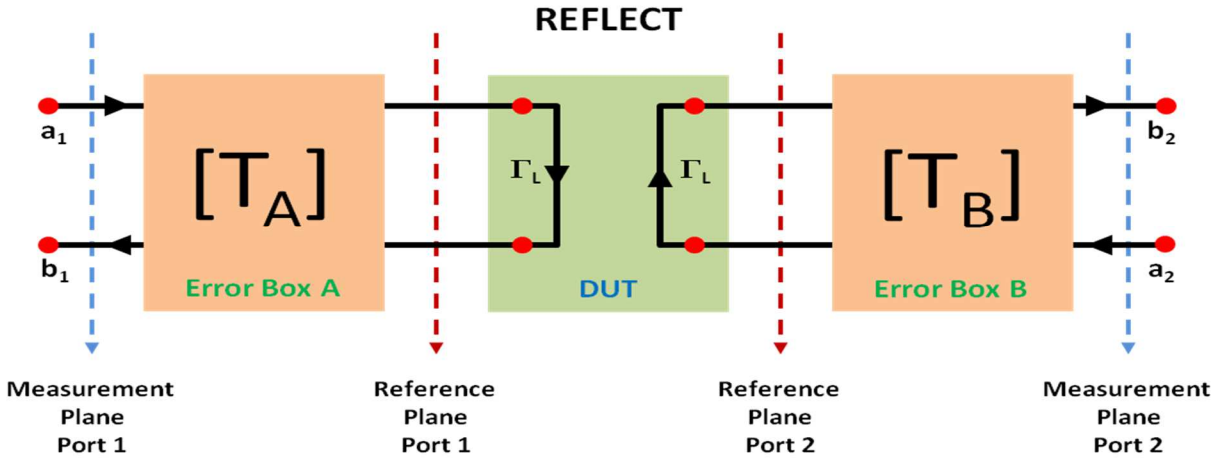

(b)

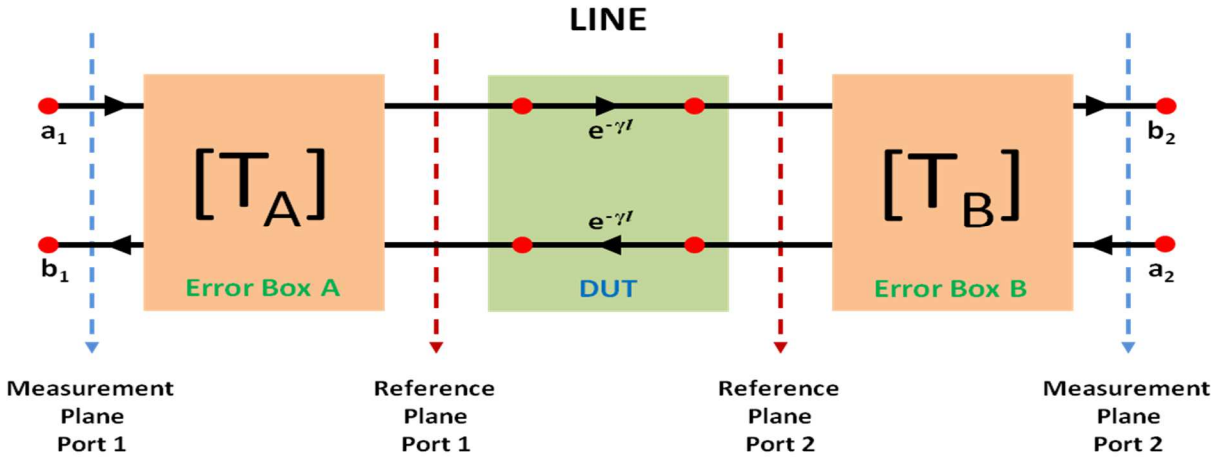

(c)

Figure 3.8. TRL calibration process (a) Thru. (b) Reflect. (c) Line.

However, TRL error model has only eight unknowns. Since there are more measurements than unknowns, two important characteristics can also be determined. These characteristics are the complex reflection coefficient (Γ) of the reflect and the propagation constant (γ) of the line. This is important because these characteristics do not have to be specified for the TRL calibration technique. In other calibration techniques, the accuracy of the measurements is dependent on the specified calibration standards. The only standard that needs to be known for the TRL calibration is the characteristic impedance of the line. In order to complete calibration, forward and reverse isolation are measured as the leakage from port 1 to port 2 and vice versa with each port terminated. As a result, all twelve terms of the two-port error model are determined.

The measured transfer matrices of the thru and line connections are

$$\mathrm{R_t} = \mathrm{T_A T_t T_B} \tag{113}$$

$$\mathrm{R}_l = \mathrm{T_A T}_l \mathrm{T_B} \tag{114}$$

$$\mathrm{T_t} = \begin{bmatrix} 1 & 0 \\ 0 & 1 \end{bmatrix} \tag{115}$$

$$\mathrm{T}_l = \begin{bmatrix} \mathrm{e}^{-\gamma l} & 0 \\ 0 & \mathrm{e}^{\gamma l} \end{bmatrix} \tag{116}$$

where $\mathrm{T_t}$ and T_l are the transfer matrices of the thru and line connections, respectively, and γ is the complex propagation constant of the line. $\mathrm{T_A}$ and $\mathrm{T_B}$ are the transfer matrixes of the error boxes; and raw measurements are represented by $\mathrm{R_t}$ and R_l. Based on Eq. (113) and Eq. (114), we can obtain,

$$\mathrm{M} \cdot \mathrm{T_A} = \mathrm{T_A T}_l \tag{117}$$

$$\mathrm{M} = \mathrm{R}_l \mathrm{R_t^{-1}} \tag{118}$$

In Eq. (117), the only unknown is the transfer matrix of the error box A. The M matrix is obtained from the measured raw quantities. The following equations are obtained from the matrix multiplication in Eq. (117),

$$m_{11}t_{11A} + m_{12}t_{21A} = t_{11A}e^{-\gamma l} \tag{119}$$

$$m_{21}t_{11A} + m_{22}t_{21A} = t_{21A}e^{-\gamma l} \tag{120}$$

$$m_{11}t_{12A} + m_{12}t_{22A} = t_{12A}e^{-\gamma l} \tag{121}$$

$$m_{21}t_{12A} + m_{22}t_{22A} = t_{22A}e^{-\gamma l} \tag{122}$$

When we divide the Eq. (119) by the Eq. (120) and the Eq. (121) by the Eq. (122), we obtain

$$\frac{m_{11}t_{11A} + m_{12}t_{21A}}{m_{21}t_{11A} + m_{22}t_{21A}} = \frac{t_{11A}}{t_{21A}} \tag{123}$$

$$\frac{m_{11}t_{12A} + m_{12}t_{22A}}{m_{21}t_{12A} + m_{22}t_{22A}} = \frac{t_{12A}}{t_{22A}} \tag{124}$$

Then, we can obtain the following equations for the ratios of t_{11A}/t_{21A} and t_{12A}/t_{22A},

$$m_{21}\left(\frac{t_{11A}}{t_{21A}}\right)^2 + (m_{22} - m_{11})\frac{t_{11A}}{t_{21A}} - m_{12} = 0 \tag{125}$$

$$m_{21}\left(\frac{t_{12A}}{t_{22A}}\right)^2 + (m_{22} - m_{11})\frac{t_{12A}}{t_{22A}} - m_{12} = 0 \tag{126}$$

By solving the above equations, we can obtain the ratios of t_{11A}/t_{21A} and t_{12A}/t_{22A} as,

$$\frac{t_{11A}}{t_{21A}} = \frac{-(m_{22} - m_{11}) \pm \sqrt{(m_{22} - m_{11})^2 + 4m_{21}m_{12}}}{2m_{21}} \tag{127}$$

$$\frac{t_{12A}}{t_{22A}} = \frac{-(m_{22} - m_{11}) \pm \sqrt{(m_{22} - m_{11})^2 + 4m_{21}m_{12}}}{2m_{21}} \tag{128}$$

Based on the roots of the quadratic equations, we can obtain the propagation constant of the line from,

$$e^{-2\gamma l} = \frac{m_{21}(t_{11A}/t_{21A}) + m_{22}}{m_{21}(t_{12A}/t_{22A}) + m_{22}} \tag{129}$$

By inserting Eq. (127) and Eq. (128) into the Eq. (129), we obtain

$$e^{-2\gamma l} = \frac{m_{11} + m_{22} \pm R}{m_{11} + m_{22} \mp R} \tag{130}$$

where

$$R = \sqrt{(m_{22} - m_{11})^2 + 4m_{21}m_{12}} \tag{131}$$

The solutions of Eq. (130) are reciprocal to each other. This is the direct result of selecting distinct roots for t_{11A}/t_{21A} and t_{12A}/t_{22A}. The selection of the correct sign in Eq. (130) is important. The sign can be selected so that the real part of γ is less than unity since the solutions of $e^{-2\gamma l}$ are reciprocal.

As a result, transfer parameter ratios of t_{11A}/t_{21A} and t_{12A}/t_{22A} have been determined using the thru and line measurements. In order to characterize the error box A, we need to determine the ratio of t_{11A}/t_{22A}. If we multiply the both sides of Eq. (113) with the inverse of T_A, resulting

$$\frac{1}{t_{11A}t_{22A}-t_{12A}t_{21A}}\begin{bmatrix} t_{22A} & -t_{12A} \\ -t_{21A} & t_{11A} \end{bmatrix}\begin{bmatrix} r_{11t} & r_{12t} \\ r_{21t} & r_{22t} \end{bmatrix}=\begin{bmatrix} t_{11B} & t_{12B} \\ t_{21B} & t_{22B} \end{bmatrix} \tag{132}$$

The following ratios can be obtained from Eq. (132),

$$\frac{t_{12B}}{t_{11B}}=\frac{r_{12t}-(t_{12A}/t_{22A})r_{22t}}{r_{11t}-(t_{12A}/t_{22A})r_{21t}} \tag{133}$$

$$\frac{t_{21B}}{t_{22B}}=\frac{(t_{11A}/t_{21A})r_{21t}-r_{11t}}{(t_{11A}/t_{21A})r_{22t}-r_{12t}} \tag{134}$$

$$\frac{t_{11B}}{t_{22B}}\frac{t_{11A}}{t_{22A}}=\frac{(t_{12A}/t_{22A})r_{21t}-r_{11t}}{(t_{21A}/t_{11A})r_{12t}-r_{22t}} \tag{135}$$

In order to determine t_{11A}/t_{22A}, one more equation which is obtained from reflect measurement is needed. From reflect measurements, we obtain two equations as,

$$\frac{t_{11A}}{t_{22A}}=\frac{S_{11m}-(t_{12A}/t_{22A})}{\Gamma_L(1-S_{11m}(t_{21A}/t_{11A}))} \tag{136}$$

$$\frac{t_{11B}}{t_{22B}}=\frac{S_{22m}+(t_{21B}/t_{22B})}{\Gamma_L(1+S_{22m}(t_{12B}/t_{11B}))} \tag{137}$$

If we write the reflection coefficient in Eq. (137) into the Eq. (136), we obtain the following relation as,

$$\frac{t_{11A}}{t_{22A}}\frac{t_{22B}}{t_{11B}}=\frac{\left(S_{11m}-\frac{t_{12A}}{t_{22A}}\right)\left(1+S_{22m}\frac{t_{12B}}{t_{11B}}\right)}{\left(1-S_{11m}\frac{t_{21A}}{t_{11A}}\right)\left(S_{22m}+\frac{t_{21B}}{t_{22B}}\right)} \tag{138}$$

By using the Eq. (135) and Eq. (138), the ratio of t_{11A}/t_{22A} is obtained as,

$$\frac{t_{11A}}{t_{22A}} = \pm\sqrt{\frac{\left(\frac{t_{12A}}{t_{22A}}r_{21t} - r_{11t}\right)\left(S_{11m} - \frac{t_{12A}}{t_{22A}}\right)\left(1 + S_{22m}\frac{t_{12B}}{t_{11B}}\right)}{\left(\frac{t_{21A}}{t_{11A}}r_{12t} - r_{22t}\right)\left(1 - S_{11m}\frac{t_{21A}}{t_{11A}}\right)\left(S_{22m} + \frac{t_{21B}}{t_{22B}}\right)}} \quad (139)$$

The nominal value of the reflect standard (open or short) is used in Eq. (134) and the sign of t_{11A}/t_{22A} is determined in Eq. (139). By using Eq. (127), Eq. (128), and Eq. (139), all three transfer parameters ratios are determined in order to characterize the error box A. The transfer parameter ratios of t_{11B}/t_{21B} and t_{12B}/t_{22B} of error box B can be determined using Eq. (133) and Eq. (134). After we determine all the ratios of t_{11A}/t_{21A}, t_{12A}/t_{22A}, t_{11A}/t_{22A}, t_{11B}/t_{21B}, t_{12B}/t_{22B}, and t_{11B}/t_{22B}, the error boxes can be de-embedded from the DUT measurements. We also determine reflection coefficient of the reflect standard and propagation constant of the line standard in TRL calibration.

3.4. Spiral Inductor Fabrication with Ni-AAO Magnetic Core

Fabrication and characterization of high performance spiral inductors with a magnetic core on glass substrates were demonstrated. The porous anodic aluminum oxide (AAO) templates with average pore diameter of 70 nm and thickness of 18 μm were fabricated and electroplated with Ni to serve as a magnetic core for spiral inductors. The 3.5 turns spiral inductors were fabricated on Ni-AAO templates by using standard photolithography and Cu electroplating processes. The fabricated spiral inductors has a dimension of 1370 μm x 1010 μm with 5μm thickness, 15 μm trace width, 15 μm spacing, 400 μm outer diameter, and 220 μm inner diameter. The RF characterization of spiral inductors was performed over a frequency range of 1 - 20 GHz. The inductance of spiral inductors with a magnetic core was measured to be 10.12 nH and enhanced 21% at 5 GHz compared to an air core of the same coil size. The quality

factor of 14.48 was obtained at 5 GHz. The AAO template with ferromagnetic nanowires promises a great potential in serving as a magnetic core for fabrication of high performance spiral inductors for RFIC.

3.4.1. Experimental

High purity (99.99%, 0.25 mm thick) aluminum foils were used for AAO template fabrication. Aluminum foils were ultrasonically degreased in acetone and isopropyl alcohol, and then rinsed in deionized water. Native oxide layer on aluminum foils were removed in a mixture solution of H_3PO_4 (6 wt %) and CrO_3 (2 wt %) at 65^oC for 10 min prior to anodization. AAO templates were prepared by using a two-step anodization process. In the first anodization step, aluminum foils were anodized in 0.3M oxalic acid solution at 60V and at 1^oC for 2 h. After the first anodization, the AAO template was chemically etched. The second anodization step was performed for 3 h under the same conditions. Highly-ordered porous AAO templates were obtained at the end of second anodization step. After two-step anodization process, a rectangle with 4 cm^2 area was opened on the back side of the template by etching the aluminum substrate in an aqueous solution of $CuCl_2 \cdot HCl$ at room temperature. Then, the remaining barrier layer at the pore bottoms was removed in a 10wt% H_3PO_4 solution at 30^oC for 35 min. Finally, open-through porous AAO templates were obtained. The average pore diameter and interpore distance (center to center distance between neighboring pores) were measured to be 70 nm and 150 nm, respectively. The thickness of the AAO templates was measured to be 18 μm and the calculated pore density was 5.13×10^9 pores/cm^2.

The electroplating process was carried out in a commercial Ni bath (Techni Nickel HT-2, Technic Inc.) at 45^oC using a two-electrode cell. A 200 nm Au layer was coated onto one side of

the porous AAO template by electron-beam evaporation to serve as the working electrode and a Ni anode was used as the counter electrode. Ni nanowires were grown in nanopores of AAO templates by constant current pulses (8 mA/cm^2).

The spiral inductors of 3.5 turns were fabricated on Ni electroplated AAO templates and have a dimension of 1370 μm x 1010 μm with 5μm thickness, 15 μm trace width, 15 μm spacing, 400 μm outer diameter, and 220 μm inner diameter. After Ni electroplating process, Au layer was removed by wet chemical etching. A 1 μm thick SU-8 negative photoresist layer was spin coated to serve a permanent electrical insulating layer between the magnetic core and the spiral inductor. After that Cr/Cu (30 nm/300 nm) were deposited by electron-beam evaporation to serve as an adhesion and a seed layer, respectively. A 7 μm thick AZ4620 positive photoresist was spin coated and patterned by photolithography process. 5.5 μm thick Cu was electroplated to form the coil, signal pads, and ground pads of the spiral inductor. After that, 10 μm photoresist was spin coated and via holes were patterned and electroplated with Cu. A 200 nm Cu seed layer was deposited to serve a seed layer for air bridge electroplating. 10 μm photoresist was spin coated and air bridges were patterned. 5 μm thick Cu was electroplated to form the air bridge. After that, positive photoresist was removed, Cr and Cu layers were etched and fabrication of spiral inductors was completed. Finally, fabricated spiral inductors on Ni-AAO magnetic core was attached on a glass substrate. Figure 3.9 shows the schematic diagram of spiral inductor fabrication process on Ni-AAO magnetic core. ((a) Ni electroplating into the nanopores. (b) Removal of gold seed layer. (c) Negative resist spin coating, Cr/Cu adhesion/seed layer deposition, and positive resist spin coating. (d) Photolithography, patterning, and first layer (coil) Cu electroplating. (e) Positive resist spin coating, photolithography, patterning, second layer (via hole) Cu electroplating. (f) Cu seed layer deposition and positive resist spin coating. (g) Positive

resist spin coating, photolithography, patterning, and third layer (air bridge) Cu electroplating. (h) Positive photoresist and Cr/Cu adhesion/seed layer removal.) The RF characterization of spiral inductors was performed using a vector network analyzer (HP 8510C).

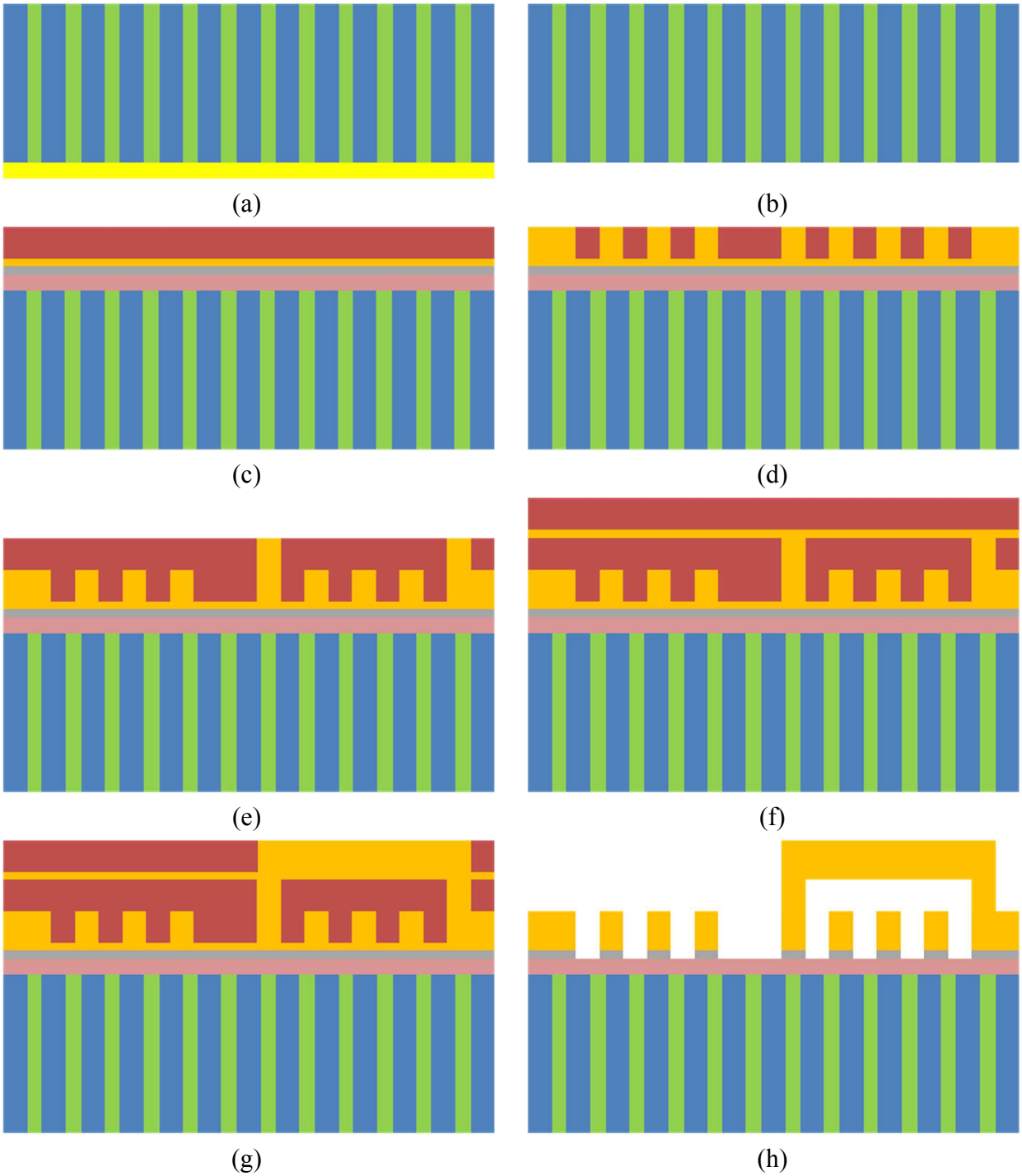

Figure 3.9. Schematic diagram of spiral inductor fabrication process.

3.4.2. Results and Discussion

The SEM images of fabricated 3.5 turn spiral inductors on Ni-AAO magnetic core are shown in Figure 3.10. ((a) top view of the spiral inductor. (b) top view of the coil part. (c) top view of the air bridge. (d) tilted view of the air bridge.) The design parameters of spiral inductors are as follows: 5μm thickness, 15 μm trace width, 15 μm spacing, 220 μm inner diameter, 400 μm outer diameter, and 1370 μm x 1010 μm in dimension.

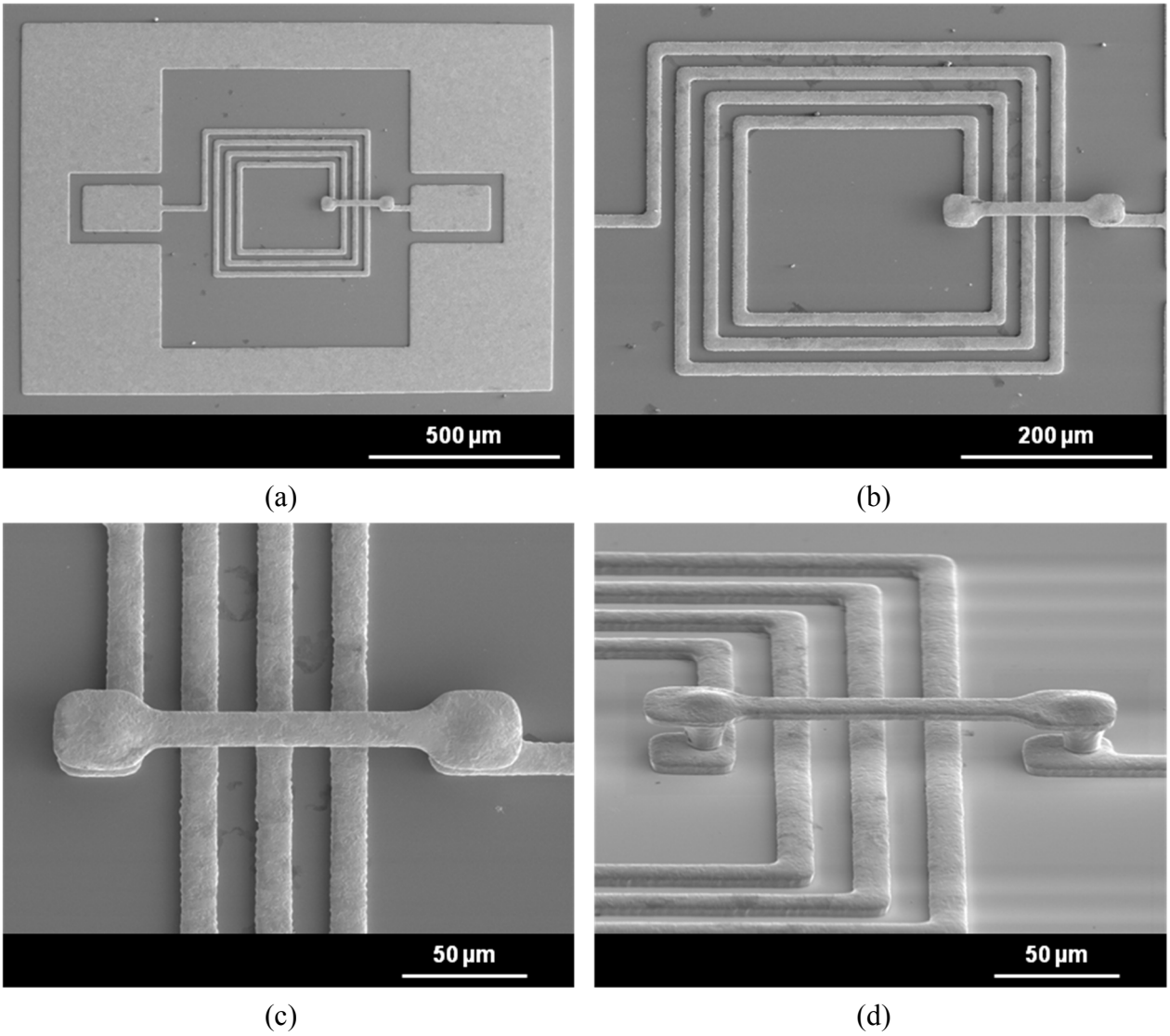

(a) (b)

(c) (d)

Figure 3.10. SEM images of fabricated spiral inductors.

The RF characterization of spiral inductors was performed using a vector network analyzer (HP 8510C) and air coplanar probes (ACP40-W-GSG-200, Cascade Microtech). The two-port de-embedded S-parameters were measured by using thru-reflect-line (TRL) calibration technique over a frequency range of 1 to 20 GHz. The two-port de-embedded S-parameters are then transformed into Y-parameters. From Y-parameters, inductance (L), and quality factor (Q) of spiral inductors were extracted as follows **[139, 153-154]**:

$$L = \frac{\mathrm{Im}\,(1 / Y_{11})}{2\,\pi\,f} \tag{140}$$

$$Q = \frac{\mathrm{Im}\,(1 / Y_{11})}{\mathrm{Re}\,(1 / Y_{11})} \tag{141}$$

Figure 3.11 shows the measured inductance data of fabricated spiral inductors over a frequency range of 1 to 12 GHz with (magnetic core) and without (air core) the integration of nickel into the nanopores of AAO templates.

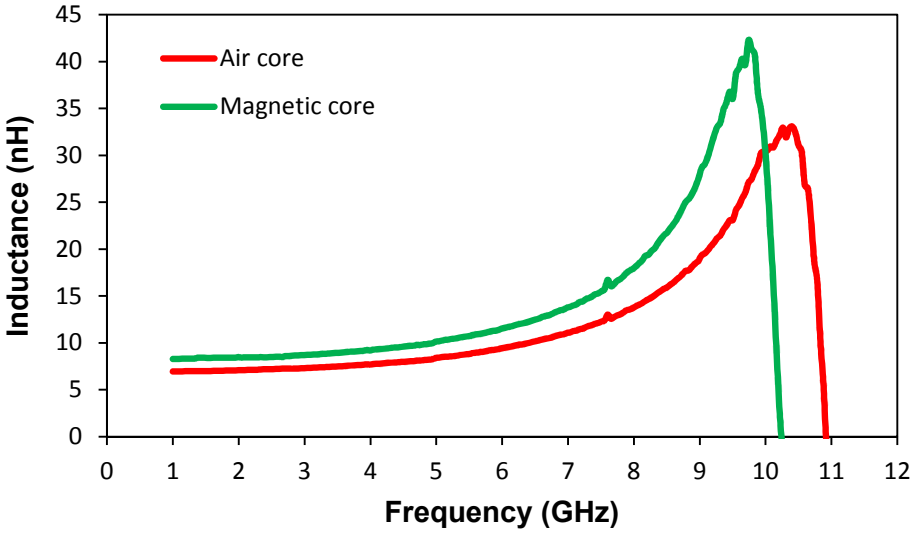

Figure 3.11. Measured inductance data of spiral inductors.

Figure 3.12 shows the measured quality factor data of fabricated spiral inductors over a frequency range of 1 to 12 GHz with (magnetic core) and without (air core) the integration of nickel into the nanopores of AAO templates.

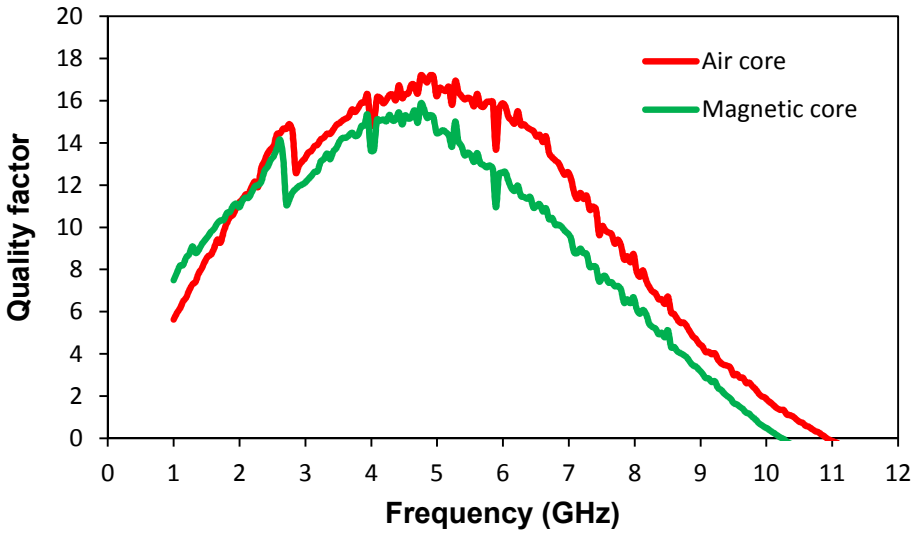

Figure 3.12. Measured quality factor data of spiral inductors.

According to Figure 3.11, the inductance values were measured to be 8.39 nH and 10.12 nH at 5 GHz for air core and magnetic core spiral inductors, respectively. The inductance enhancement of 21% was obtained with magnetic core over an air core. The resonance frequencies were 10.92 and 10.24 GHz for air core and magnetic core inductors, respectively. Based on Figure 3.12, the maximum quality factor values were measured to be 16.22 and 14.48 at 5 GHz for air core and magnetic core spiral inductors, respectively. Quality factor of magnetic core spiral inductors decreased 10.72% at 5 GHz. The reduction in quality factor is due to the higher coil resistance of magnetic core inductors. The resistance of the spiral inductors can also be extracted from Y-parameters as following **[155]**:

$$R = \mathrm{Re}\,(1 / Y_{11}) \tag{142}$$

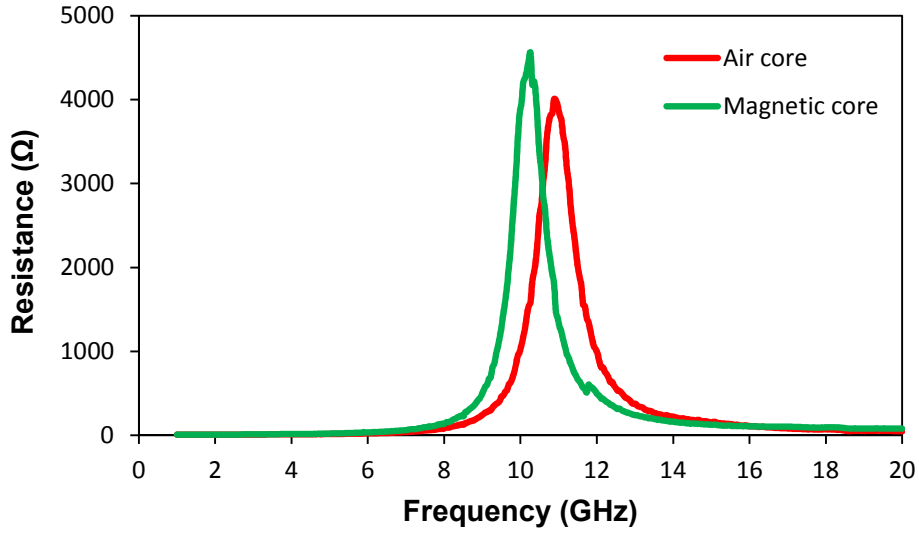

Figure 3.13. Measured resistance data of spiral inductors.

Figure 3.13 shows the measured resistance data of air core and magnetic core spiral inductors for the whole frequency range (1 to 20 GHz). Magnetic core spiral inductors exhibits higher coil resistance up to the resonant frequency. The coil resistance values were measured to be 16.22 and 21.91 Ω at 5 GHz for air core and magnetic core inductors, respectively. The quality factor at 5 GHz was calculated and confirmed by the following expression:

$$Q = (2\,\pi\,f)(L\,/\,R) \tag{143}$$

Inductance, quality factor, resistance values at 5 GHz and resonant frequency values of air core and magnetic core spiral inductors were summarized in Table 3.4.

Table 3.4. High frequency electrical characteristics of spiral inductors

Design	L (nH)	Q	R (Ω)	f_R (GHz)
Air core	8.39	16.22	16.22	10.92
Magnetic core	10.12	14.48	21.91	10.24

3.4.3. Conclusions

The 3.5 turns spiral inductors were fabricated on porous anodic aluminum oxide (AAO) templates. High frequency RF characterizations of spiral inductors were studied with and without the integration of ferromagnetic material. The inductance enhancement of 21% was achieved with magnetic core inductors at 5 GHz. The maximum quality factor value of magnetic core inductors was measured to be 14.48 at 5 GHz. The resonance frequency of 10.26 GHz was obtained for magnetic core inductors. Since porous AAO templates are self-laminated and patterned, they have potential application for spiral inductor fabrication by eliminating all the complexities of fabrication processes to overcome the FMR effect and Eddy current loss.

CHAPTER 4

DEEP, HIGH ASPECT RATIO ETCHES IN POROUS ANODIC ALUMINUM OXIDE TEMPLATES FOR MEMS APPLICATIONS

High precision, high aspect ratio structures are needed for a variety of microelectromechanical systems (MEMS) applications. For most MEMS applications, such structures are typically 50 microns to several hundred microns tall, and have pattern resolutions of a few microns. These can be used to form structural or electromechanical components for microsystems. Currently, there are only a few processes available to the MEMS designer for producing deep etches. These include LIGA **[156]**, photostructurable glass such as Fotorun **[157]**, photostructurable polymers such as SU-8 **[158]** and PSR **[159]**. The most common technology for producing high aspect ratio structures for MEMS is deep reactive ion etching (DRIE), sometimes referred to as the "Bosch" process, which uses a high energy plasma process to perform deep vertical etches in silicon **[160]**.

Despite the successes of the DRIE process for MEMS applications, it has several significant shortcomings which limit its adoption for many microstructure applications. Although efforts have been made to use DRIE for etching glass and sapphire structures **[161]**, DRIE is primarily useful for etching structures in silicon, making it unlikely to be used for non-silicon applications or for applications requiring low cost materials. The DRIE process is expensive and time consuming, requiring expensive dedicated etching equipment, use of corrosive gasses, including SF_6 and C_4F_6 (which are regulated), produces non-uniform etches across a wafer, and requires many minutes, sometimes even hours, of etch time on the tool **[162]**.

Other technologies, such as LIGA and SU-8 are highly specialized, and while they can be used for making simple structures, they are generally not useful for producing MEMS-like structures, which require additional materials, and sacrificial etches or undercut etches. Both produce only extruded structures (2.5D) of a single material. LIGA is specialized for producing simple mold inserts for precision injection molding, while SU-8 is useful primarily for making simple plastic structures.

We have explored anodic aluminum oxide (AAO) films for use in producing high aspect ratio structures that can be used for MEMS applications. We have found that under certain conditions, this material can be manufactured with highly anisotropic structure, resulting in corresponding highly anisotropic etch properties. When etched in a simple wet etchant, this film results in deep etch structures that have very high aspect ratios. The resulting AAO structures have surprisingly high aspect ratios and can be produced with high resolution. The relatively low cost for the material, combined with low cost of etchant and ease of processing, make this an attractive alternative to expensive, complex processes such as DRIE. AAO can be processed to include other films, such as metals, to produce complex structures. Indeed, aluminum oxide is a mechanically strong material and has excellent dielectric properties, making this a compelling alternative to silicon for producing MEMS structures.

4.1. Experimental

4.1.1. AAO Template Fabrication

High purity (99.99%, 0.25 mm thick, Alfa Aesar) aluminum foils were used for the fabrication of nanoporous AAO templates. Aluminum foils were ultrasonically degreased in acetone and isopropyl alcohol, and then rinsed in deionized water. The native oxide layer on

aluminum foils were removed in an aqueous solution of phosphoric acid (6 wt %) and chromic acid (2 wt %) at 70°C for 15 minutes prior to anodization. Alumina templates were prepared by using a two-step hard anodization process **[28, 163]**. In the first anodization step, aluminum foils were anodized in 0.3M oxalic acid solution at 60V and at 1°C for 15 minutes. After the first anodization, the AAO template was chemically etched in the same H_3PO_4 and CrO_3 mixture solution at 70°C for 20 minutes. In the second anodization step, aluminum foils were anodized for 10 minutes under the same conditions as in the first step to create a thin (~1.5 μm) layer of AAO on aluminum surface before performing the hard anodization. This thin oxide layer protects the aluminum foil from breakdown effects and provide uniform oxide growth at high voltages [8]. After 10 minutes of anodization at 60V, the anodization voltage was gradually increased from 60V to 90V for hard anodization at a rate of 0.5V/s. The hard anodization process was performed at 90V for 6 hours. At the end of second anodization step, thick porous AAO templates were fabricated.

4.1.2. Etch Mask Deposition and Patterning

After the fabrication of thick porous AAO templates, two types of experiments were performed. In both experiments, a thin layer of Cu (300 nm) was deposited on fabricated AAO templates by electron-beam evaporation to serve as a seed layer for the Cu and Ni electroplating processes. In the first experiment, 6 μm thick AZ-5214 positive photoresist was spin coated and patterned by photolithography process. A 4.5 μm thick Cu layer was electroplated to form an etch mask for etching of MEMS structures. After that, positive photoresist was removed with acetone and Cu seed layer was chemically etched. In the second experiment, 5 μm thick Shipley-1827 positive photoresist was spin coated and patterned by photolithography process. A 5 μm

thick Ni layer was electroplated to form an etch mask for etching of MEMS structures, and in some cases, for use as a structural element of the final device. After Ni electroplating process, photoresist was dissolved in acetone and un-patterned Cu seed layer was selectively etched in Cu etchant 49-1 solution (Transene, Danvers, MA).

4.1.3. Deep Etch of AAO Templates

After metal electroplating, prepared porous AAO templates were chemically etched to fabricate various types of posts, holes, and MEMS structures. Acidic and basic wet chemicals have been widely used in order to etch alumina templates such as H_3PO_4 **[22, 61, 164]** and NaOH **[48, 60, 95, 97]**. In our work, AAO templates were immersed in 0.5M NaOH solution to etch unprotected regions. After this final process, deep and high aspect ratio etches were obtained in AAO templates. Schematic diagrams of fabrication processes for both experiments are shown in Figure 4.1 ((a)Two-step anodization process. (b) Cu seed layer deposition process. (c) Photoresist spin coating process. (d) Photolithography and patterning processes. (e) Cu electroplating process. (f) Removal of photoresist. (g) Etching of Cu seed layer. (h) Etching of AAO template.) and Figure 4.2 ((a) Anodization of aluminum foils. (b) Deposition of Cu seed layer. (c) Spin coating of photoresist. (d) Photolithography and mask pattern transfer. (e) Ni electroplating. (f) Photoresist removal. (g) Selective etching of Cu seed layer. (h) Wet chemical etching of porous alumina templates.) Morphological characterizations of porous AAO templates were performed by scanning electron microscopy (FEI Quanta 3D FEG SEM).

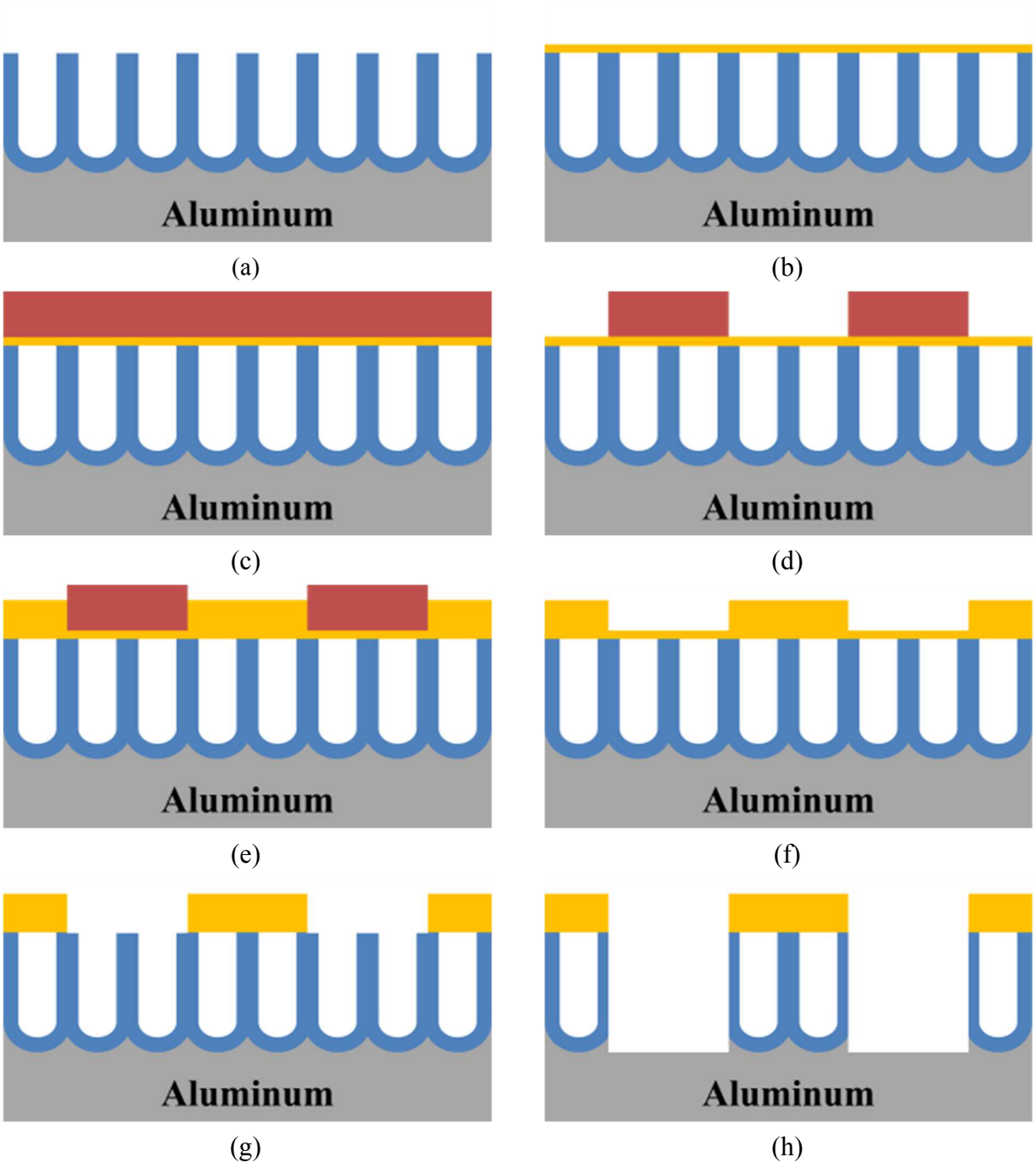

Figure 4.1. Schematic diagram of fabrication processes in case of Cu etch mask.

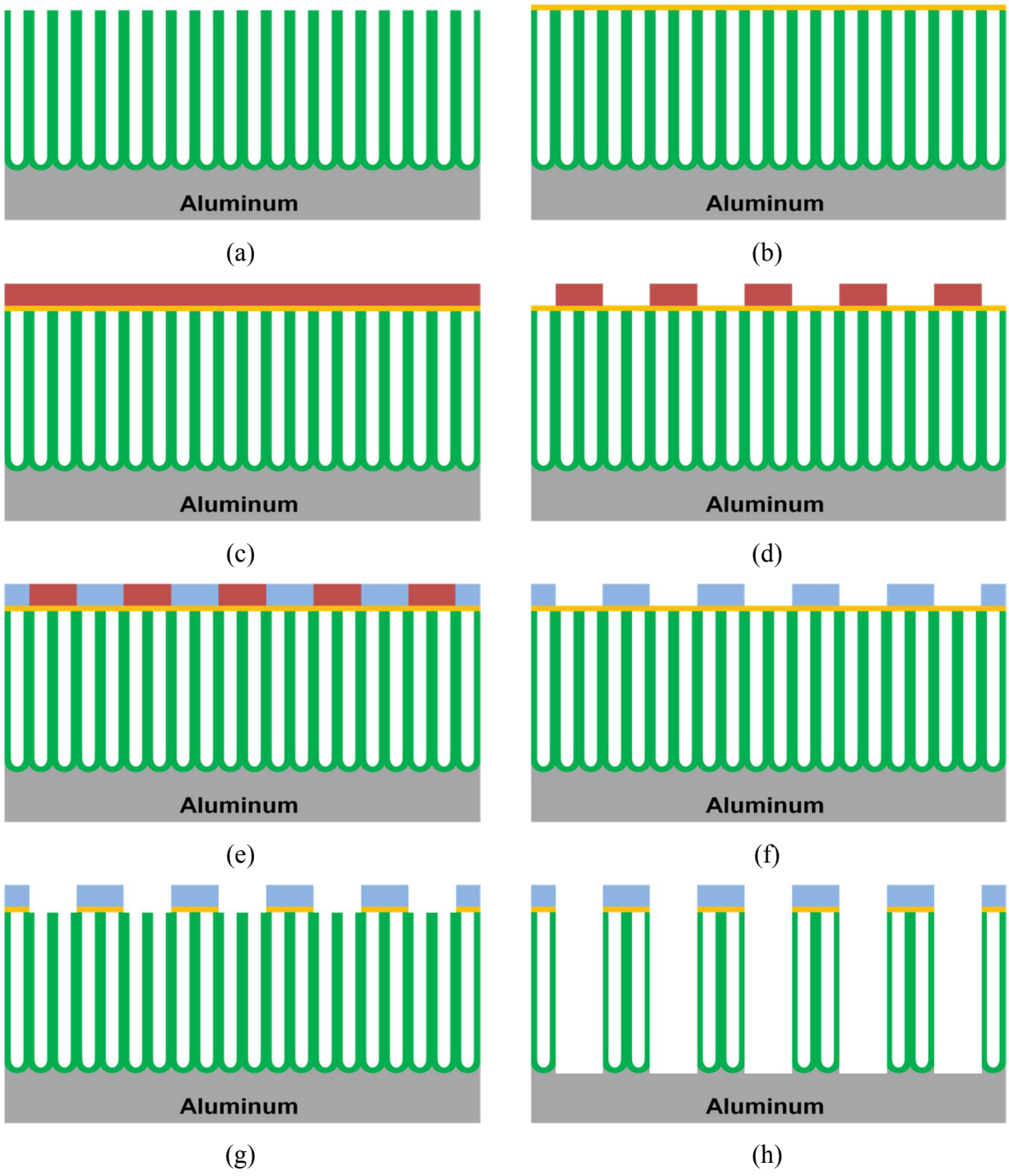

Figure 4.2. Schematic diagram of fabrication processes in case of Ni etch mask.

4.2. Results and Discussion

Figure 4.3 shows the SEM images of thick porous AAO templates anodized in 0.3M oxalic acid solution. ((a) Top view. (b) Cross-section view closer to the top surface. (c) Full cross-section view.) The average pore diameter and interpore distance (center to center distance between neighboring pores) were measured to be 55 nm and 150 nm, respectively. The thickness of the AAO templates was measured to be 100 μm.

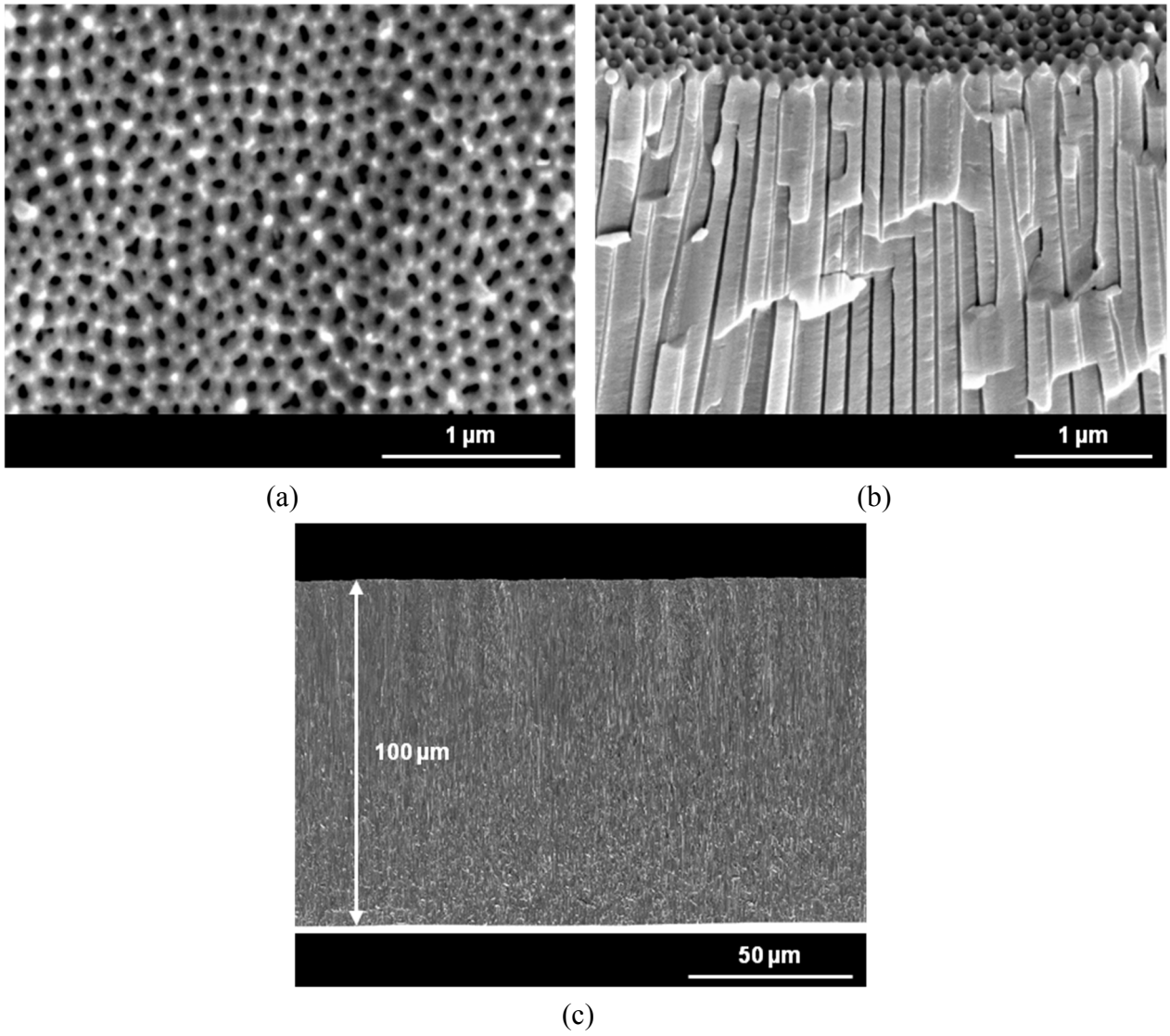

Figure 4.3. SEM images of thick AAO templates.

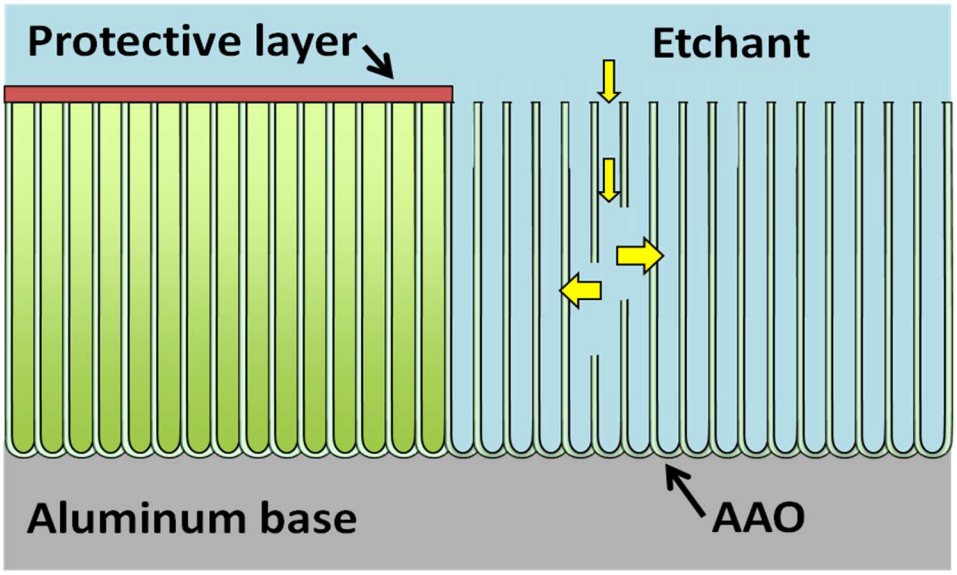

(a)

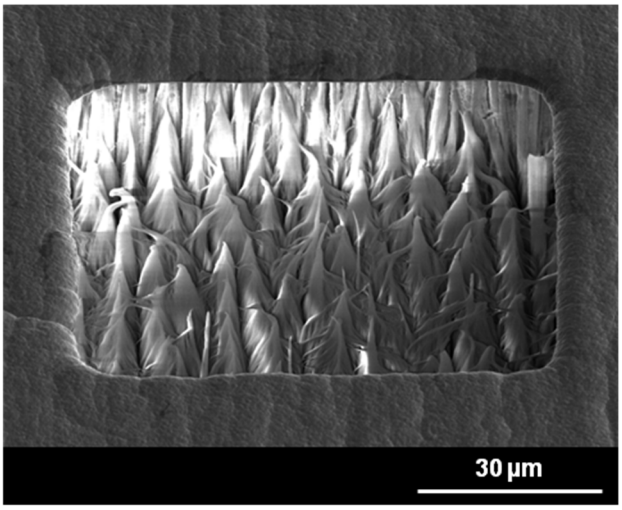

(b)

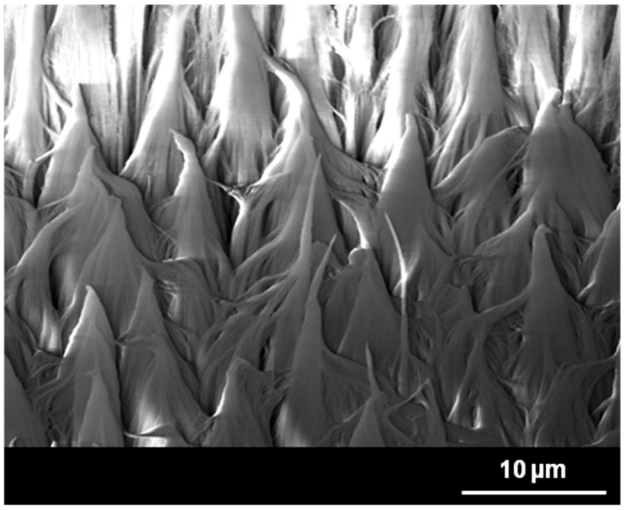

(c)

Figure 4.4. Etching mechanism of AAO templates.

Figure 4.4 shows the illustration of a possible etching mechanism of AAO templates and SEM pictures of a square pattern after 30 minutes of etch. ((a) Illustration of AAO etching mechanism. (b) SEM image of etched patterned after 30 minutes. (c) Closer view of etched region.) In this mechanism, the etching solution enters the nanopores of exposed AAO templates and etches away the sidewalls of the pores (Figure 4.4(a)). The etching occurs equally and

laterally at all depths in the AAO material and all exposed pores are etched simultaneously, allowing for quick removal of the material **[165, 166]** Since etching takes place throughout the nanopores, unprotected regions are etched quickly and etching is not affected by the area and the thickness of the etch region. In the protected regions, the etchant must etch through many layers to make progress, meaning that etch in the lateral direction is slow. Thus, due to the vertical porous nature of AAO templates, the regions exposed to the etching solution are etched much faster than the unexposed regions. The difference in etch rates results the formation of vertical sidewalls after the etching process.

Figure 4.5 shows the SEM images of AAO templates after etching process in 0.5M NaOH solution. In Figure 4.5(a), a thin layer of Cu (300 nm) deposited by e-beam was used as an etch mask. In Figure 4.5(b), a thick layer of Cu (4.5 μm) deposited by electroplating was used as an etch mask. Vertical sidewalls with minimum undercut were obtained in both experiments. Figure 4.5(c) shows the SEM image of a cylindrical pattern. In this case, AAO templates were exposed to etching solution long period of time to understand the effect of the etchant to the alumina. In order to provide more protection during this long etch, a 4.5 μm thick electroplated Cu was used as an etch mask. Initial diameter of the full cylinder was 100 μm. After obtaining the 100 μm thick full cylinder, etching process was performed longer and more undercut was observed. The measured undercut from top to bottom was in the range of 28 μm to 35 μm, resulting sloped sidewalls with 86º angle. This image shows that after removing the alumina, the etching solution then begins to attack the aluminum base and etches it much faster than the horizontal etch of the AAO. The etched portion of aluminum base was measured to be 34 μm in depth. Thus, bottom of the nanopores become unprotected and was attacked by the etchant, yielding more undercut at the bottom of the alumina.

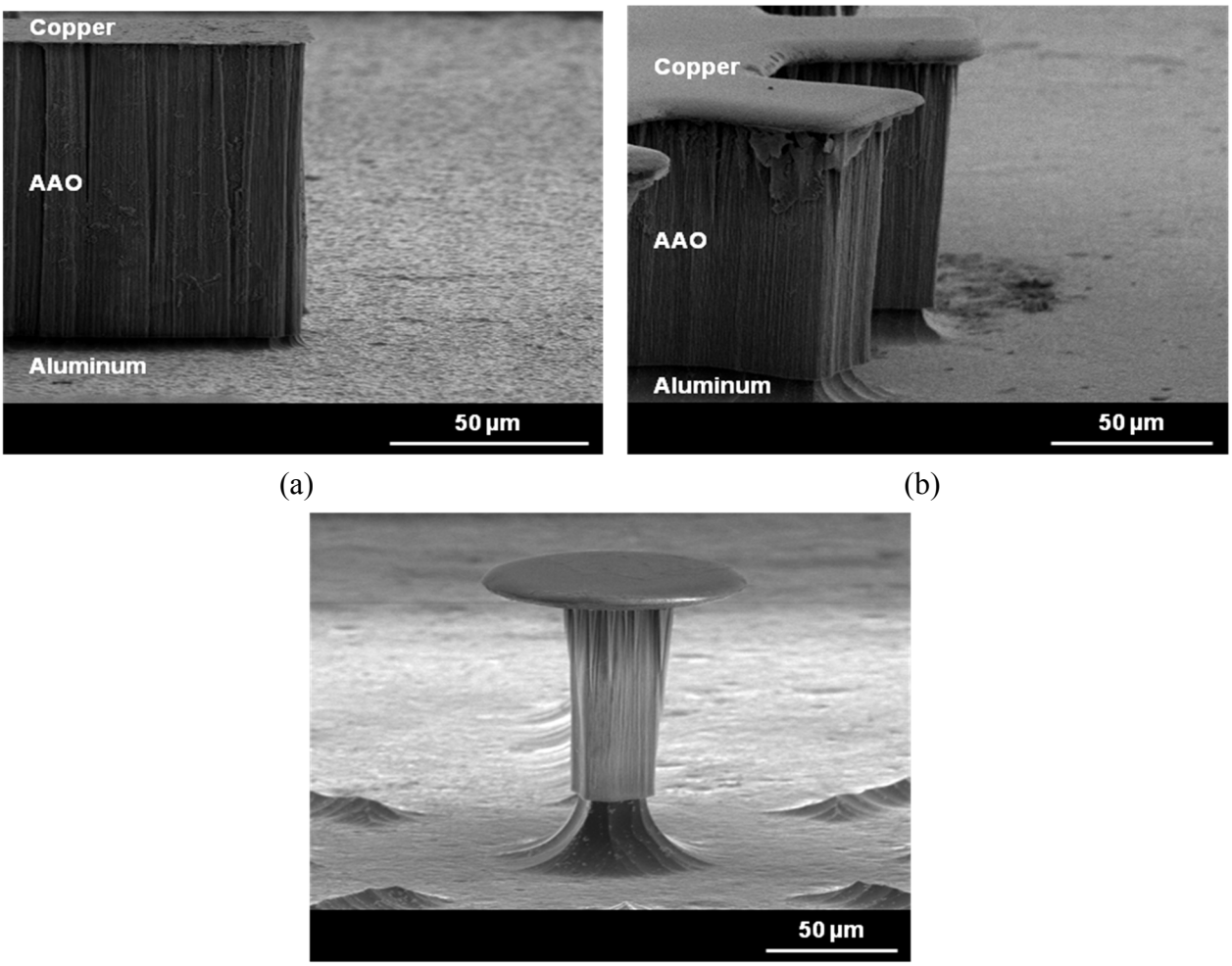

Figure 4.5. SEM images of AAO templates after wet chemical etching process.

Figure 4.6 shows the SEM images of etched 100 µm thick rectangle post arrays with a thin layer of Cu as an etch mask. The widths of the arrays are 25, 50, 100, and 150 µm, respectively. The lengths of the arrays are 500 µm. Figure 4.7 shows the SEM images of etched 100 µm thick square arrays with a thin layer of Cu as an etch mask. The widths of the arrays are 50, 100, and 150 µm, respectively. Figure 4.8 shows the SEM images of etched 100 µm thick circle arrays with a thin layer of Cu as an etch mask. The diameters of the arrays are 20, 50, and 100 µm, respectively.

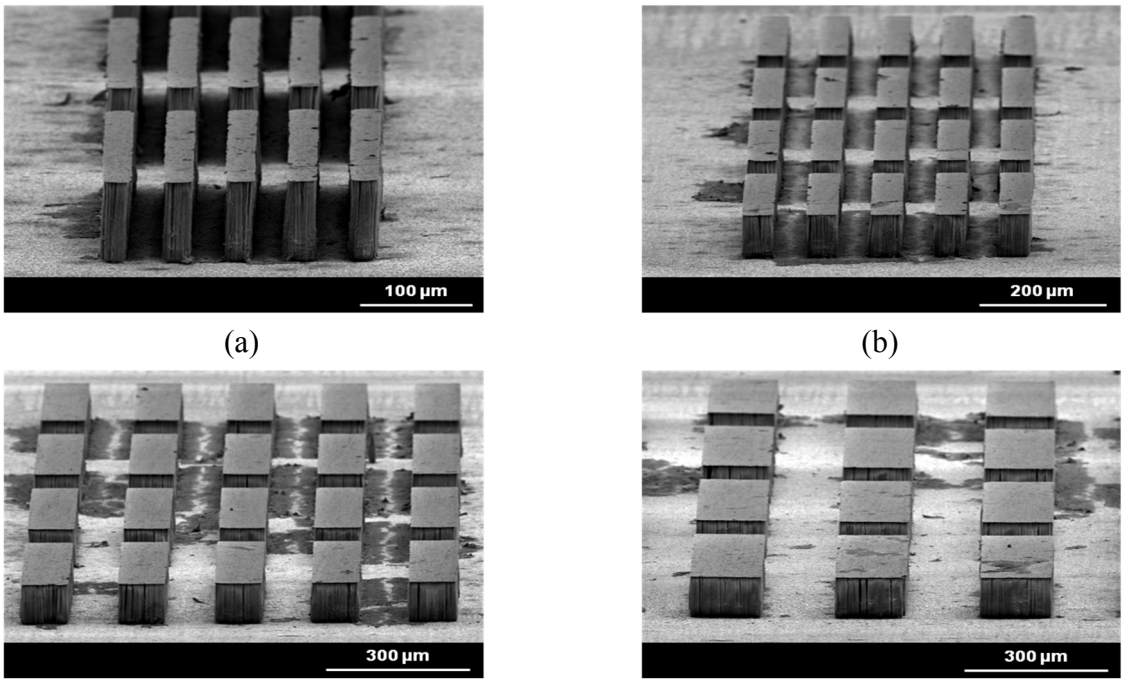

(a) (b)

(c) (d)

Figure 4.6. SEM images of etched rectangle post arrays.

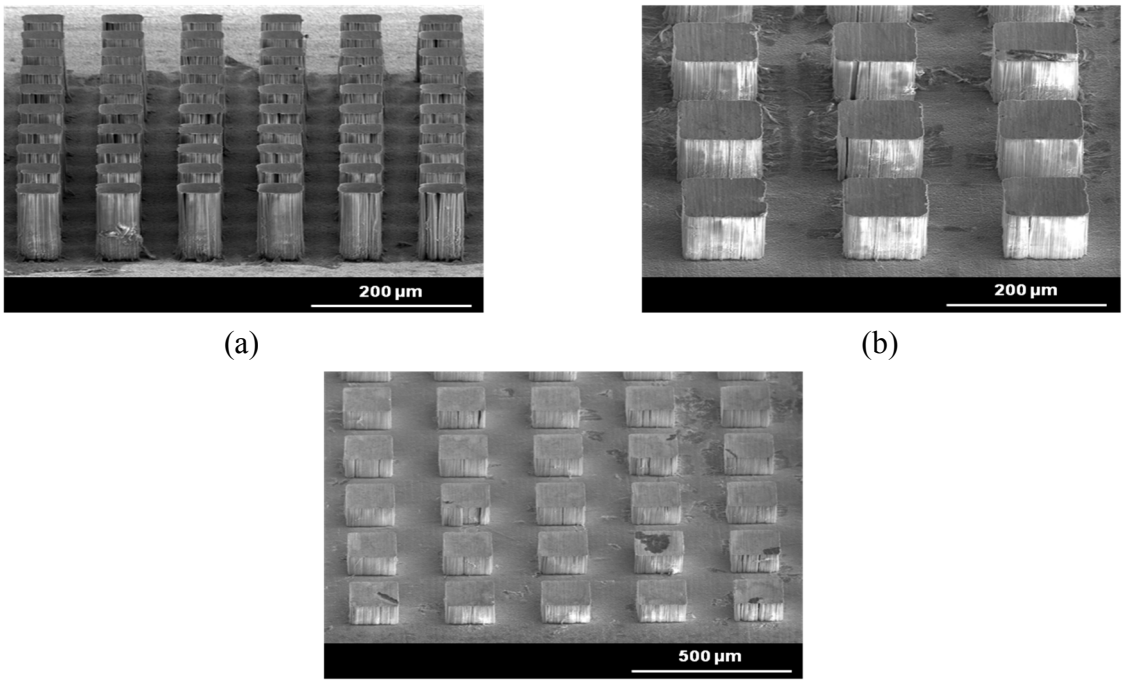

(a) (b)

(c)

Figure 4.7. SEM images of etched square post arrays.

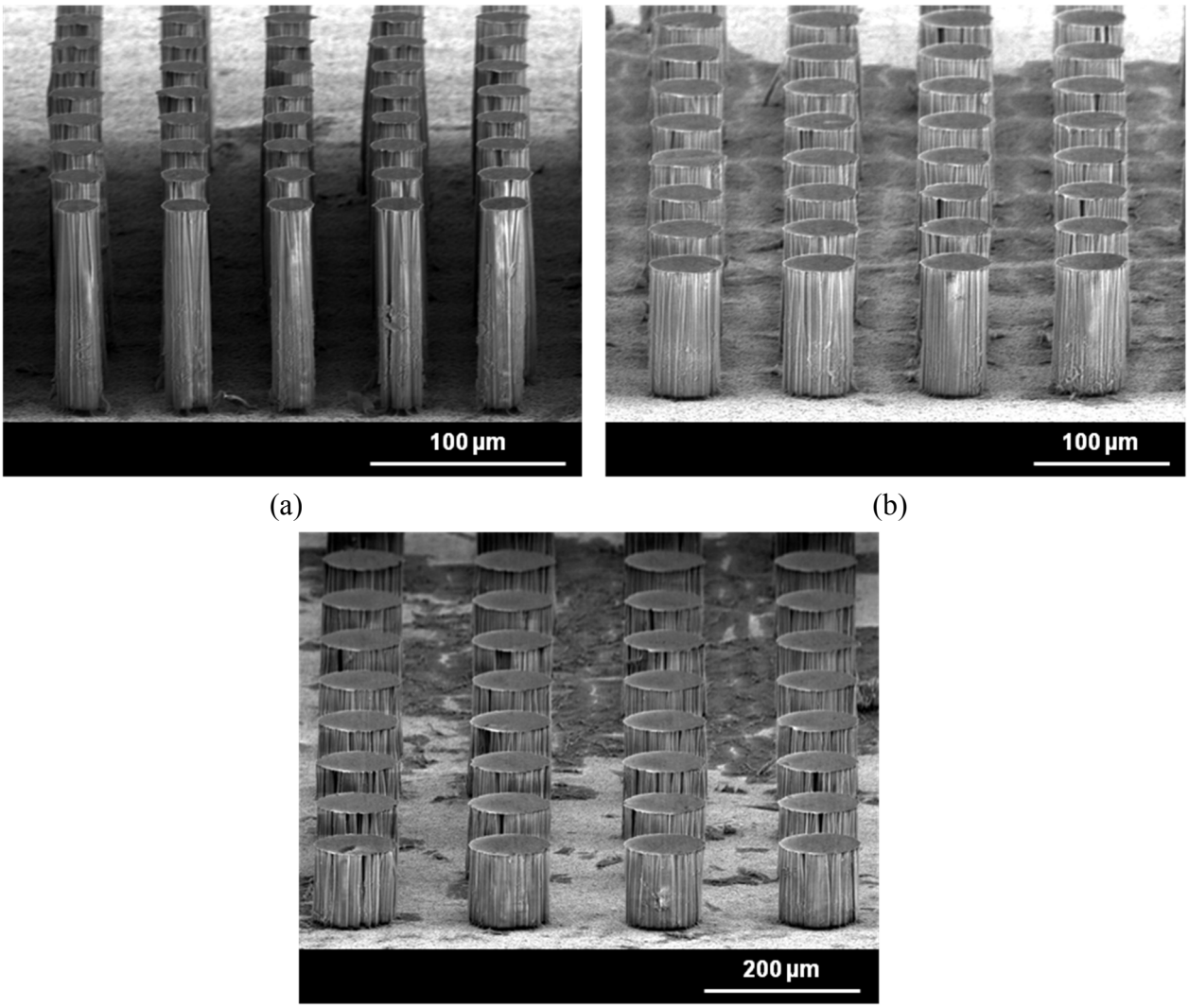

(a) (b)

(c)

Figure 4.8. SEM images of etched circle post arrays.

Figure 4.9 shows the SEM images of etched 100 µm deep square hole arrays with a thick layer of Cu as an etch mask. The widths of the arrays are 20, 30, 40, 50, 60, and 80 µm, respectively. Figure 4.10 shows the SEM images of etched 100 µm deep circle hole arrays with a thick layer of Cu as an etch mask. The diameters of the arrays are 45, 65, and 80 µm, respectively.

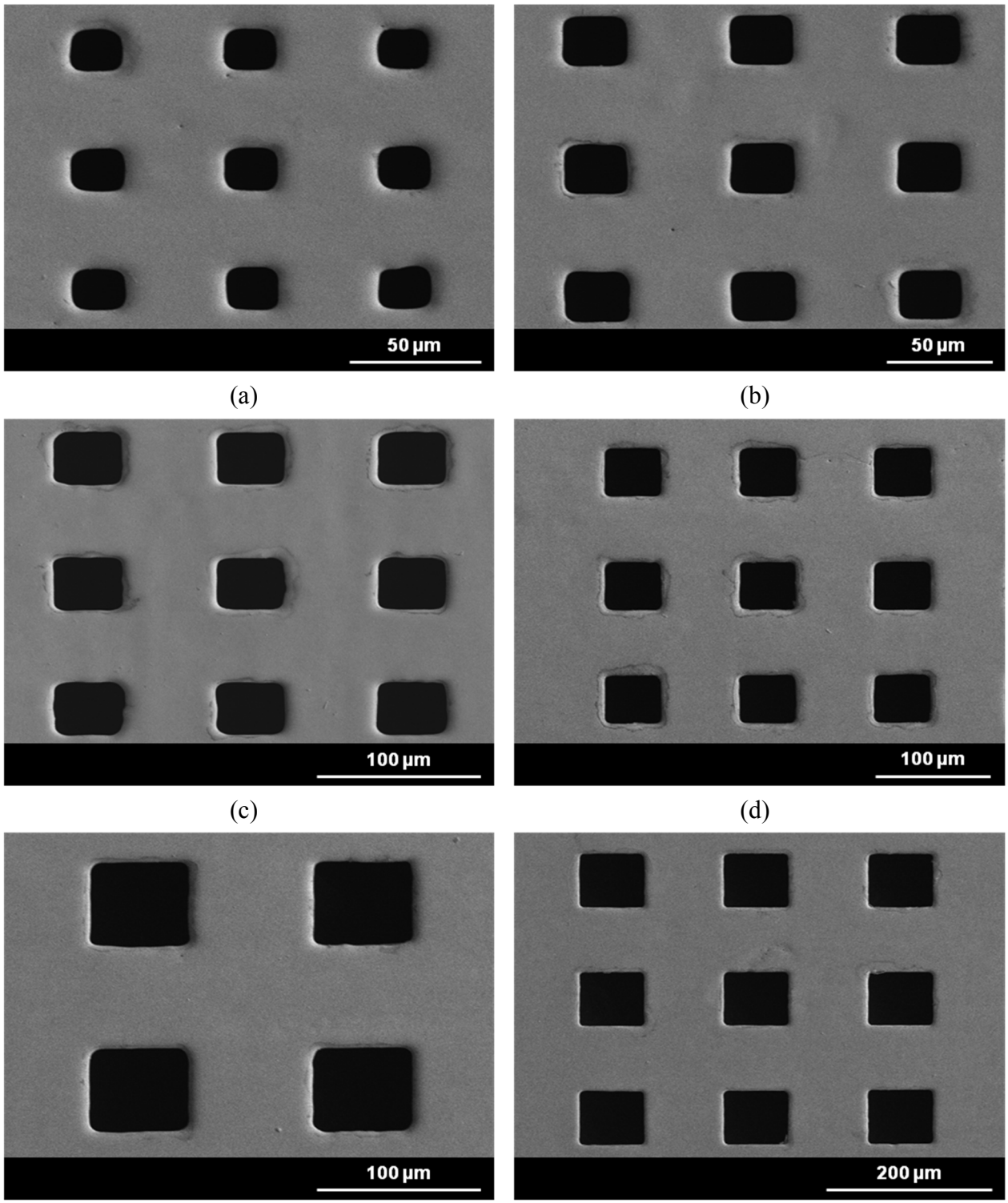

Figure 4.9. SEM images of etched square hole arrays.

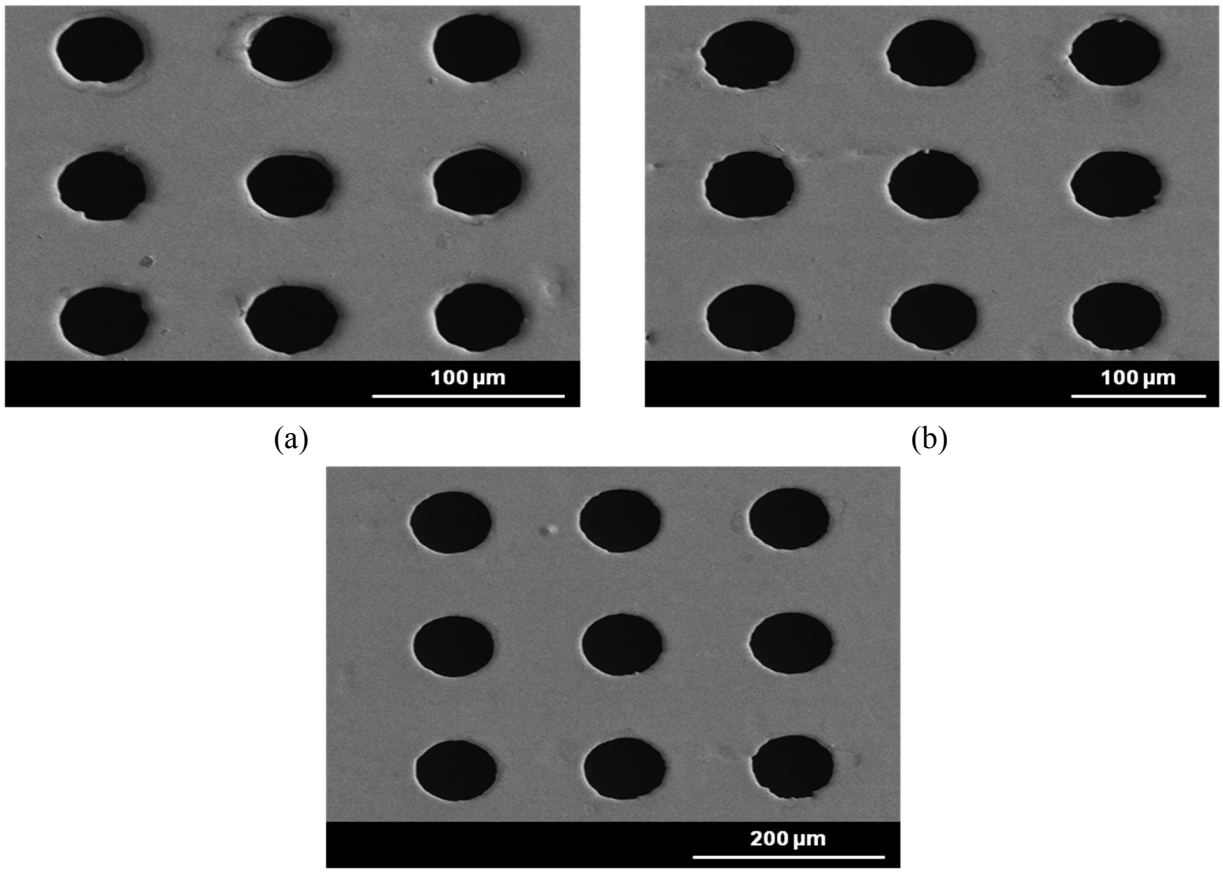

(a) (b)

(c)

Figure 4.10. SEM images of etched circle hole arrays.

Figure 4.11 (a) shows the SEM images of etched 100 µm thick rectangle posts separated with a 45^{o} angle and a circle post in the middle. The rectangle posts have a dimension of 50 µm x 200 µm, and the diameter of the circle post is 100 µm. Figure 4.11 (b) shows rectangle holes separated with a 45^{o} angle and a circle hole in the middle. Figure 4.11 (c) shows etched posts patterned by letters. Figure 4.11 (d) shows etched holes patterned by letters. The thickness of the posts and the depth of the holes were measured to be 100 µm. Based on the results in Figure 4.11, we see that the wet chemical etching of AAO templates is not dependent on the mask geometry and any type of pattern with any geometry can be fabricated with desired thickness or depth.

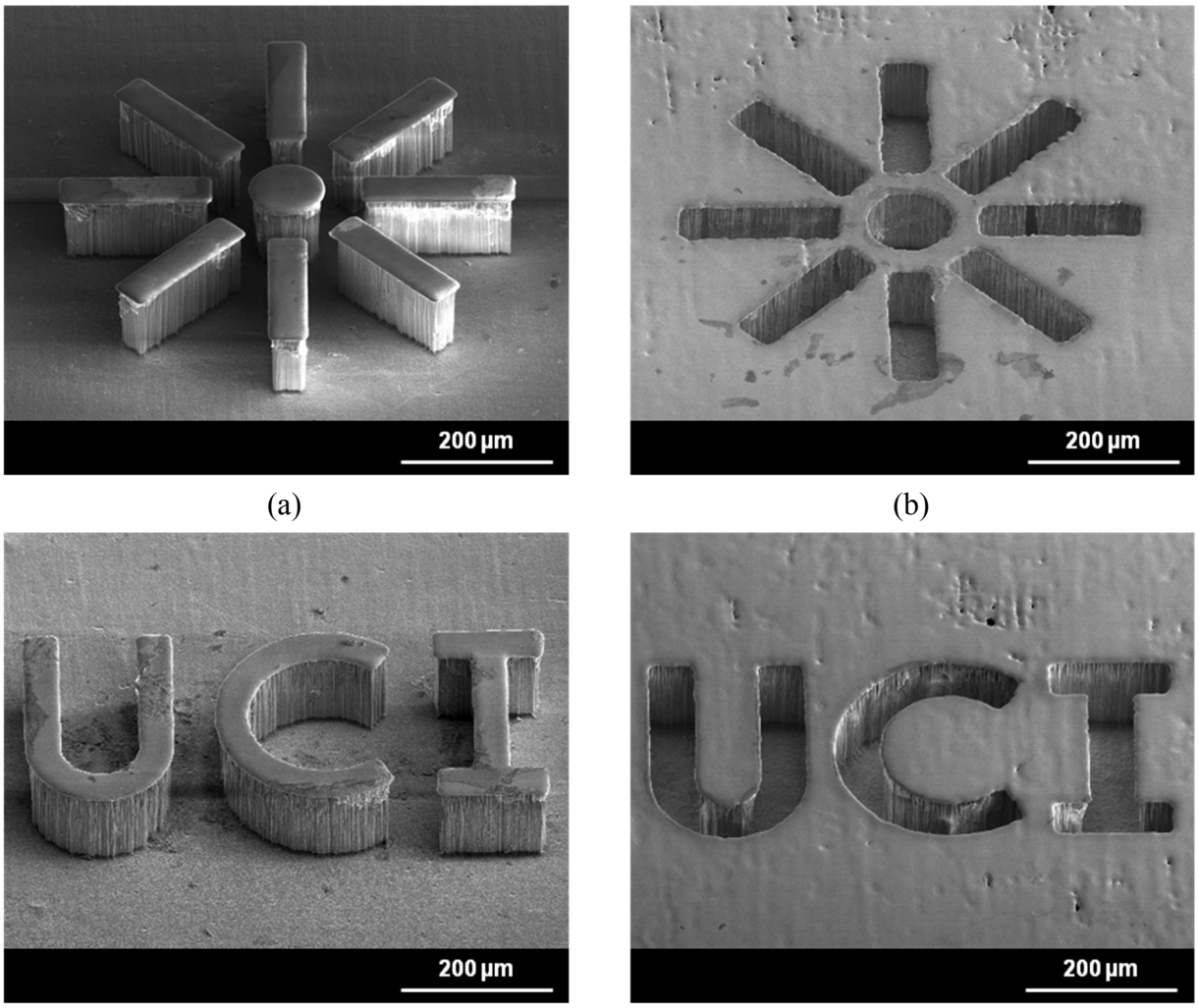

(a) (b)

(c) (d)

Figure 4.11. SEM images of etched posts and holes with desired geometry.

Figure 4.12(a) shows the SEM image of a traditional micro-gear structure made out of porous aluminum oxide. The fabricated 12-tooth gear has 160 µm inner diameter, 400 µm outer diameter, 60 µm tooth width, 62 µm tooth length, and 100 µm thickness. As seen in SEM image, wet chemical etch resulted vertical sidewalls with minimum undercut (~5 µm) demonstrating the ability to fabricate arbitrary geometries. An aluminum etch would release this micro-gear structure.

Figure 4.12(b) shows the SEM image of a mold to fabricate micro-gears. As seen in this image, AAO films can also be used as a mold material to fabricate MEMS structures by electroforming of desired metals (such as nickel and copper) in the nonconducting AAO mold. For this purpose, the metal etch mask should be removed before electroforming or non-conductive materials such as silicon dioxide or silicon nitride can be used as an etch mask. After electroforming of desired metal, alumina template and etch mask can be removed to release fabricated MEMS structure in metal.

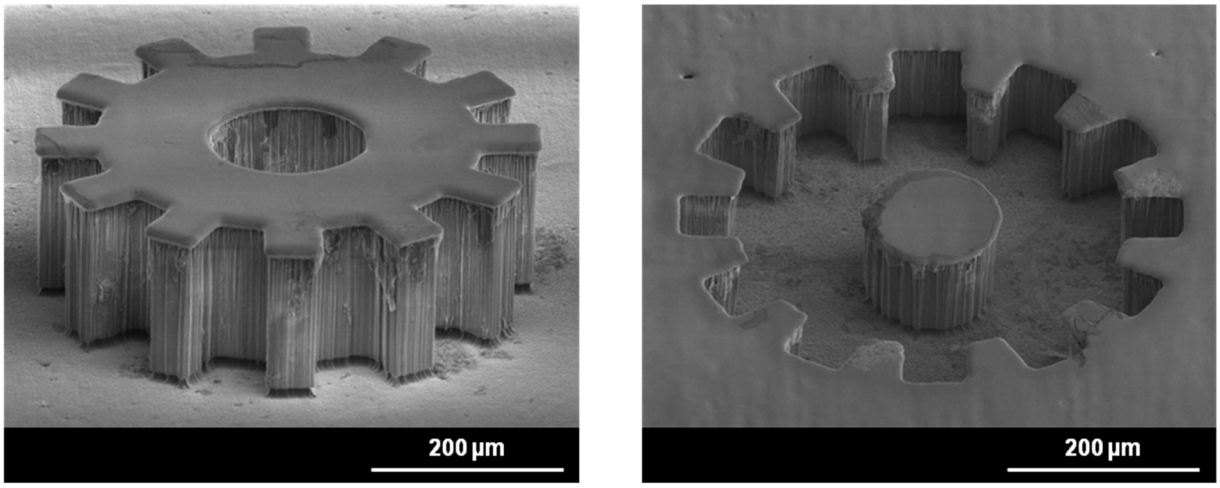

(a) (b)

Figure 4.12. SEM images of MEMS structures for micro-gear applications.

Figure 4.13 shows the SEM and microscope images of another version of micro-gear structure made out of 100 µm thick porous aluminum oxide. Three different types of micro-gears were fabricated. The first type of micro-gear has 30-tooth, 60 µm tooth length, 400 µm inner diameter, and 865 µm outer diameter. The second type of micro-gear has 20-tooth, 60 µm tooth length, 300 µm inner diameter, and 700 µm outer diameter. The third type of micro-gear has 16-tooth, 60 µm tooth length, 200 µm inner diameter, and 500 µm outer diameter.

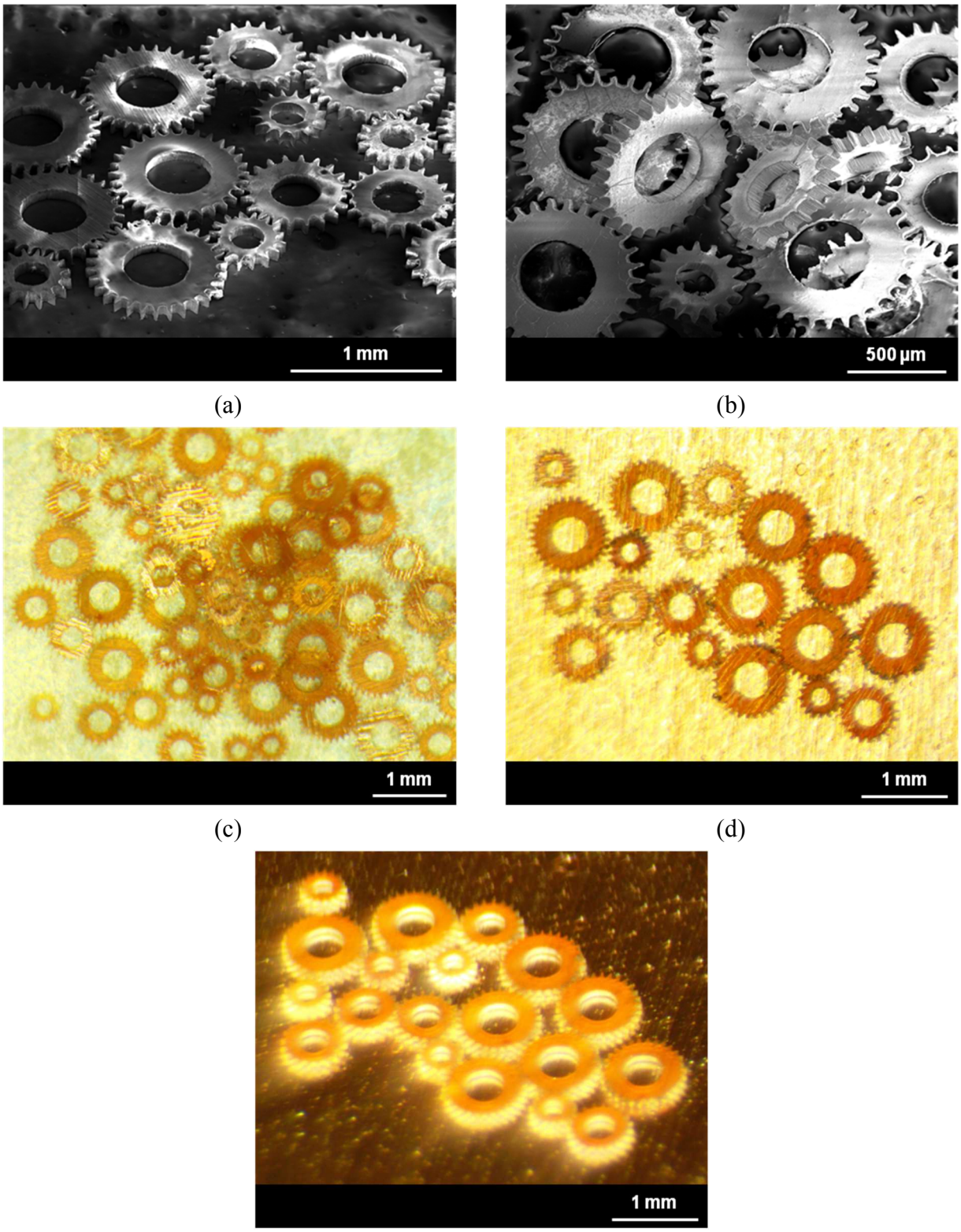

Figure 4.13. SEM and microscope images of AAO micro-gears.

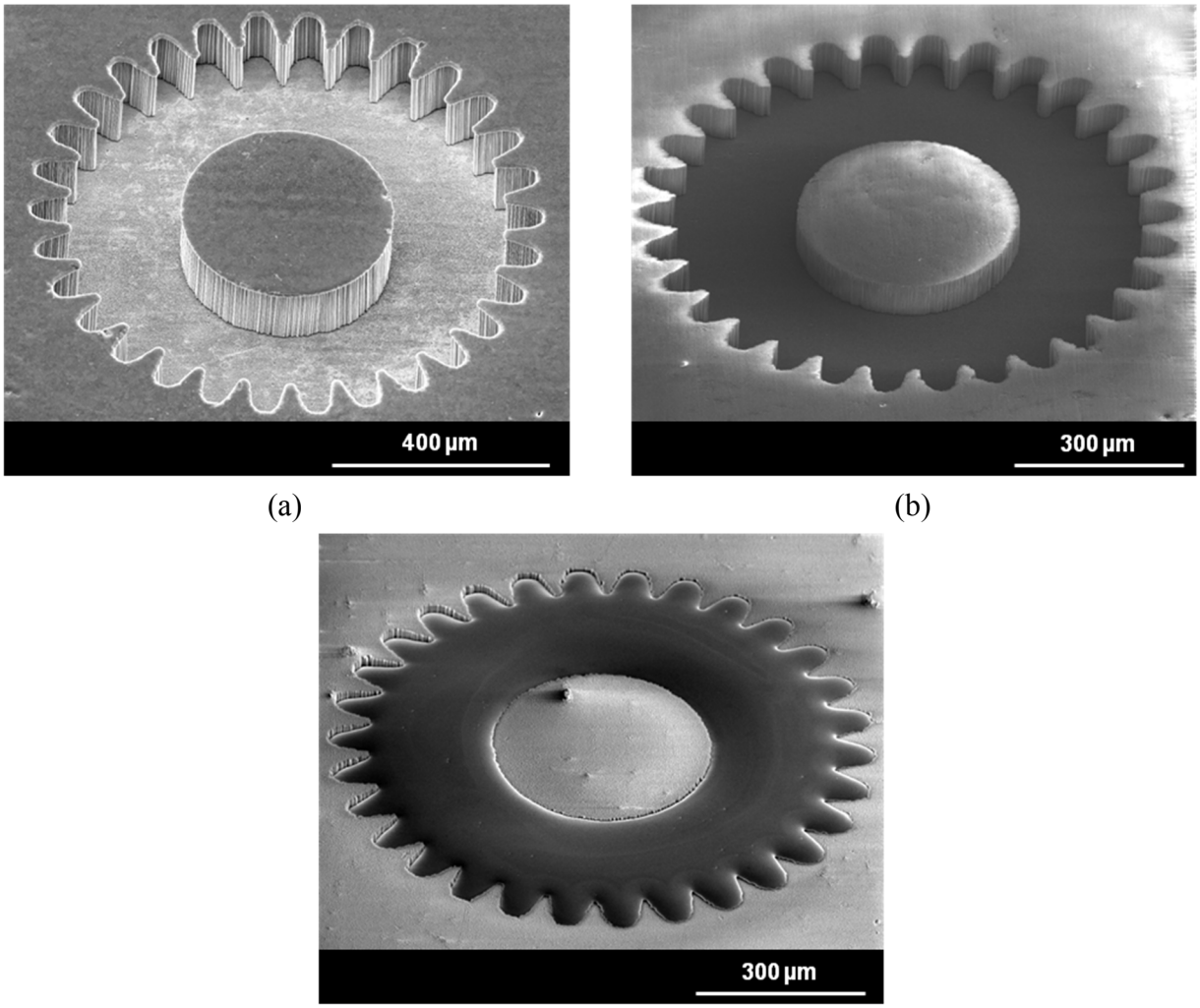

(a) (b)

(c)

Figure 4.14. Process flow for fabrication of metal micro-gears.

Figure 4.14 shows the process flow for fabrication of metal micro-gears by using AAO templates as a mold material. After transferring the gear patterns by photolithography, AAO templates were etched in 0.5M NaOH solution. A 5 µm thick electroplated copper were used as an etch mask during wet chemical etching process (Figure 4.14 (a)). Before electroplating the desired metal into the etched regions, copper etch mask was removed (Figure 4.14 (b)). After removal of copper etch mask, electroplating of copper and nickel was performed into the etched

regions of AAO templates and on aluminum substrate. (Figure 4.14 (c)). Finally, aluminum substrate and AAO templates were etched and metal micro-gears were released.

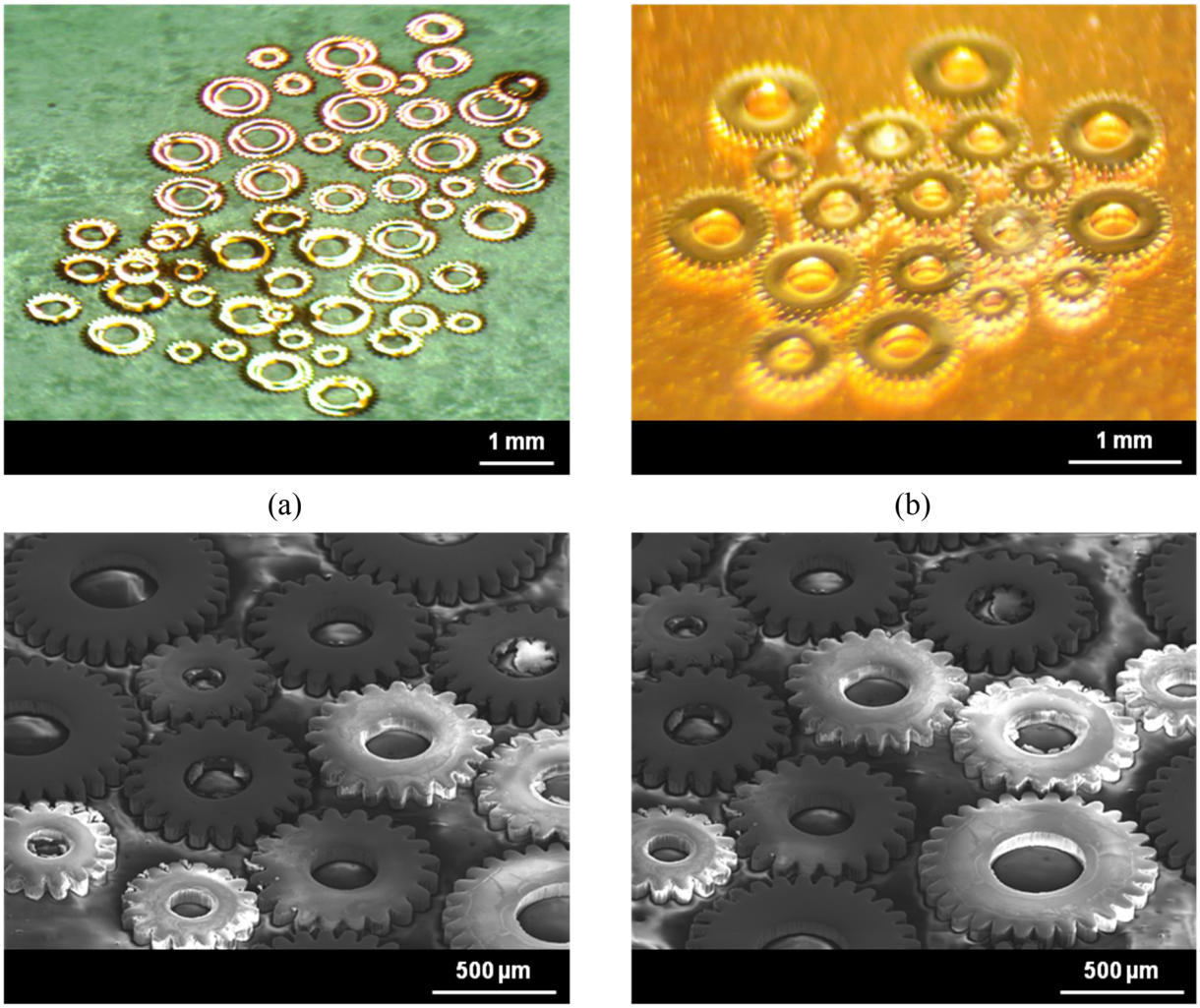

(a) (b)

(c) (d)

Figure 4.15. Microscope and SEM images of copper micro-gears.

Figure 4.15 shows the microscope and SEM images of micro-gears made out of copper by using AAO templates as a mold material. The first type of micro-gear has 30-tooth, 60 µm tooth length, 375 µm inner diameter, and 950 µm outer diameter. The second type of micro-gear

has 20-tooth, 60 µm tooth length, 275 µm inner diameter, and 750 µm outer diameter. The third type of micro-gear has 16-tooth, 60 µm tooth length, 175 µm inner diameter, and 555 µm outer diameter. The thickness of copper micro-gears was measured to be 92 µm.

Figure 4.16 shows the microscope images of micro-gears made out of nickel by using AAO templates as a mold material. All type of nickel micro-gears has same inner and outer diameters and tooth length as in copper micro-gears. The thickness of nickel micro-gears was measured to be 60 µm.

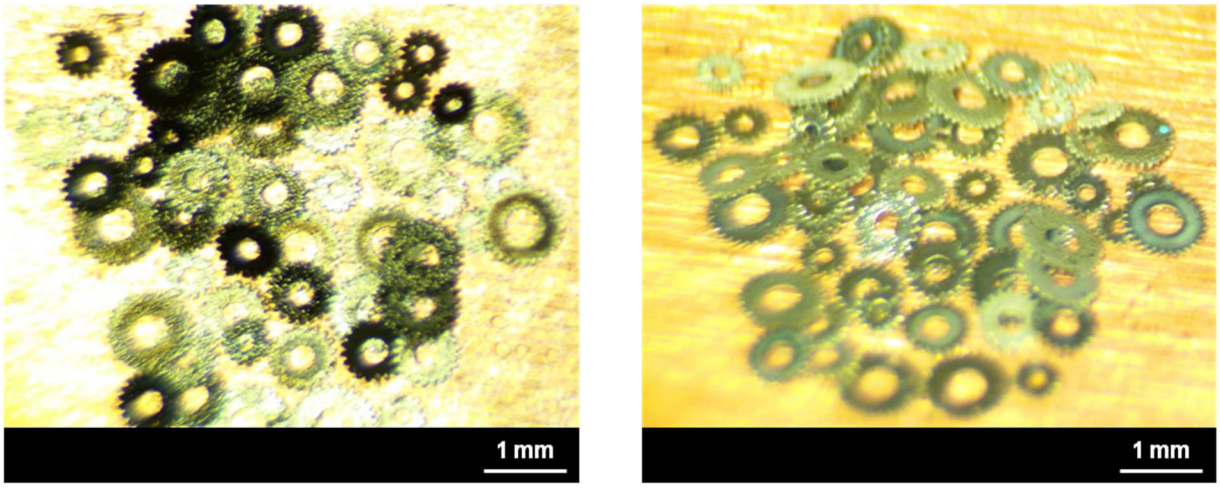

(a) (b)

Figure 4.16. Microscope images of nickel micro-gears.

Figure 4.17 and Figure 4.18 show the SEM images of common MEMS structures. These structures were fabricated by the processes described in Figure 4.2. Electroplated Ni (5 µm) was used as a structural material. Figure 4.17(a) shows the SEM image (tilted view) of a cantilever structure with 190 µm beam length, 24 µm beam width, 300 µm x 300 µm pad size, 14 µm pad hole diameter, 40 µm beam spacing, and 585 µm x 480 µm cavity size. Figure 4.17(b) shows the top view of the cantilever. Figure 4.17(c) shows the SEM image (tilted view) of a floating

membrane structure with 24 µm tether width, 128 µm tether length, 410 µm x 410 µm pad size, 14 µm pad hole diameter, and 600 µm x 600 µm cavity size. Figure 4.17(d) shows the top view of the floating membrane.

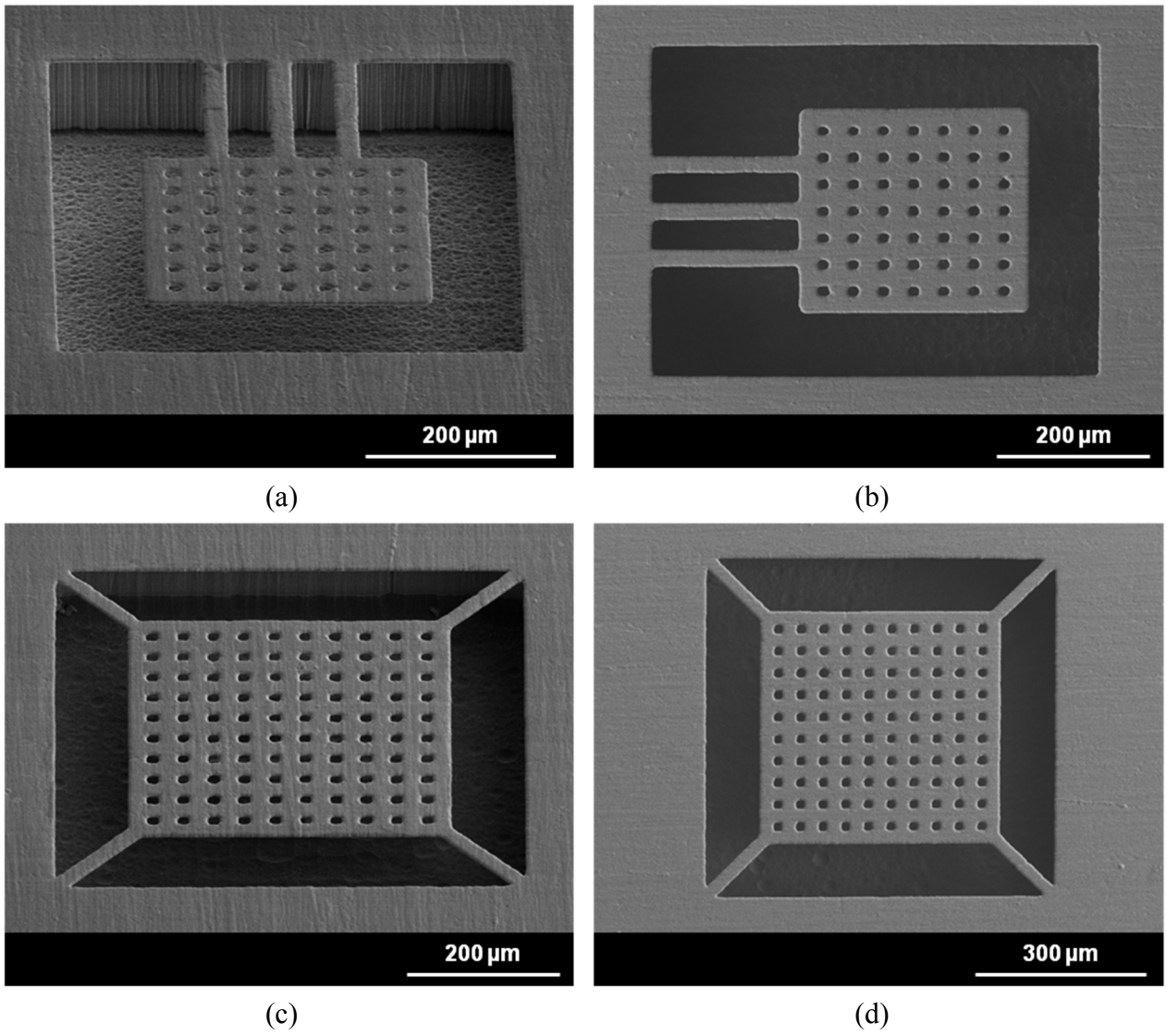

(a) (b)

(c) (d)

Figure 4.17. SEM images of MEMS structures: cantilever and floating membrane.

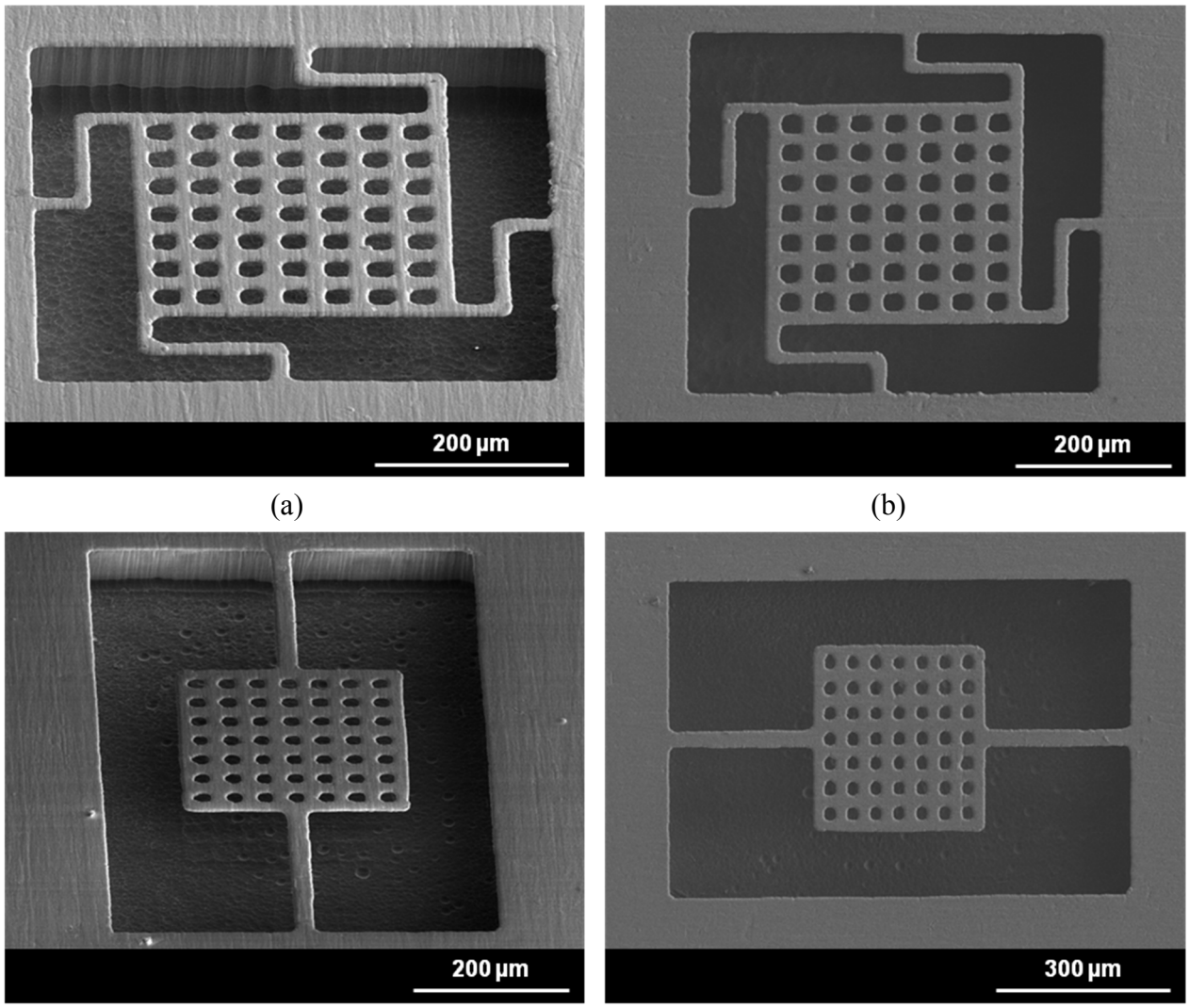

(a) (b)

(c) (d)

Figure 4.18. SEM images of MEMS structures: spring pad and torsional.

Figure 4.18(a) shows the SEM image (tilted view) of a spring pad structure with 18 µm flexure width, 325 µm x 325 µm pad size, 26 µm pad hole diameter, and 530 µm x 530 µm cavity size. Figure 4.18(b) shows the top view of the spring pad. Figure 4.18(c) shows the SEM image (tilted view) of a torsional structure with 25 µm torsional beam width, 250 µm torsional beam length, 290 µm x 290 µm pad size, 20 µm pad hole diameter, and 485 µm x 790 µm cavity

size. Figure 4.18(d) shows the top view of the torsional. The depth of the cavities for all structures was measured to be 100 μm.

Figure 4.19 shows the SEM image of another version of MEMS cantilever structure. In this design, three rectangular cantilever beams were fabricated next to each other. Electroplated nickel was used as a structural material. Each cantilever structure has a dimension of 100 μm in width, 595 μm in length, 35 μm in pad hole diameter, 5 μm in thickness, and 920 μm x 1220 μm in cavity size.

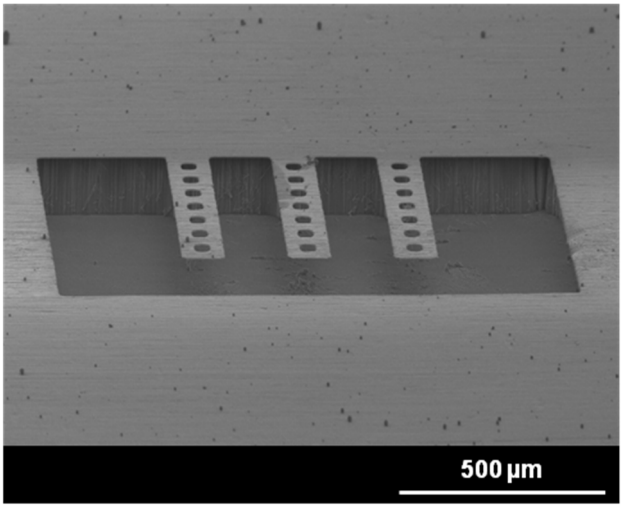

Figure 4.19. SEM image of rectangular cantilever beams.

In these fabrication processes, we demonstrated that AAO templates can also be used as a sacrificial layer material in addition to using them as a structure and a mold material. A variety of common MEMS devices can be built using this approach.

The dynamic behavior of rectangular cantilever beams in Figure 4.19 was studied by laser Doppler vibrometer (Polytech MSA-500 Micro System Analyzer) in order to extract the natural resonance frequencies and the vibration mode shapes of cantilever beams. A laser Doppler vibrometer (LDV) is a precision optical transducer that is used to make non-contact

vibration velocity and displacement measurement of a target surface. In laser Doppler vibrometer, the beam from the laser with a frequency of f_o, is divided into a reference beam and a test beam with a beam splitter. Then, the test beam passes through the Bragg cell which adds a frequency shift of f_b to the reference beam. Then, the test beam with a shifted frequency of f_o+f_b is directed to the target surface. The motion of the target surface adds a Doppler shift (f_d) to the test beam. The Doppler frequency shift is described as

$$f_d = 2v(t)\cos(\alpha) / \lambda \tag{144}$$

where v(t) is the velocity of the target as a function of time, α is the angle between the laser beam and the velocity vector, and λ is the wavelength of the light. Some portion of the scattered light from the target surface is collected by the LDV and is reflected by the beam splitter to the photodetector. This scattered light with a frequency of $f_o+f_b+f_d$ is combined with the reference beam at the photodetector. The photodetector measures the intensity of the combined light of which the beat frequency is equal to the difference frequency between the reference beam and the scattered beam. The output of the photodetector is a standard frequency modulated signal with the Brag cell frequency as the carrier frequency and the Doppler shift as the modulation frequency. This signal is then demodulated by the demodulator inside the instrument controller to derive the velocity versus time of the vibrating target. Figure 4.20 shows the schematic diagram of a typical laser Doppler vibrometer.

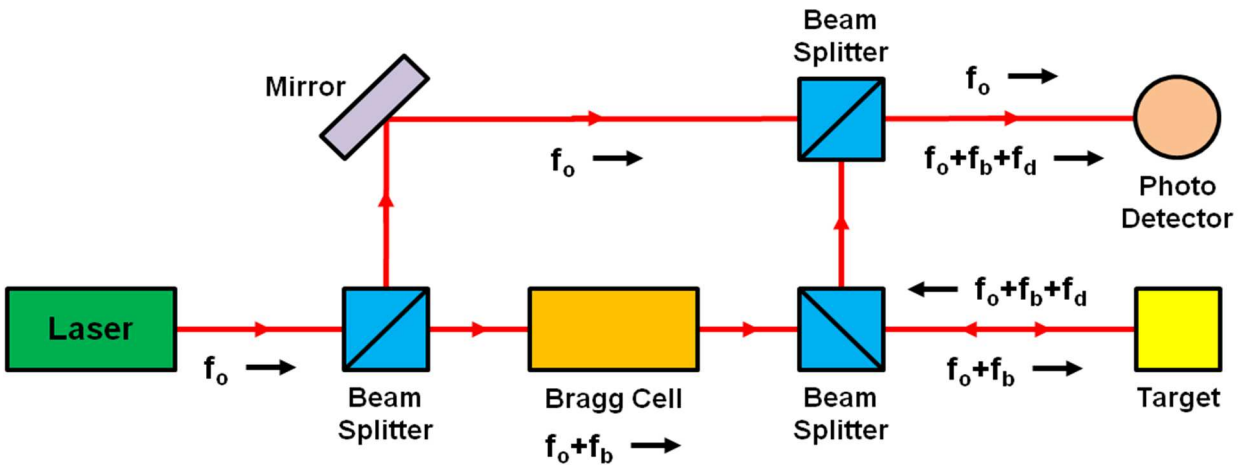

Figure 4.20. Schematic diagram of a laser Doppler vibrometer.

In this experiment, rectangular cantilever beam array was actuated by a piezoelectric actuator which is capable of excitation frequencies in the MHz range. The cantilever beams were placed on piezoelectric actuator and piezoelectric actuator was vibrated by a periodic chirp waveform, a signal in which the frequency increases with time. After that, natural resonance frequencies and corresponding vibration mode shapes of cantilever beams were extracted by laser Doppler vibrometer. Figure 4.21 shows the frequency spectrum of velocity (velocity as a function of excitation frequency) of a fabricated rectangular cantilever beam array in air. Figure 4.22 shows the frequency spectrum of displacement (displacement as a function of excitation frequency) of a fabricated rectangular cantilever beam array in air. Since our cantilever beam array system is undamped, resonance peaks appear at forcing frequencies which are equal to the natural frequencies of the system. In other words, when the externally applied forces are absent, free vibration takes place and the system oscillates at its natural frequencies. At resonance frequencies, vibration amplitudes of velocity and displacement of the system increase steadily, tending towards infinity. Natural resonance frequency is dependent on the spring constant and the mass of a vibrating body.

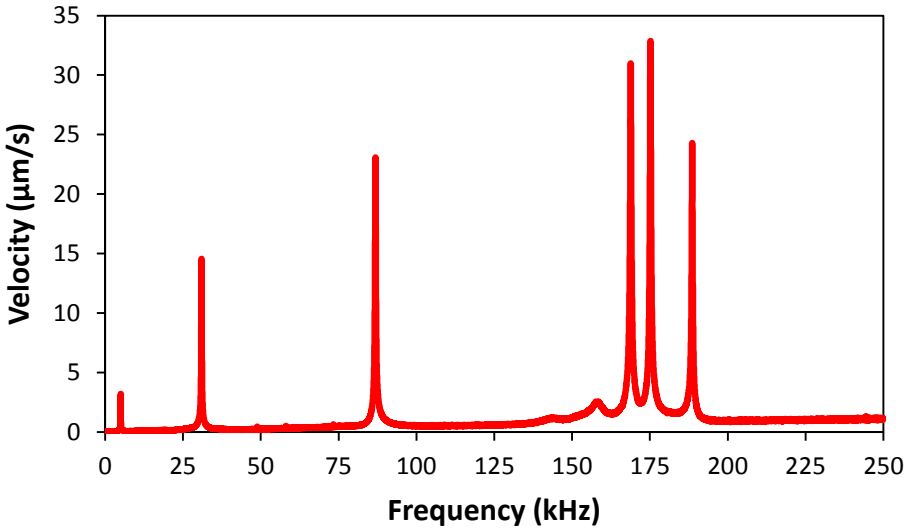

Figure 4.21. Frequency spectrum of velocity of a fabricated cantilever beam array in air.

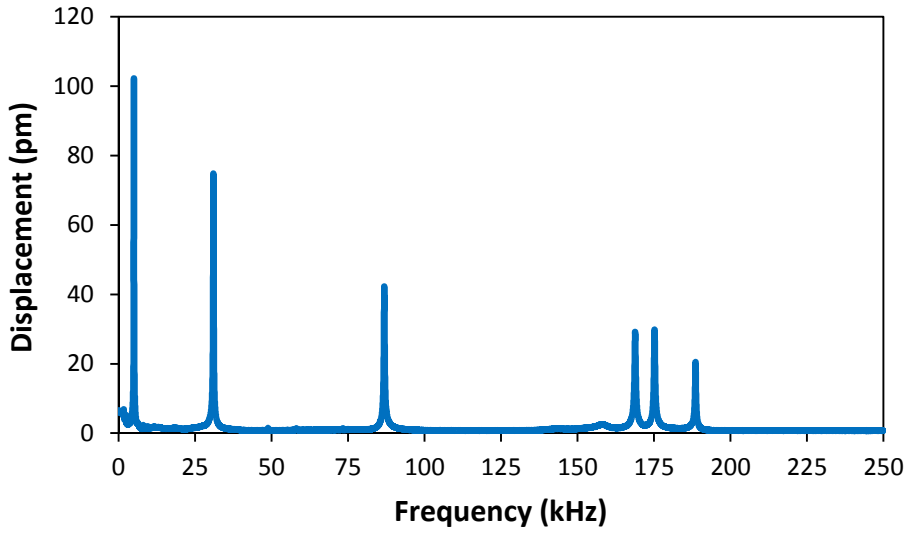

Figure 4.22. Frequency spectrum of displacement of a fabricated cantilever beam array in air.

Based on the measurements of frequency spectrum of velocity and displacement of a fabricated cantilever array, the first, second, third, fourth, fifth, and sixth natural resonance frequencies are 5 kHz, 30.97 kHz, 86.81 kHz, 168.84 kHz, 175.18 kHz, and 188.59 kHz, respectively. Figure 4.23 shows the vibration mode shapes (deformation patterns) of cantilever

beams associated with natural resonance frequencies. Cantilever array show torsional vibration mode shapes at frequencies of 175.18 kHz and 188.59 kHz.

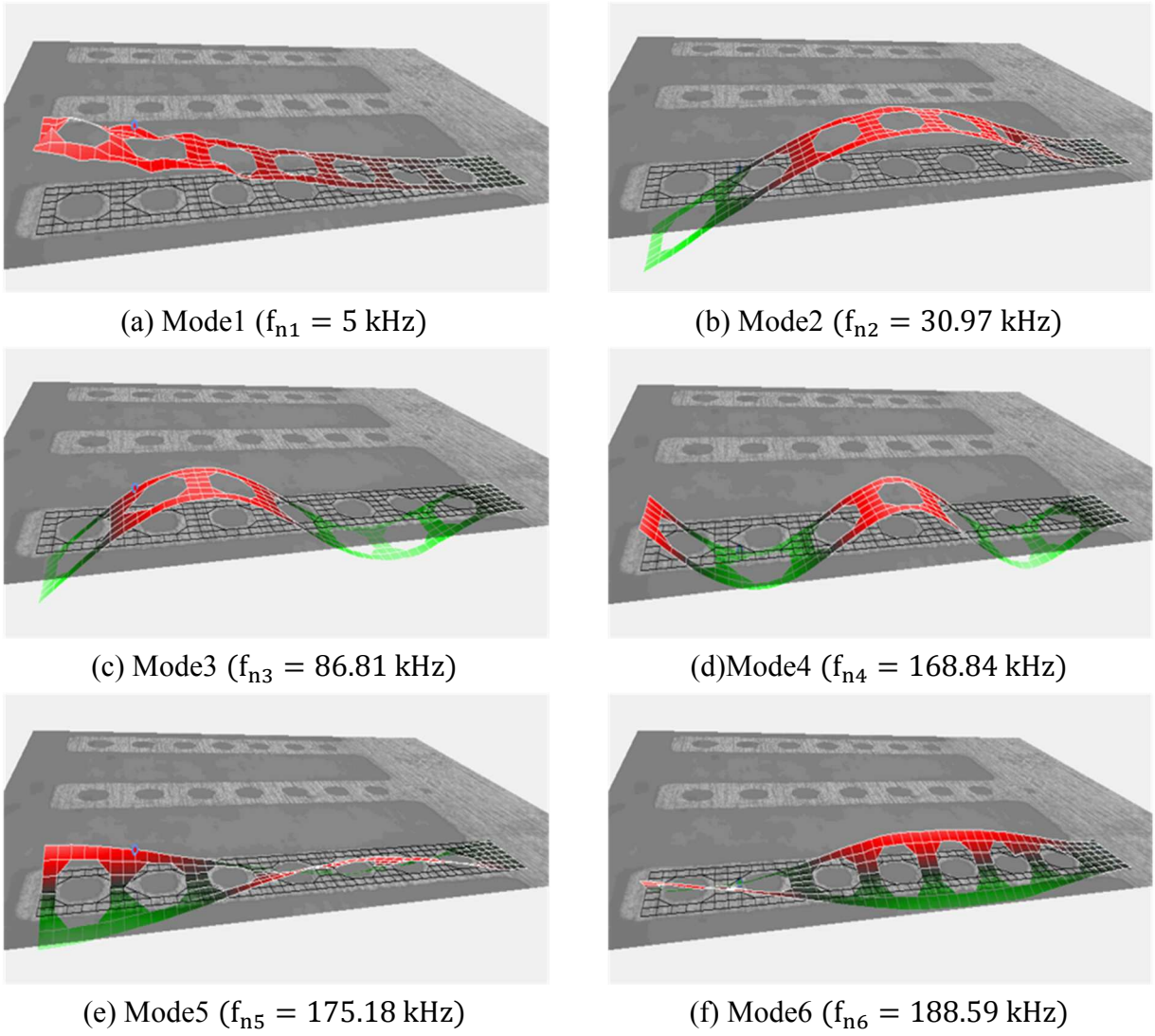

(a) Mode1 ($f_{n1} = 5$ kHz) (b) Mode2 ($f_{n2} = 30.97$ kHz)

(c) Mode3 ($f_{n3} = 86.81$ kHz) (d)Mode4 ($f_{n4} = 168.84$ kHz)

(e) Mode5 ($f_{n5} = 175.18$ kHz) (f) Mode6 ($f_{n6} = 188.59$ kHz)

Figure 4.23. Vibration mode shapes of cantilever beams associated with natural resonance frequencies.

The natural resonance frequency of a cantilever beam for each vibration mode is defined as,

$$f_n = \frac{(\alpha_n)^2}{2\pi}\sqrt{\frac{EI}{\rho AL^4}} \tag{145}$$

where E, ρ, I, A, L, and α_n are the Young's modulus and density of the nickel, moment of inertia, cross-section area, and length of the cantilever beam, and constant, respectively. The constants α_n for the six normal modes of vibration are 1.8751, 4.6941, 7.8547, 10.9955, 14.1372, and 17.2787, respectively. The moment of inertia and cross-section area for the cantilever beam are defined as, $I = (wt^3)/12$ and $A = wt$, respectively. When we substitute I and A into Eq. (145), we obtain the natural resonance frequency as,

$$f_n = \frac{(\alpha_n)^2}{2\pi}\sqrt{\frac{E(wt^3/12)}{\rho(wt)L^4}} = \frac{(\alpha_n)^2}{2\pi}\sqrt{\frac{Et^2}{12\rho L^4}} \tag{146}$$

According to the Eq. (146), the calculated natural resonance frequencies for the four normal modes of vibrations are 4.9728 kHz, 31.164 KHz, 87.258 KHz, and 170.99 KHz, respectively. The calculated values are in good agreement with measured ones.

The general solution for the vibration mode shapes is defined as,

$$\begin{aligned} X(x) = {} & C_1[\cos(\beta_n x) + \cosh(\beta_n x)] + C_2[\cos(\beta_n x) - \cosh(\beta_n x)] \\ & + C_3\left[\sin(\beta_n x) + \sinh(\beta_n x)\right] + C_4[\sin(\beta_n x) - \sinh(\beta_n x)] \end{aligned} \tag{147}$$

where C_1, C_2, C_3, and C_4 are constants.

Using the first boundary condition, C_1 may be found as,

$$X(0) = 0 = C_1(2) \quad \rightarrow \quad C_1 = 0 \tag{148}$$

Taking the first derivative of Eq. (147) and using the second boundary condition, C_3 may be found as,

$$\begin{aligned} \frac{dX(x)}{dx} = 0 = C_2[-\sin(\beta_n x) - \sinh(\beta_n x)] + C_3[\cos(\beta_n x) + \cosh(\beta_n x)] \\ + C_4[\cos(\beta_n x) - \cosh(\beta_n x)] = C_3(2) \quad \rightarrow \quad C_3 = 0 \end{aligned} \tag{149}$$

The second and third derivates of Eq. (147) and remaining boundary conditions result

$$\frac{d^2X(L)}{dx^2} = C_2[-\cos(\beta_n L) - \cosh(\beta_n L)] + C_4[-\sin(\beta_n L) - \sinh(\beta_n L)] = 0 \tag{150}$$

$$\frac{d^3X(L)}{dx^3} = C_2[\sin(\beta_n L) - \sinh(\beta_n L)] + C_4[-\cos(\beta_n L) - \cosh(\beta_n L)] = 0 \tag{151}$$

When we combine Eq. (150) and eq. (151), we obtain

$$C_4 = C_2 \frac{-\cos(\beta_n L) - \cosh(\beta_n L)}{\sin(\beta_n L) - \sinh(\beta_n L)} \tag{152}$$

Therefore, for a cantilever beam with a free end Eq. (147) reduces to

$$\begin{aligned} X_n(x) = C_2 \Bigg\{ [\cos(\beta_n x) - \cosh(\beta_n x)] \\ + \left[\frac{-\cos(\beta_n L) - \cosh(\beta_n L)}{\sin(\beta_n L) - \sinh(\beta_n L)}\right][\sin(\beta_n x) - \sinh(\beta_n x)] \Bigg\} \end{aligned} \tag{153}$$

In order for the dynamic solution for the displacement to be equal to the static solution (at time $t = 0$), C_2 should be equal to 0.5. With this value for C_2, $X_n(0) = 0$ and $X_n(L) = 1$. By inserting Eq. (152) into either Eq. (150) or Eq. (151), the frequency equation for a cantilever beam can be obtained as,

$$\cos(\beta_n L)\cosh(\beta_n L) = -1 \tag{154}$$

The solutions for $\beta_n L$ can be found by solving the Eq. (154). The solutions for $\beta_n L$ for the six normal modes of vibration are 1.8751, 4.6941, 7.8547, 10.9955, 14.1372, and 17.2787, respectively and are equal to α_n in Eq. (145). The first four normal modes of vibration of fabricated cantilever beams based on the Eq. (153) are shown in Figure 4.24.

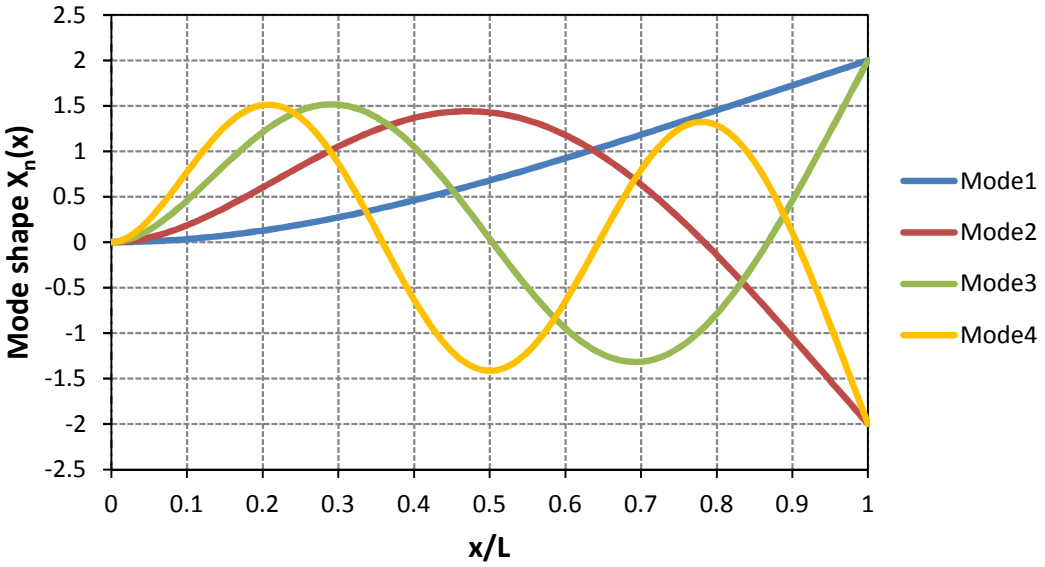

Figure 4.24. The first four modes of vibration of fabricated cantilever beams.

The fabricated cantilever beam array can also be actuated by an external magnetic field since they were made out of nickel and can be used as a MEMS switch. Figure 4.25 shows the

magnetic actuation of the cantilever beam array without an external magnetic field (a) and with an external magnetic field (b).

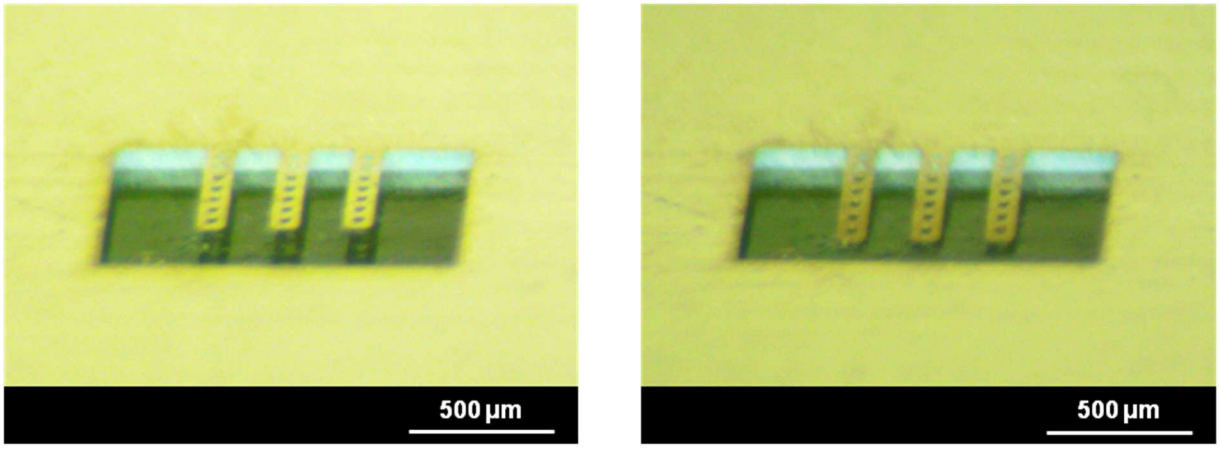

(a) (b)

Figure 4.25. Magnetic actuation of the cantilever beam array.

Another promising application of AAO templates is to laminate them with a PCB and perform the wet chemical etching afterwards. For this purpose, AAO templates patterned with cantilever beam array were laminated on a 6-layer PCB with a 5-turn octagonal coil in each layer by using epoxy, and then wet chemical etching of AAO templates with 0.5M NaOH solution was carried out. Since NaOH solution does not attack PCB layer, this wet chemical etching process can be performed after lamination process. Figure 4.25(a) shows the microscope image of fabricated coil on PCB and Figure 4.25(b) shows the microscope image of the laminated AAO template on PCB layer after wet chemical etching process. Hybrid integration of AAO templates with PCB allows us to combine different manufacturing processes together. Figure 4.25 (c) and (d) show the cross-section view of hybrid integration and etching processes.

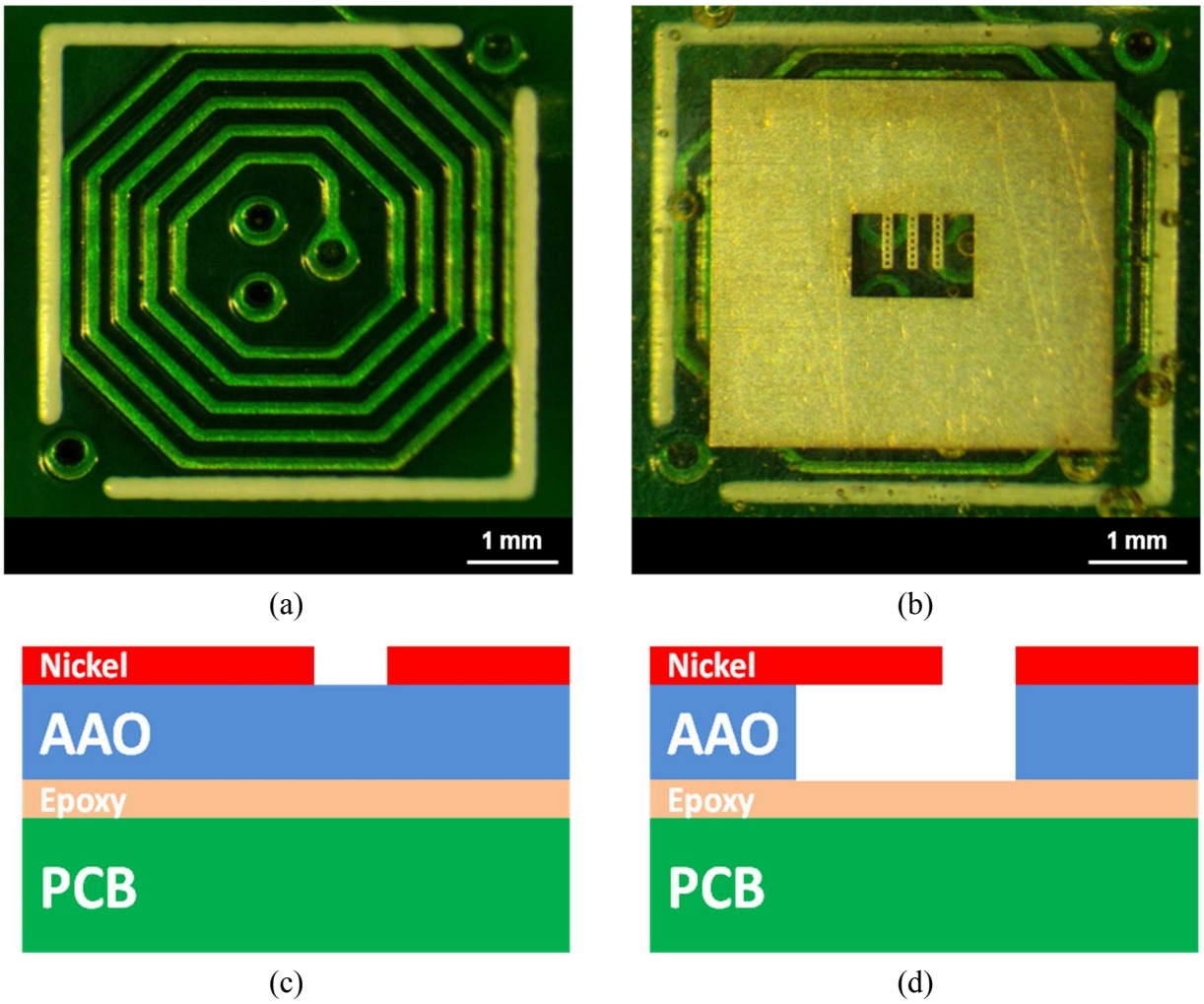

Figure 4.26. Hybrid integration of an AAO template with a PCB layer.

4.3. Conclusions

In this study we have demonstrated that under correct process conditions, anodic aluminum oxide (AAO) templates can be prepared to be thick (~100 microns) and highly anisotropic, containing a high density of vertical nanopores. Since the AAO growth process is electrochemical in nature, the templates can in principle be produced inexpensively over large areas. Using a simple metal protective layer which covers the AAO surface, one can selectively etch AAO using a simple wet etch in sodium hydroxide. Etching with this chemical resulted in

highly vertical etch structures, indicating a highly anisotropic etch mechanism. Our belief is that the etch is enhanced by the vertical nanopores, allowing etchant to enter the long vertical tubes and destroy the AAO material from within the pores, and allowing the etch to occur equally along the length of the pores. Images of the material during etch suggest that this is generally the mechanism.

The vertical structures in AAO could be produced as both isolated structures as well as deep holes for cavities. We were able to demonstrate structures as small as 20 microns in dimension, suggesting a 5:1 aspect ratio at minimum, although the near vertical sidewall slopes indicate much higher aspect ratios are possible. The slow rate of etching in the lateral direction is beneficial for producing deep etches, however, this means that undercut etch is difficult to perform in the same etch. For our MEMS structures, we performed 1 to 2 hour etch to remove enough material from under the metal structure to produce freestanding structures.

Each step of the process utilizes wet chemistry (anodization, electroplating, etch), which means that this process can be low cost. It is relatively easy to integrate other materials such as metals and polymers into this process, since AAO is structurally able to support deposition processes on its surface and since the processes are performed at moderate temperature and do not require high vacuum. Indeed, we anticipate that a host of exotic and specialty materials can be integrated into this process, including biological materials and nanostructures.

We have demonstrated that AAO templates can make excellent substrates for producing MEMS structures using low cost and facile processes. The ability to integrate a wide variety of secondary materials (such as nickel or copper in our examples) is also very exciting. Wet chemical etching can be used to etch deep vertical structures in the AAO material, which can then be used as a structural part of the MEMS device, and undercut can be performed to produce

freestanding structures. In addition, AAO templates can be used as a structure material to fabricate microstructures. Furthermore, the AAO material may be used as a mold for micromolding polymer parts or electroforming structures in metal. AAO is an excellent structural material and dielectric, making this an exciting candidate non-silicon replacement material for many MEMS applications requiring vertical microstructures.

CHAPTER 5

SUMMARY, CONCLUSIONS AND FUTURE WORKS

In this dissertation, highly anisotropic nature of porous anodic aluminum oxide templates has been explored for electronic and MEMS applications.

In the first part of the dissertation, porous AAO templates integrated with ferromagnetic material were studied for spiral inductors as a magnetic core. For this purpose, AAO templates with average pore diameter of 70 nm and thickness of 18 μm were fabricated and electroplated with Ni to serve as a magnetic core for spiral inductors. The 3.5 turns spiral inductors were fabricated on Ni-AAO templates by using standard photolithography and Cu electroplating processes. The fabricated spiral inductors has a dimension of 1370 μm x 1010 μm with 5μm thickness, 15 μm trace width, 15 μm spacing, 400 μm outer diameter, and 220 μm inner diameter. The high frequency RF characterization of spiral inductors was performed over a frequency range of 1 - 20 GHz with and without the integration of ferromagnetic material. The inductance of spiral inductors with a magnetic core was measured to be 10.12 nH and enhanced 21% at 5 GHz compared to an air core of the same coil size. The maximum quality factor value of 14.48 was obtained at 5 GHz. The resonance frequency of 10.24 GHz was obtained for magnetic core inductors. Since porous AAO templates are self-laminated and patterned, they have potential application as a magnetic core for spiral inductor fabrication by eliminating all the complexities of fabrication processes to overcome the FMR effect and Eddy current loss.

In the second part of the dissertation, the applications of porous AAO templates as a structure material, a mold material for electroforming, and a sacrificial layer material for MEMS applications were demonstrated. First of all, wet chemical etching mechanism of porous AAO

templates was explained in detail. After that, deep, high aspect ratio structures such as rectangle, square and cylindrical posts and holes with vertical side walls were fabricated by wet chemical etching of 100 μm thick porous AAO templates in 0.5M NaOH solution. Based on the initial etch studies, we showed that the wet chemical etching of AAO templates is not dependent on the mask geometry and any type of pattern with any geometry can be fabricated with desired thickness or depth. In order to use porous AAO templates as a structure material, three different types of micro-gears made out of aluminum oxide with a thickness of 100 μm were fabricated. In order to demonstrate the usage of porous AAO templates as a mold material, AAO templates were etched and then desired metals such as copper and nickel were electroplated into etched regions. By using this technique, three different types of copper and nickel micro-gears were fabricated. The thicknesses of the fabricated copper micro-gears were measured to be 92 μm and nickel micro-gears were measured to be 60 μm. Another application area of porous AAO templates is to use them as a sacrificial layer material. For this purpose, various types of MEMS devices such as cantilever, floating membrane, spring pad, and torsional were fabricated by nickel electroplating process on porous AAO templates, and then cavities under these structures were created by wet chemical etching of AAO templates. Finally, hybrid integration of porous AAO templates with PCB layers by using epoxy was demonstrated. Since porous AAO templates are highly anisotropic and can be prepared at various thicknesses, desired MEMS structures can be fabricated by a straightforward and low cost wet etching process of AAO templates. In addition, the relatively low cost for the material, combined with low cost of etchant and ease of processing, make this attractive alternative to expensive, complex processes such as DRIE. Furthermore, porous AAO templates are mechanically strong material and have excellent

dielectric properties, making them a compelling alternative to silicon for producing MEMS structures and devices.

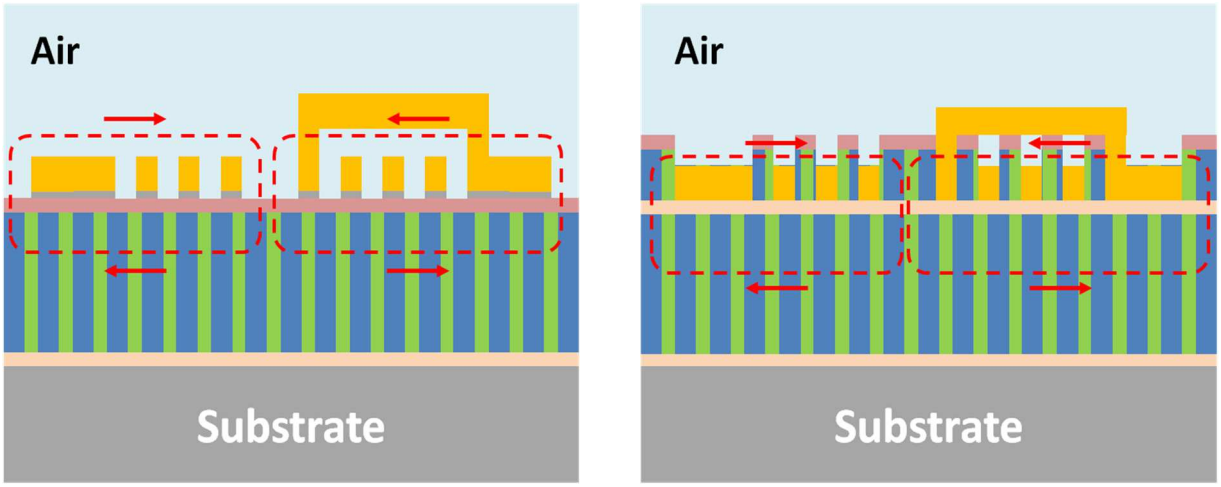

(a) (b)

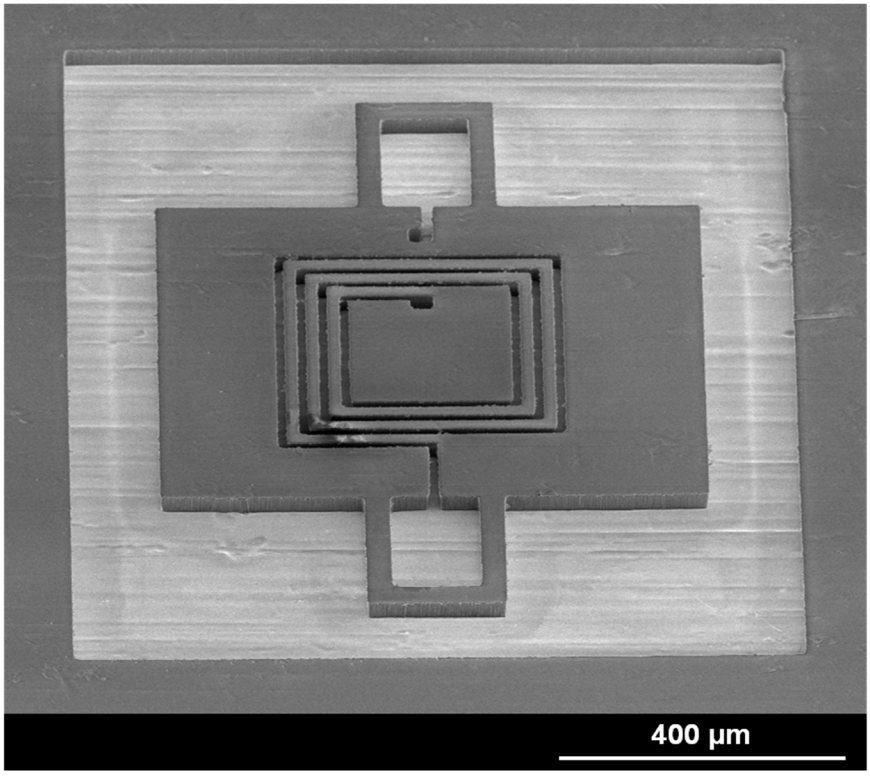

(c)

Figure 5.1. Integration way of spiral inductors into the AAO templates.

In order to increase the performance of spiral inductors, ferromagnetic materials with higher permeability such as iron, cobalt, and their alloys with nickel can be electroplated into the nanoporous of AAO templates. In addition to the electroplating of high permeability ferromagnetic materials, spiral inductors can be embedded into the AAO templates to create a close loop for magnetic flux to increase its performance. By integration of spiral inductors into the AAO templates enables the magnetic flux to concentrate into the ferromagnetic material and will increase the magnetic flux intensity, and therefore, will enhance the inductance of spiral inductors. These two approaches may be the possible future works to fabricate high performance spiral inductors. Figure 4.27 shows the possible integration way of spiral inductor into the AAO template. Figure 4.27(a) shows single magnetic core application which was studied in this dissertation. Figure 4.27(b) shows the laminated magnetic core application. Figure 4.27(c) shows the wet chemically etched AAO template for the integration of spiral inductors. The wet chemical etch capability of AAO templates also provides to fabricate thick spiral inductors for high power inductor applications.

Another possible future work might be the integration of different materials and processes by using AAO templates. Figure 4.28 shows the integration of a polymer type material into the patterned micrometer size holes in AAO template and metallization process for fabrication of flexible devices. This kind of integration is hard to perform in conventional MEMS technology. For this purpose, the circular pattern is transferred into the AAO template by wet chemical etching. Then, polymer filling process and successive metallization process on polymer material are performed. Finally, AAO template is etched by wet chemical and fabricated flexible device is released.

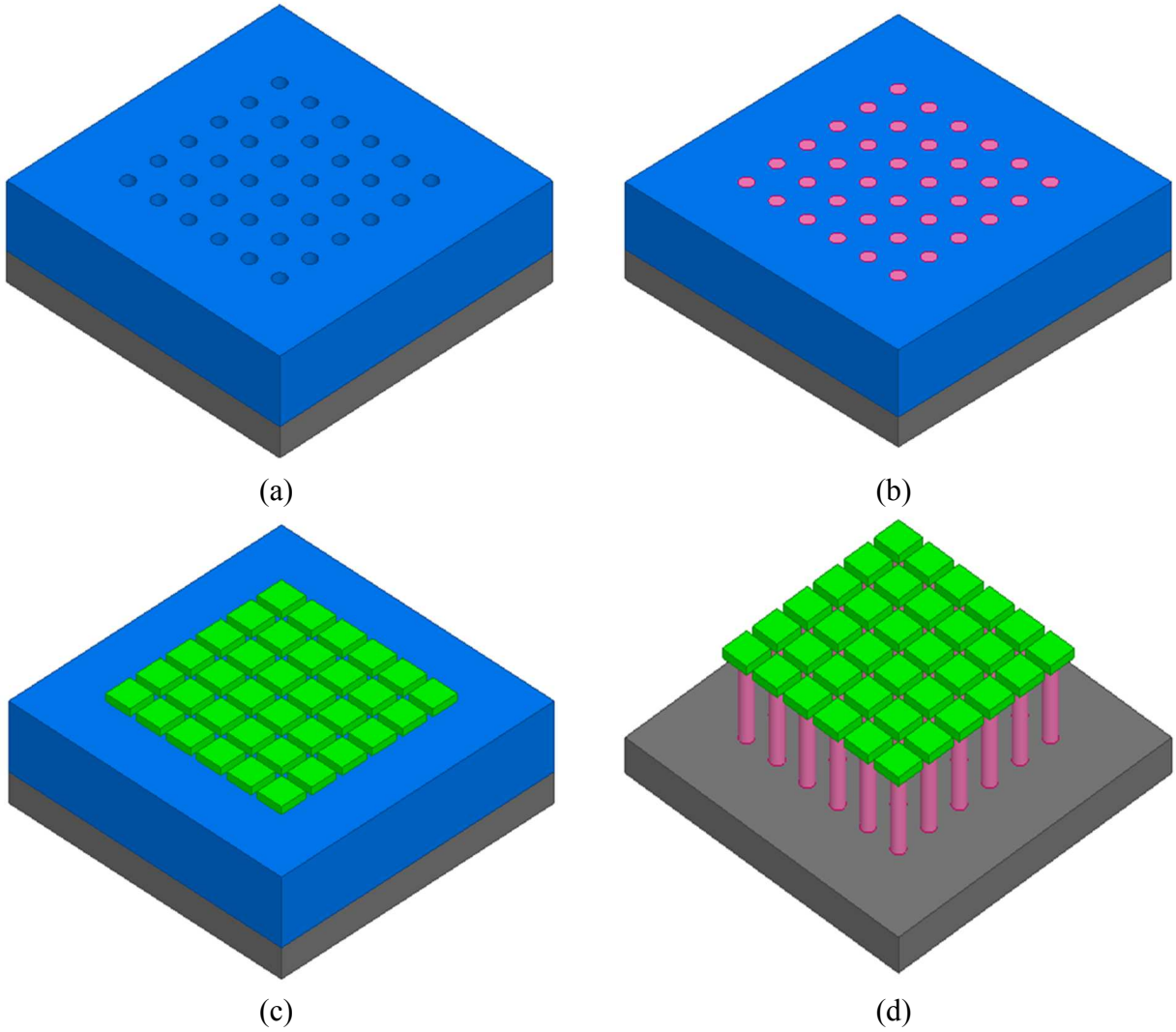

Figure 5.2. Hybrid integration of a polymer material into the AAO templates.

AAO templates can also be used to fabricate laterally movable platform for switching applications in MEMS. For this purpose, the pattern is transferred into the AAO template by wet chemical etching. Then, desired metals are electroplated into the etched regions. In this approach, two types of metal can be electroplated. The former one will be used as a sacrificial layer and be etched away and the latter one will be used a structural material and be anchored to the AAO template. Then, the protective mask will be removed and second lithography process will be performed to protect AAO template that will serve as an anchor. After that, AAO

template is etched away by wet chemical. Finally, protective mask is removed, electroplated metal sacrificial layer is etched away and laterally movable platform is released. Figure 4.29 shows the fabrication steps of laterally movable platform based on AAO templates.

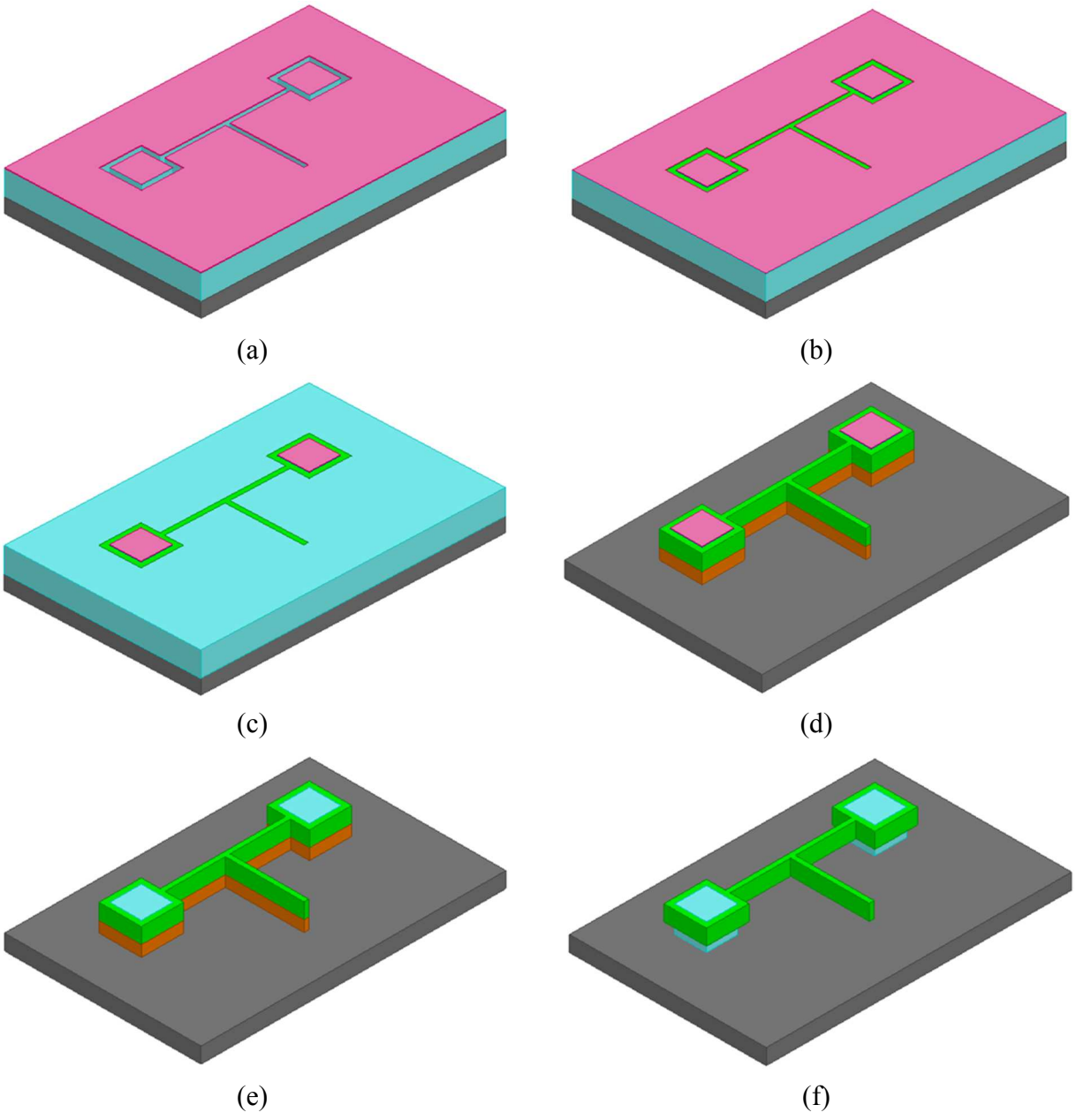

Figure 5.3. Fabrication process of laterally movable platform based on AAO templates.

In this design, the platform can be actuated parallel (in-plane mode) to the substrate by an electromagnetic force. For this purpose, a permanent magnet is attached at the bottom of the substrate which provides an external magnetic field perpendicular to the substrate. When a current flows through the platform, the Lorentz force is generated and provides the deflection of the platform which is parallel to the substrate. The direction of the deflection depends on the current flow direction. Figure 4.30 shows the working principle of the laterally movable platform.

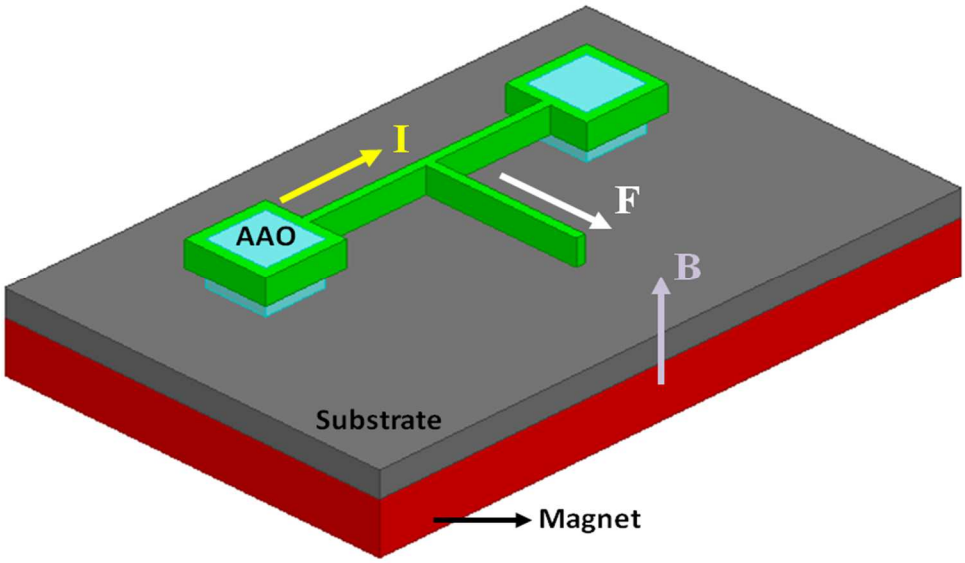

Figure 5.4. Working principle of the laterally movable platform.

The Lorentz force exerted on a moving charged particle in the presence of an external magnetic field is defined as,

$$\vec{F} = q\vec{v} \times \vec{B} \tag{155}$$

where q is the charge on the particle, υ is the velocity of the particle, and B is the magnetic flux density. The Lorentz force can also be expressed in the form of a current flowing through a conductor interacting with an external magnetic field as,

$$F = B\,I\,L\sin(\theta) \tag{156}$$

where I is the current and θ is the angle between the current and the magnetic field.

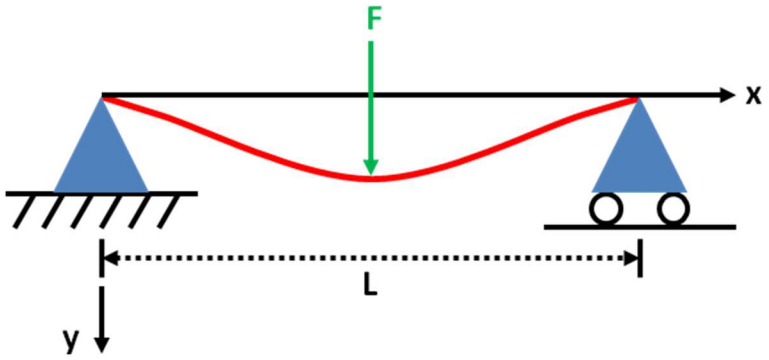

Figure 5.5. Clamped-clamped beam with a concentrated force at the center.

The lateral deflection can be determined by the following equations for the clamped-clamped beam with a concentrated force at the center (Figure 4.31) as,

$$y = \frac{F\,x}{12\,E\,I}\left(\frac{3\,L^2}{4} - x^2\right) \quad \text{for } 0 < x < \frac{L}{2} \tag{157}$$

where F, L, E and I are the applied force, length of the beam, Young's modulus of the beam material, and moment of inertia, respectively. The maximum deflection at the center of the load ($x = L/2$) is defined as,

$$y_{max} = \frac{F\,L^3}{48\,E\,I} \tag{158}$$

Figure 4.32 shows the representation of the deformation shape of a clamped-clamped beam with a concentrated force at the center. Since concentrated force is applied at the center of the beam, maximum deflection occurs at the center of the beam.

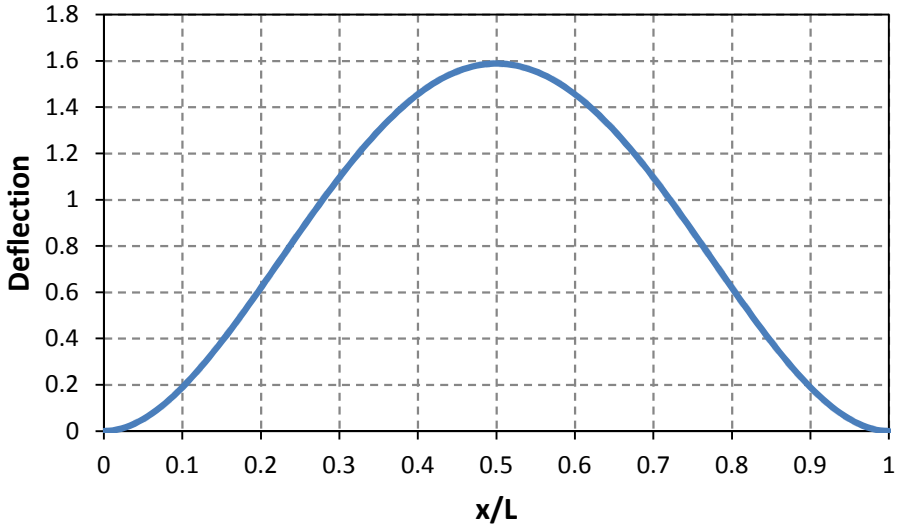

Figure 5.6. Deformation shape of a clamped-clamped beam.

REFERENCES

[1] G. Gorokh, A. Mozalev, D. Solovei, V. Khatko, E. Llobet, and X. Correig, "Anodic formation of low-aspect-ratio porous alumina films for metal-oxide sensor application," *Electrochim. Acta*, vol. 52, pp. 1771-1780, 2006.

[2] J. Spiegel, C. Renaux, M. Darques, J. De La Torre, L. Piraux, P. Simon, J.-P. Raskin, and I. Huynen, "Ferromagnetic Inductors on Commericial Nanoporous Anodic Alumina," *Proceedings of the 39th European Microwave Conference*, pp. 582-585, 2009.

[3] S. Z. Chu, S. Inoue, K. Wada, and K. Kurashima, "Fabrication of integrated arrays of ultrahigh density magnetic nanowires on glass by anodization and electrodeposition," *Electrochim. Acta,* vol. 51, pp. 820-826, 2005.

[4] H. Oshima, H. Kikuchi, H. Nakao, T. Morikawa, K. Matsumoto, K. Nishio, H. Masuda, and K.-I. Itoh, "Improvement of Magnetic Recording Characteristics by Narrowing the Array Pitch of Nanohole Patterned Media," *Japan. J. Appl. Phys.*, vol. 44, pp. L1355-L1357, 2005.

[5] T. R. B. Foong, Y. Shen, X. Hu, and A. Sellinger, "Template-Directed Liquid ALD Growth of TiO_2 Nanotube Arrays: Properties and Potential in Photovoltaic Devices," *Adv. Funct. Mater.*, vol. 20, pp. 1390-1396, 2010.

[6] X. Gao, J. Chen, and C. Yuan, "Enhancing the performance of free-standing TiO_2 nanotube arrays based dye-sensitized solar cells via ultraprecise control of the nanotubes wall thickness," *J. Power Sources*, vol. 240, pp. 503-509, 2013.

[7] N. J. Gerein, and J. A. Haber, "Effect of ac Electrodeposition Conditions on the Growth of High Aspect Ratio Copper Nanowires in Porous Aluminum Oxide Templates," *J. Phys. Chem. B*, vol. 109, pp. 17372-17385, 2005.

[8] G. Sauer, G. Brehm, and S. Schneider, "Highly ordered monocrystalline silver nanowires arrays," *J. Appl. Phys.*, vol. 91, pp. 3243-3247, 2002.

[9] Saedi, and M. Ghorbani, "Electrodeposition of Ni-Fe-Co alloy nanowires in modified AAO template," *Mater. Chem. Phys*., vol. 91, pp. 417-423, 2005.

[10] C. T. Sousa, A. Apolinario, D. C. Leitao, A. M. Pereira, J. Ventura, and J. P. Araujo, "Precise control of the filling strategies in branched nanopores," *J. Mater. Chem.*, vol. 22, pp. 3110-3116, 2012.

[11] R. C. Furneaux, W. R. Rigby, and A. P. Davidson, "The formation of controlled-porosity templates from anodically oxidized aluminum," *Nature*, vol. 337, pp. 147-149, 1989.

[12] H. Masuda, and K. Fukuda, "Ordered Metal Nanohole Arrays Made by a Two-Step Replication of Honeycomb Structures of Anodic Alumina," *Science*, vol. 268, pp. 1466-1468, 1995.

[13] H. Masuda, H. Yamada, M. Satoh, H. Asoh, M. Nakao, and T. Tamamura, "Highly ordered nanochannel-array architecture in anodic alumina," *Appl. Phys. Lett.*, vol. 71, pp. 2770-2772, 1997.

[14] O. Jessensky, F. Muller, and U. Gösele, "Self-organized formation of hexagonal pore arrays in anodic alumina," *Appl. Phys. Lett.*, vol.72, pp. 1173-1175, 1998.

[15] A. P. Li, F. Müller, A. Birner, K. Nielsch, and U. Gösele, "Hexagonal pore arrays with a 50-420 nm interpore distance formed by self-organization in anodic alumina," *J. Appl. Phys.*, vol. 84, pp. 6023-6026, 1998.

[16] G. Bailey, and G. C. Wood, "The Morphology of Anodic Films Formed on Aluminum in Oxalic Acid," *Trans. Inst. Metal Finish.*, vol. 52, pp. 187-199, 1974.

[17] G. E. Thompson, G. C. Wood, "Porous anodic film formation on aluminum," *Nature*, vol. 290, pp. 230-232, 1981.

[18] M. A. Kashi, and A. Ramazani, "The effect of temperature and concentration on the self-organized pore formation in anodic alumina," *J. Phys. D: Appl. Phys.*, vol. 38, pp. 2396-2399, 2005.

[19] X. Zhao, S.-K. Seo, U.-J. Lee, and K.-H. Lee, "Controlled Electrochemical Dissolution of Anodic Aluminum Oxide for Preparation of Open-Through Pore Structures," *J. Electrochem. Soc.*, vol. 154, pp. C553-C557, 2007.

[20] M. Shaban, H. Hamdy, F. Shahin, J. Park, and S. W. Ryu, "Uniform and Reproducible Barrier Layer Removal of Porous Anodic Alumina Membrane," *J. Nanosci. Nanotech.*, vol. 10, pp. 3380-3384, 2010.

[21] A. Santos, L. Vojkuvka, J. Pallares, J. Ferré-Borrull, and L. F. Marsal, "In situ electrochemical dissolution of the oxide barrier layer of porous anodic alumina fabricated by hard anodization," *J. Electroana. Chem.*, vol. 632, pp. 139-142, 2009.

[22] J. Zhang, J. E. Kielbasa, and D. L. Carroll, "Controllable fabrication of porous alumina templates for nanostructures synthesis," *Mater. Chem. Phys.*, vol. 122, pp. 295-300, February 2010.

[23] H. Masuda, F. Hasegwa, and S. Ono, "Self-Ordering of Cell Arrangement of Anodic Porous Alumina Formed in Sulfuric Acid Solution," *J. Electrochem. Soc.*, vol. 144, pp. L127-L130, 1997.

[24] G. D. Sulka, and K. G. Parkola, "Anodising potential influence on well-oredered nanostructures formed by anodization of aluminum in sulfuric acid," *Thin Solid Films*, vol. 515, pp. 338-345, 2006.

[25] H. Masuda, K. Yada, and A. Osaka, "Self-Ordering of Cell Configuration of Anodic Porous Alumina with Large-Size Pores in Phosphoric Acid Solution," *Jpn. J. Appl. Phys.*, vol. 37, pp. L1340-L1342, 1998.

[26] K. Nielsch, J. Choi, K. Schwirn, R. B. Wehrspohn, and U. Gösele, "Self-ordering Regimes of Porous Alumina: The 10% Porosity Rule," *Nano Lett.*, vol. 2, pp. 677-680, 2002.

[27] L. Zaraska, G. D. Sulka, and M. Jaskula, "The effect of n-alcohols on porous anodic alumina formed by self-organized two-step anodizing of aluminum in phosphoric acid," *Surf. Coat. Technol.*, vol. 204, pp. 1729-1737, 2010.

[28] W. Lee, R. Ji, U. Gösele, and K. Nielsch, "Fast fabrication of long-range ordered porous alumina templates by hard anodization," *Nature Mat*., vol. 5, pp. 741-747, 2006.

[29] D. Crouse, Y.-H. Lo, A. E. Miller, and M. Crouse, "Self-ordered pore structure of anodized aluminum on silicon and pattern transfer," *Appl. Phys. Lett.*, vol. 76, pp. 49-51, 2000.

[30] W. Lee, K. Nielsch, and U. Gösele, "Self-ordering behavior of nanoporous anodic aluminum oxide (AAO) in malonic acid anodization," *Nanotech.*, vol. 18, pp. 475713-475720, 2007.

[31] S. Ono, M. Saito, M. Ishiguro, and H. Asoh, "Controlling factor of self-ordering of anodic porous alumina," *J. Electrochem. Soc.*, vol. 151, pp. B473-B478, 2004.

[32] N. B. Pilling, and R. E. Bedworth, "The Oxidation of Metals at High Temperatures," *J. Inst. Met.*, vol. 29, pp. 529-591, 1923.

[33] C. Xu, and W. Gao, "Pilling-Bedworth ratio for oxidation of alloys," *Mat. Res. Innovat.*, vol. 3, pp. 231-235, 2000.

[34] Z. Su, G. Hähner, and W. Zhou, "Investigation of the pore formation in anodic aluminum oxide," *J. Mater. Chem.*, vol. 18, pp. 5787-5795, 2008.

[35] Z. Su, and W. Zhou, "Formation Mechanism of Porous Anodic Aluminum and Titanium Oxides," *Adv. Mater.*, vol. 20, pp. 3663-3667, 2008.

[36] V. P. Parkhutik, and V. I. Shershulsky, "Theoretical modeling of porous oxide growth on aluminum," *J. Phys. D: Appl. Phys.*, vol. 25, pp.1258-1263, 1992.

[37] J. H. Yuan, F. Y. He, D. C. Sun, and X. H. Xia, "A Simple Method for Preparation of Through-Hole Porous Anodic Alumina Membrane," *Chem. Mater.*, vol. 16, pp. 1841-1844, 2004.

[38] H. Masuda, and M. Satoh, "Fabrication of gold nanodot array using anodic porous alumina as an evaporation mask ," *Jpn. J. Appl. Phys.*, vol. 35, pp. L126-L129, 1996.

[39] Y. C. Sui, and J. M. Saniger, "Characterization of anodic porous alumina by AFM," *Mater. Lett.*, vol. 48, pp. 127-136, 2001.

[40] L. Zaraska, G. D. Sulka, and M. Jaskula, "Anodic alumina templates with defined pore diameters and thicknesses obtained by adjusting the anodizing duration and pore opening/widening time," *J. Solid. State Electrochem.*, vol. 15, pp. 2427-2436, 2011.

[41] A. Dekker, and A. Middelhoek, "Transport Numbers and the Structure of Porous Anodic Films on Aluminum," *J. Electrochem. Soc.*, vol. 117, pp. 440-448, 1970.

[42] H. Takahashi, and M. Nagayama, "The Determination of the Porosity of Anodic Oxide Films on Aluminum by the Pore-Filling Method," *Corros. Sci.*, vol. 18, pp. 911, 1978.

[43] J. H. Yuan, W. Chen, R. J. Hui, Y. L. Hu, and X. H. Xia, "Mechanism of one-step voltage pulse detachment of porous anodic alumina templates," *Electrochi. Acta*, vol. 51, pp. 4589-4595, 2006.

[44] S. Zhao, K. Chan, A. Yelon, and T. Veres, "Preparation of open-through anodized aluminum oxide films with a clean method," *Nanotech.*, vol. 18, pp. 245304, 2007.

[45] H. de L. Lira, and R. Paterson, "New and modified anodic alumina templates Part III. Preparation and characterization by gas diffusion of 5 nm pore size anodic alumina templates," *J. Membr. Sci.*, vol. 206, pp. 375-387, 2002.

[46] L.-M. Gao, P.-P. Wang, X.-Q. Wu, and X.-P. Song, "Electro-chemical detachment process of through-hole porous anodic alumina membrane," *J. Inorg. Mater.*, vol. 20, pp. 1417-1422, 2005.

[47] M. M. Crouse, A. E. Miller, D. T. Crouse, and A. A. Ikram, "Nanoporous Alumina Template with In Situ Barrier Oxide Removal, Synthesized from a Multilayer Thin Film Precursor," *J. Electrochem. Soc.*, vol. 152, pp. D167-D172, 2005.

[48] S. Wen, and J. A. Szpunar, "Direct electrodeposition of highly ordered magnetic nickel nanowires on silicon wafer," *Micro Nano Lett.*, vol. 1, pp. 89-93, 2006.

[49] Y. Yang, H. Chen, Y. Mei, J. Chen, X. Wu, and X. Bao, "Anodic alumina template on Au/Si substrate and preparation of CdS nanowires," *Sol. State Comm.*, vol. 123, pp. 279-282, 2002.

[50] O. Rabin, P. R. Herz, Y.-M. Lin, A. I. Akinwande, S. B. Cronin, and M. S. Dresselhaus, "Formation of Thick Porous Anodic Alumina Films and Nanowire Arrays on Silicon Wafers and Glass," *Adv. Funct. Mater.*, vol. 13, pp. 631-638, 2003.

[51] K. Kim, M. Kim, and S. M. Cho, "Pulsed electrodeposition of palladium nanowires arrays using AAO template," *Mater. Chem. Phys.*, vol. 96, pp. 278-282, 2006.

[52] S. Z. Chu, K. Wada, S. Inoue, and S. Todoroki, "Formation and Microstructures of Anodic Alumina Films from Aluminum Sputtered on Glass Substrate," *J. Electrochem. Soc.*, vol. 149, pp. B321-B327, 2002.

[53] T. R. B. Foong, A. Sellinger, and X. Hu, "Origin of the Bottlenecks in Preparing Anodized Aluminum Oxide (AAO) Templates on ITO Glass," *Ame. Chem. Soc.*, vol. 2, pp. 2250-2256, 2008.

[54] A. N. Banerjee, and S. W. Joo, "Auto-barrier-thinning effect under rapid anodization of nanoporous alumina membrane," *Phys. Stat. Sol.*, vol. 5, pp. 238-240, (2011).

[55] S. Z. Chu, K. Wada, S. Inoue, and S. Todoroki, "Fabrication and characteristics of nanostructures on glass by Al anodization and electrodeposition," *Electrochim. Acta*, vol. 48, pp. 3147-3153, 2003.

[56] M. S. Sander, and L.-S. Tan, "Nanoparticle Arrays on Surfaces Fabricated Using Anodic Alumina Films as Templates," *Adv. Funct. Mater.*, vol. 13, pp. 393-397, 2003.

[57] A. P. Li, F. Müller, and U. Gösele, "Polycrystalline and Monocrystalline Pore Arrays with Large Interpore Distance in Anodic Alumina," *Electrochem. Sol. State Lett.*, vol. 3, pp. 131-134, 2000.

[58] N. Taşaltın, S. Öztürk, N. Kılınç, H. Yüzer, and Z. Z. Öztürk, "Fabrication of vertically aligned Pd nanowires array in AAO template by electrodeposition using neutral electrolyte," *Nano. Res. Lett.*, vol. 5, pp. 1137-1143, 2010.

[59] J. P. Wu, I. W. M. Brown, T. Kemmitt, and M. E. Bowden, "Hierarchical Anodic Alumina Template-assisted Fabrication of Nanowires," *Inter. Conf. Nanosci. Nanotech.*, pp. 29-32, 2010.

[60] G. Meng, A. Cao, J.-Y. Cheng, A. Vijayaraghavan, Y. J. Jung, M. Shima, and P. M. Ajayan, "Ordered Ni nanowires tip arrays sticking out of the anodic aluminum oxide template," *J. Appl. Phys.*, vol. 97, pp. 064303, March 2005.

[61] C.-W. Hsu, Z.-D. Chou, and G.-J. Wang, "Fabrication of High-Aspect-Ratio Alumina-Nickel Coaxial Nanorod Array by Electrodeposition," *J. Microelectromech. Sys.*, vol. 19, pp. 849-853, August 2010.

[62] C. G. Jin, W. F. Liu, C. Jia, X. Q. Xiang, W. L. Cai, L. Z. Yao, and X. G. Li, "High-filling, large-area Ni nanowires arrays and the magnetic properties," *J. Crys. Grow.*, vol. 258, pp. 337-341, 2003.

[63] F. Li, R. M. Metzger, and W. D. Doyle, "Influence of Particle Size on the Magnetic Viscosity and Activation Volume of α-Fe Nanowires in Alumite Films," *IEEE Trans. Magn.*, vol. 33, pp. 3715-3717, 1997.

[64] I. Kaitsu, R. Inamura, J. Toda, and T. Morita, "Ultra High Density Perpendicular Magnetic Recording Technologies," *Fujitsu Sci. Tech. J.*, vol. 42, pp. 122-130, 2006.

[65] H. J. Richter, "The transition from longitudinal to perpendicular recording," *J. Phys. D: Appl. Phys.*, vol. 40, pp. R149-R177, 2007.

[66] S. Dubois, J. M. Beuken, L. Piraux, J. L. Duvail, A. Fert, J. M. George, and J. L. Maurice, "Perpendicular giant magnetoresistance of NiFe/Cu and Co/Cu multilayered nanowires," *J. Magn. Magn. Mater.*, vol. 165, pp. 30-33, 1997.

[67] A. Blondel, J. P. Meier, B. Doudin, and J.-Ph. Ansermet, "Giant Magnetoresistance of Nanowires of Multilayers," *Appl. Phys. Lett.*, vol. 65, pp. 3019-3021, 1994.

[68] F. J. García-Vidal, and J. B. Pendry, "Collective Theory for Surface Enhanced Raman Scattering," *Phys. Rev. Lett.*, vol. 77, pp. 1163-1166, 1996.

[69] M. Kahl, and E. Voges, "Analysis of plasmon resonance and surface-enhanced Raman scattering on periodic silver structures," *Phys. Rev. B*, vol. 61, pp. 14078-14088, 2000.

[70] D. A. Genov, A. K. Sarychev, V. M. Shalaev, and A. Wei, "Resonant Field Enhancements from Metal Nanoparticle Arrays," *Nano Lett.*, vol. 4, pp. 153-158, 2004.

[71] H.-H. Wang, C.-Y. Liu, S. B. Wu, N.-W. Liu, C.-Y. Peng, T.-H. Chan, C.-F. Hsu, J.-K. Wang, and Y.-L. Wang, "Highly Raman-Enhancing Substrates Based on Silver Nanoparticle Arrays with Tunable Sub-10 nm Gaps," *Adv. Mater.*, vol. 18, pp. 491-495, 2006.

[72] G. Sauer, G. Brehm, S. Schneider, H. Graener, G. Seifert, K. Nielsch, J. Choi, P. Göring, U. Gösele, P. Miclea, and R. B. Wehrspohn, "In situ surface-enhnaced Raman spectroscopy of monodisperse silver nanowire arrays," *J. Appl. Phys.*, vol. 97, pp. 024308, 2005.

[73] X. Ao, and S. He, "Negative refraction of left-handed behavior in porous alumina with infiltrated silver at an optical wavelength," *Appl. Phys. Lett.*, vol. 87, pp. 101112, 2005.

[74] L. Menon, W. T. Lu, A. L. Friedman, S. P. Bennett, D. Heiman, and S. Sridhar, "Negative index metamaterials based on metal-dielectric nanocomposites for imaging applications," *J. Appl. Phys.*, vol. 93, pp. 123117, 2008.

[75] J. Yao, Z. Liu, Y. Liu, Y. Wang, C. Sun, G. Bartal, A. M. Stacy, and X. Zhang, "Optical Negative Refraction in Bulk Metamaterials of Nanowires," *Science*, vol. 321, pp. 930, 2008.

[76] L. Qin, S. Park, L. Huang, and C. A. Mirkin, "On-Wire Lithography," *Science*, vol. 309, pp. 113-115, 2005.

[77] L. Qin, S. Zou, C. Xue, A. Atkinson, G. C. Schatz, and C. A. Mirkin, "Designing, fabricating, and imaging Raman hot spots," *Proc. Nat. Acad. Sci.*, vol. 103, pp. 13300-13303, 2006.

[78] S. R. Nicewarner-Peña, R. G. Freeman, B. D. Reiss, L. He, D. J. Peña, I. D. Walton, R. Cromer, C. D. Keating, and M. J. Natan, "Submicrometer Metallic Barcodes," *Science*, vol. 294, pp. 137-141, 2001.

[79] J. J. Mock, S. J. Oldenburg, D. R. Smith, D. A. Schultz, and S. Schultz, "Composite Plasmon Resonant Nanowires," *Nano Lett.*, vol. 2, pp. 465-469, 2002.

[80] L. Vila, P. Vincent, L. D.-D. Pra, G. Pirio, E. Minoux, L. Gangloff, S. Demoustier-Champagne, N. Sarazin, E. Ferain, R. Legras, L. Piraux, and P. Legagneux, "Growth and Field-Emission Properties of Vertically Aligned Cobalt Nanowire Arrays," *Nano Lett.*, vol. 4, pp. 521-524, 2004.

[81] N. V. Quy, N. D. Hoa, W. J. Yu, Y. S. Cho, G. S. Choi, and D. Kim, "The use of anodic aluminum oxide templates for triode-type carbon nanotube field emission structures toward mass-production technology," *Nanotechnology*, vol. 17, pp. 2156-2160, 2006.

[82] S. Mátéfi-Tempfli, M. Mátéfi-Tempfli, and L. Piraux, "Fabrication of nanowires and nanostructures: combining template synthesis with pattering methods," *Appl. Phys. A*, vol. 96, pp. 603-608, 2009.

[83] D. Kim, J.-E. Bourée, and S. Y. Kim, "Calculation of the field enhancement for a nanotubes array and its emission properties," *J. Appl. Phys.*, vol. 105, pp. 084315, 2009.

[84] F. Favier, E. C. Walter, M. P. Zach, T. Benter, and R. M. Penner, "Hydrogen Sensors and Switches from Electrodeposited Palladium Mesowire Arrays," *Science*, vol. 293, pp. 2227-2231, 2001.

[85] K. T. Kim, S. J. Sim, and S. M. Cho, "Hydrogen Gas Sensor Using Pd Nanowires Electro-Deposited Into Anodized Alumina Template," *IEEE Sens. J.*, vol. 6, pp. 509-513, 2006.

[86] A. Kolmakov, Y. Zhang, G. Cheng, and M. Moskovits, "Detection of CO and O_2 Using Tin Oxide Nanowire Sensors," *Adv. Mater.*, vol. 15, pp. 997-1000, 2003.

[87] J. S. Tresback, and N. P. Padture, "Low-temperature gas sensing in individual metal-oxide-metal heterojunction nanowires," *J. Mater. Res.*, vol. 23, pp. 2047-2052, 2008.

[88] K. Nielsch, F. Müller, A.-P. Li, and U. Gösele, "Uniform Nickel Deposition into Ordered Alumina Pores by Pulsed Electrodeposition," *Adv. Mater.*, vol. 12, pp. 582-586, 2000.

[89] S. Gayen, M. K. Sanyal, B. Satpati, and A. Rahman, "Diameter-dependent coercivity of cobalt nanowires," *Appl. Phys. A*, vol. 112, pp. 775-780, 2013.

[90] C. Schönenberger, B. M. I. van der Zande, L. G. J. Fokkink, M. Henny, C. Schmid, M. Krüger, A. Bachtold, R. Huber, H. Birk, and U. Staufer, "Template Synthesis of Nanowires in Porous Polycarbonate Templates: Electrochemistry and Morphology," *J. Phys. Chem.*, vol. 101, pp. 5497-5505, 1997.

[91] J. Choi, G. Sauer, K. Nielsch, R. B. Wehrspohn, and U. Gösele, "Hexagonally Arranged Monodisperse Silver Nanowires with Adjustable Diameter and High Aspect Ratio," *Chem. Mater.*, vol. 15, pp. 776-779, 2003.

[92] O. C. Trusca, D. Cimpoesu, J.-H. Lim, X. Zhang, J. B. Wiley, A. Diaconu, I. Dumitri, A. Stancu, and L. Spinu, "Interaction Effects in Ni Nanowire Arrays," *IEEE Trans. Magn.*, vol. 44, pp. 2730-2733, 2008.

[93] J. Qin, J. Nogues, M. Mikhaylova, A. Roig, J. S. Muñoz, and M. Muhammed, "Differences in the Magnetic Properties of Co, Fe, and Ni 250-300 nm Wide Nanowires Electrodeposited in Amorphous Anodized Alumina Templates," *Chem. Mater.*, vol. 17, pp. 1829-1834, 2005.

[94] S.-G. Cho, B. Yoo, K. H. Kim, and J. Kim, "Magnetgic and Microwave Properties of NiFe Nanowires Embedded in Anodized Aluminum Oxide (AAO) Templates," *IEEE Trans. Magn.*, vol. 46, pp. 420-423, 2010.

[95] C.-G. Wu, H. L. Lin, and N.-L. Shau, "Magnetic nanowires via template electrodeposition," *J. Solid State Electrochem.*, vol. 10, pp. 198-202, August 2005.

[96] H. D. Yan, P. Lemmens, H. Dierke, S. C. White, F. Ludwig, and M. Schilling, "Iron/Nickel Nanowire Growth in Anodic Aluminum Oxide Templates: Transfer of Length Scales and Periodicity," *J. Phys.*, vol. 145, pp. 012079, 2009.

[97] J. Liu, F. Wang, J. Zhai, and J. Ji, "Controllable growth and magnetic characterization of electrodeposited nanocrystalline Ni-P nanotubes and nanowire arrays inside AAO template," *J. Electroanaly. Chem.*, vol. 642, pp. 103-108, February 2010.

[98] A. Fert, and L. Piraux, "Magnetic nanowires," *J. Magn. Magn. Mater.*, vol. 200, pp. 338-358, 1999.

[99] S. Yang, H. Zhu, D. Yu, Z. Jin, S. Tang, and Y. Du, "Preparation and magnetic property of Fe nanowire array," *J. Magn. Magn. Mater.*, vol. 222, pp. 97-100, 2000.

[100] J. U. Cho, J.-H. Wu, J. H. Min, S. P. Ko, J. Y. Soh, Q. X. Liu, and Y. K. Kim, "Control of magnetic anisotropy of Co nanowires," *J. Magn. Magn. Mater.*, vol. 303, pp. e281-e285, 2006.

[101] D. N. Davydov, P. A. Sattari, D. AlMawlawi, A. Osika, T. L. Haslett, and M. Moskovits, "Field emitters based on porous aluminum oxide templates," *J. Appl. Phys.*, vol. 86, pp. 3983-3987, 1999.

[102] A. Ramazani, M. A. Kashi, M. Alikhani, and S. Erfanifam, "Fabrication of high aspect ratio Co nanowires with cotrolled magnetization direction using ac and pulse electrodeposition," *Mater. Chem. Phys.*, vol. 112, pp. 285-289, 2008.

[103] D. AlMawlawi, N. Coombs, and M. Moskovits, "Magnetic properties of Fe deposited into anodic aluminum oxide pores as a function of particle size," *J. Appl. Phys.*, vol. 70, pp. 4421-4425, 1991.

[104] X. Y. Zhang, G. H. Wen, Y. F. Chan, R. K. Zheng, X. X. Zhang, and N. Wang, "Fabrication and magnetic properties of ultrathin Fe nanowire arrays," *Appl. Phys. Lett.*, vol. 83, pp. 3341-3343, 2003.

[105] D. AlMawlawi, C. Z. Liu, and M. Moskovits, "Nanowires formed in anodic oxide nanotemplates," *J. Mater. Res.*, vol. 9, pp. 1014-1018, 1994.

[106] C. K. Preston, and M. Moskovits, "Optical Characterization of Anodic Aluminum Oxide Films Containing Electrochemically Deposited Metal Particles. 1. Gold in Phosphoric Acid Anodic Aluminum Oxide Films," *J. Phys. Chem.*, vol. 97, pp. 8495-8503, 1993.

[107] M. Sun, G. Zangari, M. Shamsuzzoha, and R. M. Metzger, "Electrodeposition of highly uniform magnetic nanoparticle arrays in ordered alumite," *Appl. Phys. Lett.*, vol. 78, pp. 2964-2966, 2001.

[108] A. J. Yin, J. Li, W. Jian, A. J. Bennett, and J. M. Xu, "Fabrication of highly ordered metallic nanowire arrays by electrodeposition," *Appl. Phys. Lett.*, vol. 79, pp. 1039-1041, 2001.

[109] R. M. Metzger, V. V. Konovalov, M. Sun, T. Xu, G. Zangari, B. Xu, M. Benakli, and W. D. Doyle, "Magnetic Nanowires in Hexagonally Ordered Pores of Alumina," *IEEE Trans. Magn.*, vol. 36, pp. 30-35, 2000.

[110] N. Kallithrakas-Kontos, R. Moshohoritou, V. Ninni, and I. Tsangaraki-Kaplanoglou, "Investigation of the relationship between the reflectance and the deposited nickel and tin amount on the aluminum anodic oxide film," *Thin Solid Films*, vol. 326, pp. 166-170, 1998.

[111] G. P. Sklar, K. Paramguru, M. Misra, and J. C. LaCombe, "Pulsed electrodeposition into AAO templates for CVD growth of carbon nanotubes arrays," *Nanotechnology*, vol. 16, pp. 1265-1271, 2005.

[112] J. M. Baik, M. Schierhorn, and M. Moskovits, "Fe Nanowires in Nanoporous Alumina: Geometric Effect versus Influence of Pore Walls," *J. Phys. Chem. C*, vol. 112, pp. 2252-2255, 2008.

[113] D. C. Leitao, C. T. Sousa, J. Ventura, J. S. Amaral, F. Carpinteiro, K. R. Pirota, M. Vazquez, J. B. Sousa, and J. P. Araujo, "Characterization of electrodeposited Ni and $Ni_{80}Fe_{20}$ nanowires," *J. Non-Crystalline Solids*, vol. 354, pp. 5241-5243, 2008.

[114] G. P. Hatch, and R. E. Stelter, "Magnetic design considerations for devices and particles used for biological hig-gradient magnetic separation (HGMS) systems," *J. Magn. Magn. Mater.*, vol. 225, pp. 262-276, 2001.

[115] E. C. Stoner, and E. P. Wohlfarth, "A Mechanism of Magnetic Hysteresis in Heterogeneous Alloys," *Phil. Trans. R. Soc.*, vol. 240, pp. 599-642, 1948.

[116] E. W. Lee, "Magnetostriction and Magnetomechanical Effects," *Rep. Prog. Phys.*, vol. 18, pp. 184-229, 1955.

[117] W. H. Meiklejohn, and C. P. Bean, "New Magnetic Anisotropy," *Phys. Rev.*, vol. 105, pp. 904-913, 1957.

[118] J. S. Kouvel, C. D. Graham, and I. S. Jacobs, "Ferromagnetism and Antiferromagnetism in Disordered Ni-Mn Alloys," *J. Phys. Rad.*, vol. 20, pp. 198-202, 1959.

[119] T. Li, Y. Sui, Z. Huang, S. Yang, B. Gu, and Y. Du, "Spin-configuration-related ferromagnetic resonance in nickel nanowire array," *J. Phys.: Condens. Matter.*, vol. 17, pp. 3637-3645, 2005.

[120] L.-P. Carignan, C. Lacroix, A. Ouimet, M. Ciureanu, A. Yelon, and D. Ménard, "Magnetic anisotropy in arrays of Ni, CoFeB, and Ni/Cu nanowires," *J. Appl. Phys.*, vol. 102, pp. 023905, 2007.

[121] A. Sklyuyev, M. Ciureanu, C. Akyel, P. Ciureanu, and A. Yelon, "Microwave studies of magnetic anisotropy of Co nanowire arrays," *J. Appl. Phys.*, vol. 105, pp. 023914, 2009.

[122] S. Pathak, and M. Sharma, "Electron spin resonance in electrodeposited cobalt nanowire arrays," *Adv. Mat. Lett.*, vol. 3, pp. 526-532, 2012.

[123] M. Demand, A. Encinas-Oropesa, S. Kenane, U. Ebels, I. Huynen, and L. Piraux, "Ferromagnetic resonance studies of nickel and permalloy nanowire arrays," *J. Magn. Magn. Mater.*, vol. 249, pp. 228-233, 2002.

[124] C. A. Ramos, M. Vazquez, K. Nielsch, K. Pirota, J. Rivas, R. B. Wehrspohn, M. Tovar, R. D. Sanchez, and U. Gösele, "FMR characterization of hexagonal arrays of Ni nanowires," *J. Magn. Magn. Mater.*, vol. 272-276, pp. 1652-1653, 2004.

[125] U. Ebels, J.-L. Duvail, P. E. Wigen, L. Piraux, L. D. Buda, and K. Ounadjela, "Ferromagnetic resonance studies of Ni nanowire arrays," *Phys. Rev. B.*, vol. 64, pp. 144421, 2001.

[126] A. Encinas-Oropesa, M. Demand, L. Piraux, I. Huynen, and U. Ebels, "Dipolar interactions in arrays of nickel nanowires studied by ferromagnetic resonance," *Phys. Rev. B*, vol. 63, pp. 104415, 2001.

[127] J. Smit, and H. G. Beljers, "Ferromagnetic resonance absorption in BaFe12O19, a highly anisotropic crystal," *Philips Res. Rep.*, vol. 10, pp. 113-130, 1955.

[128] A. Popa, M. Jivanescu, D. Toloman, O. Raita, and L. M. Giurgiu, "Ferromagnetic resonance measurements on Co nanowires," *J. Phys.*, vol. 182, pp. 012073, 2009.

[129] G. Ababei, A. Popa, N. Lupu, L. M. Giurgiu, and H. Chiriac, "Ferromagnetic resonance of NiFe/Cu multilayered nanowires," *J. Optoelect. Adv. Mater.*, vol. 13, pp. 405-408, 2011.

[130] I. Dumitru, F. Li, J. B. Wiley, D. Cimpoesu, A. Stancu, and L. Spinu, "Study of Magnetic Interactions in Metallic Nanowire Networks," *IEEE Trans. Magn.*, vol. 41, pp. 3361-3363, 2005.

[131] B. Viala, A. S. Royet, R. Cuchet, M. Aïd, P. Gaud, O. Valls, M. Ledieu, and O. Acher, "RF Planar Ferromagnetic Inductors on Silicon," *IEEE Trans. Magn.*, vol. 40, no. 4, pp. 1999-2001, Jul. 2004.

[132] V. Korenivski, "GHz magnetic film inductors," *J. Magn. Magn. Mater.*, vol. 215-216, pp. 800-806, 2000.

[133] R.-F. Jiang, N. N. Shams, M. T. Rahman, and C.-H. Lai, "Exchange-Coupled IrMn/CoFe Multilayers for RF-Integrated Inductors," *IEEE Trans. Magn.*, vol. 43, no. 10, pp. 3930-3932, Oct. 2007.

[134] D. S. Gardner, G. Schrom, P. Hazucha, F. Paillet, T. Karnik, and S. Borkar, "Integrated On-Chip Inductors With Magnetic Films," *IEEE Trans. Magn.*, vol. 43, no. 6, pp. 2615-2617, Jun. 2007.

[135] W. Xu, S. Sinha, T. Dastagir, H. Wu, B. Bakkaloglu, D. S. Gardner, Y. Cao, and H. Yu, "Performance Enhancement of On-Chip Inductors With Permalloy Magnetic Rings," *IEEE Electron Device Lett.*, vol. 32, no. 1, pp. 69-71, Jan. 2011.

[136] M. Yamaguchi, M. Baba, and K.-I. Arai, "Sandwich-Type Ferromagnetic RF Integrated Inductor," *IEEE Trans. Microw. Theory Tech.*, vol. 49, no. 12, pp. 2331-2335, Dec. 2001.

[137] A. M. Crawford, D. Gardner, and S. X. Wang, "High-Frequency Microinductors With Amorphous Magnetic Ground Planes," *IEEE Trans. Magn.*, vol. 38, no. 5, pp. 3168-3170, Sep. 2002.

[138] H. Wu, D. S. Gardner, W. Xu, and H. Yu, "Integrated RF On-Chip Inductors With Patterned Co-Zr-Ta-B Films," *IEEE Trans. Magn.*, vol. 48, no. 11, pp. 4123-4126, Nov. 2012.

[139] M. C. Hsu, T. Y. Chao, Y. T. Cheng, C. M. Liu, and C. Chen, "The Inductance Enhancement Study of Spiral Inductor Using Ni-AAO Nanocomposite Core," *IEEE Trans. Nanotech.*, vol. 8, no. 3, pp. 281-285, May 2009.

[140] D. S. Gardner, G. Schrom, P. Hazucha, F. Paillet, T. Karnik, S. Borkar, R. Hallstein, T. Dambrauskas, C. Hill, C. Linde, W. Worwag, R. Baresel, and S. Muthukumar, "Integrated on-chip inductors using magnetic material (invited)," *J. Appl. Phys.*, vol. 103, 07E927, 2008.

[141] P. Pereira, M. H. Fino, and F. V. Coito, "Using Discrete-Variable Optimization for CMOS Spiral Inductor Design," *Proc. Int. Conf. Microelectron. ICM*, pp. 324-327, 2009.

[142] G. Stojanovic, and L. Zivanov, "Comparison of Optimal Design of Different Spiral Inductors," *24th Int. Conf. Microelectron.*,vol. 2, pp. 16–19, May 2004.

[143] M. del Mar Hershenson, S. S. Mohan, S. P. Boyd, and T. H. Lee, "Optimization of Inductor Circuits via Geometric Programming," *Proc. 1999 Des. Autom. Conf.*, pp. 994-998, 1999.

[144] C. Patrick Yue, and S. Simon Wong, "Physical Modeling of Spiral Inductors on Silicon," *IEEE Trans. Electron Devices.*, vol. 47, pp. 560-568, March 2000.

[145] S.S. Mohan, M.D.M. Hershenson, S.P. Boyd, and T.H. Lee, "Simple Accurate Expressions for Planar Spiral Inductances," *IEEE J. Solid-State Circuits*, vol. 34, pp. 1419-1420, Oct. 1999.

[146] S. Jenei, B. K. J. C. Nauwelaers, and S. Decoutere, "Physics-Based Closed-Form Inductance Expression for Compact Modeling of Integrated Spiral Inductors," IEEE J. Solid-State Circuits," vol. 37, pp. 73-76, 2002.

[147] H. M. Greenhouse, "Design of Planar Rectangular Microelectronic Inductors," *IEEE Trans. Parts, Hybrids, and Packaging*, vol. PHP-10, pp. 101-109, June 1974.

[148] F. W. Grover, "Inductance Calculations: working Formulas and Tables," Van Nostrand, Princeton, N. J., 1946, Dover, New York, N. Y., 1962.

[149] H. E. Bryan, "Printed Inductors and Capacitors," *Tele-Tech. Electron. Ind.*, vol. 68, Dec. 1955.

[150] S. Asgaran, "New Accurate Physics-Based Closed-Form Expressions for Compact Modelling and Design of On-chip Spiral Inductors," *Proc. 14th Inter. Conf. Microelectron.*, pp. 247-250, Dec. 2002.

[151] S. S. Mohan, "The Design, Modelling and Optimization of On-chip Inductor and Transformer Circuits," Ph.D. Thesis, Stanford University, Dec. 1999.

[152] G. F. Engen, and C. A. Hoer, "Thru-Reflect-Line: An Improved Technique for Calibrating the Dual Six-Port Automatic Network Analyzer," *IEEE Trans. Microwave Theory and Techniques*, vol. MTT-27, pp. 987-993, Dec. 1979.

[153] C. B. Sia, B. H. Ong, K. W. Chan, K. S. Yeo, J.-G. Ma, and M. A. Do, "Physical Layout Design Optimization of Integrated Spiral Inductors for Silicon-Based RFIC Applications," *IEEE Trans. Electron Devices*, vol. 52, pp. 2559-2567, Dec. 2005.

[154] A. M. Niknejad, and R. G. Meyer, "Analysis, Design, and Optimization of Spiral Inductors and Transformers for Si RFIC's," *IEEE J. Solid-State Circuits*, vol. 33, pp. 1470-1481, Oct. 1998.

[155] M.-C. Hsieh, Y.-K. Fang, C.-H. Chen, S.-M. Chen, and W.-K. Yeh, "Design and Fabrication of Deep Submicron CMOS Technology Compatible Suspended High-Q Spiral Inductors," *IEEE Trans. Electron Devices*, vol. 51, pp. 324-331, March 2004.

[156] E. W. Becker, W. Ehrfeld, P. Hagmann, A. Maner, and D. Münchmeyer, "Fabrication of microstructures with high aspect ratios and great structural heights by synchrotronradiation lithography, galvanoforming, and plastic moulding (LIGA process)," *Microelect. Eng.*, vol. 4, pp. 35-56, May 1986.

[157] T. R. Dietrich, W. Ehrfeld, M. Lacher, M. Krämer, and B. Speit, "Fabrication technologies for microsystems utilizing photoetchable glass," *Microelect. Eng.*, vol. 30, pp. 497-504, January 1996.

[158] H. Lorenz, M. Despont, N. Fahmi, N. LaBianca, P. Renaud, and P. Vettiger, "SU-8: a low-cost negative resist for MEMS," *Micromech. and Miroeng.*, vol. 7, pp. 121-124, April 1997.

[159] J.-H. Pai, Y. Wang, G. T. Salazar, C. E. Sims, M. Bachman, G.P. Li, and N. L. Allbritton, "A Photoresist with Low Fluorescence for Bioanalytical Applications," *Anal. Chem.*, vol. 79, pp. 8774-8780, November 2007.

[160] S. Franssila, “Introduction to Microfabrication,” Second Ed., John Wiley & Sons, Hoboken, New Jersey, 2010.

[161] X. Li, T. Abe, and M. Esashi, :Deep reactive ion etching of Pyrex glass using SF_6 plasma,” *Sens. Act. A: Phys.*, vol. 87, pp. 139-145, January 2001.

[162] F. Laermer, and A. Urban, “Challenges, developments and applications of silicon deep reactive ion etching,” *Microelct. Eng.*, vol. 67-68, pp. 349-355, June 2003.

[163] A. K. Kasi, J. K. Kasi, N. Afzulpurkar, E. Bohez, A. Tuantranont, and B. Mahaisavariya, “Novel anodic aluminum oxide (AAO) nanoporous membrane for wearable hemodialysis device,” *ICCE*, pp. 98-101, August 2010.

[164] C.-W. Hsu, and G.-J. Wang, “Fabrication of Patterned Array of Alumina-Metal Coaxial Nanorods,” *DTIP of MEMS and MOEMS*, April 2009.

[165] S. Tan, M. Reed, H. Han, and R. Boudreau, “High Aspect Ratio Microstructures on Porous Anodic Aluminum Oxide,” *Proceedings of the 8th International Workshop on MEMS*, Amsterdam, pp. 267-272, 1995.

[166] A.-P. Li, F. Müller, A. Birner, K. Nielsch, and Ulrich Gösele, “Fabrication and Microstructuring of Hexagonally Ordered Two-Dimensional Nanopore Arrays in Anodic Alumina,” *Adv. Mater.*, vol. 11, pp. 483-487, 1999.